Queen Mary, University of London
Department of Electronic Engineering and Computer Science

Novel and Compact Reconfigurable Antennas for Future Wireless Applications

Tamer Aboufoul

October 2013

Submitted in part fulfilment of the requirements for the degree of
Doctor of Philosophy in Electronic Engineering and Computer Science of
Queen Mary, University of London

Declaration

I herewith certify that all material in this dissertation which is not my own work has been properly acknowledged.

Tamer Aboufoul

Abstract

The development of reconfigurable antennas is considered to be very promising in modern and future communication systems. Reconfigurable antennas have made use of many reconfiguration techniques that are centred upon switching mechanisms such as p-i-n diodes or MEMS. Other techniques such as optical switches, mechanical structure changing or the ability to change the permeability or permittivity of smart substrate materials have also been used. Reconfigurable antennas have created new horizons for many types of applications especially in Cognitive Radio, Multiple Input Multiple Output Systems, personal communication systems, satellites and many other applications.

Cognitive Radio is one of the potential wireless applications that may place severe demands on RF systems designers and particularly antenna designers, when it comes to providing flexible radio front-ends capable of achieving the set objectives of the technology. The aim of this work is to investigate possible roles that different categories of reconfigurable antenna can play in cognitive and smart radio. Hence, the research described in this thesis focuses on investigating some novel methods to frequency-reconfigure compact ultra-wideband antennas to work in different bands; this will offer additional filtering to the radio front-end. In the ultra-wideband mode, the antenna senses the spectrum for available bands with less congestion and interference and hence decides on the most suitable part to be reconfigured to, allowing reliable and efficient communication links between the radio devices. Ultra-wideband antenna with reconfigurable integrated notch capability is also demonstrated to provide further enhancement to interference rejection and improve the overall communication link. Furthermore, the design of novel pattern and polarisation reconfigurable antennas will be also investigated to assist Cognitive Radio through spatial rather than frequency means.

An ultimate target for this research is to combine different degrees of re-

configuration into one compact, state of the art antenna design that meets the growing demand of cognitive and smart radio devices for more intelligent and multi-functional wireless devices within the personal area network domains and beyond.

Acknowledgement

First and foremost, I would like to express my deepest gratitude to my supervisor (Dr. Akram Alomainy) for his discussions, encouragement and valuable advice and guidance throughout my research. I would also like to thank Prof. Xiaodong Chen and Dr. Rostyslav Dubrovka for their positive and fruitful comments during my research. Also, thanks to Dr. Massimo Candotti for his assistance with measurement settings. Above all, I am grateful to my parents, my brothers, my sister and all my family for their continuous encouragement, support, love and sacrifice throughout my studies.

Tamer Aboufoul
London, July 2013

List of Publications

Journals

1. **T. Aboufoul**, A. Alomainy and C. Parini, "UWB Antenna for Cognitive Radio Applications Using GaAs FET Switches," *IEEE Antennas and Wireless Propagation Letters*, vol. 11, no. , pp. 392–394, 2012.

2. **T. Aboufoul**, A. Alomainy and C. Parini, "Reconfigured and Notched Tapered Slot UWB Antenna for Cognitive Radio Applications," *International Journal of Antennas and Propagation*, vol. 2012, Article ID 160219, 8 pages, 2012.

3. **T. Aboufoul**, A. Alomainy and C. Parini, "Polarisation Reconfigurable Ultra Wideband Antenna for Cognitive Radio Applications," *Microwave and optical technology letters*, vol. 55, pp. 501-506, Mar. 2013.

4. **T. Aboufoul**, A. Alomainy, X. Chen and C. Parini, "Pattern Reconfigurable Planar Circular Ultra-Wideband Monopole Antenna," *IEEE Transaction on Antennas and Propagation*, vol. 61, no. 10, pp. 4973–4980, October 2013.

5. **T. Aboufoul**, A. Alomainy, X. Chen and C. Parini, "Multiple-Parameter Reconfiguration in a Single Planar Ultra-Wideband Antenna for Advanced Wireless Communication Systems," *IET Microwaves, Antennas and Propagation, special issue on Emerging Integrated Reconfigurable Antenna Technologies*, under review.

Conferences

1. **T. Aboufoul** and A. Alomainy, "Single Element Reconfigurable Planar Ultra Wideband Antenna for Cognitive Radio Front End," *4th Intl. Conference on Cognitive Radio and Advanced Spectrum Management (CogART 2010)*, October 2011, Barcelona, Spain.

2. **T. Aboufoul** and A. Alomainy, "Printed UWB Circular Disc Monopole Antenna," *Antennas & Propagation Conference, 2011. LAPC 2011.* Loughborough , vol., no., pp. x-xx, 14–15 Nov. 2011.

3. **T. Aboufoul** and A. Alomainy, "Frequency Reconfigured UWB Circular Disc Monopole Antenna Using PIN Diodes and GaAs FET Switches," *Advanced Electromagnetics Symposium*, Paris, France, April, 2012.

4. **T. Aboufoul** and A. Alomainy, "Reconfigured and Notched Tapered Slot UWB Antenna," *IEEE International Symposium on Antennas and Propagation*, Chicago, USA. July 2012.

5. **T. Aboufoul**, Q. Abbasi, A. Alomainy and C. Parini "Frequency and Pattern Reconfigured Planar UWB Antenna Array for Future Cognitive Radio Portable Devices," *IEEE International Conference on Ultra-Wideband (ICUWB2012)*, Syracuse, NY USA, Sep. 2012

6. **T. Aboufoul**, I. Shoaib, A. Alomainy and X. Chen, "Pattern Reconfigurable Planar UWB Antenna Array for Future Cognitive Radio Portable Devices," *Antennas & Propagation Conference, LAPC 2012*, vol., no., pp. 1–4, 12–13 Nov. 2012.

7. **T. Aboufoul**, A. Alomainy and C. Parini,"A Planar Dual Fed UWB Monopole Antenna with Polarization Diversity for Cognitive Radio Sensing," *Antennas & Propagation Conference, LAPC 2012*, vol., no.,

pp. 1–4, 12–13 Nov. 2012.

8. **T. Aboufoul**, K. Ali, A. Alomainy and C. Parini, "Combined Pattern and Frequency Reconfiguration of Single Element Ultra Wideband Monopole Antenna for Cognitive Radio Devices," *7th European Conference on Antennas and Propagation (EuCAP), 2013*, Gothenburg Sweden, pp. 932–936, 8–11 April 2013.

9. **T. Aboufoul**, A. Alomainy, X. Chen and C. Parini, "Pattern Reconfiguration of a Single Element Ultra-Wideband Antenna for Cognitive Radio Applications, " *3rd Conference on Applied Radio Systems Research and Smart Wireless Communications ARSR-SWICOM*, Luton, Bedfordshire UK, May 2013.

10. **T. Aboufoul**, A. Alomainy and C. Parini, "Polarisation Reconfigurable Ultra Wideband Antenna for Cognitive Radio Devices," *International Symposium on Antennas and Propagation Society (APSURSI)*, Florida, USA, 7–13 July 2013.

11. **T. Aboufoul**, A. Alomainy, X. Chen and C. Parini, "Multi-Mode Reconfiguration of a Compact Ultra-wideband Antenna," *PIERS 2013*, Stockholm Sweden, 12–15 August 2013.

12. **T. Aboufoul**, A. Alomainy and C. Parini, "Reconfiguration of Ultra Wideband Antenna for Multi-band Operation in Cognitive Radio Application ," *8th European Conference on Antennas and Propagation (EuCAP), 2014*, accepted.

List of Abbreviations

3D	Three-Dimensional
ADS	Advanced Design System
AR	Axial Ratio
AUT	Antenna Under Test
AZO	Aluminium Zinc Oxide
BER	Bit Error Rate
BPF	Band-Pass Filter
CPW	Coplanar Waveguide
CP	Circular Polarisation
CPLD	Complex Programmable Logic Device
CR	Cognitive Radio
CST	Computer System Technology
DARPA	Defence Advanced Research Projects Agency
dB	decibel
dBi	decibel isotropic
dBic	decibel isotropic circular
dc	Direct Current
DCS	Digital Cellular Service
DGS	Defected Ground Structure
DSA	Dynamic Spectrum Access
DSP	Digital Signal Processing
EM	ElectroMagnetic

ETSI	European Telecommunications Standards Institute
FCC	Federal Communications Commission
FET	Field-Effect Transistor
FR4	Flame Retardant 4
FPGA	Field-Programmable Gate Array
GaAs	Gallium Arsenide
GPS	Global Positioning System
GSM	Global System for Mobile Communications
I/O	Input/Output
IEEE	Institute of Electrical and Electronics Engineers
IL	Insertion Loss
ISM	Industrial, Scientific and Medical
LHCP	Left Hand Circular Polarisation
LOS	Line of Sight
LP	Linear Polarisation
LPF	Low-Pass Filter
MEMs	MicroElectroMechanical systems
MIMO	Multiple Input Multiple Output
Ofcom	Office of Communications
PCB	Printed Circuit Board
PCS	Personal Communications Service
PET	PiezoElectric Transducer
PU	Primary User
QF	Quality Factor
QMUL	Queen Mary, University of London
QoS	Quality of Service
RF	Radio Frequency

RFID	Radio Frequency IDentification
RHCP	Right Hand Circular Polarisation
RL	Return Loss
RLC	Resistor, Inductor, and a Capacitor
SDR	Software Defined Radio
SGH	Standard Gain Horn
SMA	Sub Miniature version A
SNR	Signal to Noise Ratio
SOD-323	Small Outline Diode Package 323
SPDT	Single Pole Double Throw
SPST	Single Pole Single Throw
SRF	Self Resonant Frequency
TSA	Tapered Slot Antenna
TV	TeleVision
TVWS	TeleVision White Space
UK	United Kingdom
US	United States
USRP	Universal Software Radio Peripheral
UWB	Ultra-WideBand
VNA	Vector Network Analyser
VSWR	Voltage Standing Wave Ratio
Wi-Fi	Wireless Fidelity
WiMax	Worldwide Interoperability for Microwave Access
WLAN	Wireless Local Area Network
XG	neXt Generation

Contents

1 Introduction **31**

1.1 Background 31

1.1.1 Definition of Cognitive Radio 33

1.1.2 Evolution of Cognitive Radio 33

1.1.3 Advantages of Cognitive Radio 35

1.2 Motivation and Research Challenges 36

1.3 Organization of the Thesis 37

2 Review of Reconfigurable Antennas **40**

2.1 Introduction 40

2.2 Fundamentals of Antennas 41

2.3 Reconfigurable Antennas Characteristics 43

2.3.1 Types of Reconfigurable Antennas 44

2.3.2 Mechanisms for Reconfiguration 45

2.3.3 Linearity in Switching Devices 45

2.3.4 Reliability of Switching Devices 47

2.4 Review of Previously Designed Reconfigurable Antennas . . . 47

2.4.1 Frequency Reconfigurable Antennas 49

2.4.2 Pattern Reconfigurable Antennas 61

2.4.3 Polarisation Reconfigurable Antennas 66

2.4.4 Combination of Different Reconfigurable Antennas . . 68
2.5 Summary and Analysis 71

3 Frequency Reconfigurable Ultra-wideband Antennas 73
3.1 Introduction 73
3.2 Antenna Design 73
3.3 Principle of Operation 75
3.4 Numerical and Experimental Analysis 78
3.4.1 Ultra-wideband Operation 78
3.4.2 Reconfigurable Bands 79
3.4.3 Radiation Patterns and Gain 81
3.4.4 Surface Current 86
3.5 Reconfigurable Antenna Efficiency 88
3.5.1 The Wheeler Cap Method 89
3.5.2 Applying The Wheeler Cap Method to Wideband Antennas 91
3.5.3 Measurement Results of Frequency Reconfigurable Ultra-wideband Antenna Efficiency Using the Wideband Wheeler Cap Method 93
3.6 Applying p-i-n Diode Switches to Reconfigurable Antennas . 95
3.7 GaAs FET Switches for Frequency Reconfigurable Antennas . 101
3.7.1 Integrating GaAs FET Switches in the Antenna Design 103
3.7.2 Simulation and Experimental Results 104
3.8 Frequency Reconfiguration of Compact Co-planar Waveguide Fed (CPW-fed) Tapered Ultra-Wideband Antenna . . . 109
3.8.1 Antenna Design and Operation 109
3.8.2 Simulation and Measurement Results 112

3.9 Applicability in Cognitive Radio 119
3.10 Summary 121

4 Pattern-Reconfigurable Ultra-wideband Antenna 123

4.1 Introduction 123
4.2 Antenna Design and Operation 124
4.3 Performance Analysis 129
4.3.1 Parametric Study 129
4.3.2 Surface Current 135
4.3.3 Experimental Evaluation 136
4.4 Summary 144

5 Polarisation-Reconfigurable Ultra-wideband Antennas 145

5.1 Introduction 145
5.2 Polarisation Reconfigurable Ultra-wideband Antenna Element 147
5.2.1 Antenna Design 147
5.2.2 Proposed Antenna Performance Analysis 150
5.3 Tuning Circular Polarisation Bandwidth of the Polarisation Reconfigurable Antenna 157
5.3.1 Antenna Re-design 157
5.3.2 Numerical and Experimental Results 160
5.4 Applications in Cognitive Radio 168
5.5 Summary 170

6 Planar Ultra-wideband Antenna with Multiple Degrees of Reconfiguration 171

6.1 Introduction 171
6.2 The Proposed Antenna Design 172

6.3 DC Biasing and Power Consumption 176
6.4 Principles of Operation and Design Guidelines 180
6.4.1 Frequency Reconfiguration 180
6.4.2 Pattern Reconfiguration 186
6.4.3 Polarisation Reconfiguration 189
6.5 Proposed Antenna Performance Analysis 192
6.5.1 Frequency Reconfiguration 192
6.5.2 Pattern Reconfiguration 194
6.5.3 Polarisation Reconfiguration 197
6.6 Summary 201

7 Conclusions and Future Work **203**

7.1 Conclusions 203
7.2 Key Contributions 206
7.3 Future Work 207

List of Tables

2.1 Pros and cons of switching devices in reconfigurable antennas. 48

3.1 Simulated and measured realised gain of the ultra-wideband mode and the reconfigurable modes 85

3.2 Comparison between the simulated and measured values of the antenna total efficiency η_t, S denotes simulated results and M is for the measured results 95

3.3 Simulated and measured realised gain and total efficiency for the GaAs FET reconfigured ultra-wideband antenna in the ultra-wideband mode. 107

3.4 Simulated and measured realised gain for the GaAs FET reconfigured ultra-wideband antenna. 108

3.5 Simulated and measured total efficiency for the GaAs FET reconfigured ultra-wideband antenna. 109

3.6 Operating modes of reconfigured ultra-wideband TSA antenna. 111

3.7 Simulated (S) and measured (M) realised peak gain values in (dBi) for the reconfigured ultra-wideband TSA antenna. . . . 118

3.8 Measured total efficiency of the reconfigured ultra-wideband TSA antenna. 119

4.1 Dimensions of the proposed antenna. 125

4.2 Operation modes of the antenna 128
4.3 Bias configuration of the antenna 128
4.4 Measured gain ratio between the $+x$ direction and $-x$ direction and the maximum realised gain in the xz-plane for the proposed antenna 144

5.1 Dimensions of the polarisation reconfigured ultra-wideband antenna. 148
5.2 Operation modes of the proposed antenna. 150
5.3 Dimensions of ANT. II. 159
5.4 Operation modes of ANT. II 159
5.5 Simulated and measured gain of ANT. II. 166

6.1 Dimensions of the proposed antenna 173
6.2 Switches states for different operation modes of the proposed reconfigurable antenna. In each operating mode, all of the 10 switches $(a - j)$ have to be set to their corresponding state as in the table columns. 177
6.3 DC biasing and power consumption for different operation modes of the proposed reconfigurable antenna. In each operating mode, all of the 12 voltages $(V_0 - V_{11})$ have to be set to their corresponding values as in the table columns. 178
6.4 Simulated BSF operation for the four stubs in the proposed design 183

List of Figures

2.1 Reconfigurable antenna geometry and prototype in[45]. 50

2.2 Reconfigurable antenna geometry in[46]. 50

2.3 Reconfigurable antenna geometry and prototype in[19]. 51

2.4 Reconfigurable antenna geometry in[47]. 52

2.5 Reconfigurable antenna geometry and prototype in[48]. 52

2.6 Reconfigurable antenna geometry in [49]. 53

2.7 Reconfigurable antenna structure in [50].a) Radiating Patch, b)Ground Plane, c) Complete Antenna. 55

2.8 Reconfigurable antenna prototype in [51]. 56

2.9 Reconfigurable antenna prototype in [52]. 56

2.10 Reconfigurable antenna geometry in [53]. 58

2.11 General topology of the reconfigurable slot bow-tie antenna. (a) antenna topology. (b) Right side of the reconfigurable antenna [15]. 59

2.12 Halved Vivaldi with reconfigurable band rejection [54]. 59

2.13 Vivaldi with reconfigurable band rejection [55]. 60

2.14 Reconfigurable antenna geometry in [56]. 62

2.15 Reconfigurable antenna geometry in [57]. 63

2.16 Reconfigurable antenna geometry in [58]. 63

2.17 3-D view of the pattern-reconfigurable wideband antenna in [59]. 64
2.18 3-D view of the pattern-reconfigurable wideband antenna in [60]. 64
2.19 Geometry and prototype of the pattern-reconfigurable wideband antenna in [61]. 65
2.20 Reconfigurable antenna geometry in [62]. 66
2.21 Reconfigurable antenna geometry in [63]. 67
2.22 Reconfigurable antenna geometry in [64]. 67
2.23 Reconfigurable antenna geometry in [65]. 69
2.24 Reconfigurable antenna geometry in [66]. 70
2.25 Reconfigurable antenna prototype in [23]. 70
2.26 Reconfigurable antenna geometry in [67]. 71

3.1 Geometry of the reconfigurable ultra-wideband disk monopole antenna. 74
3.2 Prototype of the reconfigurable ultra-wideband disk monopole antenna. 76
3.3 Simulated impedance curves for the ultra-wideband antenna. 77
3.4 Simulated impedance curves for the ultra-wideband antenna reconfigured at 2.4 GHz. 77
3.5 Proposed filter when switches f, f' are ON. 78
3.6 Scattering parameters of the filter when switches f, f' are ON. 78
3.7 Simulated (dotted red line) and measured (solid blue line) return loss curves when all switches are OFF (e.g., ultra-wideband case). 79

3.8 Simulated and measured return loss curves when antenna is configured in: a) Band I at 2.4 GHz, b) Band II: 3.3 to 4.4 GHz, c) Band III: 4.1 to 5.4 GHz, d) Band IV: 5 GHz, e) Dual band: 2.4, 5 GHz, and f) Band V : 6.5 to 7.5 GHz. . . 82
3.9 Simulated (solid red line) and measured (dotted blue line) normalised E-plane and H-plane radiation patterns when the antenna is configured at : a) 2.4 GHz in Band I, b) 5 GHz in Band IV , c) 3.3 GHz in Band II, d) 4.4 GHz in Band III, and e) 7 GHz in Band V. 83
3.10 Simulated 3D realised gain when the antenna is configured at 2.4 GHz in Band I. 84
3.11 Simulated 3D realised gain when the antenna is configured at 3.3 GHz in Band II. 84
3.12 Schematic diagram of the gain transfer method. 85
3.13 Simulated current distribution of the ultra-wideband antenna at (a) 2.4 GHz, b) 6 GHz. 87
3.14 Simulated current distribution of the 2.4 GHz reconfigured ultra-wideband antenna in Band I at (a) 2.4 GHz, (b) 6 GHz. 87
3.15 Simulated current distribution on the 7 GHz reconfigured ultra-wideband antenna in Band V at (a) 3 GHz, (b) 7 GHz. 88
3.16 Power fractions inside the wideband Wheeler cap. 91
3.17 Antenna radiation efficiency measurement setup using a cylindrical wideband Wheeler cap probed by an Agilent N5230C PNA-L network analyser (the cap is completely closed when taking measurements). 93

3.18 Measured total efficiency η_t when the antenna is working in the ultra-wideband mode and when configured in Band I at 2.4 GHz and Band II 3.3–4.4 GHz 94
3.19 p-i-n diode $BAR64-03W$ equivalent circuit when it is: (a) forward biased, (b) reverse biased. 97
3.20 Simulated return loss for the reconfigured ultra-wideband antenna at 2.4 GHz when the dc bias lines are not RF choked (blue dashed line) and when the dc lines lines are RF choked using lumped elements (e.g., $R = 4.3\ K\Omega, L = 220\ nH$)(solid red line). The simulated return loss curve with no biasing lines is identical to the case when using lumped elements as RF chokes. 97
3.21 Simulated current distribution on the 2.4 GHz reconfigured ultra-wideband antennas: (a) dc lines without chokes, (b) dc lines with small passive elements values ($R = 100\ \Omega, L = 5\ nH$), and (c) dc lines with big passive element values($R = 4.3\ K\Omega, L = 220\ nH$). 98
3.22 Simulated 3D realised gain patterns of the 2.4 GHz reconfigured ultra-wideband antenna: (a) dc lines without chokes, (b) dc lines with small passive element values ($R = 100\ \Omega, L = 5\ nH$) , and (c) dc lines with big passive element values($R = 4.3\ K\Omega, L = 220\ nH$). 98
3.23 The fabricated frequency reconfigurable antenna with p-i-n diode switches. 99
3.24 Simulated and measured return loss of the 2.4 GHz reconfigured antenna when the p-i-n diodes are reversed biased. . . . 99

3.25 Simulated and measured return loss of the 2.4 GHz reconfigured antenna when the p-i-n diodes are forward biased. . . . 100
3.26 Geometry of the proposed reconfigurable ultra-wideband antenna design using GaAs FET switches; (a) Top view, (b) Bottom view. 103
3.27 Prototype of the ultra-wideband reconfigured antenna using GaAs FET switches. 104
3.28 Simulated (solid red lines) and measured (dashed blue lines) return loss curves when the antenna is in the ultra-wideband mode. 105
3.29 Simulated (solid lines) and measured (dashed lines) return loss curves when the antenna is reconfigured at: I) 2.1–2.6 GHz, II) 3.6–4.6 GHz, III) 2.8–3.4 GHz and 4.9–5.8 GHz. . . 106
3.30 Simulated (solid red line) and measured (dotted blue line) normalised E-plane (Y-Z) and H-plane (X-Z) radiation patterns, when antenna is configured at: (a) 2.4 GHz in band I (b) 4.2 GHz in band II 107
3.31 Simulated (solid red line) and measured (dotted blue line) normalised E-plane (Y-Z) and H-plane (X-Z) radiation patterns, when antenna is configured at: (c) 3.3 GHz in Band IIIa (d) 5.4 GHz in band IIIb. 108
3.32 Geometry of the reconfigured Tapered Slot antenna (a) Top view, (b) Bottom view. 110
3.33 Antenna Prototype; (a) Top view, (b) Bottom view. 111
3.34 Simulated (dashed lines) and measured (solid lines) return loss curves when antenna is in ultra-wideband mode and in the notched ultra-wideband mode. 112

3.35 Simulated (dashed lines) and measured (solid lines) return loss curves when antenna is reconfigured in Band I: 3–4 GHz and Band II: 4.5–5.5 GHz. 113
3.36 Simulated current distribution of the notched ultra-wideband antenna at (a) 5 GHz (normal operation frequency) and (b) 5.8 GHz (notched frequency). 113
3.37 Simulated current distribution of the reconfigured ultra-wideband antenna in Band I: (a) 3.4 GHz, (b) 5 GHz, and Band II: (c) 3.4 GHz, (d) 5 GHz. 115
3.38 Simulated input impedance curves for the ultra-wideband antenna and when the antenna is configured to operate in Band I. 116
3.39 Simulated (dotted blue line) and measured (solid red line) normalised E-plane (YZ) and H-plane (XZ) radiation patterns, when antenna is in the ultra-wideband mode, (a) 3.4 GHz (b) 5 GHz. 117
3.40 Simulated (dotted blue line) and measured (solid red line) normalised E-plane (YZ) and H-plane (XZ) radiation patterns, when the antenna is configured at: (a) 3.4 GHz in Band I (b) 5 GHz in Band II. 118
3.41 Comparison between simulated total efficiency when the antenna is operating in different modes. 119

4.1 Geometry of the proposed pattern-reconfigurable ultra-wideband antenna. 125
4.2 Equivalent circuit of the HPND-4005 p-i-n diode in the: a) ON state, b) OFF state. 127

4.3 Prototype of the proposed pattern-reconfigurable ultra-wideband antenna. 127
4.4 Circuit diagram of the dc-bias circuit of the proposed reconfigurable antenna. 128
4.5 Effects of L' (the total stub length) on the return loss of the proposed ultra-wideband antenna. 130
4.6 Effects of L' (the total stub length) on the radiation gain pattern cut along the xz plane at 4.4 GHz. 131
4.7 Effects of W' (the stub width) on the return loss of the proposed ultra-wideband antenna. 133
4.8 Effects of W' (the stub width) on the radiation gain pattern cut along the xz plane at 4.4 GHz. 133
4.9 Effects of d' (the distance between the stub and the antenna y-axis) on the return loss of the proposed ultra-wideband antenna. 134
4.10 Effects of d'(the distance between the stub and the antenna y-axis) on the radiation gain pattern cuts along the xz plane at 4.4 GHz. 134
4.11 Simulated average surface current distributions at 4 GHz on the top and bottom metallisation (while the substrate is hidden), when the antenna is operating in: a) Mode–0, b) Mode–1.136
4.12 Simulated and measured return loss curves when the proposed antenna is operating in Mode–0. 137
4.13 Simulated and measured return loss curves when the proposed antenna is operating in Mode–1 and Mode–2. 138

4.14 Simulated 3-D normalised realised gain patterns when the antenna is operating at 4.5 GHz in: a) Mode–0, b) Mode–1, and c) Mode–2. 139
4.15 Simulated (black curves) and measured (grey curves) normalised radiation patterns in the H-plane when the antenna is operating in: a) Mode–0, b) Mode–1, and c) Mode–2. Solid lines are for the (co-polar) component and dashed lines represent the (cross-polar) component. 140
4.16 Simulated (black curves) and measured (grey curves) normalised radiation patterns at 4.5 GHz in the E-plane, when the antenna is operating in different modes. Solid lines are for the (co-polar) component and dashed lines represent the (cross-polar) component. 141
4.17 Prototype mounted inside the anechoic chamber, the antenna's SMA connector is covered with absorber and the dc wires are shielded with aluminium foil. 142

5.1 A circularly polarised wave as in [113]. 146
5.2 Geometry of the proposed polarisation reconfigurable ultra-wideband antenna. 148
5.3 Prototype of the proposed polarisation reconfigurable ultra-wideband antenna. 149
5.4 Simulated (S) (solid lines) and measured (M) (dashed lines) return loss curves for the proposed antenna when it is working in the LP, LHCP and RHCP states. 151

5.5 Simulated 3-D realised gain patterns for the proposed antenna at 7 GHz when the antenna is reconfigured to work in different states: (a) LP state , b) LHCP state, co-polarisation, (c) LHCP state, cross-polarisation, d) RHCP state, co-polarisation component, e) RHCP state, cross-polarisation component . . 152
5.6 Measured co-polarisation (solid lines) and cross-polarisation (dashed lines) normalised radiation patterns in the xz and yz planes at 7 GHz when the proposed antenna is reconfigured to work in different polarisation states, a) LP state, b) LHCP state, c) RHCP state. 154
5.7 Simulated surface current distributions when the antenna is in the LHCP state at 7 GHz when the phase is advancing from 0° to 270°. 155
5.8 Simulated and measured realised gain and axial ratio, when the antenna is reconfigured in the LHCP state. 156
5.9 Geometry of the polarisation reconfigurable ultra-wideband antenna (ANT II). 158
5.10 Prototype of ANT II 158
5.11 Simulated (solid lines) and measured (dashed lines) return loss curves for ANT II when it is working in the LP, LHCP-Band I and LHCP–Band II. 160
5.12 Simulated (solid black lines) and measured (dashed grey lines) normalised radiation patterns for ANT II when it is working in the LP state, a) 4 GHz, b) 6 GHz. 162

5.13 Simulated (solid lines) and measured (dashed lines) normalised radiation patterns for ANT II when it is reconfigured in the LHCP state, a) 6 GHz in Band I, b) 5 GHz in Band II. The co-polarisation (LHCP component) is shown in black colour and cross-polarisation (RHCP component) is shown in grey. . 163
5.14 Simulated (solid lines) and measured (dashed lines) normalised radiation patterns for ANT II when it is reconfigured in the RHCP state, a) 6 GHz in Band I, b) 5 GHz in Band II. The co-polarisation (RHCP component) is shown in grey colour and cross-polarisation (LHCP component) is shown in black. 164
5.15 Simulated (S) and Measured (M) Axial ratio, when the antenna is reconfigured in the LP and LHCP state (Band I and Band II). 166
5.16 Simulated surface current vector distribution when the antenna is working in the LHCP-Band I at, a) 7 GHz$\angle 0°$, b) 7 GHz $\angle 90°$, c) 7 GHz$\angle 180°$, and d) 7 GHz$\angle 270°$. 167
5.17 Spectrum sharing in the polarisation domain in a simple CR network. Secondary devices (SU) are communicating with their antennas configured as RHCP while primary (legacy) users (PU) antennas are configured as LHCP, assuming line-of-sight (LOS) operation. 168

6.1 Geometry of the proposed reconfigurable ultra-wideband antenna. a) Front view, b) Back view. 172
6.2 Prototype of the proposed reconfigurable ultra-wideband antenna. a) Front view, b) Back view. 173

6.3 3-D Geometry of the proposed antenna showing the p-i-n diodes labellings and orientations when mounted on the antenna and the labelling of the bias wires coming from the power supply and soldered on the antenna PCB. 174

6.4 Circuit diagram of the dc-bias circuit of the proposed reconfigurable antenna. Current limiting resistances are external to the antenna and they are in series with the wires (V_7, V_8, V_{11}) coming from the dc power supply. 176

6.5 A BPF filter using four quarter wavelength stub resonators connected to a microstrip line. The stub lengths are as illustrated in Figure 6.1 and Table 6.1. The width of each stub is W'= 4 mm and the vertical distances between stubs d=2.5 mm. 180

6.6 Effects of the stub width (W') on the quality factor (Q) of stub B. 181

6.7 Simulated insertion loss of the filter when only stub resonator, B, is connected to the main microstrip feedline using a switch, while the switch is mimicked in simulations as: a) a strip of copper metallisation with a width equals to the stub width, b) strip of copper metallisation when the width is equal to the real switch width (0.2 mm), and c) 4.7 Ω resistance in series with a 0.15 nH inductor (i.e., the equivalent circuit of the ON p-i-n diode switch). 182

6.8 Simulated return and insertion losses of the proposed BPF in Figure 6.5. All p-i-n diodes are switched ON. 183

6.9 Effects of the vertical distance between the stubs (d) on insertion loss of the proposed BPF. 184

6.10 Contour plots of simulated average surface current distributions at f_o , when the antenna is operating in: a) Omni-directional-mode, b) Directional-mode. 187
6.11 Contour plots of simulated average surface current excited at f_o: a) x–directed current with no slit in the radiator, b) x–directed current with a slit in the radiator, c) y–directed current with no slit in the radiator, d)y–directed current with a slit in the radiator 190
6.12 Simulated and measured return loss curves when the proposed antenna is operating in the ultra-wideband mode and in Band–I. 193
6.13 Simulated (black curves) and measured (grey curves) normalised radiation patterns in the H-plane (xz) and E-plane (yz) when the antenna is operating in the ultra-wideband mode at: a) 3 GHz, b) 5 GHz, and c) 7 GHz. Solid lines are for the (co-polar) component and dashed lines represent the (cross-polar) component. 195
6.14 Simulated (black curves) and measured (grey curves) normalised radiation patterns when the antenna is operating in Band-I at 5 GHz: a) H-plane (xz), b) E-plane (yz). Solid lines are for the (co-polar) component and dashed lines represent the (cross-polar) component. 196
6.15 Simulated and measured return loss curves when the proposed antenna is operating in Mode–II and Mode–III. 197

6.16 Simulated (black curves) and measured (grey curves) normalised radiation patterns in the H-plane when the antenna is operating in: a) Mode–II at 3 GHz, b) Mode–III at 3 Ghz, c) Mode–II at 5 GHz and d) Mode–III at 5 GHz. Solid lines are for the (co-polar) component and dashed lines represent the (cross-polar) component. 198
6.17 Simulated and measured return loss curves when the proposed antenna is operating in the LHCP and RHCP modes. . 199
6.18 Simulated (black curves) and measured (grey curves) normalised radiation patterns for the H-plane (xz) and E-plane (yz) at 4.8 GHz when the antenna is operating in: a) LHCP mode, b)RHCP mode. Solid lines are for the LHCP components and dashed lines represent the RHCP components. . . . 200
6.19 Measured axial ratio at broadside when the antenna is reconfigured in the LP and LHCP/RHCP modes. 201

1 Introduction

1.1 Background

Reconfigurable antennas are distinguished from their conventional counterparts by the fact that they can change their operation parameters (such as frequency, patterns or polarisation) upon request or feedback from a specific control mechanism. The reconfiguration is achieved through redistribution of the surface currents; this will result in changes in the antenna impedance or radiation properties [1]. Reconfigurable antennas apply various techniques and methods to achieve the required change in one or more of its operation parameters. The most common technique is based on using switches such as p-i-n diodes, Gallium Arsenide Field Effect Transistors (GaAs FETs) or Micro-ElectroMechanical System (MEMS) switches. Other techniques include the use of optical switches or mechanical structure alteration to achieve the necessary change in the antenna configuration and these are promising methods to overcome the enormous biasing problems of the electronic switches.

Reconfigurable antennas have recently received a substantial increase in interests from both academic and industrial groups and establishments due to their attractive characteristics in advanced and novel applications such as Cognitive Radio (CR), Multiple Input Multiple Output (MIMO) Sys-

tems, personal communication systems, satellites, military communications and many other applications. Unlike current conventional communication systems, future wireless communication systems (e.g., Cognitive Radio and smart WLAN) will benefit most from flexible radio front-ends (flexibility in terms of operation and performance parameters). Taking for example the main motivation behind Cognitive Radio (CR) systems, some frequency bands in the spectrum are heavily used while there are still some, at a specific geographical location or at a certain time, largely unoccupied. Hence reconfigurable antennas will allow CR to change its operational frequency according to spectrum availability and also user demands from link quality and data rate prospective [2,3]. There are many approaches of how to deploy these reconfigurable antennas in CR systems, one of these approaches is to use an omnidirectional ultra-wideband antenna to sense the spectrum, while another reconfigurable narrowband (either on the same board or adjacent one) can be used for communication. Another approach can be achieved through the use of ultra-wideband antenna that can be reconfigured into multiple predefined narrow passbands and hence achieving both spectrum sensing and communicating functionality within one element saving cost and reducing complexity [4]. The later approach might have its drawbacks in terms of power consumption and interference from the compact biasing circuitry; however, it provides significant advantage for the compact one unit CR device aimed for potential smart wireless applications.

The following sections will briefly introduce the main principles and motivations of Cognitive Radio and hence setting the scene for the antenna element aspect of the overall proposed system detailed in this thesis.

1.1.1 Definition of Cognitive Radio

The software defined radio (SDR) Forum and IEEE approved the definition of a Cognitive Radio as follows:

- Radio in which communications systems are aware of their environment, and can make decisions about their radio operating behaviour based on some information and predefined objectives. The environmental information may or may not include location information related to communication systems [5].
- Cognitive Radio that uses SDR, adaptive radio and other technologies to automatically adjust its behaviour to achieve desired objectives.

It is worth mentioning here the four most popular interpretations of Cognitive Radio as follows [6]:

- Full CR: also called Mitola Radio, in which every possible parameter observed by the radio is taken into account while the device is making a decision on the way it operates.
- Spectrum sensing CR: in which radio frequency spectrum is the only parameter that is observed and used in decision making.
- Licensed band CR: in which the device is capable of using licensed spectrum in addition to unlicensed spectrum.
- Unlicensed band CR: in which the device is allowed to use license exempt or free license spectrum only.

1.1.2 Evolution of Cognitive Radio

The spectrum measurement studies were conducted as early as 1995 to investigate the spectrum use. In 1999, Mitola had started the CR research [2]. In

the United States, CR research focused on dynamic spectrum access (DSA) and secondary use of spectrum. The XG-project funded by DARPA was the most notable project in the spectrum management research. The success of XG has driven further study in the field of CR technology. Several researchers (such as Lessig, Reed, and Peha) have also boosted the research by pointing out the flaws in the current use of the spectrum [7].

Many groups have emerged to work on standardising CR technology: IEEE 802.22 and more recently ETSIs Reconfigurable Radio Systems Technical Committee on CRs and SDRs. Also, the SDR forum has studied some CR-related issues. Recently, IEEE 802.22 is the the most advanced standardisation activity that aims to provide dynamic access to the new vacant TV spectrum. In the United States, the FCC proposed to allow opportunistic access to TV bands in 2004 [8]. Prototype CRs operating in this mode were presented to the FCC by many big industrial companies such as Motorola and Microsoft in 2008 [9]. After some extensive tests, the FCC adopted in November 2008 a second report to allow the operation of cognitive devices in TVWS [10].

Furthermore, the UK regulatory body, Ofcom, was proposing to allow licence exempt use of interleaved spectrum for cognitive devices [11]. On 23 September 2010, the FCC released the final rules for the cognitive use of TV white spaces in the US [12]. This solution is based on database architecture in which CR devices should have geo-location capabilities by downloading tables from a database without performing additional sensing before transmitting [13]. However the report mentions that while FCC are eliminating the sensing requirement, they are encouraging further research to improve sensing capabilities because they believe it might improve the spectrum efficiency in the TV spectrum and will be an important tool for

providing opportunistic access to other spectrum bands [13].

On 26 January 2011, the FCC opted for license of the spectrum geo-location data base to multiple leading technology companies such as Google, Telcordia, Neustar and Comsearch. So far, the details of the database architecture are not complete [14].

1.1.3 Advantages of Cognitive Radio

- There is only a finite amount of the EM spectrum, yet there is a tremendous increase of demand without any signs of stopping in the near future. Cognitive Radio will allow efficient use of the spectrum by dynamically allowing users from crowded frequency bands to use adjacent free bands.

- Cognitive Radio will be many radios in one, allowing different services that are currently available in separate devices [6].

- Cognitive Radio will always find the best performance and quality of service (QoS) for the end user.

- Cognitive Radio will liberate the spectrum and allow spectrum trading between service providers [6]. Moreover, Cognitive Radio will allow service providers to improve their coverage and network capacity.

- Cognitive Radio will greatly benefit joint emergency operations (e.g., police, fire and ambulance services) during major emergency scenarios.

- Cognitive Radio will benefit military communications and increase the reliability of military communication networks by dynamically allowing friendly forces to be connected regardless of enemy interference and jamming.

1.2 Motivation and Research Challenges

The current research challenges that motivate this research and emphasise the need for designing efficient, compact and cost-effective reconfigurable antennas for Cognitive Radio and smart wireless applications can be summarised as follows:

- The antenna requirements for Cognitive Radio communication or even smart wireless systems are still not clear yet. It is almost true that reconfigurable antennas will be used instead of conventional antennas and it is more likely that a combined narrowband and wideband antenna will be very useful in a Cognitive Radio system.

- Most of the reconfigurable antennas that have been demonstrated for Cognitive Radio combine wideband and narrowband functionality but those antennas are bulky and very complex; moreover, a significant number of reconfigurable antennas that had been reported in the literature were only capable to switch between two or few bands and to increase the number of reconfigured frequency bands, a new redesign is required(e.g., increasing antenna size).

- The efficiency of reconfigurable antennas is not often characterised, although the loss associated with the switching and biasing elements is significant. Since the efficiency relates the incident and radiated power of an antenna, the antenna efficiency should be an important parameter to characterise the filtering performance of the antenna [15].

- Research in reconfigurable antennas for future wireless communication systems has centred primarily on frequency reconfiguration and the applicability and possible benefits of applying new designs of po-

larisation or pattern reconfigurable elements in future Cognitive Radio devices have not yet been fully exploited.

- Antenna element designs that combine three possible multiple reconfiguration categories (e.g., frequency, pattern and polarisation) have not existed in the past literature, in spite of their importance in increasing the flexibility and functionality and improving the performance of future Cognitive Radio and smart wireless systems.

1.3 Organization of the Thesis

This thesis is organised in seven chapters as follows:

Chapter 2: This chapter discusses reconfigurable antennas characteristics and investigates the types of reconfigurable antennas and the mechanism of their reconfiguration. A brief comparison between different reconfiguration techniques is presented. Besides, a review of a variety of previously designed reconfigurable antennas is addressed with concentration on their main drawbacks.

Chapter 3: This chapter introduces a novel frequency reconfigured ultra-wideband circular disk monopole antenna for Cognitive Radio applications. Reconfiguration is realised by connecting the main feedline of the antenna to variable length stubs controllable by switches. Simulations are performed to investigate the main characteristics of the antenna (e.g., return loss, radiation patterns, gain and efficiency) before and after reconfiguration. Three prototypes of this reconfigured antenna have been manufactured to compare the measured and simulated results. In the first prototype the switches were hard wired (e.g., using adhesive copper bridges to represent a switch in the ON state and removing it in the OFF state). p-i-n diodes

and GaAs transistors have been used in the second and third prototype, respectively. Finally, using a similar technique, A compact ultra-wideband TSA (Tapered Slot Antenna) was reconfigured to work in an ultra-wideband mode and in different frequency bands and another mode of operation was added (e.g., ultra-wideband mode with notched band operation), this can increase the flexibility of the reconfigurable antenna which might lead to an enhanced Cognitive Radio performance.

Chapter 4: This chapter demonstrates a novel compact ultra-wideband microstrip monopole antenna with reconfigurable patterns capability. The antenna's radiation patterns can be shaped to concentrate energy in specific directions while minimising the gain in other unwanted directions, without significantly affecting the impedance bandwidth of the antenna. A fully functional prototype has been developed and tested. The proposed antenna could be a suitable candidate for advanced and smart radio applications such as Cognitive Radio (CR) as it can enhance the radio front-end flexibility and performance by adding the benefits of pattern diversity, specifically in multipath environments.

Chapter 5: A novel compact ultra-wideband microstrip monopole antenna with reconfigurable polarisation capability, that can be switched from linear polarisation (LP) to right hand circularly polarisation (RHCP) or left hand circular polarisation (LHCP) is presented and detailed in this chapter. Moreover, the circular polarisation CP bandwidth (RHCP or LHCP) can be changed at different frequency bands. In Cognitive Radio devices, polarisation reconfiguration, in addition to frequency and pattern reconfiguration, is needed to improve the performance of Cognitive Radio systems.

Chapter 6: As no attempt has yet been reported to combine the main three categories of reconfigurable antennas, namely frequency, pattern, po-

larisation, in one single design. Thereby, in this chapter the author goes one step further in the design of reconfigurable antennas, and presents a novel flexible multi-operation reconfigurable antenna that meets the growing demand of CR devices for more intelligent and multi-functional antennas.

Chapter 7: This chapter concludes the research that has been done in this thesis and give suggestions for future investigations and work.

2 Review of Reconfigurable Antennas

2.1 Introduction

Current radio architectures are exploring the application of different types of advanced antenna concepts to enhance performance and also to enable the transition to more efficient radio front-ends with main processing emphasis shared with the radiating element leading to greener systems. For the Cognitive Radio (CR) scanning and communication, special antennas (reconfigurable antennas) should be used. Such elements may involve frequency, pattern or polarisation reconfiguration and if needed the combination of one or more of these parameters. There are many approaches of how to deploy frequency reconfigurable antennas in CR systems, one of these approaches is to use an omnidirectional ultra-wideband antenna to sense the spectrum, while another reconfigurable narrowband antenna can be used for communication. Another approach can be achieved by using an ultra-wideband antenna that can be reconfigured into multiple predefined narrow pass-bands and hence providing efficient use of the fabrication space and confine the control mechanism to a specific board rather than a distributed system leading to further losses. There are several techniques in which antennas can be reconfigured such as switching in or out parts of the antenna

structure or adjusting the loading or matching of the antenna externally or even changing the antenna geometry by mechanical movements. MEMS switches, p-i-n diodes and varactors have been widely used in antenna reconfiguration, but they are all different in terms of the loss they introduce, control voltage, cost, linearity, reliability and power efficiency.

Generally speaking, in order to successfully integrate reconfigurable antennas in future commercial or military CR systems, proper design and optimisation of these new reconfigurable antennas should be investigated and we should consider some important design issues such as high efficiency, space constraints, low profile, high speed tuning and spurious free radiation.

2.2 Fundamentals of Antennas

An antenna is defined as a means for radiating or receiving electromagnetic waves. To characterise an antenna, some key parameters such as return loss, radiation patterns, directivity, gain and polarisation are usually defined as follows:

- **Return Loss and Bandwidth**

  Return loss is the ratio of the power incident on the antenna input terminal to the power reflected from the antenna at a particular operating frequency and it should be a positive quantity in dB.

$$RL = 10 \log \frac{P_{in}}{P_r} \tag{2.1}$$

  where RL is the return loss in dB, P_{in} is the incident power at the antenna input and P_r is the reflected power. The bandwidth of an antenna refers to the range of frequencies, where the antenna return

loss has an acceptable value. The fractional bandwidth of antenna can be calculated using (2.2) [16]

$$BW = \frac{f_2 - f_1}{f_0} \times 100\% \tag{2.2}$$

where f_1 is the lower frequency, f_2 is the higher frequency and f_0 is the centre frequency.

In a mobile handset, the criteria that usually defines the antenna's bandwidth is a return loss better than +6 dB over the frequencies of operation. In most wireless communications, the antenna is required to provide a return loss equal or better than +10 dB over its frequency bandwidth.

- **Radiation Patterns, Directivity and Gain**

  The radiation pattern depicts the radiation properties of the antenna as a function of space coordinates and it is usually determined in the far-field region [16]. Directivity D is a dimensionless quantity defined as the ratio of the radiation intensity U in a given direction to the radiation intensity averaged over all directions U_o as shown in (2.3) [16].

$$D = \frac{U}{U_o} = \frac{4\pi U}{P_r} \tag{2.3}$$

  where P_r is the power radiated by the antenna.

  The gain of an antenna is usually referenced to a standard antenna (e.g., theoretical isotropic antenna or a dipole) and it is defined as the ratio of power radiated by an antenna in a given direction, to the power that would be radiated in the same direction by an isotropic antenna when both antennas are driven by the same amount of power. The antenna gain and directivity are related by the antenna efficiency

which will be fully described in the next chapter.

- **Polarisation**

  Polarisation is defined as the orientation of the plane in which the electric field oscillates for an electromagnetic wave. The polarisation of an antenna in a given direction is the polarisation of the wave radiated by the antenna. When the direction is not stated, the polarisation is taken to be the polarisation in the direction of maximum gain [16]. Polarisation can be categorised as linear, circular and elliptical. Elliptical polarised wave is the general case in which the tip of the electric field vector (E) describes an ellipse along the propagation path. Two special cases of elliptical polarisation are linear polarisation and circular polarisation. In a linearly polarised wave, at all the time the electric field vector moves back and forth in the same plane. A linearly polarised wave is considered as horizontally/verticaly polarised if the electric field is parallel/perpendicular to the earth. In a circular polarised wave, the electric field vector remains constant in magnitude but rotates in a circular path perpendicular to the direction of propagation. For right hand circular polarisation (RHCP) and left hand circular polarisation (LHCP), the rotation of the electric field is right-hand and left-hand, respectively.

2.3 Reconfigurable Antennas Characteristics

Since the rise of research interests and work in reconfigurable antennas in the last decade, many reconfiguration techniques have been applied and evaluated theoretically, numerically and experimentally. The most common techniques utilised are centred upon switching mechanisms. By using

switches such as MEMS or p-i-n diodes with compatible antenna elements, the main characteristics of antenna operation can be changed providing frequency, pattern and polarisation reconfiguration. Other techniques such as the incorporation of varactors, optical switches and physical structure alteration to overcome the adverse effects of using switches and their biasing have also been deployed and investigated but each with its own pros and cons.

2.3.1 Types of Reconfigurable Antennas

Reconfigurable antennas can be classified mainly in four categories:

- Frequency reconfigurable antennas.

  Frequency reconfiguration is usually achieved by changing the operating frequency of an antenna while keeping the radiation characteristics unchanged.

- Radiation pattern reconfigurable antennas.

  Pattern reconfiguration is usually achieved by changing the shape of the radiation patterns, gain or any aspect of the radiation behaviour of an antenna while keeping the operating frequency unchanged.

- Polarisation reconfigurable antennas.

  Polarisation reconfiguration is usually achieved by changing the polarisation of an antenna while keeping the operating frequency unchanged.

- Combinations of the above stated categories.

2.3.2 Mechanisms for Reconfiguration

Antenna designers have made use of many reconfiguration techniques and the most common techniques are based on switching mechanisms such as p-i-n diodes [17–19], FET switches [20] and RF MEMS switches [21]. Other techniques such as the incorporation of varactors [22], optical switches [23], physical structure alteration [24], and changing substrate permittivity [25] or permeability [26], have been used to overcome problems faced when using electronic switches and biasing lines. The effects of biasing lines on reconfigurable antennas was studied in [27] and an analysis of techniques to minimise the biasing lines effects has also been studied in [28].

2.3.3 Linearity in Switching Devices

Non-linear devices in RF systems can be a major source of distortion and interference. Reconfigurable antennas can be adversely affected by the amount of distortion introduced by the non linearities of the switching devices.

When a signal, $x(t) = A\ cos(\omega t)$, is passed through a non-linear system, the output signal can be presented by the following series:

$$y(t) = \sum_{i=0}^{\infty} B_i\ A^i\ cos^i(\omega t) \tag{2.4}$$

The third-order output term (e.g., $i = 3$) can be written as:

$$B_3\ A^3\ cos^3(\omega t) = \frac{3}{4} B_3\ A^3\ cos(\omega t) + \frac{1}{4} B_3\ A^3\ cos(3\omega t) \tag{2.5}$$

It should be noticed that the third order term has a negative coefficient B_3 and a cubic dependence on the magnitude of the input signal and that is the reason for gain compression when the input power to a non linear

system is increased [29]. In a similar way, when two tones with frequencies f_1 and f_2 are in the passband of a non linear system, they will generate third-order terms, with cubic dependence on the input signal magnitude, located at $2f_2 - f_1$ and $2f_1 - f_2$ and these terms will cause intermodulation distortion [29].

The non-linear relation between the varactor's input reverse voltage and its capacitance gives rise to intermodulation distortion [30]. Conductivity modulation of the charge within the intrinsic regions of the p-i-n diodes in the ON state [31] and the capacitance modulation in the OFF state make p-i-n diodes non-linear devices [32].

FET switches can also generate some distortion because of the non-linear characteristics between the drain-source current (I_{ds}) and the drain-source voltage (V_{ds}). Improving FET switches linearity has been studied in [33] and the authors in [34] have demonstrated an FET switch which exhibits low distortion characteristics, where the third-order intercept point of 41 dBm is achieved.

MEMs switches have very high linearity characteristics. The metal to metal physical contact in MEMs is a very linear contact for a contact resistance of $1 - 2\ \Omega$ [35]. Typical MEMs switches have an input third intermodulation products larger than 65 dBm [36]. The linearity response of photoconductive silicon switches has also been studied in [37] where a third-order intercept point of 63 dBm is achieved.

The authors in [38] have studied the non linearity effects of varactor diodes used in reconfiguring a printed Yagi-Uda dipole antenna. They have concluded that a varactor diode with a higher power rating and larger tuning range is required if their designed antenna is to be used for long range cognitive radio communications. Moreover, they concluded that reconfigurable

antennas which use switching devices should have non linearity specifications placed on them. The author in [39] has also studied the effects of varactor non linearities in frequency-reconfigurable patch antenna and found that it suffers from gain compression and non reciprocity relationship, as the transmitting antenna must handle higher power levels than the receiving antenna.

2.3.4 Reliability of Switching Devices

Reliability of a device indicates the the probability of a device to perform its function satisfactorily under a specified environmental condition for a predetermined period of operating time [40]. p-i-n diodes, varactors and FET switches are reliable solid state devices [41]. MEMs switches are lacking reliability due to the mechanical failure of moving parts [23]. Most MEMS devices have components (e.g., membrane or cantilever) that are prone to common failure mechanisms (e.g., fatigue or stiction) [42]. Various approaches to improve MEMs reliability have been recently published in [35, 42, 43] and the research on this topic is still ongoing.

Table 2.1 gives a brief discussion about the pros and cons of some of the switch technologies that can be used in reconfigurable antennas.

2.4 Review of Previously Designed Reconfigurable Antennas

In this section, a comprehensive review of some of the reconfigurable antennas found in the open literature are presented and they are grouped based on the four categories mentioned in Section 2.3.1.

Device	Diagram	Description and Operation	Pros	Cons
p-i-n diodes	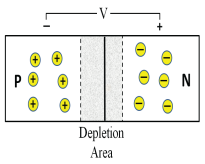	It has highly doped p-type and n-type regions separated by a wide lightly-doped intrinsic region. At high frequencies, when forward biased it acts like a low resistance and open circuit when reverse biased. [44].	• Low ON state loss. • Low OFF state capacitance. • Reasonable linearity. • Mature technology	• High dc power consumption. • Complex biasing.
FETs	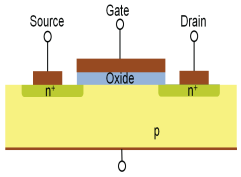	Increasing the gate voltage allows current to flow between the source and drain. [44].	• Low ON state loss. • Low OFF state capacitance. • Low dc power consumption. • Good linearity. • Widely available in the 2.4 and 5 GHz bands	• Ultra-wideband SPST switches are not commercially available yet.
MEMs	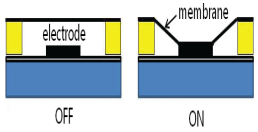	Tiny mechanical switches made on a substrate. An electrostatic force pulls the beam down when a voltage is applied [44].	• Very Low ON state loss. • Very low OFF state capacitance. • Highly linear.	• Slow switching speed. • High actuation voltage (20–90 V). • Low reliability.
Varactors	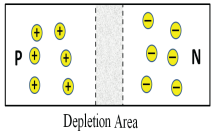	It is a diode with a thin depletion layer and the capacitance is inversely proportional to the square root of the applied voltage [44].	• Continuous tunable operation. • Low dc power consumption	• Highly non-linear. • Analogue bias voltage required.
Optical switches	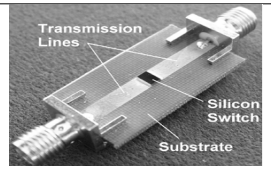	When silicon is illuminated by light, it changes from an insulator state to a near conducting state [23].	• Avoidance of biasing lines that could disturb the antenna performance.	• Not easy to integrate in some wireless devices.

Table 2.1: **Pros and cons of switching devices in reconfigurable antennas.**

2.4.1 Frequency Reconfigurable Antennas

In the open literature, a large number of frequency reconfigurable antennas that can switch between two or more narrowband operations. These antennas have enormous applications in RF systems where multiple functions and operations are the main objectives. A reconfigurable tri-band H-shaped antenna with frequency selectivity feature for compact wireless communication systems is proposed in [45] as shown in Figure 2.1. A varactor diode connecting the upper and lower arms of the H-shape radiator is used for frequency reconfigurability. The antenna can work in three frequency modes: 1) single band at 1.88 GHz, 2) dual band at 1.88 and 2.4 GHz, and 3) a tri band at 1.57, 1.88 and 2.4 GHz. A compact printed multi band antenna suitable for reconfigurable wireless communication systems is presented in [46] as shown in Figure 2.2. By adding four varactors to the design, it becomes a reconfigurable design, enabling the bands to be electrically and independently tuned over wide ranges. A reconfigurable wideband and multiband C-Slot patch antenna with dual-patch elements is proposed and studied in [19] as shown in Figure 2.3. Two p-i-n diode switches are used to switch ON and OFF two patch elements to operate the antenna in two different dual-band modes or a wideband mode.

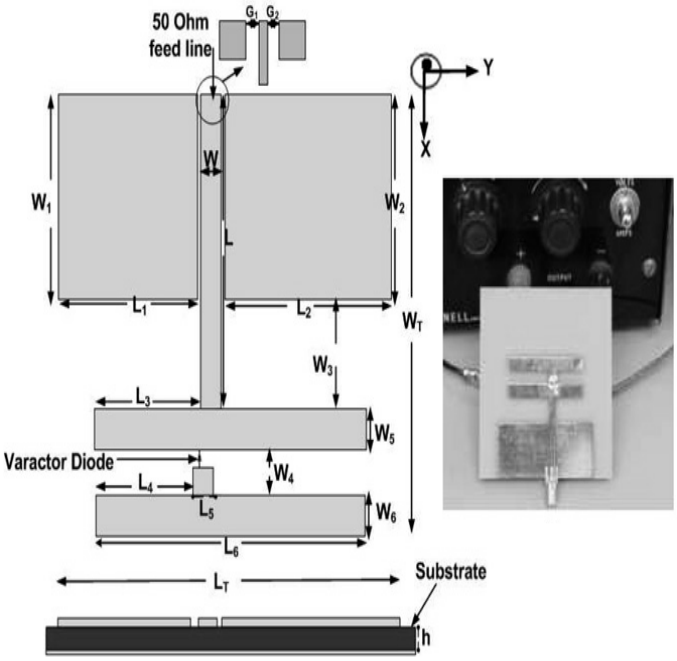

Figure 2.1: **Reconfigurable antenna geometry and prototype in[45].**

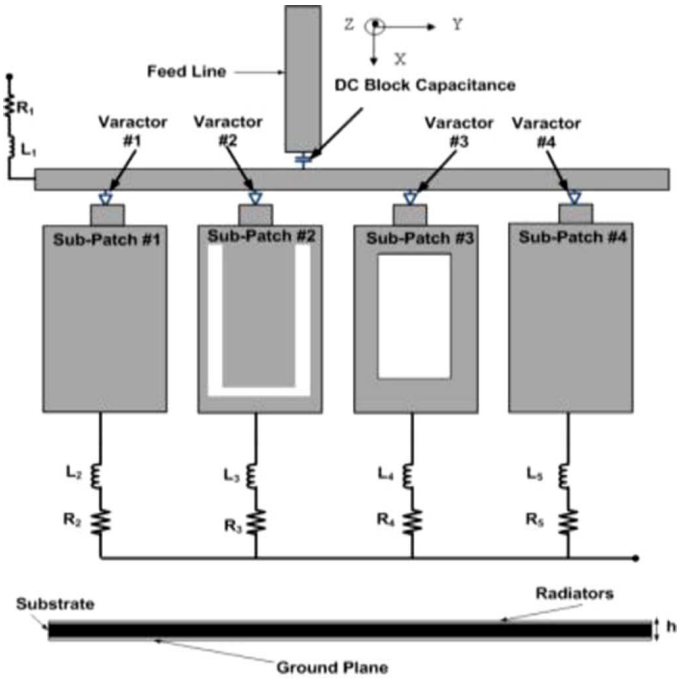

Figure 2.2: **Reconfigurable antenna geometry in[46].**

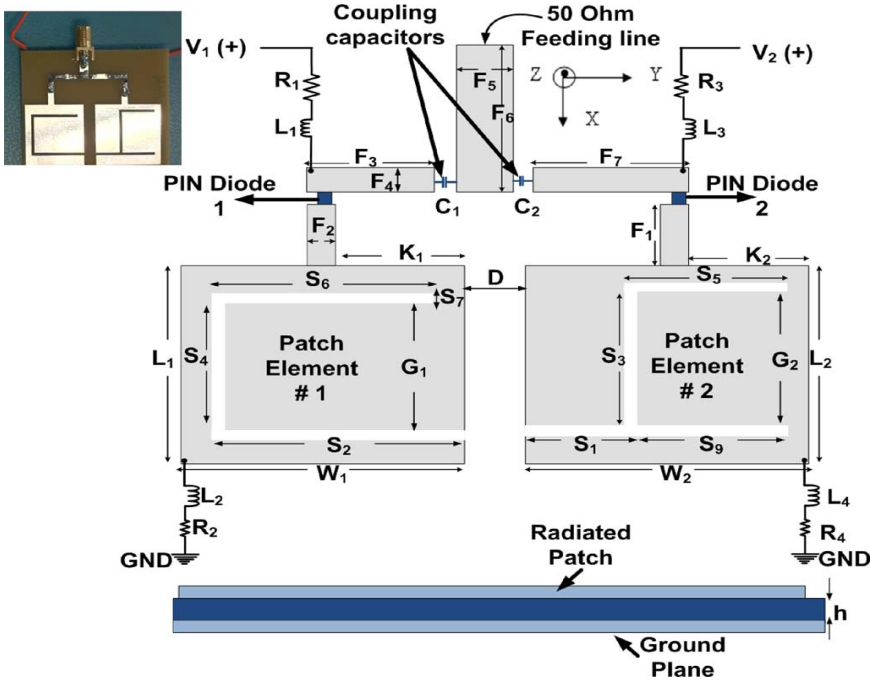

Figure 2.3: **Reconfigurable antenna geometry and prototype in[19].**

For CR scanning and communication, three types of frequency reconfigurable antennas operation can be deployed as follows :

(a) **Ultra-wideband to narrowband using separate excitation ports**

One of the approaches to deploy reconfigurable antennas in CR RF front-ends is to use an ultra-wideband antenna for sensing the spectrum and another reconfigurable narrow band antenna for communication purpose, thereby we have two different ports for the antenna. Some of the designs from this type of reconfigurable antennas are shown in Figures 2.4, 2.5 and 2.6 [47–49]. The structure in [47] is a novel combination of wideband and narrowband antenna into the same volume. The wideband antenna is a CPW fed printed hour-glass shaped monopole which operates from 3 to 11 GHz. The narrowband antenna is a microstrip patch printed on the reverse side of the sub-

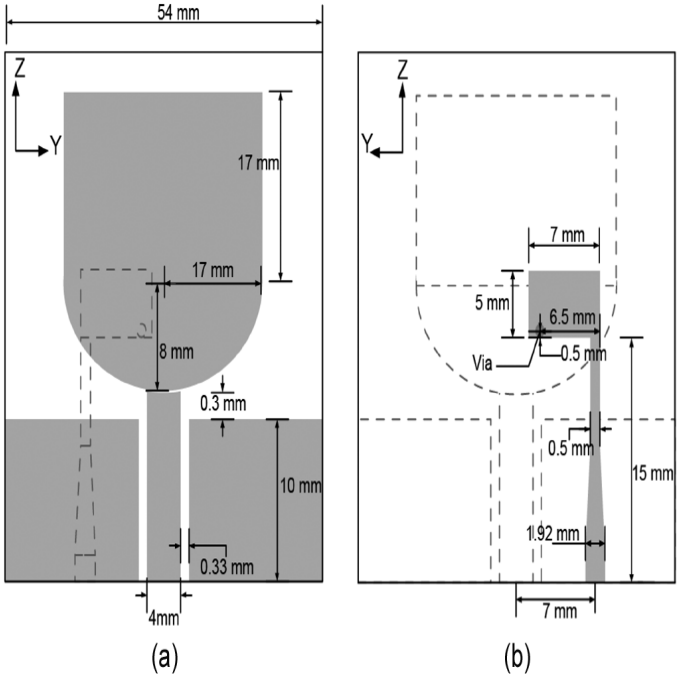

Figure 2.4: **Reconfigurable antenna geometry in[47].**

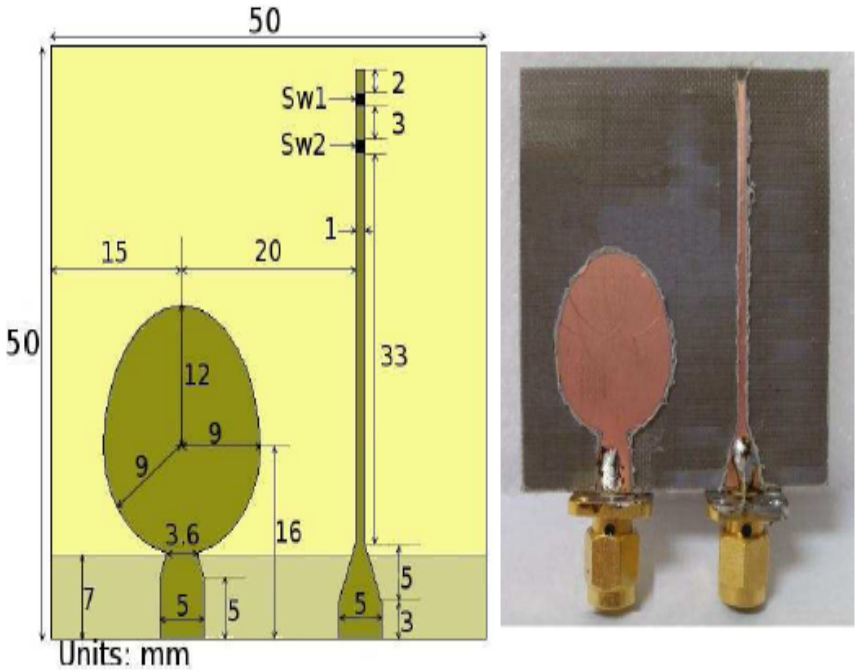

Figure 2.5: **Reconfigurable antenna geometry and prototype in[48].**

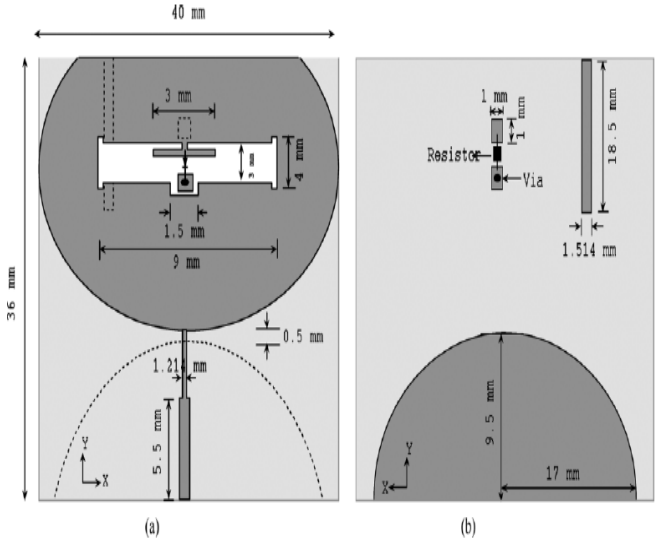

Figure 2.6: **Reconfigurable antenna geometry in [49].**

strate, and connected to the wideband antenna via a shorting pin and designed to operate from 5.15 to 5.35 GHz. This design can be suitable for Cognitive Radio applications where a wideband antenna is required for spectrum sensing and a narrowband antenna for operation which can be tuned over a wide bandwidth using an external tuning circuit. The ultra-wideband and WLAN bands were chosen to demonstrate the integration principle. Although this antenna is compact in size, it still has some drawbacks and the major drawback comes from the two antenna ports and the isolation between them, is degrading the whole performance due to the coupling between the wideband and narrowband antenna. The antenna also works in a single narrow band (4.9–5.35 GHz) and therefore to work in additional narrow bands some external tuning circuits are required.

The antenna in [48] has two antennas on the same board. One of them is an egg-shaped patch sensing antenna. The design of the patch,

the partial ground plane and the feed matching section guarantee an ultra-wideband response for the sensing antenna. The second antenna is the communicating antenna and it is a microstrip line connected to a 50 Ω feed line via a matching section. This structure has multiple resonances in the 3.1 to 10.6 GHz ultra-wideband frequency range. Switches are incorporated along the antenna. By controlling these switches, the length of the antenna is changed, thus leading to various resonance frequencies. Additional switches can be used to obtain more resonances. The major drawback of this antenna is the isolation issue between the two antenna ports, this limited isolation degrades the whole performance due to the coupling between the wideband and narrowband antenna. Moreover, to obtain more resonances, the antenna has to be increased in size.

The antenna in [49] has an elliptical disc monopole as an ultra-wideband radiator, covering the band from 3 to 11 GHz, and a another reconfigurable narrow slot antenna is used for communicating in the operating range of 5–6 GHz. The narrowband antenna is incorporated into the resonator disc without degrading the sensing antenna performance. This is due to the strategical location of the narrowband slot antenna being chosen where the current distribution on the elliptical radiator is very small.

(b) **Ultra-wideband to narrow band using same excitation port**
Another approach to deploy frequency reconfigurable antenna in Cognitive Radio is to use one antenna for both sensing and communication by reconfiguring an ultra-wideband antenna to work into multiple predefined frequency bands. Figures 2.7, 2.8 and 2.9 show some designs

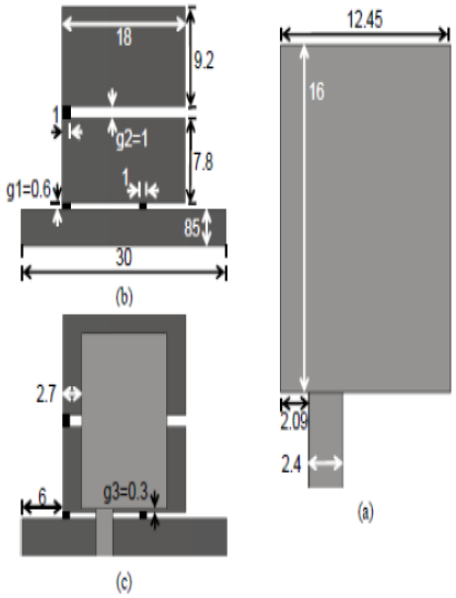

Figure 2.7: **Reconfigurable antenna structure in [50].a) Radiating Patch, b)Ground Plane, c) Complete Antenna.**

that use this approach. The antenna in [50] shows the ability to switch between a narrow and ultra-wide impedance bandwidth, this is achieved by simply removing part of the ground plane from beneath the patch to obtain a wideband radiation. When all three switches are closed, the two ground planes are connected together electrically. The combined structure operates as a narrowband patch radiator and when all three switches are open the antenna is in the ultra-wideband mode of operation (3.7 to 11 GHz). The drawback of this antenna is the difficulty of tuning the antenna by changing the size of the patch ground plane. The structure in [51] is a novel vivaldi antenna with added switched band functionality to operate in a wideband or narrow-band mode. The antenna reconfiguration is realised by inserting four pairs of switchable ring slots into the ground plane of the structure.

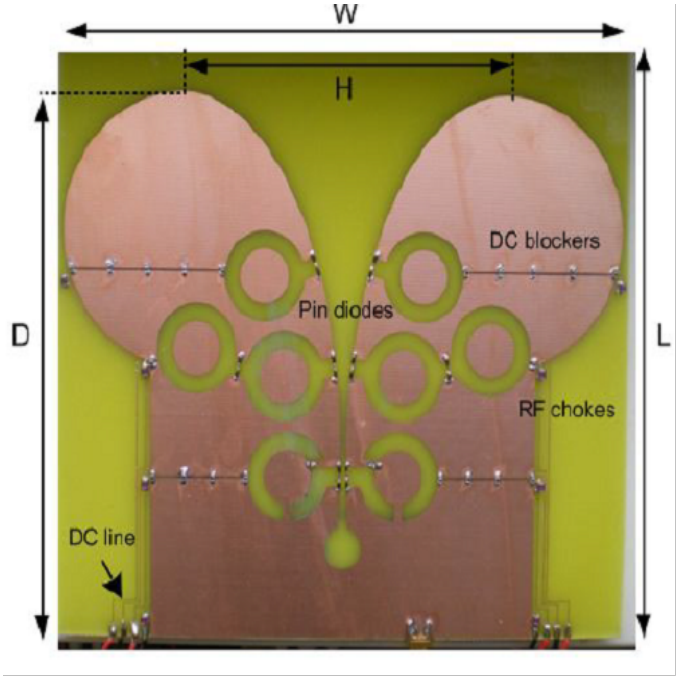

Figure 2.8: **Reconfigurable antenna prototype in [51].**

Figure 2.9: **Reconfigurable antenna prototype in [52].**

A wide bandwidth mode from 1.0 to 3.2 GHz and three narrowband modes can be selected. A fully functional prototype with p-i-n diodes switches has been developed. The drawbacks of this antenna are its size and complexity. The whole size of the antenna is 14.5 $cm \times 14$ cm, and there is large number of passive elements (26 surface mount inductors and capacitors, and almost 16 active elements). The antenna can be reconfigured into three narrowband regions and one of these bands (the narrow mid-band mode)has not achieved better than 10 dB return loss. Moreover, a redesign is needed to achieve more sub bands (e.g., a longer version of the antenna). The antenna in [52] is different from [51] as the reconfiguration process relies not on switching between different resonator positions but on varying the resonators electrical length, this antenna has seven modes of operations(e.g., one ultra-wideband + six narrow bands)

(c) **Ultra-wideband with notch band reconfiguration**

Another type of reconfigurable antennas that targeted the CR operation is the ultra-wideband antennas with reconfigurable band notch. Several designs of ultra-wideband antenna with band rejection characteristics have been successfully implemented. One of these antennas is shown in Figure 2.10. In this antenna [53], a U-shaped slot is placed within the monopole and a MEMS switch is used to short the resonant slot when the band rejection (5.2–6 GHz) is not required. Another antenna exhibiting a very wide bandwidth with reconfigurable rejection within the band is presented in [15], the antenna, as shown in Figure 2.11, is a bow-tie antenna operating from 1.5 to 5 GHz with slot etched along the bow-tie upper edge. p-i-n diodes are used as switching elements to short the slot at variable distances from the antenna

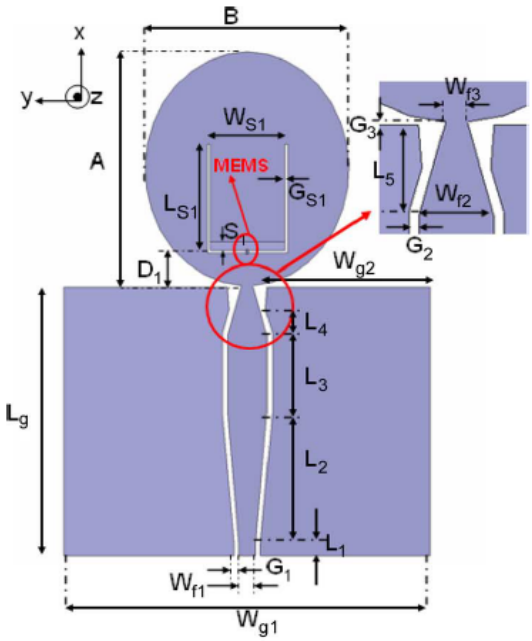

Figure 2.10: **Reconfigurable antenna geometry in [53].**

symmetry axis and thus obtaining different rejection bands. In [54], a vivaldi antenna having the capability of dynamically rejecting interferers was presented, only half of the vivaldi is used and placed over a ground plane as shown in Figure 2.12. The rejection filter has two microstrip resonators and two varactor diodes coupled to the slot of the vivaldi antenna. In [55], the authors have proposed a vivaldi antenna integrated with a microstrip line resonator with tunable band notches, the wide tuning range is obtained by using three varactors and up to seventeen tunable stop-bands can be obtained.

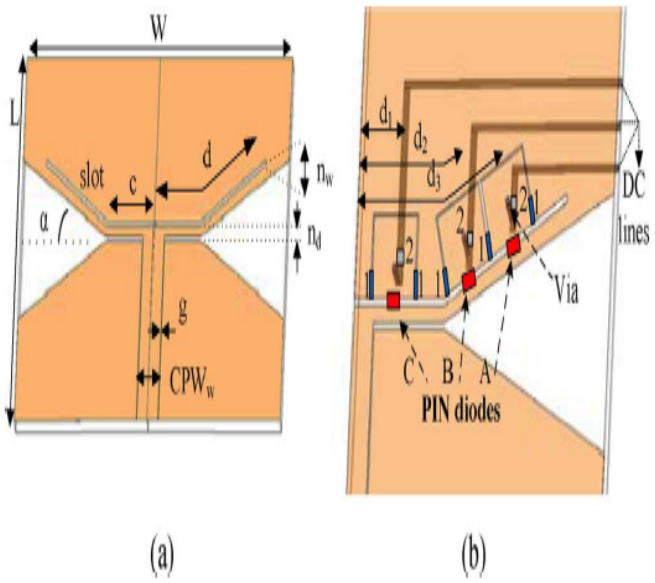

Figure 2.11: **General topology of the reconfigurable slot bow-tie antenna. (a) antenna topology. (b) Right side of the reconfigurable antenna [15].**

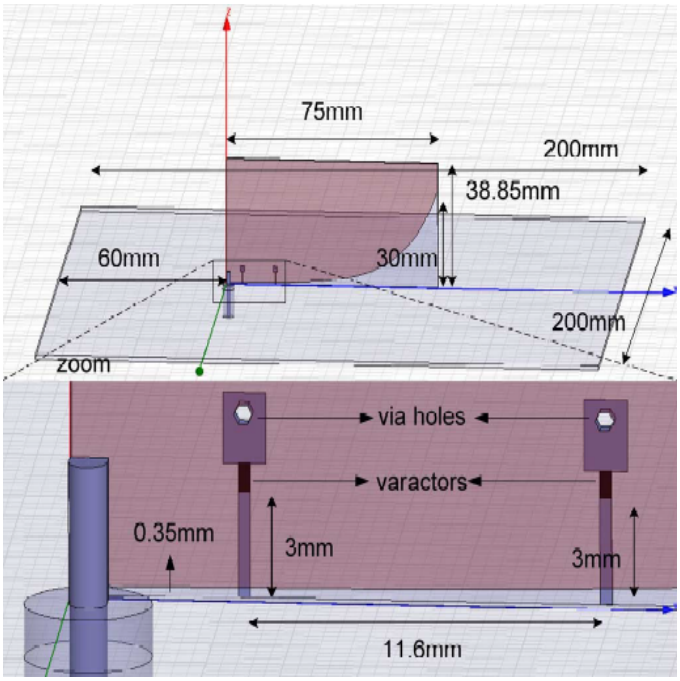

Figure 2.12: **Halved Vivaldi with reconfigurable band rejection [54].**

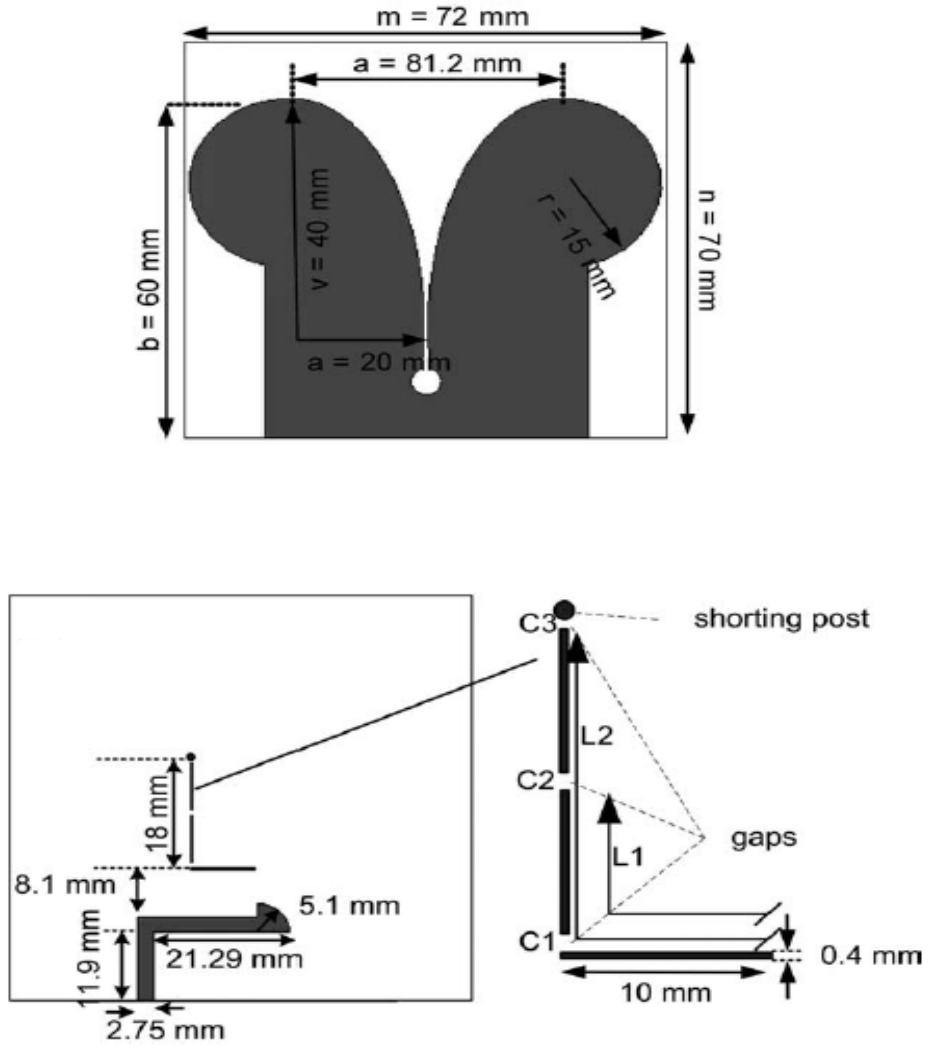

Figure 2.13: **Vivaldi with reconfigurable band rejection [55].**

2.4.2 Pattern Reconfigurable Antennas

In addition to frequency reconfigurable structures, there have been extensive research work and investigations about reconfiguration of radiation characteristics of antenna elements. Three of these narrowband antennas are shown in Figures 2.14, 2.15 and 2.16. In [56], the proposed antenna operates over DCS 1800 and PCS 1900 and consists of a dipole-loaded loop and a director. By using two p-i-n diodes switches, the proposed antenna can switch between two different beam directions with no input impedance variation. In [57], an antenna working at 2.3 GHz, is pattern reconfigured by using three p-i-n diode switches. This antenna can operate as a monopole antenna with an omnidirectional pattern or a dipole antenna with a reflector to obtain directional radiation patterns. In [58], a compact antenna consisting of a U-slot patch and eight shorting posts is presented. The antenna center frequency is 5.32 GHz and each edge of the square patch is connected to two shorting posts using two p-i-n diodes. The proposed antenna radiation patterns can be switched between three different patterns in the same frequency band. The three different radiation patterns are broadside pattern, conical pattern with maximum power in ZY plane and finally a conical pattern with maximum power level in the ZX plane.

Few published designs have discussed pattern reconfiguration of wideband and ultra-wideband antennas. In [59], a slotted bow-tie antenna with wideband pattern reconfigurability over 60 % bandwidth is designed. The antenna is fairly complex as it has a switchable feed network (from coplanar waveguide to slot line transition) using four p-i-n diodes with an associated complex dc bias network as shown in Figure 2.17. In [60], the same principle of reconfiguration as [59] is used but with only two p-i-n diodes. The antenna biasing is still complex and the fabrication of the antenna involves

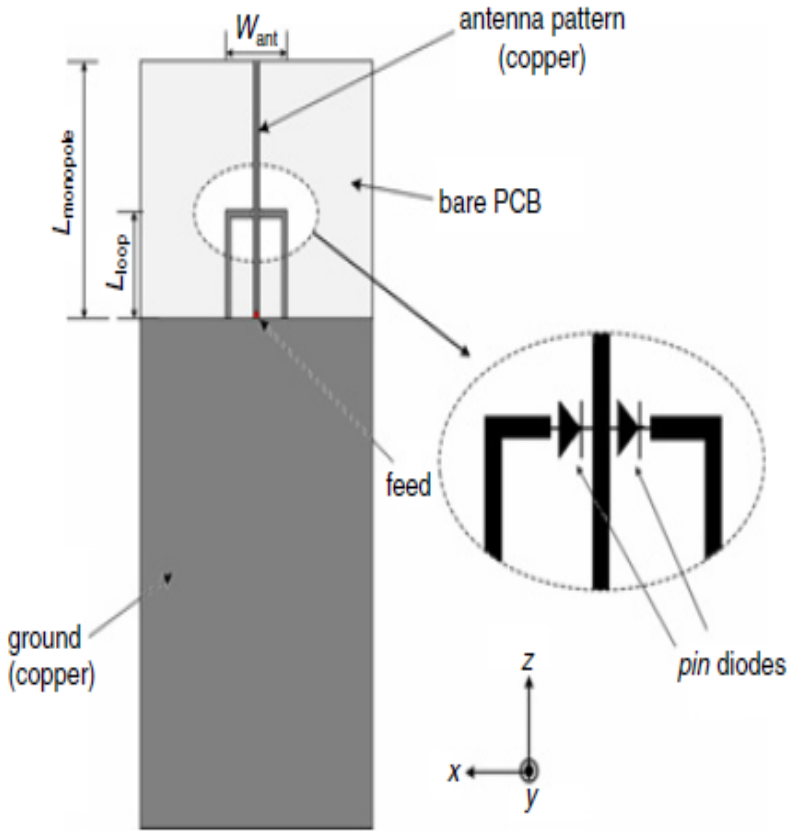

Figure 2.14: **Reconfigurable antenna geometry in [56].**

several via holes that increase the total fabrication cost and complexity as shown in Figure 2.18. In [61], a wideband pattern-reconfigurable antenna that changes operation from a vivaldi shaped slot mode to a monopole mode, providing three different radiation patterns over a 50.4 % bandwidth is discussed and analysed and shown in Figure 2.19. However, there is no implementation of real switches and it is believed that the dc biasing design of the switches would be complex.

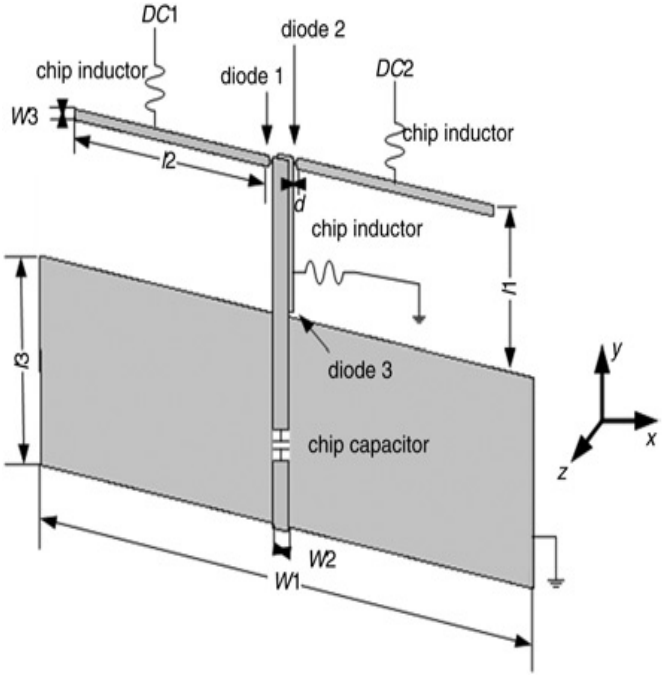

Figure 2.15: **Reconfigurable antenna geometry in [57].**

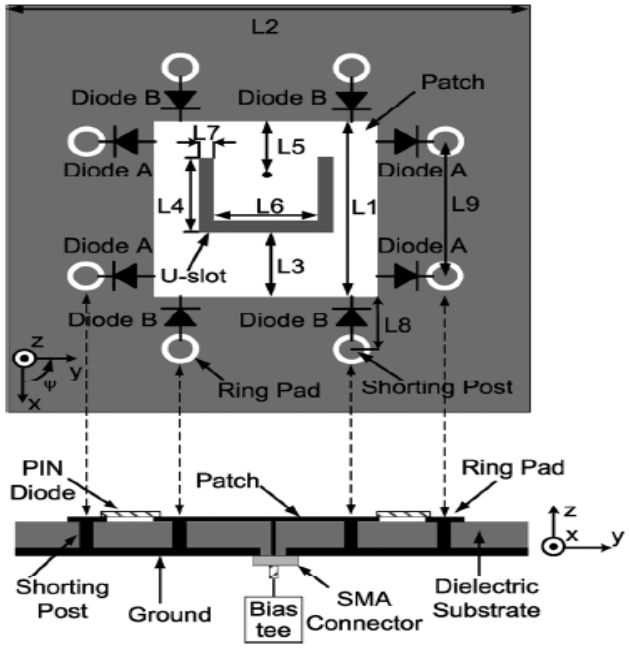

Figure 2.16: **Reconfigurable antenna geometry in [58].**

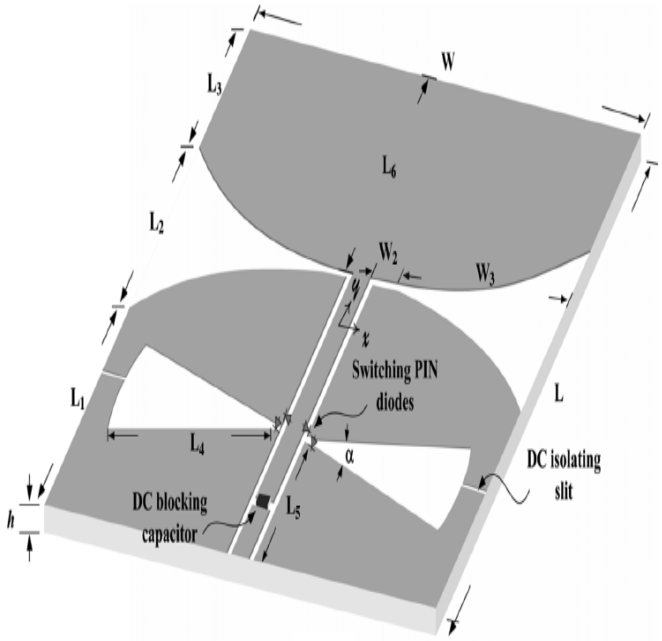

Figure 2.17: **3-D view of the pattern-reconfigurable wideband antenna in [59].**

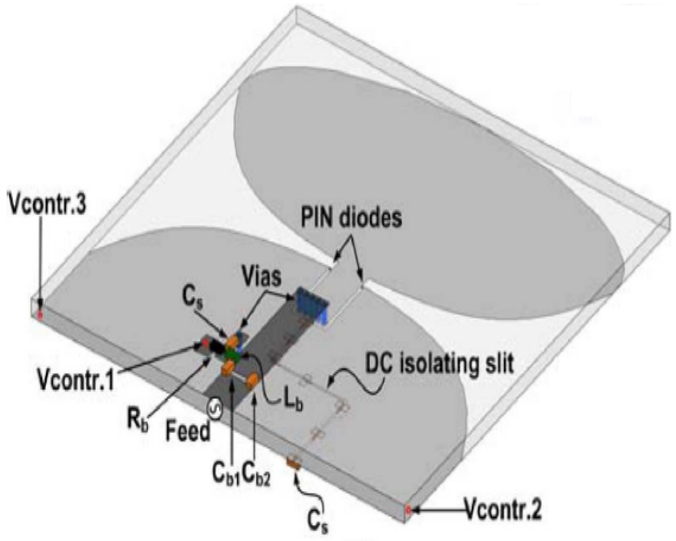

Figure 2.18: **3-D view of the pattern-reconfigurable wideband antenna in [60].**

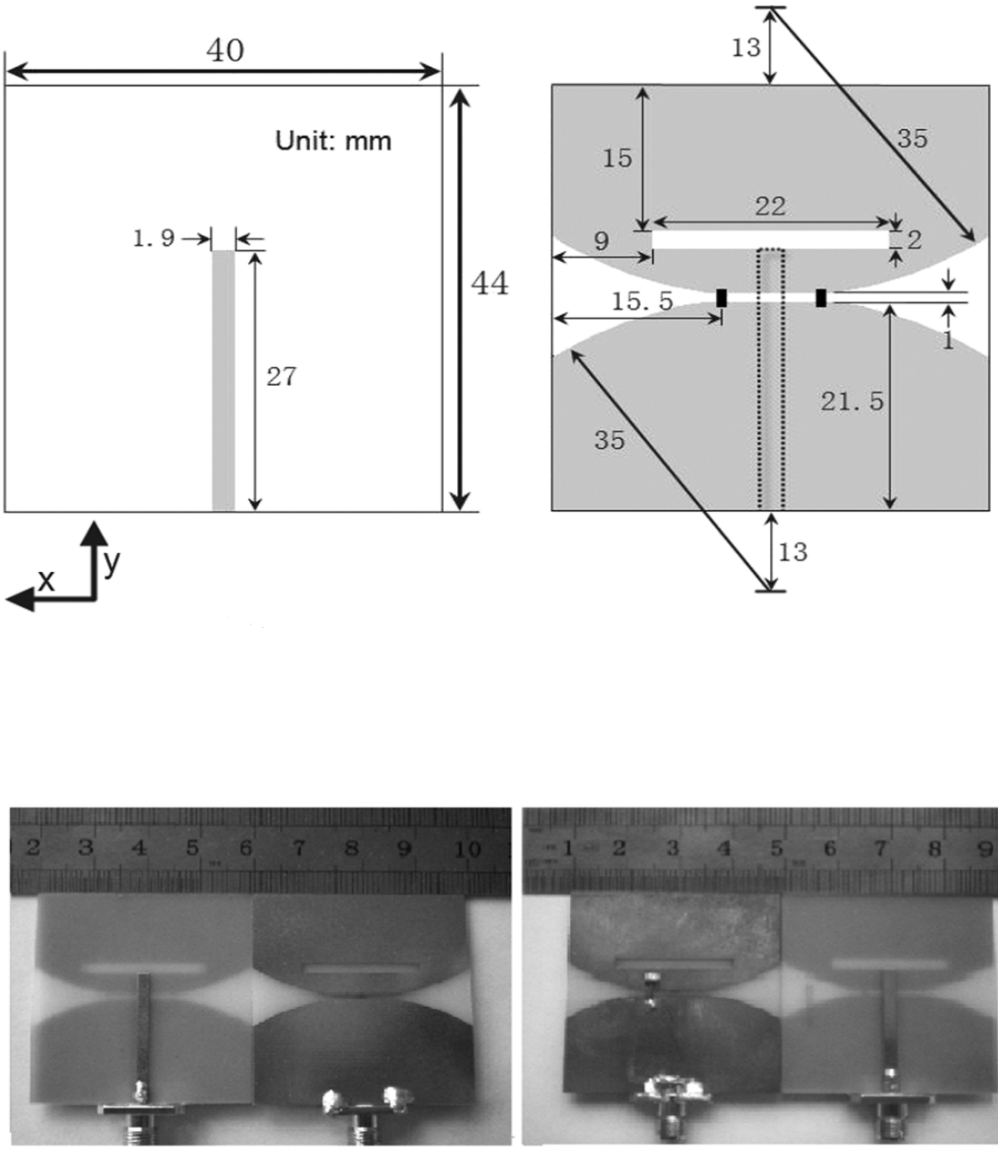

Figure 2.19: **Geometry and prototype of the pattern-reconfigurable wide-band antenna in [61].**

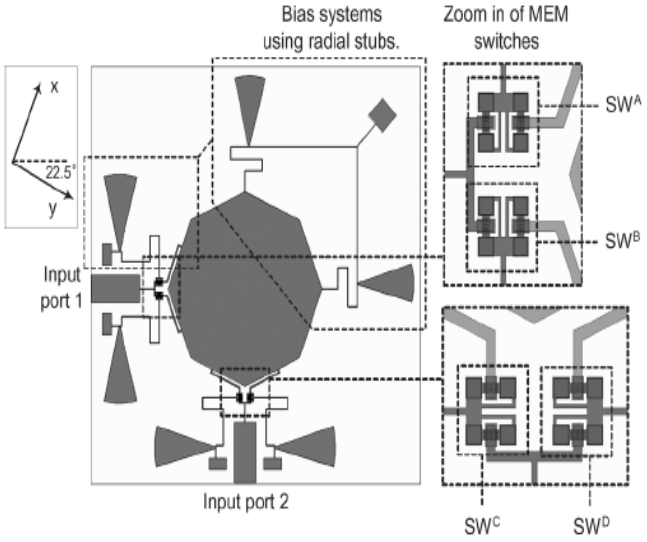

Figure 2.20: **Reconfigurable antenna geometry in [62].**

2.4.3 Polarisation Reconfigurable Antennas

In the open literature, many reconfigurable antennas with polarisation diversity between linear and circular polarisation or between LHCP and RHCP have been discussed. Three of these polarisation-reconfigurable antennas are shown in Figures 2.20, 2.21 and 2.22. In [62], a two port antenna operating at 3.82 GHz and consists of an octagonal patch that is by means of RF-MEMS switches capable of reconfiguring its polarisation from vertical/horizontal to slant $\pm 45°$. The drawback of this antenna lies in the complexity of the design, especially the feeding structure and the biasing network.

In [63], a microstrip patch with two truncated corners operating at 5.8 GHz can switch its polarisation from LHCP to RHCP using two piezoelectric transducer (PET) controlled perturbers, the choice for these kind of switches is due to their simple dc biasing circuit. In [64], a single fed circular microstrip antenna operating at 2.45 GHz with polarisation reconfigurable

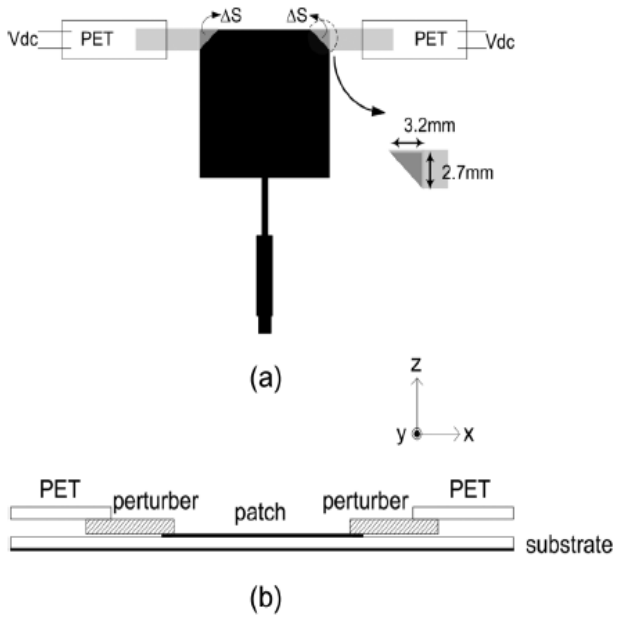

Figure 2.21: **Reconfigurable antenna geometry in [63].**

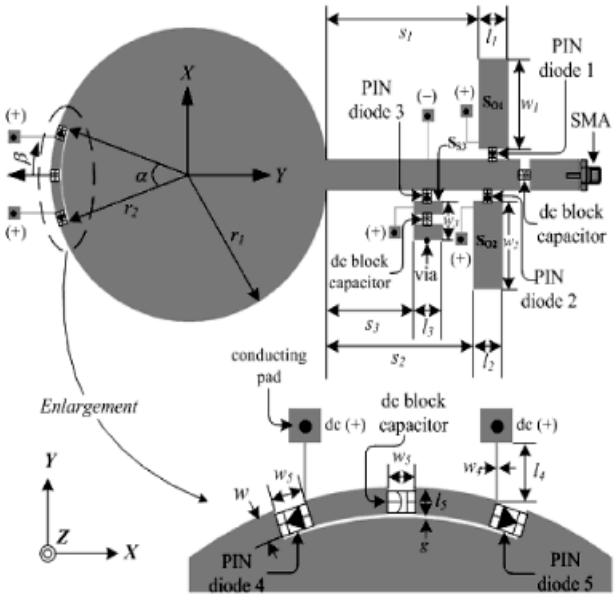

Figure 2.22: **Reconfigurable antenna geometry in [64].**

capability from linear polarisation (LP) to right hand circular polarisation (RHCP) or left hand circular polarisation (LHCP) is presented. Reconfigurability is achieved by inserting an arc-shaped slot at the top of the patch and controlling the shorting of this slot using two p-i-n diodes. The impedance matching has to be maintained by applying three stubs to the antenna feedline controlled by another three p-i-n diodes.

2.4.4 Combination of Different Reconfigurable Antennas

It might be possible to combine different categories of reconfigurable antennas in one single design, this flexibility will improve the performance of the antenna when deployed in nowadays fast changing different communication systems. Four of these antennas are shown in Figures 2.23–2.26.

In [65] a reconfigurable microstrip antenna with combined radiation pattern selectivity and polarisation diversity is presented. The antenna consists of four rectangular patches printed on one substrate, a feed network made by three Wilkinson power divider printed on another substrate and the ground plane is sandwiched between the two substrates. There are twelve ideal switches allowing reconfiguring the antenna to work in a conical radiation patterns with linear polarisation or broadside radiation with circular polarisation (CP) with a 3 dB axial-ratio fractional bandwidth of 14%.

In [66] a reconfigurable antenna with frequency and polarisation agility is presented, the antenna can be switched by means of p-i-n diodes between vertical, horizontal and 45° slant polarisation. Moreover, by using varactor diodes, the operating frequency of each polarisation can be independently reconfigured between 1.35–2.25 GHZ for the horizontal or vertical polarisation and from 1.35–1.9 GHz for the slant 45° polarisation. In [23] a frequency and pattern reconfigurable dipole antenna using photoconducting switches

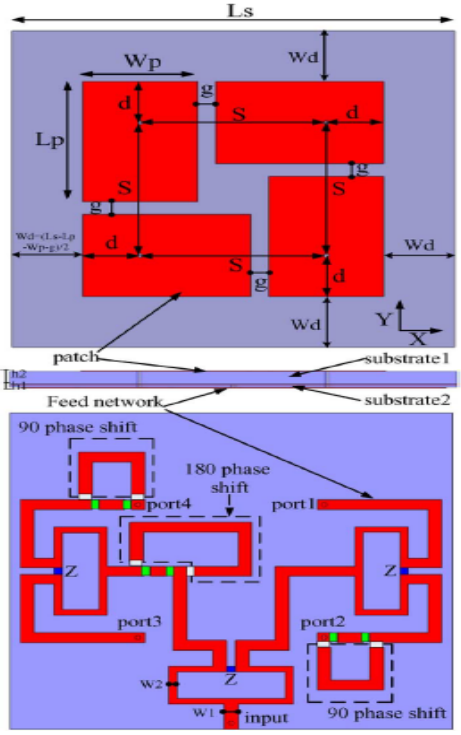

Figure 2.23: **Reconfigurable antenna geometry in [65].**

is presented. Two silicon switches are placed on small gaps in both dipole arms equidistant from the centre feed. When the antenna is frequency reconfigured, a frequency shift of nearly 40% (from 2.26 GHz to 3.15 GHz) is achieved. Moreover, when the antenna is pattern reconfigured, the direction of maximum gain shifts by 19° and there is also a much larger shift of about 50° in the E-plane pattern nulls. In [67], a novel reconfigurable microstrip antenna capable of frequency and pattern reconfiguration using five photoconductive switches is also proposed. The antenna can operate at three distinct frequency bands and at each frequency, the E-plane patterns can be reconfigured to five modes.

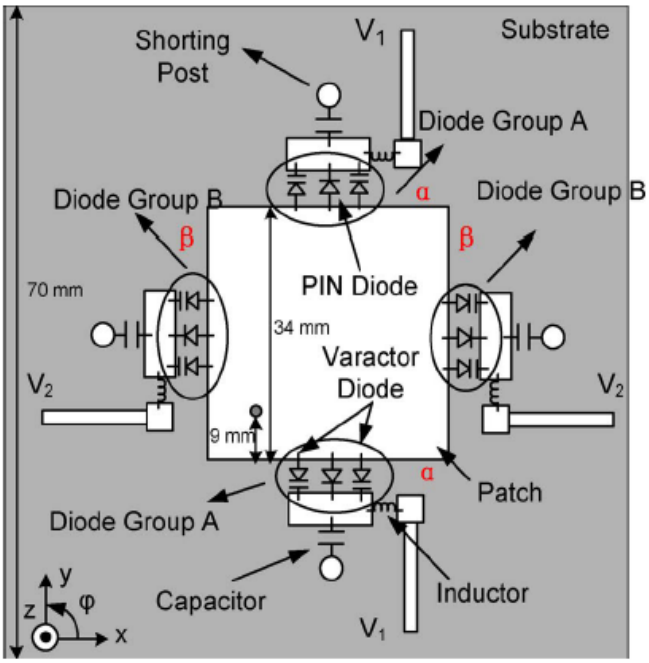

Figure 2.24: **Reconfigurable antenna geometry in [66].**

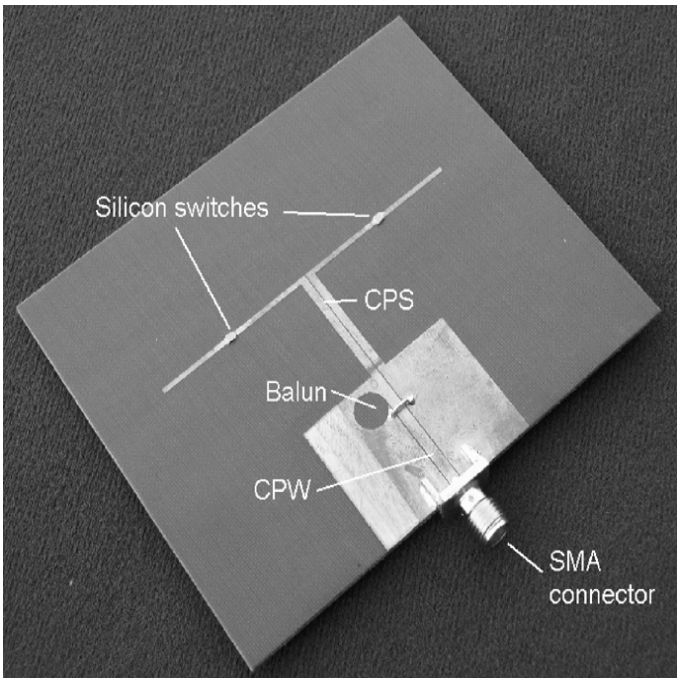

Figure 2.25: **Reconfigurable antenna prototype in [23].**

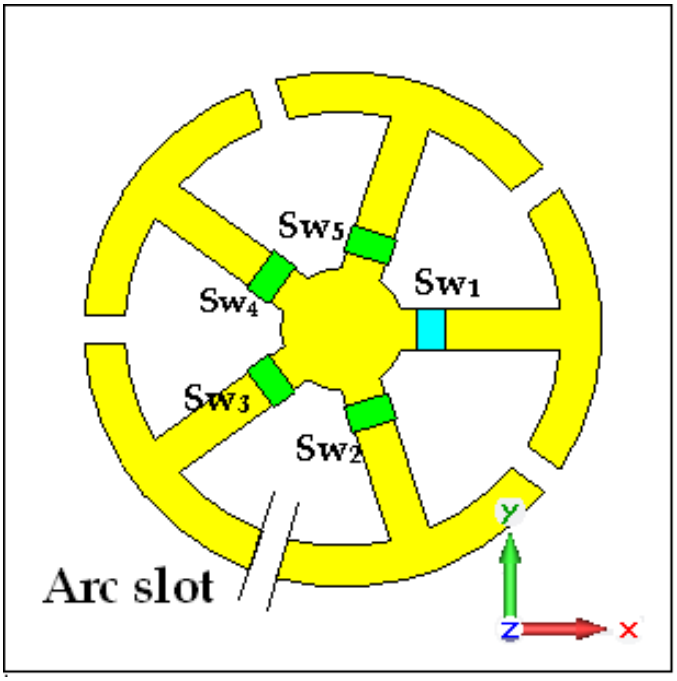

Figure 2.26: **Reconfigurable antenna geometry in [67].**

2.5 Summary and Analysis

- From the previously discussed reconfigurable antennas we notice that p-i-n diodes are easy to use as reconfiguration elements, this is because they are biased by low voltage but they are limited in terms of bandwidth of operation and they require large dc biasing currents to reduce their insertion losses. On the other hand the use of RF MEMs provides high bandwidth, less losses and high efficiency but they require a high +/- voltage to turn them on and they are lacking reliability. Currently no publications are available in the open literature that use GaAs FET switches to reconfigure ultra-wideband antennas.

- The use of varactors is considered to be a good reconfiguration method especially when we are tuning the antenna's operation frequency or tuning the rejection notch bands, however many issues appear in terms

of achieving voltage variations in biasing varactors and the difficulty in finding a varactor with significant capacitance range and on top of that, they are highly non linear devices that introduce many unwanted harmonics.

- Physical alterations of an antenna structure such as rotating or bending of one or more of the parts of the antenna eliminates the biasing problems, but they are generally difficult and designers are still looking for an easy way to implement mechanical reconfiguration. Another technique that reduces biasing problems is using optical switches which requires no dc biasing lines, but they are not easy to integrate in portable wireless devices.

- Although many reconfigurable antenna designs have targeted polarisation and pattern reconfiguration, applying these design in Cognitive Radio and exploiting their full potential in future smart wireless applications is still not clear. Some researchers and engineers in the field of reconfigurable antennas are looking for new techniques that achieve low losses; while others are trying to optimize and improve the existing methods. In general, the main goal is to reach a compromise between enhanced performance and increased system complexity. In the following chapters, novel and simple reconfiguration techniques are presented to reduce the size, cost, complexity and losses that are present in current designs.

3 Frequency Reconfigurable Ultra-wideband Antennas

3.1 Introduction

One of the approaches to deploy reconfigurable antennas in Cognitive Radio devices is to use the same antenna for both sensing and communication by reconfiguring the ultra-wideband sensing antenna to communicate into multiple predefined frequency bands. In this chapter, some novel designs for frequency-reconfigurable ultra-wideband antennas which can be used in Cognitive Radio and smart wireless applications will be presented. The operation principles of configuration are explained alongside with numerical and experimental investigations and analysis of the main characteristics of the designed antennas.

3.2 Antenna Design

Several different types of antennas have been designed for ultra-wideband applications. Among these designs, the planar circular disc monopole antenna features very simple structure, good return loss characteristics over wide operating bandwidth, satisfactory radiation properties and most importantly ease of fabrication and also integration with printed circuit boards

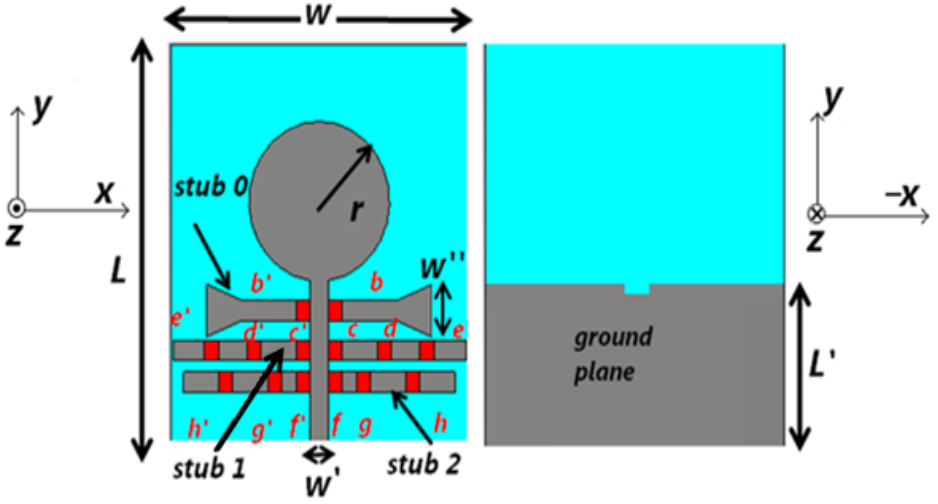

Figure 3.1: **Geometry of the reconfigurable ultra-wideband disk monopole antenna.**

[68]. The proposed ultra-wideband reconfigurable circular disk monopole antenna is based on the design presented in [68] in which there is no frequency reconfiguration. The geometry of the proposed reconfigurable ultra-wideband disk monopole antenna is illustrated in Figure 3.1.

The antenna has a circular disc monopole with a radius of 10 mm, 50 Ω microstrip feedline and stubs of different lengths are printed on the same side of an FR-4 dielectric substrate with a thickness of 1.5 mm and relative permittivity of 4.7. $L = 50\ mm$ and $W = 42\ mm$ denote the length and the width of the dielectric substrate, respectively. The widths of the microstrip feedline and the microstrip stubs are fixed at $W' = 2.6\ mm$ to achieve 50 Ω impedance [16]. The width of the triangular stub end is $W'' = 6.5\ mm$. On the backside of the substrate, the conducting ground plane has a length of only $L' = 20\ mm$. Switches (b, b') connect stub 0 to the microstrip feedline. Switches (c, d, e, c', d', e') control the length of stub 1 while switches (f, g, h, f', g', h') control the length of stub 2. The height of the feed gap between the feed point and the ground plane is fixed at 0.33 mm.

A prototype antenna was fabricated to verify the performance. Figure 3.2 shows the proposed prototype antenna. The 14 RF switches used in this prototype are realised as metal pads with dimensions 2 $mm \times 2.6$ mm. In a practical design, RF switches can be realised by means of either commercial p-i-n diodes or MEMs technology. A reconfigurable matching network employing stub tuners was designed to support multiple narrowband frequency ranges. Having 14 switches allows many reconfigurable cases but in this study the author investigates reconfiguration at:

- 2.4 GHz (ISM Band).
- 5 GHz (Wi-Fi Band).
- Dual band 2.4 GHz + 5 GHz.
- WiMAX band (3.2–4.2 GHz).
- (4.2–5.4 GHz) which is used for military fixed and mobile communication systems or in the Wi-Fi (Band–A).
- (6.5–7.5 GHz) which can be used by some fixed mobile and satellite applications.

3.3 Principle of Operation

The complete design and analysis for the conventional ultra-wideband circular disk monopole were proposed in [68], in which it has been demonstrated that the ultra-wideband operation is mainly due to overlapping of closely distributed modes of the disk monopole. The input impedance of the circular disk ultra-wideband antenna is shown in Figure 3.3. To demonstrate the principle of operation, reconfiguration at 2.4 GHz is described in this

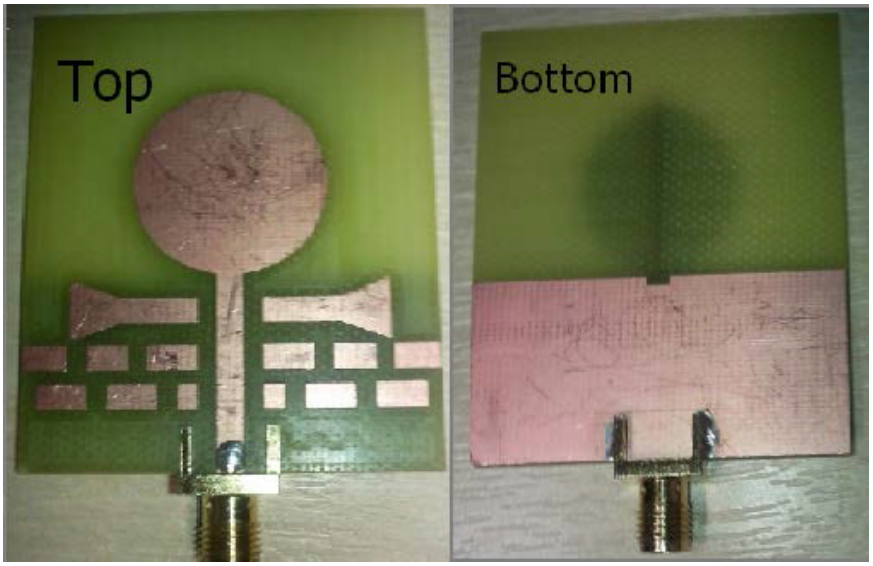

Figure 3.2: **Prototype of the reconfigurable ultra-wideband disk monopole antenna.**

section. The same principle applies for the other reconfigured bands. Figure 3.4 shows the input impedance for the ultra-wideband antenna when it is reconfigured to work at 2.4 GHz. It is quite clear from the zoomed inset that the resistance of the antenna at 2.4 GHz is almost 50 Ω and the reactance is nearly 0 Ω, indicating good impedance matching, also it can be observed that the antenna is not matched at out-of-band frequencies.

The principle of reconfiguration relies on connecting open circuit stubs to the antenna main feedline and by changing the length of the stubs, which act as resonator filters, the antenna can be reconfigured to different frequency bands. One could argue that the proposed concept is similar to connecting a tunable filter to an ultra-wideband antenna. However, the proposed filtering stubs are placed on the same substrate of the non-reconfigurable antenna in [68] without increasing the overall size of the proposed reconfigurable antenna. Moreover, the ultra-wideband antenna needs a ground plane to operate properly, so using this available space to build the filter

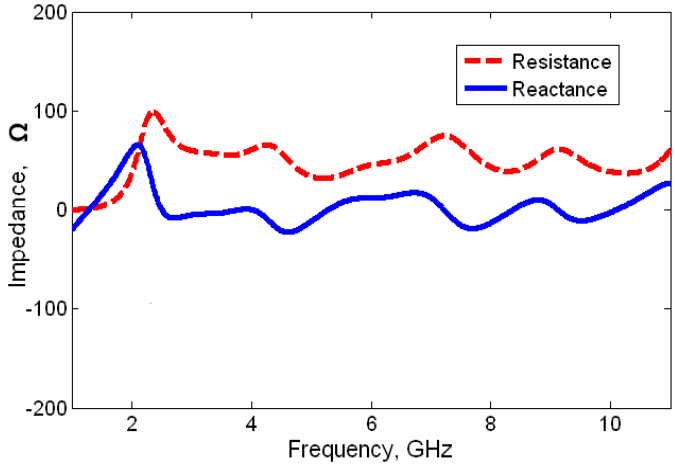

Figure 3.3: **Simulated impedance curves for the ultra-wideband antenna.**

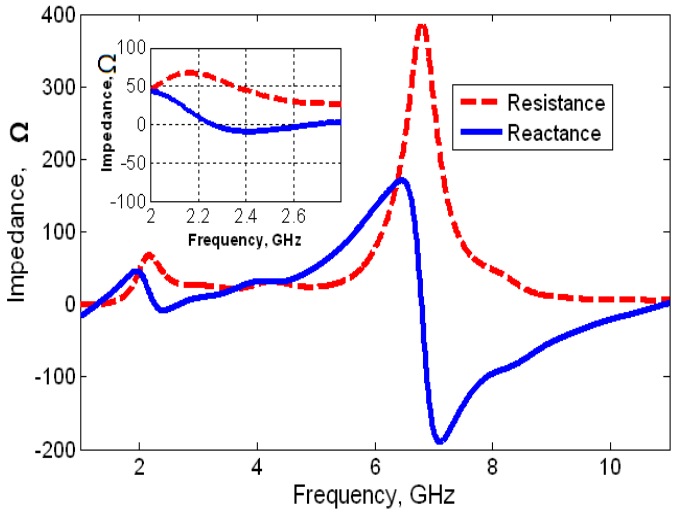

Figure 3.4: **Simulated impedance curves for the ultra-wideband antenna reconfigured at 2.4 GHz.**

adds reconfigurability without increasing the system footprint. Figure 3.5 shows the feedline of the antenna connected to stub 2 when switches f, f' are ON and the structure is simulated as a planar filter in CST Microwave Studio [69]. Figure 3.6 shows the forward transmission characteristics of the filter (e.g., return loss (RL) and insertion loss (IL)). The filter acts like a Low-Pass Filter (LPF) and when the response of this filter is cascaded

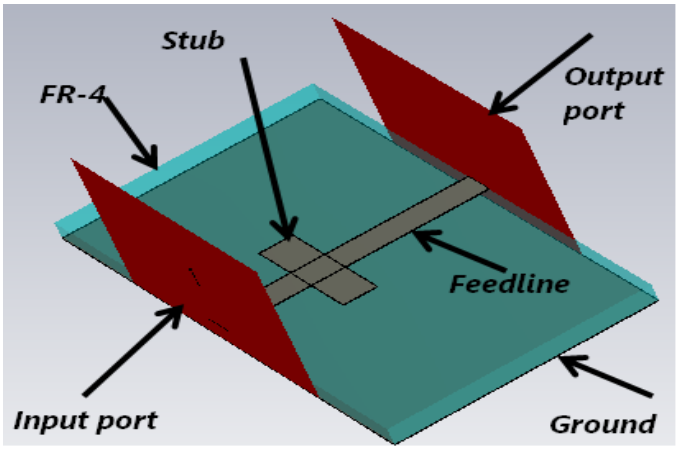

Figure 3.5: **Proposed filter when switches f, f' are ON.**

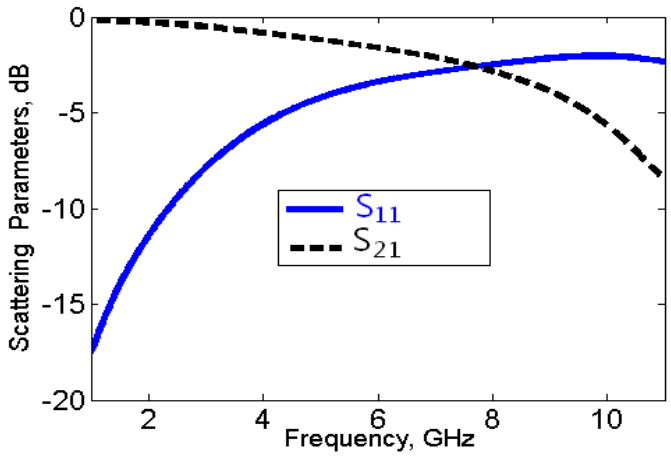

Figure 3.6: **Scattering parameters of the filter when switches f, f' are ON.**

with the ultra-wideband antenna, the antenna impedance bandwidth will be reconfigured to work at 2.4 GHz.

3.4 Numerical and Experimental Analysis

3.4.1 Ultra-wideband Operation

When all switches are OFF, the antenna functions as an ultra-wideband radiator (3.1–10.6 GHz) as regulated by FCC [70]; however, this frequency

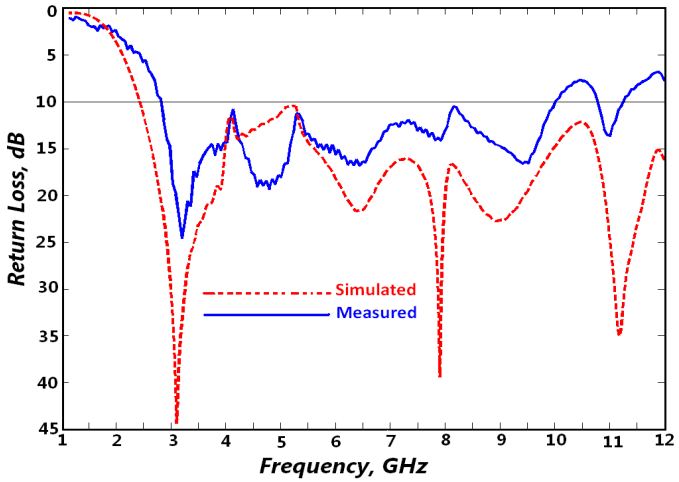

Figure 3.7: **Simulated (dotted red line) and measured (solid blue line) return loss curves when all switches are OFF (e.g., ultra-wideband case).**

range can be adjusted based on geographical locations and also applications. In this case the antenna is used to scan the whole ultra-wideband spectrum to check for any spectrum holes. Figure 3.7 shows the simulated and measured return loss curves for the ultra-wideband antenna when all stubs are disconnected from the antenna feedline. The simulated 10-dB return loss bandwidth is from 2.4–12 GHz and the measured 10-dB return loss bandwidth is from 2.8 to 10 GHz. The differences between simulated and measured values are mainly due to fabrication tolerances.

3.4.2 Reconfigurable Bands

Figure 3.8 shows the simulated and measured return loss curves of the reconfigured antenna in different bands.

a) Band I: 2.4 GHz.

   To configure the antenna to work at 2.4 GHz switches (f, f') are ON so there is a pair of 50 Ω open circuit stubs connected in parallel to

the ultra-wideband antenna feedline. The length of each stub is 4 mm and it is 6.3 mm away from the SMA input port of the ultra-wideband microstrip feedline.

b) Band II: 3.3 to 4.4 GHz.

For operation between 3.3 and 4.4 GHz, switches (f', f, g, h) are ON. The length of the stub is 24.6 mm and it is 6.3 mm away from the SMA input port of the ultra-wideband microstrip feedline.

c) Band III: 4.1 to 5.4 GHz.

For antenna reconfiguration to achieve operation between 4.1 and 5.4 GHz, switches (b, b') are ON, so there are two open circuit stubs, with triangular ends, connected to the ultra-wideband antenna feedline. The length of the stub is 14.7 mm and it is 15.5 mm away from the SMA edge input port of the ultra-wideband microstrip feedline. The triangular end of the stub has slightly increased the bandwidth of the antenna and in future designs, one could stick with normal rectangular stubs to save space on the board.

d) Band IV: 5 GHz.

To configure the antenna to work at 5 GHz, switches $(b, b', c, c', d, d', f, f', g, g', h, h')$ are ON.

e) Dual band : 2.4 and 5 GHz.

The antenna design in Fig. 3.1 provides also dual-band operation at 2.4 GHz and 5 GHz simultaneously, for this case switches (f, f', g) are ON. The length of the whole stub is 17.6 mm and it is 6.3 mm away from the SMA edge input port of the ultra-wideband microstrip feedline.

f) Band V : 6.5 to 7.5 GHz.

To configure the antenna to work between 6.5 and 7.5 GHz, switches (c, c', d, d') are ON. The length of the whole stub is 28.6 mm and it is 10.3 mm away from the SMA input port of the ultra-wideband microstrip feedline. The shift in frequency between measured and simulated results is due to the antenna fabrication tolerances.

3.4.3 Radiation Patterns and Gain

The radiation patterns have been simulated and also measured inside an anechoic chamber. The measured and the simulated normalised radiation patterns at 2.4 GHz in Band I, 3.3 GHz in Band II, 4.4 GHz in Band III, 5 GHz in Band IV and 7 GHz in Band V are plotted in Figure 3.9. Moreover, Figures 3.10 and 3.11 depict the simulated 3-D patterns of the reconfigured antenna at different frequency bands. It is noticed that the H-plane patterns are omnidirectional and they are very close to those obtained in the simulations. The simulated E-plane pattern is a doughnut shape like a traditional monopole. There are some distortions on the measured curves, these ripples are caused by the feed connector and the coaxial cable used in the measurement and every effort has been taken to minimise the effect of these artefacts on measurement quality.

The realised gain was measured using the gain-transfer method [71]. In this method, the antenna under test (AUT) gain is measured by comparing it to the gain of a standard gain horn (SGH). This method is performed by illuminating the AUT by a plane wave and the received power is measured. The AUT is then replaced with the SGH, and the received power is measured again. The simplified schematic diagram of this method is shown in Figure 3.12. The realised gain of the AUT can be calculated from (3.1) as follows

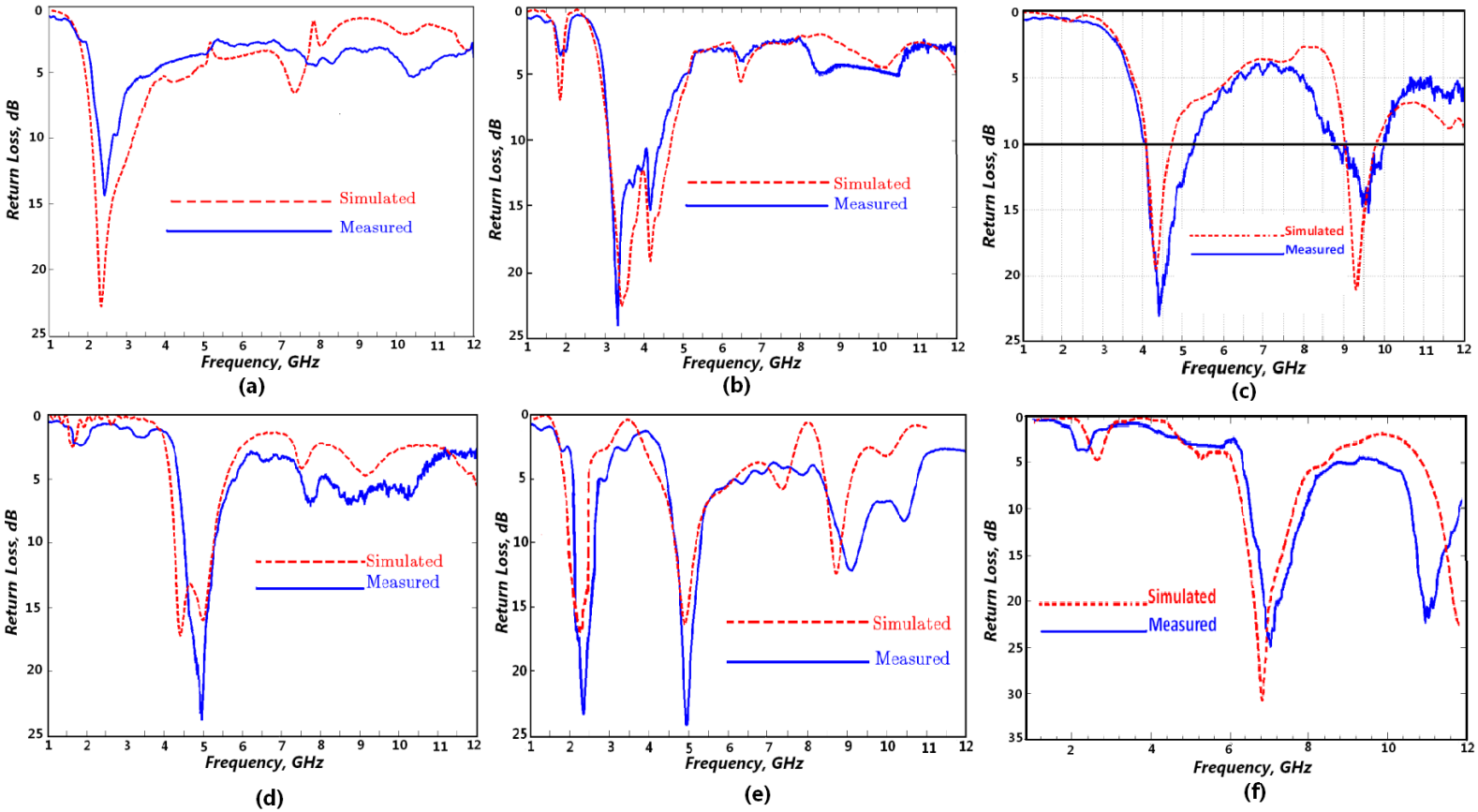

Figure 3.8: **Simulated and measured return loss curves when antenna is configured in: a) Band I at 2.4 GHz, b) Band II: 3.3 to 4.4 GHz, c) Band III: 4.1 to 5.4 GHz, d) Band IV: 5 GHz, e) Dual band: 2.4, 5 GHz, and f) Band V : 6.5 to 7.5 GHz.**

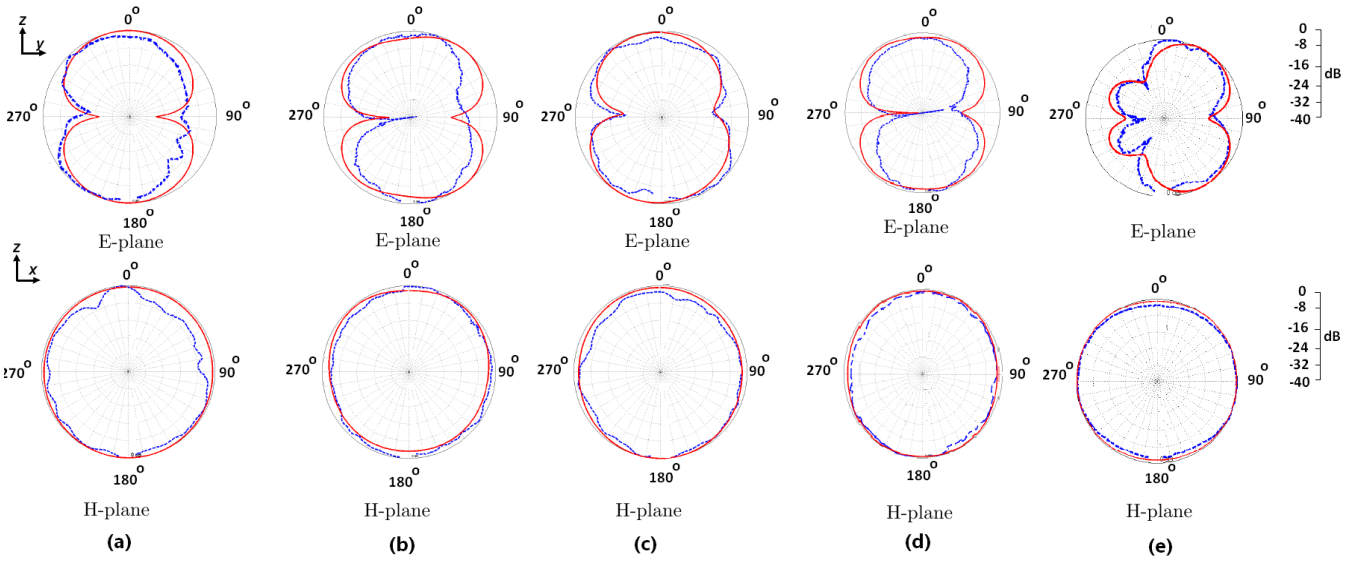

Figure 3.9: **Simulated (solid red line) and measured (dotted blue line) normalised E-plane and H-plane radiation patterns when the antenna is configured at : a) 2.4 GHz in Band I, b) 5 GHz in Band IV , c) 3.3 GHz in Band II, d) 4.4 GHz in Band III, and e) 7 GHz in Band V.**

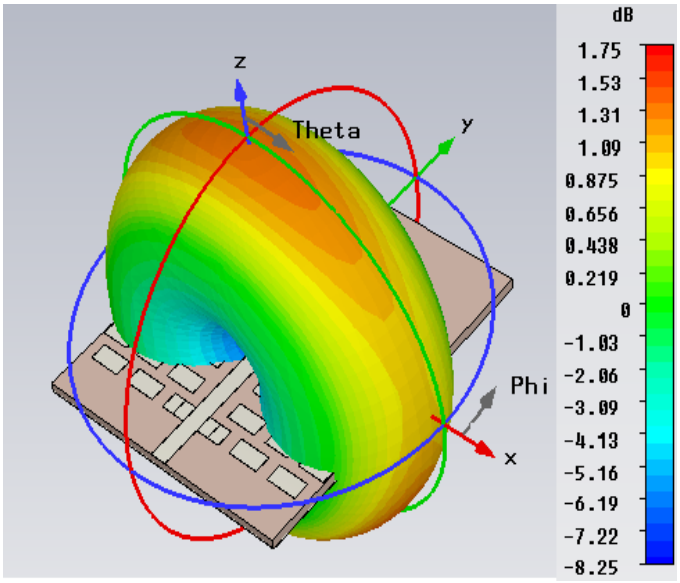

Figure 3.10: **Simulated 3D realised gain when the antenna is configured at 2.4 GHz in Band I.**

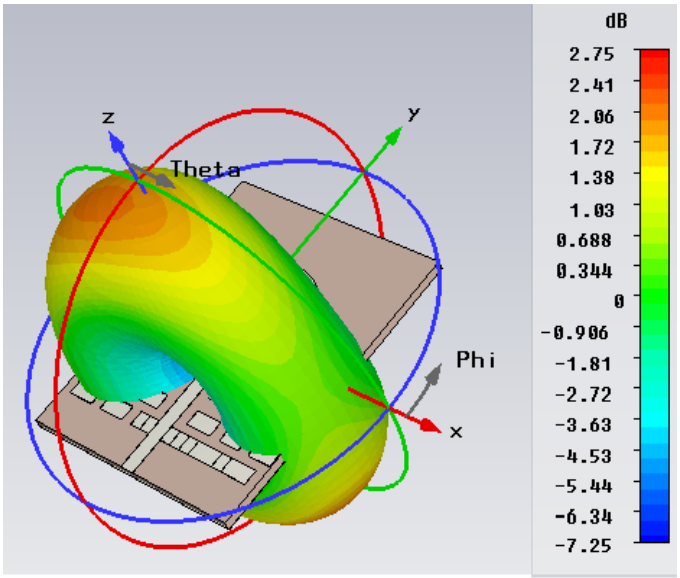

Figure 3.11: **Simulated 3D realised gain when the antenna is configured at 3.3 GHz in Band II.**

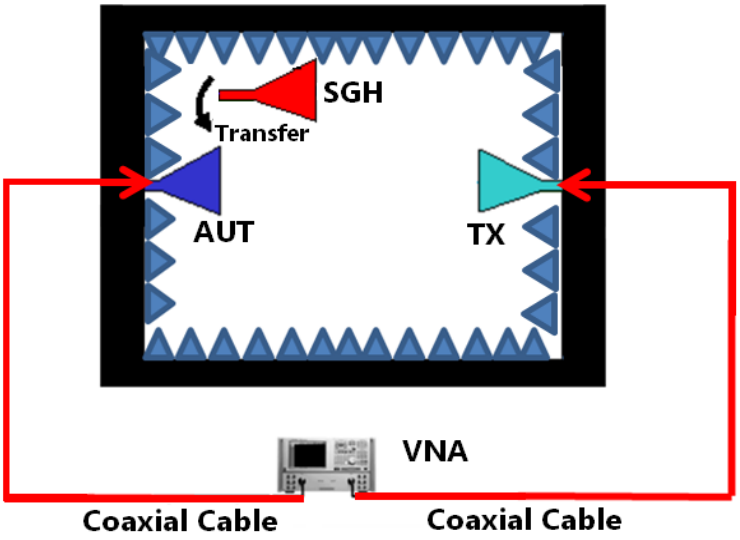

Figure 3.12: **Schematic diagram of the gain transfer method.**

	Realised Gain (dBi)			
	Ultra-wideband Mode		Reconfigurable Modes	
Frequency(GHz)	Simulated	Measured	Simulated	Measured
2.4 in Band I	1.6	1.25	1.75	2.2
3.3 in Band II	2.7	2.5	2.75	2.6
4.2 in Band II	2.2	2.1	2.6	2.5
4.4 in Band III	2.0	2.5	2.2	2.7
5.0 in Band IV	2.1	2.5	2.17	3.0
7.0 in Band V	4.1	4.4	4.09	4.6

Table 3.1: **Simulated and measured realised gain of the ultra-wideband mode and the reconfigurable modes**

$$G_{(AUT)} = G_{(SGH)} + Pr_{(AUT)} - Pr_{(SGH)} \tag{3.1}$$

where $G_{(AUT)}$ is the realised gain of the test antenna in dBi, $G_{(SGH)}$ is the gain of the standard gain horn in dBi, $Pr_{(AUT)}$ is the power received with the test antenna in dBm and $Pr_{(SGH)}$ is that power received with the standard gain horn in dBm. Table 3.1 summarises a comparison of the realised gain between the ultra-wideband case and the reconfigured cases. Due to better

matching, the reconfigured cases show slight increase in peak realised gain compared to the ultra-wideband modes at the same frequencies.

3.4.4 Surface Current

The circular disk monopole is capable of supporting multiple resonance modes, these higher order modes are the harmonics of the first resonant frequency [68]. Since these higher order modes are closely spaced, the overlapping of these resonant modes leads to the ultra-wideband characteristics. The simulated current distributions of the ultra-wideband circular disk monopole antenna are presented in Figure 3.13. Figure 3.13(a) and 3.13(b) show the average surface current at 2.4 GHz and 6 GHz, respectively. The current distribution at 6 GHz is also shown in Figure 3.13(b). The current is distributed along the edge of the circular disk and at low frequencies the antenna is operating in an oscillating mode (standing wave). However, at high frequencies the antenna starts to operate in a hybrid mode of standing and travelling wave [68].

The simulated current distributions when the ultra-wideband antenna is reconfigured to work in Band I at 2.4 GHz are presented in Figure 3.14. Figure 3.14(a) shows the average surface current at 2.4 GHz which is the reconfiguration frequency. Figure 3.14(b) presents the current distribution near 6 GHz which is an out-of-band frequency. It is interesting to see the effect of the stubs on the surface current at different frequencies. At 6 GHz (an out-of-band frequency) the stubs are perturbing the surface current and the current is significantly reduced along the radiating edges of the disk so there will be reduced radiation.

The simulated current distributions of the reconfigured ultra-wideband in Band V at 7 GHz are presented in Figure 3.15. Figure 3.15(a) shows the

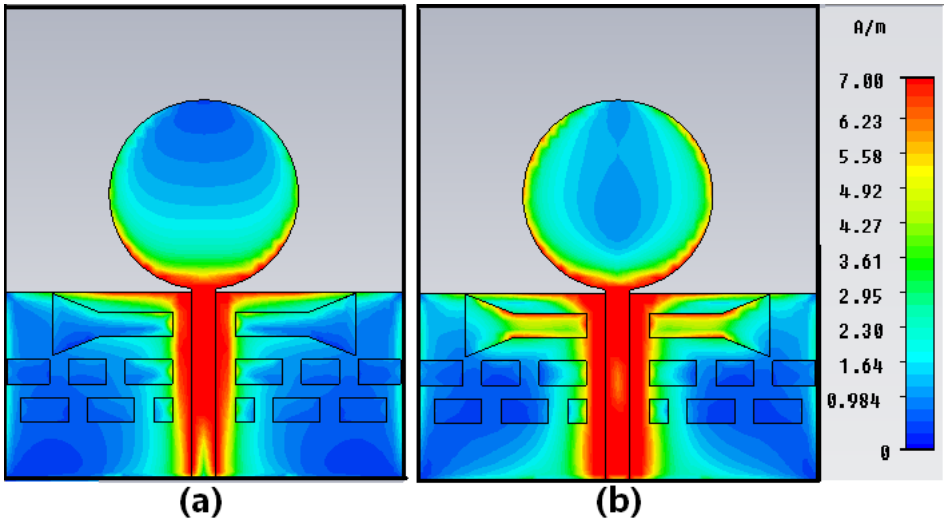

Figure 3.13: **Simulated current distribution of the ultra-wideband antenna at (a) 2.4 GHz, b) 6 GHz.**

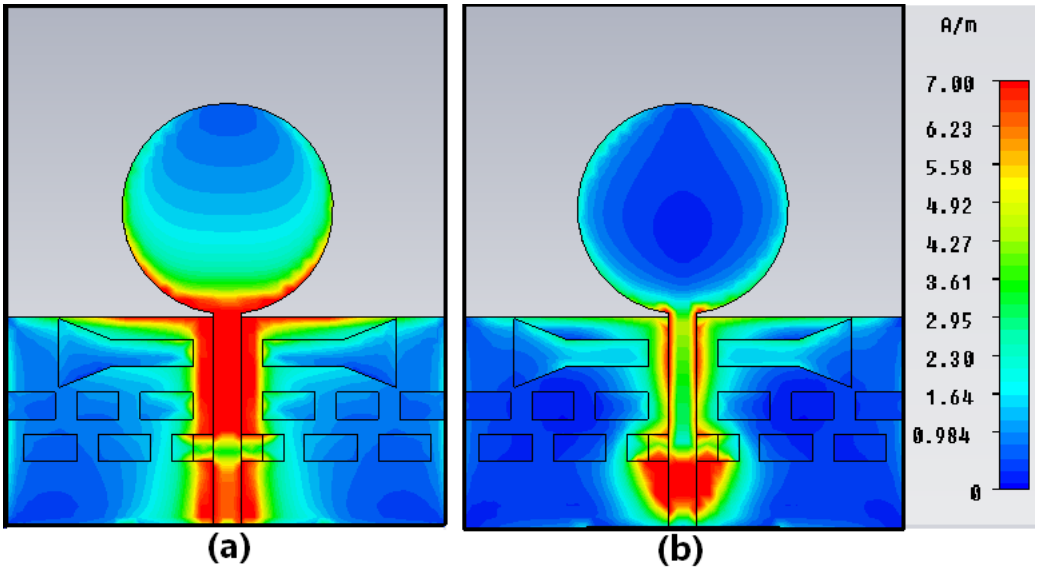

Figure 3.14: **Simulated current distribution of the 2.4 GHz reconfigured ultra-wideband antenna in Band I at (a) 2.4 GHz, (b) 6 GHz.**

average surface current at 3 GHz which is an out-of-band frequency. Figure 3.15(b) presents the current distribution near 7 GHz which is the reconfiguration frequency. It is interesting to see the effect of the stubs on the surface current at different frequencies. At 3 GHz the stubs are perturb-

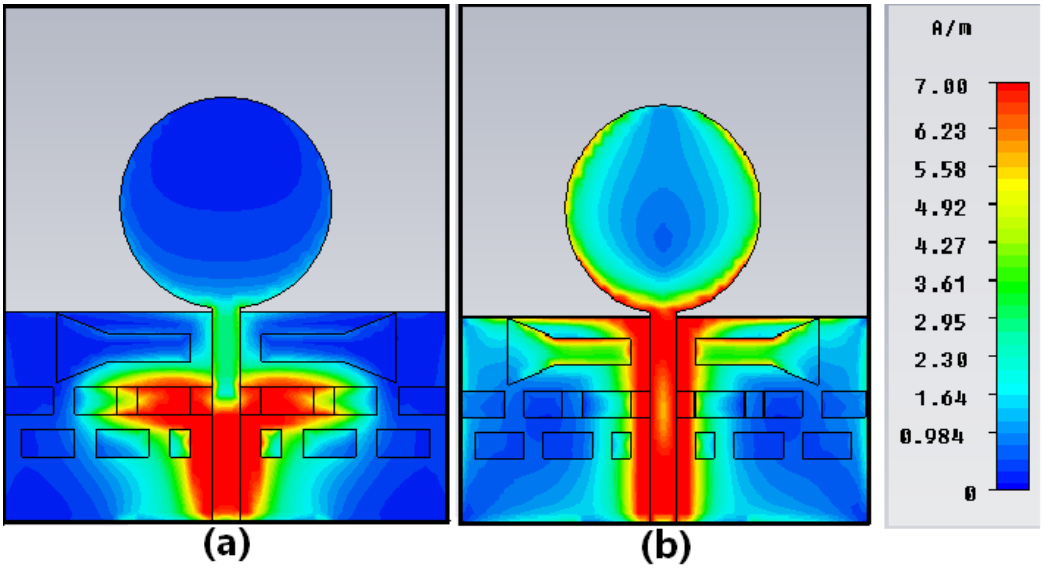

Figure 3.15: **Simulated current distribution on the 7 GHz reconfigured ultra-wideband antenna in Band V at (a) 3 GHz, (b) 7 GHz.**

ing the surface current and the current is significantly reduced along the radiating edges of the disk.

3.5 Reconfigurable Antenna Efficiency

Radiation efficiency is an important characteristic of antennas that determines the percentage of the accepted energy the antenna will radiate and hence has impact on the power consumption and the overall system performance in wireless communications. Radiation efficiency, η_r, is the fraction of the accepted power that ends up as radiated power [72]. Radiation efficiency is usually the limiting factor in the antenna performance and it can have a great effect on the overall system performance. There are several methods to measure antenna efficiency. The most accurate method is called the pattern integration method. In this method, radiation patterns are integrated over a spherical surface that completely encloses the antenna, and

this is done in the far-field region. This method requires good calibration of the anechoic chamber to achieve high accuracy. It is also often very time consuming, especially when the antenna has complicated radiation patterns or polarisation [73].

There are other methods that require less measurement and computation efforts and at the same time they provide accurate results. One of those methods is the resistance comparison method which uses two identical antennas except that they are made from two different metals, with slightly different conductivities. Measurement of the two antennas input resistance values is performed and the efficiency of either antenna is obtained according to [74] and the main drawback of this technique is the need of an extra antenna. Another technique is called the Q-Factor method [74]. It is the fastest and easiest method for this kind of measurement. The measured Q-factor is compared to the theoretical Q value of the antenna, and then the efficiency is computed. Theoretically, it is very difficult to compute the Q for an ideal lossless antenna, especially when the antenna structure is complicated.

A method that is less complex to apply to use is called the Wheeler Cap method, which was introduced by H. A. Wheeler in 1959 for measuring the radiation efficiency of small antennas [75]. Many papers adapted this method with some variations of the technique such as using different size and shapes of the cavity cap for different types of antennas [76, 77].

3.5.1 The Wheeler Cap Method

The radiation efficiency η_r of an antenna is the ratio of the total power radiated to the power accepted at the antenna terminal and can be written

as:

$$\eta_r = \frac{P_r}{P_{acc}} = \frac{P_r}{P_r + P_l} = \frac{R_r}{R_r + R_l} \tag{3.2}$$

where P_r is the radiated power, P_{acc} is the power accepted by the antenna and P_l is the power lost in the antenna due to ohmic and dielectric losses. For simple antennas, the input resistance can be described with two resistances in series, R_r and R_l, which represent the radiation resistance and the loss resistance, respectively. The sum of R_r and R_l equals the real value part of input impedance of the antenna which can be easily measured, and then it should be determined how the input resistance separates into radiation resistance and loss resistance [73].

Wheeler has enclosed the antenna with a conductive cavity sphere of radius $\frac{\lambda}{2\pi}$ to eliminate the radiation resistance R_r from the input impedance. Now, the real part of the input impedance of the antenna when enclosed by the hollow sphere is equal to the loss resistance R_l. The hollow metallic sphere of radius $\frac{\lambda}{2\pi}$ is called the radiansphere. The conducting cap should eliminate the antenna radiation while causing no disturbance to the near field. The size, shape, or electrical conductivity of the cap are not critical [74]. The Wheeler cap method is easy to implement in the lab, and it requires only two measurements: the S_{11} with and without the cap in place. The radiation efficiency can be written in the following form:

$$\eta_r = 1 - \frac{1 - |S_{11}^W|^2}{1 - |S_{11}^f|^2} \times \frac{|1 - S_{11}^f|^2}{|1 - S_{11}^W|^2} \tag{3.3}$$

Where S_{11}^f is the reflection coefficient of the antenna in free space, and S_{11}^W is the reflection coefficient performed with the wheeler cap in place [73].

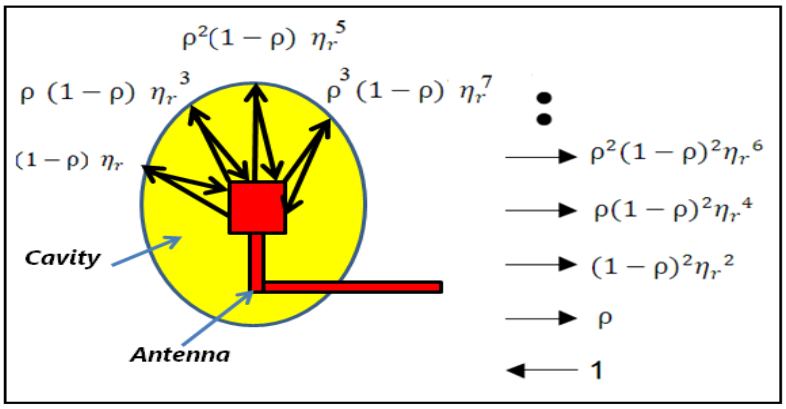

Figure 3.16: **Power fractions inside the wideband Wheeler cap.**

3.5.2 Applying The Wheeler Cap Method to Wideband Antennas

The conventional Wheeler Cap method assumes that the antenna can be modelled as a series or parallel RLC circuit. Moreover, it is assumed that the antenna input resistance can be modelled as a series of two resistances $(R_r + R_l)$. Also, it is very difficult and impractical to apply this method to wideband antennas because the cap size depends on the operating frequency and different cap size must be used at each frequency of interest.

There exists a method for evaluating the radiation efficiency of ultra-wideband antennas by using larger caps to perform the measurements [78]. For a cap radius larger than the radiansphere, the antenna will radiate freely and then receives its own transmitted-reflected signal . For a wideband antenna, the Wheeler cap should be larger than $\frac{\lambda}{2\pi}$ at the low frequency end of the band of interest [73]. This wideband Wheeler cap method assumes that reflections occur inside the cap and can be represented by power fractions [73]. The analysis of power fractions is shown in Figure 3.16. When a signal is incident on the input port of an antenna, a fraction of its power

is reflected $\rho = \frac{P_r}{Pin} = |S_{11}^f|^2$ due to impedance mismatch and the remaining fraction $(1-\rho)$ will be radiated with radiation efficiency η_r. When the antenna receives back the signal reflected from the Wheeler cap; it is absorbed by the antenna with an efficiency η_r and an impedance mismatch $(1-\rho)$ at the port. However, due to the mismatch at the port, part of the received signal is retransmitted with fraction of $\rho \times \eta_r$. This re-radiated portion is then reflected back to the antenna and now the return loss of the ultra-wideband antenna inside the Wheeler cap becomes [73]:

$$|S_{11}^W|^2 = \rho + (1-\rho)^2\eta_r^2 + \rho(1-\rho)^2\eta_r^4 + \rho^2(1-\rho)^2\eta_r^6 + \rho^3(1-\rho)^2\eta_r^8 + ... \quad (3.4)$$

$$|S_{11}^W|^2 = \rho + (1-\rho)^2\eta_r^2 \sum_{i=0}^{\infty} (\rho\eta_r^2)^i \quad (3.5)$$

The summation in the second term of (3.5) is replaced by its power series equivalent so (3.5) can be written as:

$$|S_{11}^W|^2 = \rho + (1-\rho)^2\eta_r^2 \frac{1}{1-\rho\eta_r^2} \quad (3.6)$$

Solving (3.6) for η_r and substituting for $\rho = |S_{11}^f|^2$ yields the following equation for radiation efficiency in terms of scattering parameters S_{11}^f and S_{11}^W.

$$\eta_r = \sqrt{\frac{|S_{11}^W|^2 - |S_{11}^f|^2}{1 - 2|S_{11}^f|^2 + |S_{11}^f|^2|S_{11}^W|^2}} \quad (3.7)$$

Usually we are interested in the total efficiency by including the impedance mismatch factor $(1-\rho)$. This contribution can easily be included by multiplying the radiation efficiency of (3.6) by the mismatch factor. The total efficiency η_t can then be computed using the following equation:

$$\eta_t = (1-\rho)\eta_r = (1-|S_{11}^f|^2)\sqrt{\frac{|S_{11}^W|^2 - |S_{11}^f|^2}{1-2|S_{11}^f|^2 + |S_{11}^f|^2|S_{11}^W|^2}} \tag{3.8}$$

3.5.3 Measurement Results of Frequency Reconfigurable Ultra-wideband Antenna Efficiency Using the Wideband Wheeler Cap Method

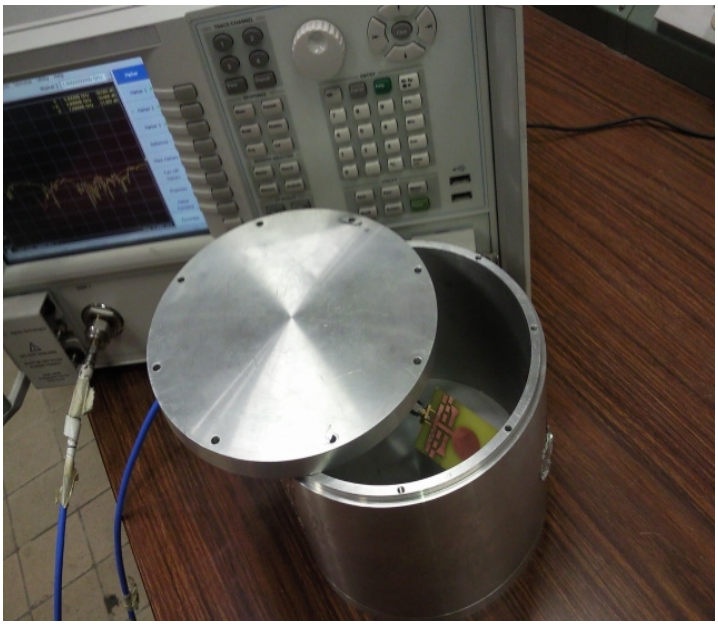

Figure 3.17: **Antenna radiation efficiency measurement setup using a cylindrical wideband Wheeler cap probed by an Agilent N5230C PNA-L network analyser (the cap is completely closed when taking measurements).**

The experimental set-up used to measure the previously proposed ultra-wideband antenna efficiency is shown in Figure 3.17. Since the dimensions of the ultra-wideband antenna are 50 $mm \times 42$ mm and at the lowest frequency of operation (e.g., 2.4 GHz), the minimum distance the antenna should be away from the wheeler cap walls is $d = \frac{\lambda}{2\pi} = \frac{c}{2\pi f} = \frac{3\times10^8}{2\pi\times2.4\times10^9} = 19.9$ mm. The Wheeler cap used is a cylindrical cap with a radius of 8 cm and the height of the cylinder is 12.5 cm. If the antenna under test is placed in

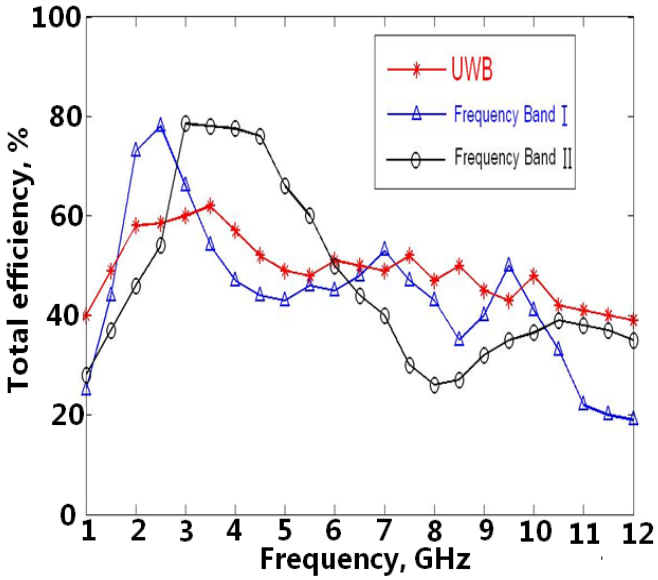

Figure 3.18: **Measured total efficiency η_t when the antenna is working in the ultra-wideband mode and when configured in Band I at 2.4 GHz and Band II 3.3–4.4 GHz**

the centre of the cylinder, we guarantee that the cap is larger than the radiansphere at 2.4 GHz. There are two measurements to make: one set of the ultra-wideband antenna return loss in free space and one when the antenna is enclosed in the Wheeler cap. In order to suppress cylindrical cavity resonance, the return loss measured when the antenna is enclosed in the cap is smoothed. Now both S_{11}^{f} and S_{11}^{W} are known and the total efficiency η_t is evaluated using (3.8).

The measured total efficiency η_t curves when the antenna is working in the ultra-wideband mode and when configured in Band I and Band II are shown in Figure 3.18. Table 3.2 shows a comparison between the simulated and measured values of the total efficiency η_t for both the ultra-wideband disk monopole and the reconfigured monopole. The differences between the simulated and measured results can be attributed to the measurement cable and connectors and the fabrication tolerances. It can also be noticed from

	Ultra-wideband Mode				Reconfigurable Modes			
	S		M		S		M	
F(GHz)	S_{11}(dB)	η_t(%)	S_{11}(dB)	η_t(%)	S_{11}(dB)	η_t(%)	S_{11}(dB)	η_t(%)
2.4 in Band I	-9.5	81	-6	58	-23	90	-14	78
3.3 in Band II	-28	91	-22	61	-22	88	-23	76
4.2 in Band II	-14	86	-12	50	-18	87	-20	75
4.4 in Band III	-13	86	-17	52	-19	83	-23	66
5.0 in Band IV	-11	77	-17	48	-17	78	-23	68

Table 3.2: **Comparison between the simulated and measured values of the antenna total efficiency η_t, S denotes simulated results and M is for the measured results**

Table 3.2 that when the antenna was reconfigured from the ultra-wideband mode to work into multiple narrowband sections, the impedance matching was better and the total efficiency has improved by $(15\% - 20\%)$ compared to the ultra-wideband case.

3.6 Applying p-i-n Diode Switches to Reconfigurable Antennas

All the previous measurements were performed using ideal switches (e.g., using copper tape to resemble a switch in the ON state and removing the piece of copper tape to resemble an OFF state switch). For this part of the work, p-i-n diodes will replace the ideal switches applied previously to investigate practical implementation aspects and issues. The p-i-n diodes used are (BAR64-03W) from Infineon [79]. These diodes are rated up to 6 GHz and they are cost-effective in comparison to many other switching elements. When they are forward biased they have low ON resistance ($<$ 1 Ω), and when reverse biased the OFF capacitance is approximately 0.17 pF as shown in Figure 3.19.

The antenna which was previously working in Band-I was re-simulated with its dc bias lines simulated as microstrip lines and using lumped passive

elements ($R = 4.3\ K\Omega, L = 220\ nH$) as RF chokes. The microstrip dc bias lines on the antenna board should have very high RF impedance; hence they have to be very thin traces. Usually 0.1 mm is the thinnest feasible trace width in the commercial PCB industry. The fabrication facilities used for this research (Antennas Measurement Laboratory at Queen Mary University of London) can manufacture boards with a minimum microstrip trace width of 0.3 mm, this leads to a 130 Ω impedance on 1.5 mm FR-4 board. From Figure 3.20, it is shown that when using dc bias lines alone (e.g., without RF chokes), the dc lines acted as stubs and changed the return loss of the antenna. When those dc lines where RF choked using sufficient values of inductance and resistance, the antenna was resonating at 2.4 GHz. Figure 3.21 shows the average current distribution on the antenna at 2.4 GHz and Figure 3.22 depicts the 3D farfield radiation pattern at 2.4 GHz. When the dc lines are not properly biased the antenna is not radiating at 2.4 GHz as shown in Figure 3.21(a) and Figure 3.22(a). When insufficient values of resistance and inductance are used to RF choke the dc lines (e.g., $R = 100\ \Omega, L = 5\ nH$), the antenna can still resonate at 2.4 GHz, but at the same time, RF will leak through the dc lines and this will affect the antenna surface current, radiation and gain as shown in Figure 3.21(b) and Figure 3.22(b). When using large values for inductance or resistance (e.g., $R = 4.3\ K\Omega, L = 220\ nH$) the antenna is resonating and radiating well at 2.4 GHz as illustrated in Figure 3.21(c) and Figure 3.22(c).

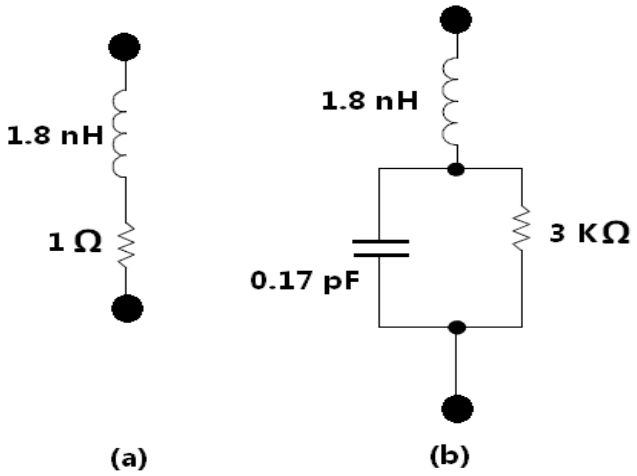

Figure 3.19: **p-i-n diode $BAR64-03W$ equivalent circuit when it is: (a) forward biased, (b) reverse biased.**

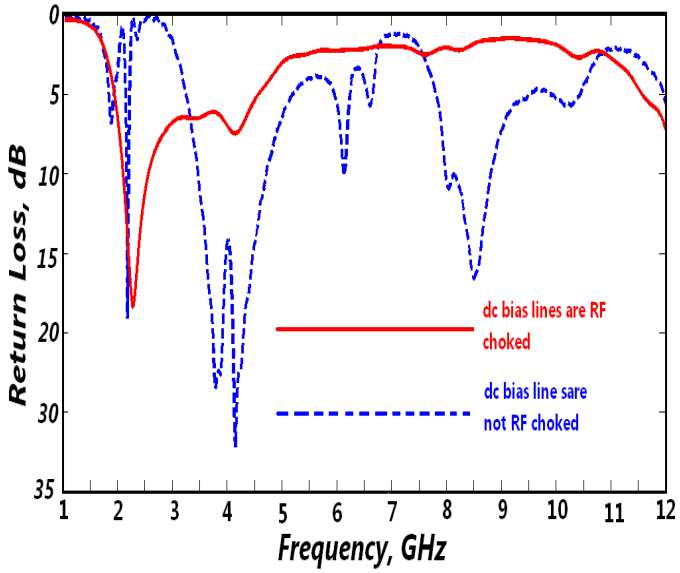

Figure 3.20: **Simulated return loss for the reconfigured ultra-wideband antenna at 2.4 GHz when the dc bias lines are not RF choked (blue dashed line) and when the dc lines lines are RF choked using lumped elements (e.g., $R = 4.3\ K\Omega, L = 220\ nH$)(solid red line). The simulated return loss curve with no biasing lines is identical to the case when using lumped elements as RF chokes.**

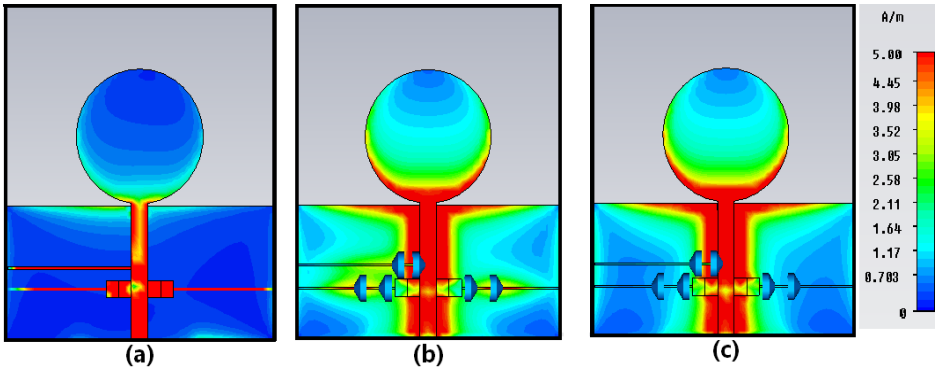

Figure 3.21: **Simulated current distribution on the 2.4 GHz reconfigured ultra-wideband antennas: (a) dc lines without chokes, (b) dc lines with small passive elements values ($R = 100\ \Omega, L = 5\ nH$), and (c) dc lines with big passive element values($R = 4.3\ K\Omega, L = 220\ nH$).**

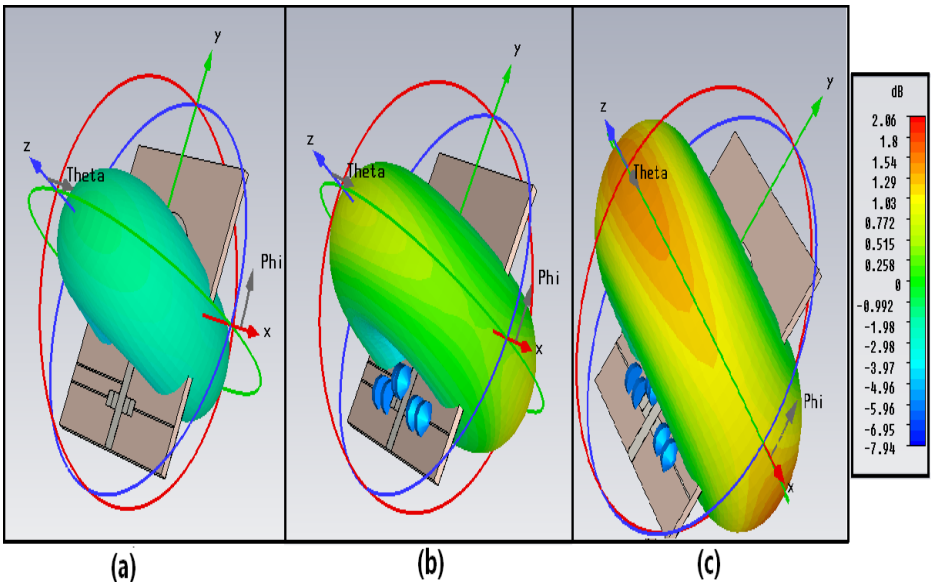

Figure 3.22: **Simulated 3D realised gain patterns of the 2.4 GHz reconfigured ultra-wideband antenna: (a) dc lines without chokes, (b) dc lines with small passive element values ($R = 100\ \Omega, L = 5\ nH$) , and (c) dc lines with big passive element values($R = 4.3\ K\Omega, L = 220\ nH$).**

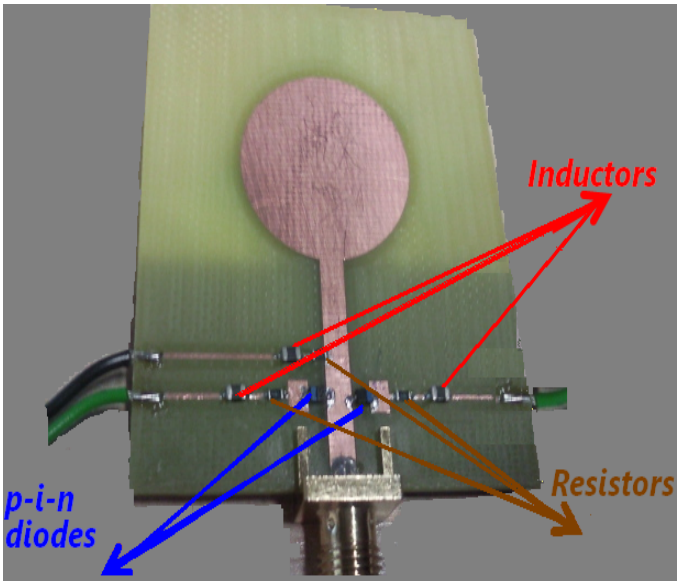

Figure 3.23: **The fabricated frequency reconfigurable antenna with p-i-n diode switches.**

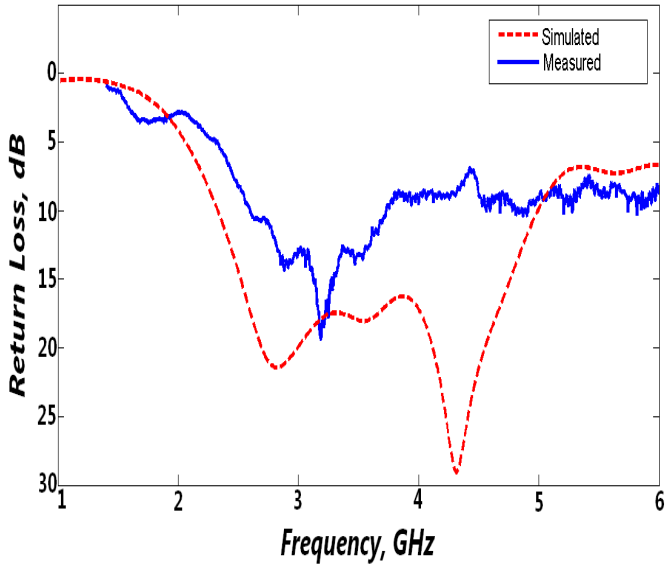

Figure 3.24: **Simulated and measured return loss of the 2.4 GHz reconfigured antenna when the p-i-n diodes are reversed biased.**

Figure 3.23 illustrates the use of p-i-n diodes with proper dc biasing in a fabricated prototype. The dc bias lines are properly RF choked using resistances ($R = 4.3\ k\Omega$) and inductors ($L = 220\ nH$). Figure 3.24 depicts

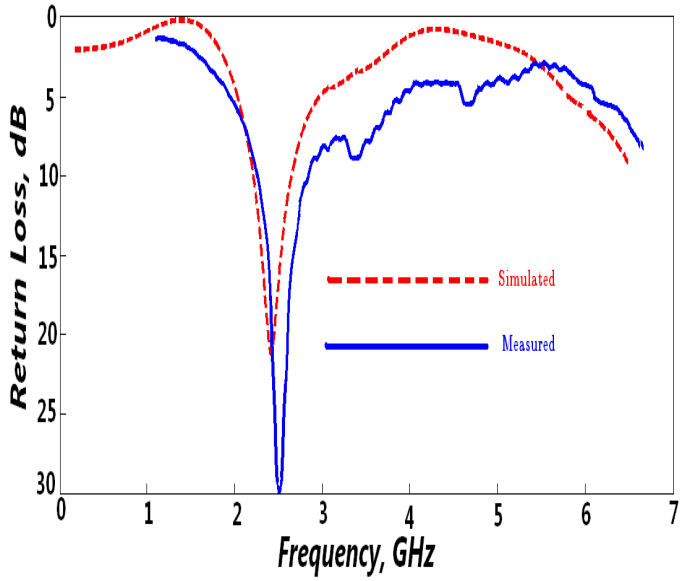

Figure 3.25: **Simulated and measured return loss of the 2.4 GHz reconfigured antenna when the p-i-n diodes are forward biased.**

the simulated and measured return loss of the ultra-wideband antenna when the p-i-n diodes are reverse biased. The antenna should be working in the ultra-wideband mode but due to the switches capacitance in the OFF state, the isolation will be degraded when the frequency increases and the ultra-wideband operation is limited. To increase the isolation, two p-i-n diodes can easily be cascaded in series but this will increase the insertion loss of the switch. The difference between the simulated and measured results here is due to the measurement cable and connectors, the fabrication tolerances and the diodes parasitics.

Figure 3.25 shows a comparison between the measured and simulated return loss curves of the antenna when configured at 2.4 GHz and the p-i-n diodes are forward biased. The measured and simulated values agree below 6 GHz. However, there is a slight de-tuning in frequency operation caused by the inductive loading. To reduce the complexity of the dc biasing, only one inductor can be used for each dc line. It is worth mentioning here that

inductors with big values should be used since the inductor impedance is $Z_L = (j \times 2\pi \times f \times L)\ \Omega$, so if inductor value of 5 nH is used, this will have an impedance of 75 Ω at 2.4 GHz, which is not sufficient to choke the RF signal leaking to the dc bias lines.

Dc biasing for the active elements in reconfigurable antennas is a very challenging task. To be properly designed, planer broadband RF chokes using multi-section quarter wavelength lines should be designed, but to reduce the size of the design, the use of passive inductors is satisfactory and the degradation in performance is not significant to cause the move for more complex designs. Most off-the-shelf inductors with large values cannot always work at high frequencies, this is because the limitation of self-resonance frequency of the inductor (SRF). For choke applications, the SRF is the frequency that provides the best signal blocking. Fortunately, there are some companies that manufacture high value inductors with a very high impedance up to 40 GHz [80]. Printed inductor and capacitor resonators can replace traditional quarter-wavelength chokes as illustrated in [81]or by using dumbbell DGS structures [82,83]. High-resistance dc lines have been investigated in [84] in which the lines are made of aluminium zinc oxide (AZO). The measured resistance of these dc line is around 200 $K\Omega$. This causes any leaked RF currents to attenuate quickly.

3.7 GaAs FET Switches for Frequency Reconfigurable Antennas

The use of ideal switches (e.g., putting metal copper bridge to resemble an ON switch state and removing it for the OFF case) is not practical and it does not take into account the degradation of the switches on the

performance of the antenna. Moreover, from the previous section it was noticed that p-i-n diodes as switches act as current control resistances and they require large amount of dc power to achieve lower insertion loss [79, 85]. Moreover, the isolation specifications are difficult to meet and p-i-n diodes require complex biasing networks; this will definitely degrade the antenna electromagnetic characteristics. MEMS RF switches provide near zero power consumption with very high isolation and very low insertion loss, they are extremely linear, but they require a voltage up converter chip (30–90V) if it is going to be used in a portable communication system. The reliability of MEMS switches is still lower than other types of switches. The assembly and wire bonding of RF MEMS switches on PCB boards are still not easy processes and the cost of the switches themselves is high; however, their performance surpasses their cost if the application they are applied to requires high performance in comparison to cost-effectiveness. In this section GaAs FET switches are going to be used in frequency-reconfigure ultra-wideband antenna monopole. GaAs switches have the following useful characteristics:

- Low insertion loss.
- Low power consumption.
- They are small in size.
- Very good switching speed performance in the nanoseconds range.
- The total cost of the switches and their assembly is reasonably low.
- The simplicity of implementation and the small number of external components are so advantageous to keep the interaction between the switches and the antenna to the minimum.

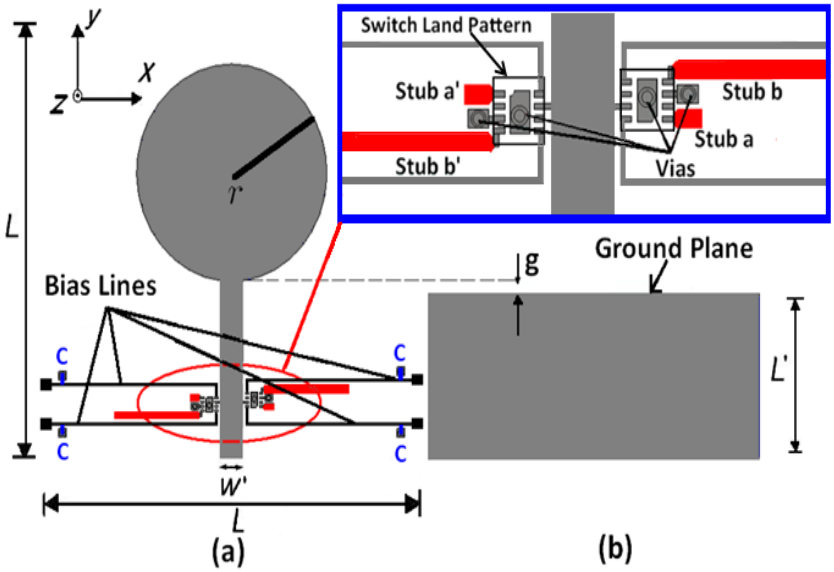

Figure 3.26: **Geometry of the proposed reconfigurable ultra-wideband antenna design using GaAs FET switches; (a) Top view, (b) Bottom view.**

3.7.1 Integrating GaAs FET Switches in the Antenna Design

The proposed reconfigurable ultra-wideband monopole antenna shown in Figure 3.26 is also based one the design in [68]. A circular disc with a radius of 12.5 mm, a 50 Ω microstrip feed line and 4 stubs (a, b, a', b') with widths of 0.75 mm are printed on one side of the dielectric substrate (the FR-4 substrate used has a thickness of 1.52 mm and ϵ_r=4.3). The length and the width of the dielectric substrate are both 50 mm. The width of the microstrip feed line is fixed at $W' = 2.9$ mm to achieve 50 Ω impedance. The length of stubs (a, a') is fixed at 1.4 mm while stubs (b, b') length is 11.25 mm. Two SPDT GaAs FET switches (SKY13298-360LF) [86] are used to connect and disconnect a combination of the four stubs to the main microstrip feedline. Each switch is biased with two dc lines, the thickness of the line is 0.1 mm and each line is decoupled with a capacitor ($C = 33$ pF).

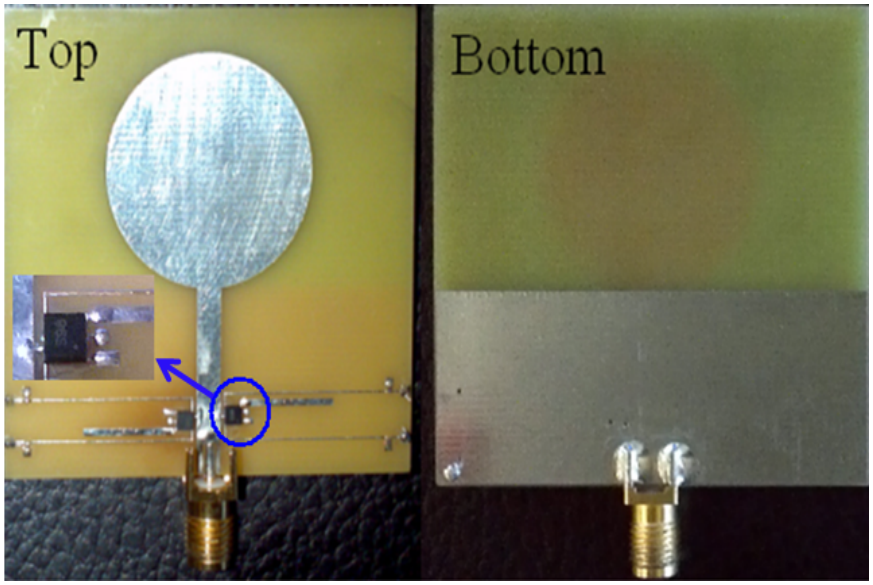

Figure 3.27: **Prototype of the ultra-wideband reconfigured antenna using GaAs FET switches.**

Each capacitor is also connected to the ground through a via. In the ON state, the drive voltage of the switch is 3.3 V and the current consumption is around 5 μA. On the backside of the substrate, the conducting partial ground plane has a length $L' = 20mm$. The height of the feed gap between the feed point and the ground plane is fixed at $g = 0.33$ mm. A prototype antenna was fabricated to verify the performance. Figure 3.27 shows the proposed prototype antenna. Having two switches and a combination of four stubs gives many reconfigurable cases but in this chapter the author investigates reconfiguration at 3 frequency sub bands: Band I: 2.1–2.6 GHz, Band II: 3.6–4.6 GHz, and Band III; which has a dual band operation(e.g., Band: IIIa (2.8–3.4 GHz) and IIIb (4.9–5.8 GHz)).

3.7.2 Simulation and Experimental Results

- **Return Loss**

  The CST Design Studio offers circuit simulation tools that allows cal-

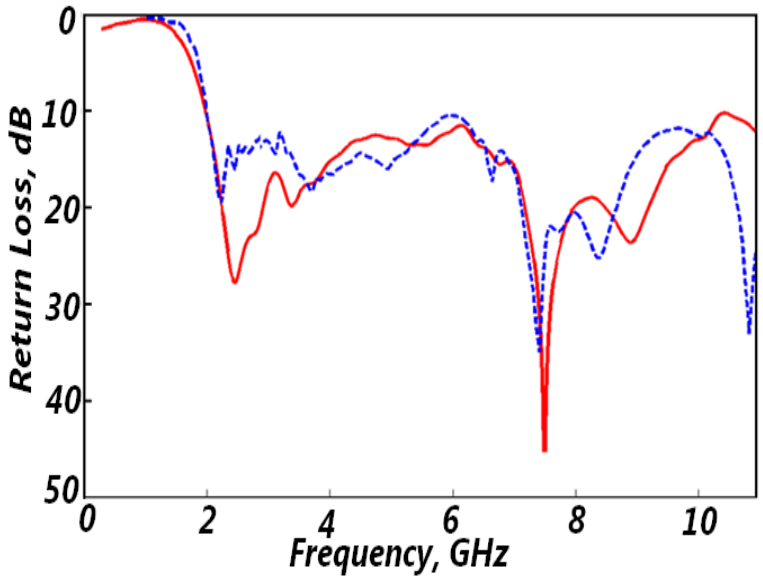

Figure 3.28: **Simulated (solid red lines) and measured (dashed blue lines) return loss curves when the antenna is in the ultra-wideband mode.**

culated results from 3D EM simulations of the antenna to be used along with the $S-parameters$ files of the FET switches [69]. The simulated and measured return loss curves for the ultra-wideband mode and for different configuration modes are shown in Figure 3.28 and Figure 3.29, respectively. When all switches are OFF, the antenna is functioning as ultra-wideband antenna and in this case the antenna is used to scan the whole ultra-wideband spectrum to check for any spectrum holes. Band I is achieved when stubs (a, a') are connected to the main feedline. Band II is achieved when stubs (b, b') are connected to the feedline, while Band III is realised when connecting stubs (a', b) to the main microstrip feedline.

- **Radiation patterns, Realised Gain and Total Efficiency**

  The radiation patterns have been simulated and also measured inside an anechoic chamber. The measured and simulated normalised radi-

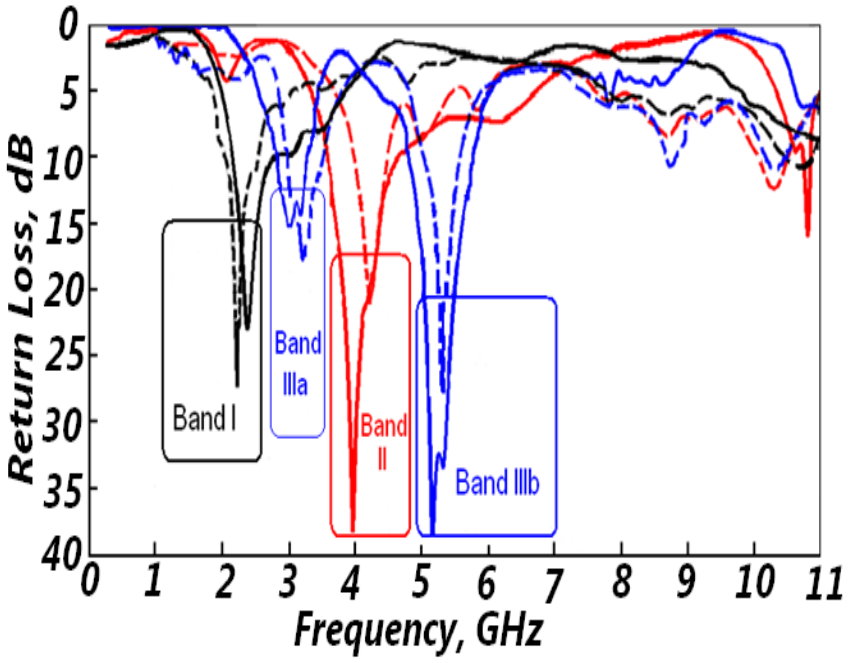

Figure 3.29: **Simulated (solid lines) and measured (dashed lines) return loss curves when the antenna is reconfigured at: I) 2.1–2.6 GHz, II) 3.6–4.6 GHz, III) 2.8–3.4 GHz and 4.9–5.8 GHz.**

ation patterns at 2.4, 4.2, 3.3 and 5.4 GHz are plotted in Figure 3.30 and Figure 3.31. The simulated and measured results match very well. The measured H-plane patterns are almost omnidirectional and they are close to those obtained in the simulation. The simulated E-plane pattern is a doughnut shape like a traditional monopole but at high frequencies the patterns become more directional and the back lobes become smaller. This is because the partial ground is getting electrically bigger compared to the wavelength. There are some distortions on the measured curves; these ripples are caused by the feed connector, the coaxial cable and the dc biasing cables that are attached to the biasing microstrip lines on the antenna board.

Table 3.3 shows the simulated and measured realised peak gain and the

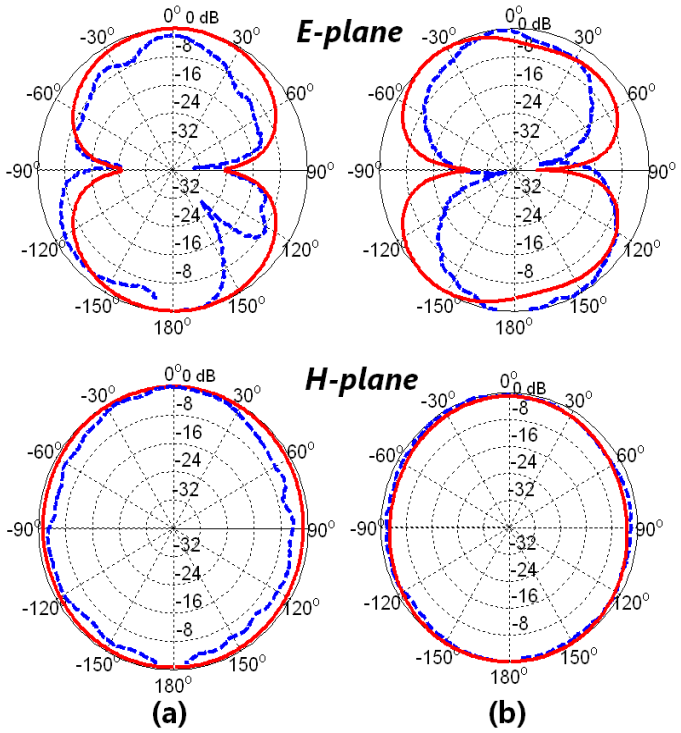

Figure 3.30: **Simulated (solid red line) and measured (dotted blue line) normalised E-plane (Y-Z) and H-plane (X-Z) radiation patterns, when antenna is configured at: (a) 2.4 GHz in band I (b) 4.2 GHz in band II**

	Realised Gain (dBi)		$\eta_t(\%)$	
Frequency(GHz)	Simulated	Measured	Simulated	Measured
2.4	2.2	1.8	90	72
4.2	2.7	2.2	91	80
3.3	2.3	2.0	88	77
5.0	3.9	3.6	89	78

Table 3.3: **Simulated and measured realised gain and total efficiency for the GaAs FET reconfigured ultra-wideband antenna in the ultra-wideband mode.**

simulated and measured total efficiency of the ultra-wideband case. Table 3.4 and Table 3.5 show the simulated and measured realised peak gain and the simulated and measured total efficiency of the reconfigured antenna at different reconfiguration frequencies in the three

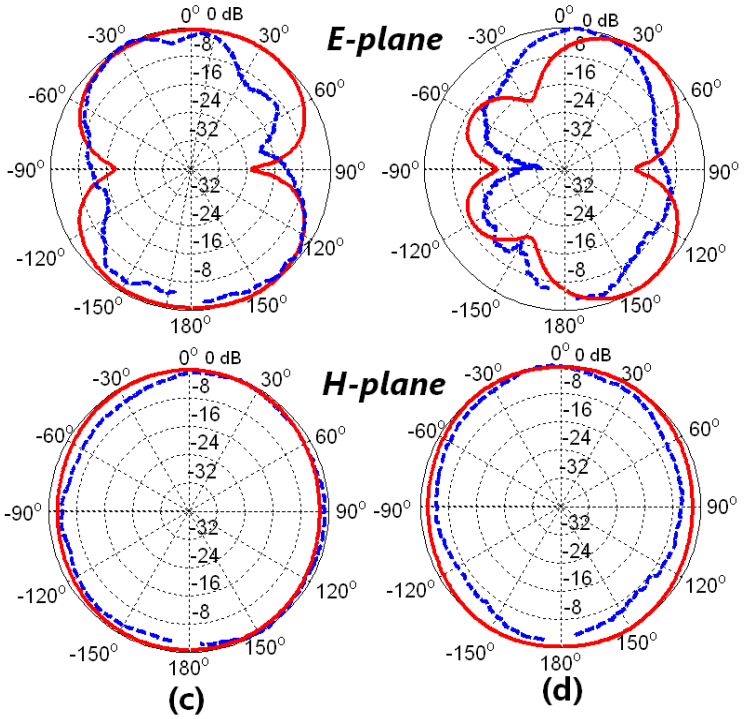

Figure 3.31: **Simulated (solid red line) and measured (dotted blue line) normalised E-plane (Y-Z) and H-plane (X-Z) radiation patterns, when antenna is configured at: (c) 3.3 GHz in Band IIIa (d) 5.4 GHz in band IIIb.**

	Realised Gain (dBi)	
Frequency(GHz)	Simulated	Measured
2.4 in Band I	2.5	2.2
4.2 in Band II	3.3	3.0
3.3 in Band IIIa	3.0	2.7
5.0 in Band IIIb	4.6	4.4

Table 3.4: **Simulated and measured realised gain for the GaAs FET reconfigured ultra-wideband antenna.**

operating bands. Generally, the reconfigured cases showed an increase in peak gain compared to the gain of the ultra-wideband antenna at the same frequencies. In addition, there is no severe degradation in the total efficiency compared to the ultra-wideband antenna efficiency.

	$\eta_t(\%)$	
Frequency(GHz)	Simulated	Measured
2.4 in Band I	86	70
4.2 in Band II	90	77
3.3 in Band IIIa	87	73
5.0 in Band IIIb	84	75

Table 3.5: **Simulated and measured total efficiency for the GaAs FET reconfigured ultra-wideband antenna.**

3.8 Frequency Reconfiguration of Compact Co-planar Waveguide Fed (CPW-fed) Tapered Ultra-Wideband Antenna

In the previous sections the author discussed how to frequency-reconfigure monopole disk antenna. However, for current small and portable devices that have very limited mounting space, it is preferable to use compact antennas, thereby in this section, the frequency-reconfiguration of a compact CPW-fed ultra-wideband Tapered Slot Antenna (TSA) [87] is investigated. The antenna reconfiguration operation principle relies on two mechanisms; in the first mechanism a resonator parasitic microstrip line electrically coupled to the TSA antenna is used to notch the TSA at a specific frequency and the second mechanism relies on changing the input impedance matching of the antenna by means of changing the length of a stub line extended from an additional small partial ground on the back side of the antenna.

3.8.1 Antenna Design and Operation

Figure 3.32 shows the geometry of the proposed reconfigured ultra-wideband TSA antenna. The proposed antenna substrate is a Taconic (TLC-30) board with a thickness of 1.52 mm, dielectric constant of 3 and loss tangent

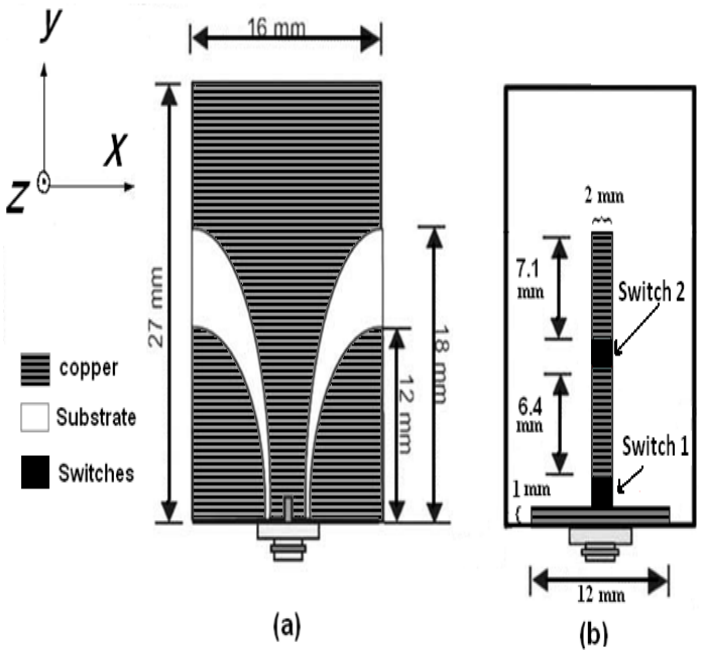

Figure 3.32: **Geometry of the reconfigured Tapered Slot antenna (a) Top view, (b) Bottom view.**

of 0.003. The width of the antenna is 16 mm and the length of the antenna is 27 mm. On the back side of the substrate, a small partial ground (12 $mm \times 1$ mm) is printed and there is a stub connected to this ground by switch 1. By changing the length of the stub we can change the input impedance matching of the antenna to work in predefined frequency bands. The length of the ground stub is determined from circuit analysis using Agilent Advanced Design System (ADS) [88]. When the stub length is 8.4 mm, the operation frequency is between 3–4 GHz. When the stub length increases to 17.5 mm and both switches 1 and 2 are ON, the frequency band of operation will change to 4.5–5.5 GHz. When the ground stub is not connected to the partial ground (e.g., switch 1 is OFF and switch 2 is ON), the stub will act as a parasitic element electrically coupled to the TSA antenna. The length of the parasitic resonator determines the notch

	Operating Mode			
Switch number	Ultra-wideband	Notched Ultra-wideband	Band I	Band II
1	OFF	OFF	ON	ON
2	OFF	ON	OFF	ON

Table 3.6: **Operating modes of reconfigured ultra-wideband TSA antenna.**

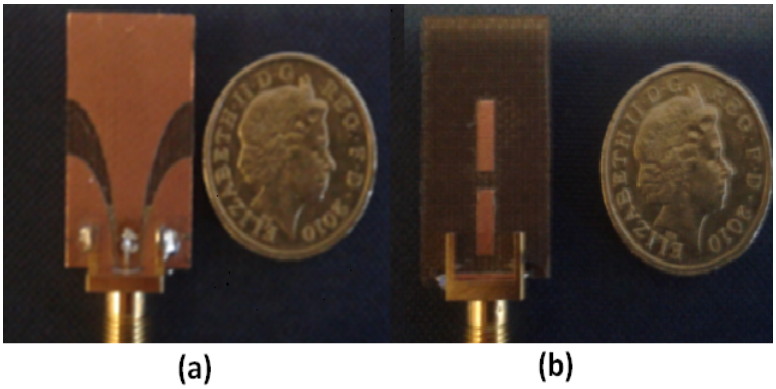

Figure 3.33: **Antenna Prototype; (a) Top view, (b) Bottom view.**

frequency and if we want to notch the upper band of WLAN at 5.8 GHZ the length of the resonator should be 15 mm which is equal to $\lambda_g/2$ where λ_g is the guided wavelength at 5.8 GHz.

Full ultra-wideband operation without any notches can be achieved by suppressing the resonance coupling of the parasitic element (e.g., the total length of the parasitic resonator is changed when switch 2 is OFF), consequently, it cannot support the resonating currents and no notch occurs at 5.8 GHz. The operation modes of the antenna for different switch states are summarised in Table 3.6. A prototype antenna was fabricated to verify the performance. Figure 3.33 shows the proposed prototype antenna. The RF switches used in this prototype are realised as metal pads with dimensions $2\ mm \times 2\ mm$.

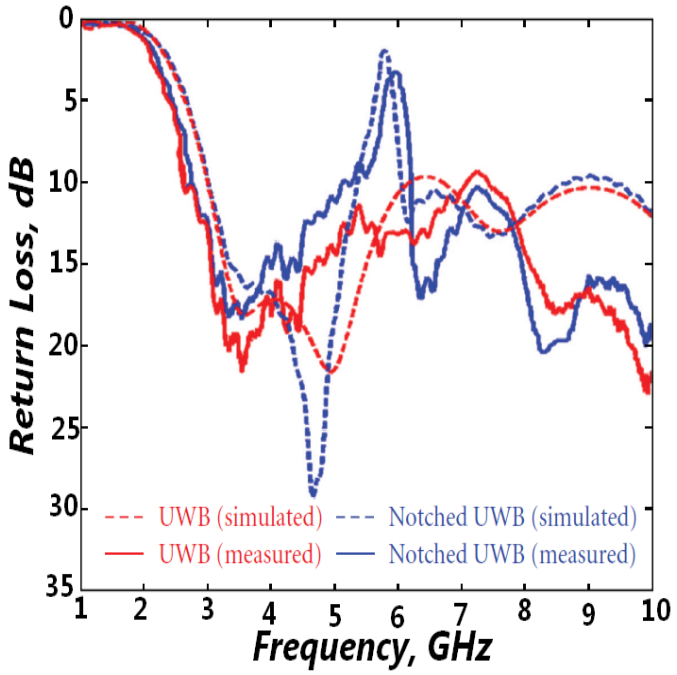

Figure 3.34: **Simulated (dashed lines) and measured (solid lines) return loss curves when antenna is in ultra-wideband mode and in the notched ultra-wideband mode.**

3.8.2 Simulation and Measurement Results

- **Return Loss**

  Figure 3.34 shows the simulated results for the return loss of the antenna when it is in the ultra-wideband mode and when it is notched around 5.8 GHz. Figure 3.35 depicts the simulated return loss when the antenna is configured to work in Band I and Band II. In general, a good agreement between simulated and measured notched frequency has been achieved. Small frequency shift of 200 MHz ($\approx$ 3.4%) between the simulated and measured results has occurred; this can be accounted for by fabrication and material tolerances.

- **Surface current**

  Figure 3.36(a) and Figure 3.36(b) show the surface current distribu-

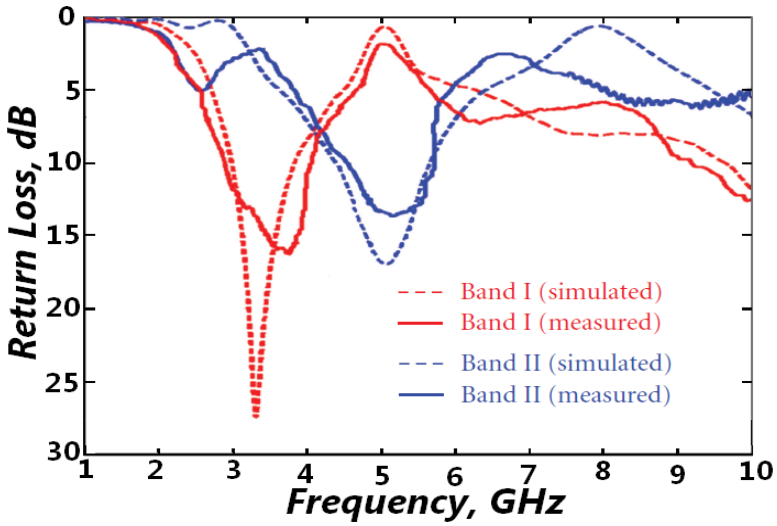

Figure 3.35: **Simulated (dashed lines) and measured (solid lines) return loss curves when antenna is reconfigured in Band I: 3–4 GHz and Band II: 4.5–5.5 GHz.**

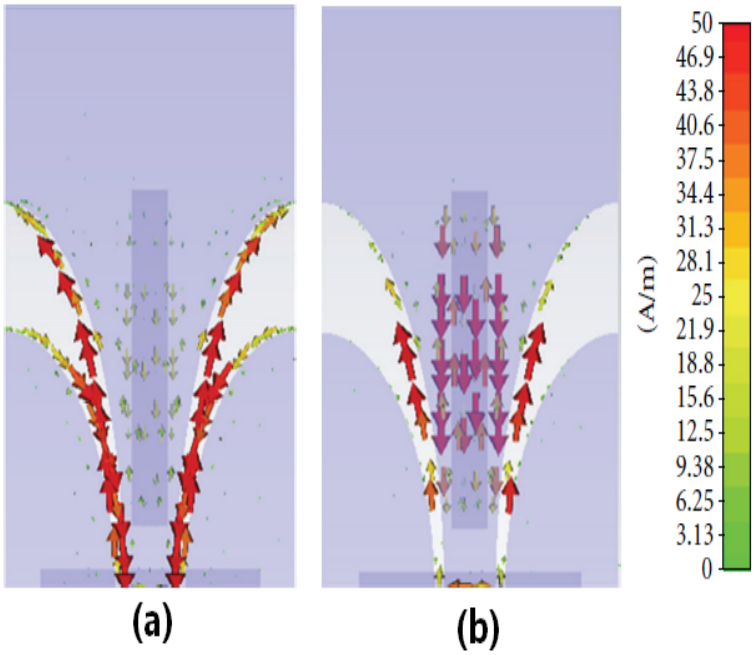

Figure 3.36: **Simulated current distribution of the notched ultra-wideband antenna at (a) 5 GHz (normal operation frequency) and (b) 5.8 GHz (notched frequency).**

tions for the notched ultra-wideband antenna at (5 GHz) in the pass-band and at the stop-band (5.8 GHz), respectively. At the stop band, the surface currents are condensed around the parasitic resonator and a strong coupling occurs (the direction of current flow on the resonator is opposite to the flow of the current on the nearby slots edges). Eventually the surface current is largely reduced along the edges of the two slots and no radiation occurs, while in the pass band frequency (5 GHz) the current flows smoothly on the edges of the slots without any perturbation by the resonator and the radiation is as normal.

Figure 3.37(a) shows the surface current distributions for the ultra-wideband antenna when it is operating in Band I at (3.4 GHz) in the pass-band and Figure 3.37(b) shows the surface current distributions for the ultra-wideband antenna when it is operating in in the same band but at 5 GHz which is an out of band frequency. Figure 3.37(c) shows the surface current distributions for the reconfigured ultra-wideband antenna when it is operating in Band II at (3.4 GHz) which is an out-of-band frequency and Figure 3.37(d) shows the surface current when the antenna is configured in Band II at (5 GHz) which is in the pass-band. At the out-of-band frequency, the stub which is connected to the partial ground will change the input impedance of the antenna and the surface current will be more dominant around the stub while the surface current along the slots of the antenna is reduced. The effect of the stubs on matching the input impedance of the antenna can also be highlighted from Figure 3.38 which depicts the input impedance of the ultra-wideband antenna when it is reconfigured to work in Band I. For the ultra-wideband operation, the antenna input resistance (R_i) should be around 50 Ω

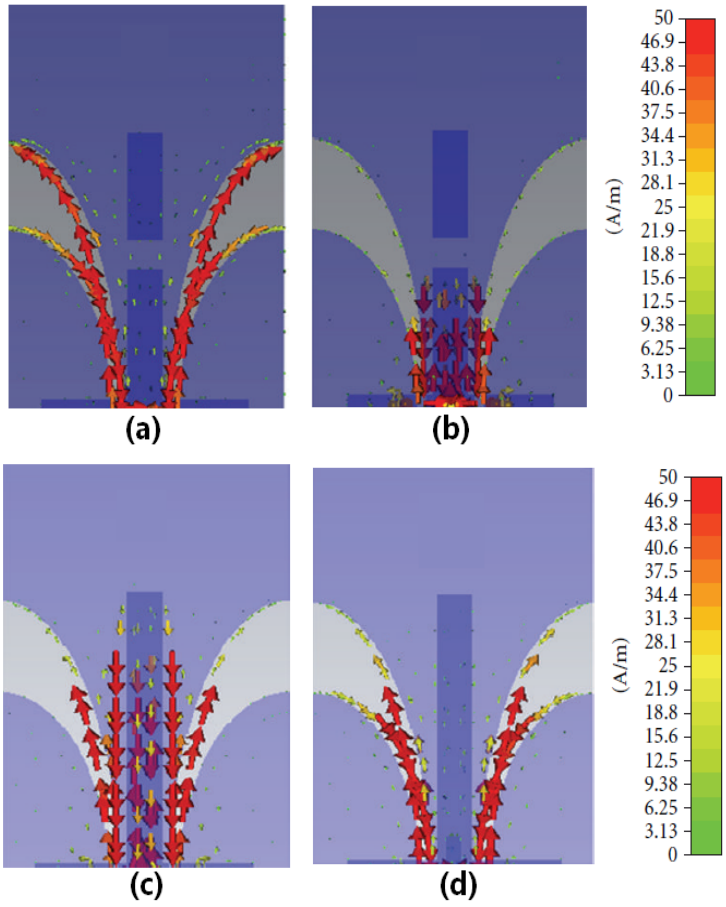

Figure 3.37: **Simulated current distribution of the reconfigured ultra-wideband antenna in Band I: (a) 3.4 GHz, (b) 5 GHz, and Band II: (c) 3.4 GHz, (d) 5 GHz.**

and the input reactance (X_i) should be close to 0 Ω for the whole operating bandwidth, while after reconfiguring the antenna to work into Band I, R_i is close to 50 Ω and X_i is around 0 Ω only at frequencies within the operating bandwidth (e.g., 3.4 GHz) and their values largely deviates from the nominal values outside the pass-band.

- **Radiation Patterns, Gain and Efficiency**

  The simulated and measured normalised radiation patterns at 3.4 GHz and 5 GHz for the ultra-wideband mode operation are plotted in Fig-

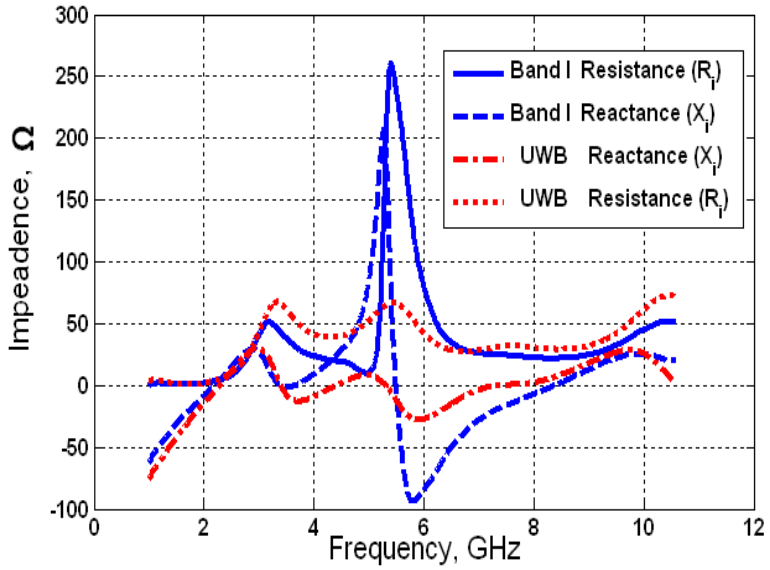

Figure 3.38: **Simulated input impedance curves for the ultra-wideband antenna and when the antenna is configured to operate in Band I.**

ure 3.39(a) and Figure 3.39(b), respectively. The simulated and measured normalised radiation patterns when the antenna is configured in Band I at 3.4 and in Band II at 5 GHz are plotted in Figure 3.40(a) and Figure 3.40(b), respectively. The H-plane patterns are omnidirectional and the E-plane patterns look like that of a dipole. The measured results agree with the simulated ones. There are some distortions on the measured curves, these ripples are caused by the feed connector and the coaxial cable used in the measurement. It is worth mentioning here that the radiation patterns did not change when the antenna was reconfigured from the ultra-wideband operation to the reconfigured cases. Table 3.7 summarises a comparison of the simulated and measured realised peak gain between the ultra-wideband case, the notched ultra-wideband and the two reconfigured cases. At 5.8 GHz (notch frequency) the ultra-wideband notched antenna showed

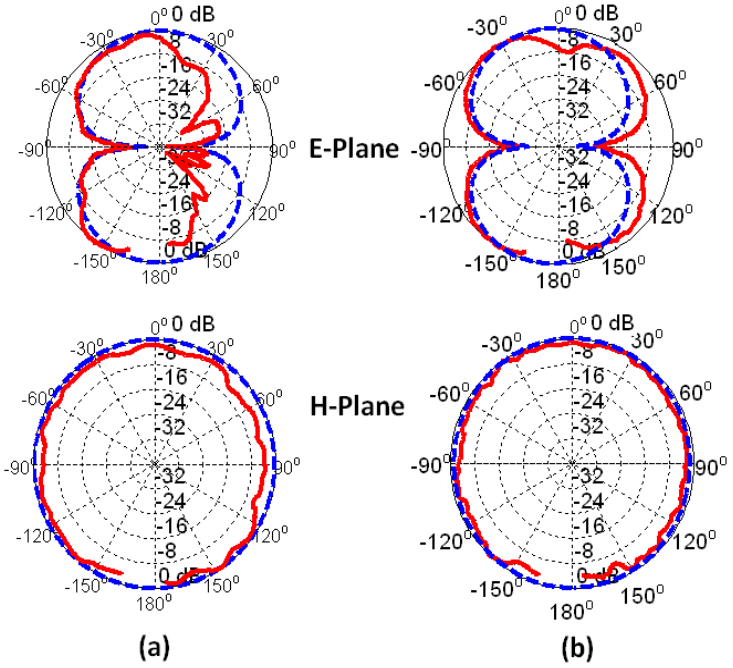

Figure 3.39: **Simulated (dotted blue line) and measured (solid red line) normalised E-plane (YZ) and H-plane (XZ) radiation patterns, when antenna is in the ultra-wideband mode, (a) 3.4 GHz (b) 5 GHz.**

reduced broadside gain compared to the ultra-wideband case and the reconfigured cases show slight increase in peak gain for pass-band frequencies compared to the ultra-wideband case.

Figure 3.41 depicts the simulated values of the total efficiency, when the antenna is operating in the ultra-wideband mode, the notched ultra-wideband mode and when the antenna is configured to work in Band I and Band II. Table 3.8 shows the measured total efficiency when the antenna is operating in the ultra-wideband mode, the notched ultra-wideband mode and when the antenna is configured to work in Band I and Band II. The measured values agree with the simulated ones and the differences between the simulated and measured results can be attributed to the measurement cable and connectors

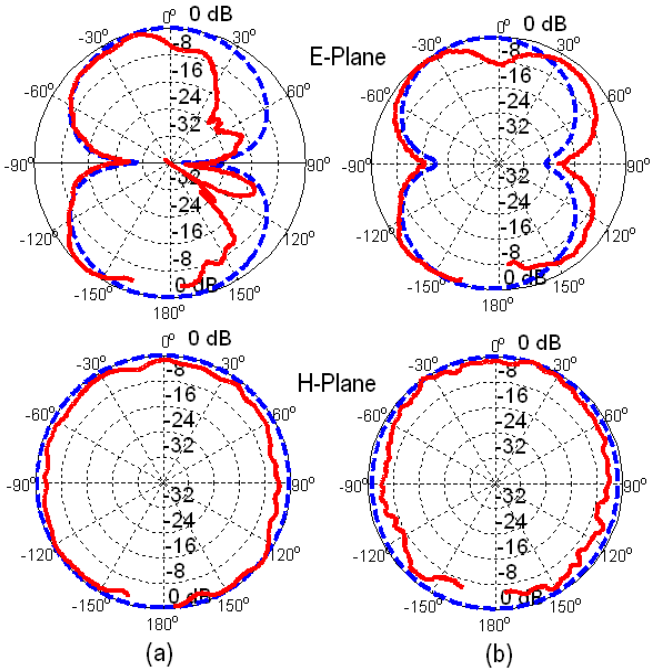

Figure 3.40: **Simulated (dotted blue line) and measured (solid red line) normalised E-plane (YZ) and H-plane (XZ) radiation patterns, when the antenna is configured at: (a) 3.4 GHz in Band I (b) 5 GHz in Band II.**

and the fabrication tolerances. From Figure 3.41 and Table 3.8 it can be noticed how poor the total efficiency gets at the notch frequency in the ultra-wideband notched case or at out-of-band frequencies close to the operating pass-band of Band I and Band II.

	UWB		**Notched UWB**		**Band I**		**Band II**	
Frequency(GHz)	S	M	S	M	S	M	S	M
3.4	1.9	2.4	1.9	2.5	2.1	3	0.8	0.7
5.0	2.9	3	3	3	-6.4	-4	3.7	3.5
5.8	3.6	3	-7	-4	1.9	2	3.8	3.7

Table 3.7: **Simulated (S) and measured (M) realised peak gain values in (dBi) for the reconfigured ultra-wideband TSA antenna.**

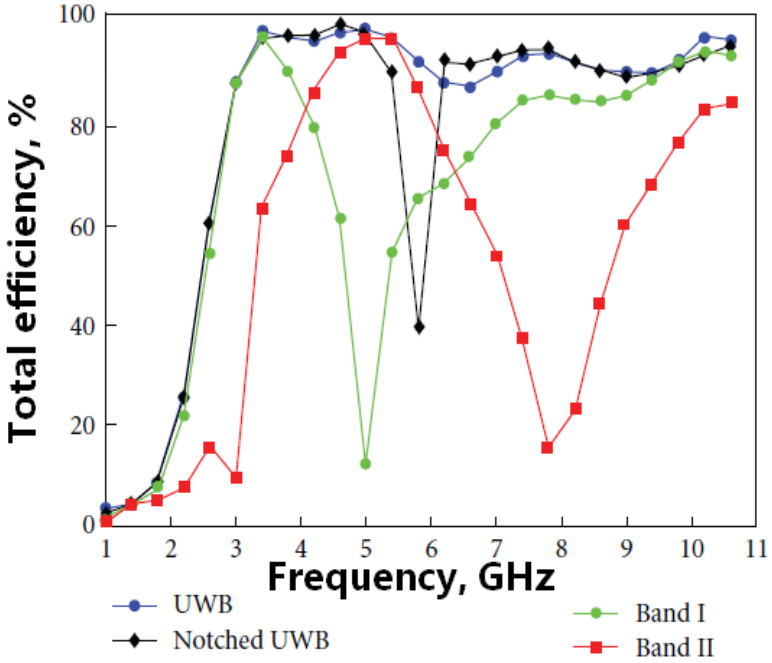

Figure 3.41: **Comparison between simulated total efficiency when the antenna is operating in different modes.**

	$\eta_t(\%)$			
Frequency(GHz)	**UWB**	**Notched UWB**	**Band I**	**Band II**
3.4	87	88	90	40
5.0	90	87	30	91
5.8	85	45	55	88

Table 3.8: **Measured total efficiency of the reconfigured ultra-wideband TSA antenna.**

3.9 Applicability in Cognitive Radio

The real time deployment of CR devices and their applications in wireless communications does not depend only on the antenna and radio element but substantially on the network and protocol layers mechanisms and techniques. However, such complex systems without a flexible radio front-end will not function as expected and will not be easily integrated into common hand-held or desk based devices intended to be used in CR networks. The

previously discussed antennas in this chapter present potential candidates for CR systems. The ultra-wideband mode of operation is capable of sensing the wider spectrum of interest and based on feedback and cognitive learning, a decision could be reached on the most suitable band for efficient communication link. Once the communication frequency is decided, the antenna elements are reconfigured applying one of the techniques discussed in this chapter and providing the flexibility needed for such smart networks with software defined control signals.

Usually sensing places severe requirements on sensitivity, linearity, and dynamic range of the Cognitive Radio RF front-end. This is because the RF signal presented at the antenna of a CR unit includes signals from close or separated transmitters and from transmitters operating at different power levels [89].

Detection of weak signals might frequently be performed in the presence of very strong signals. Thus, to relax the strict requirements placed on the RF analogue circuits it would be beneficial from a system point of view if an interfere is mitigated before it saturates the RF front-end. This can be done by using the ultra-wideband notched mode during sensing. It is worth mentioning here that not only this notched ultra-wideband mode can be good for sensing, but also it can be helpful in communication between cognitive secondary users who can still communicate more efficiently using the notched ultra-wideband channel (e.g., more allowed transmitted power and longer transmission range with higher data rate) without affecting or being affected by a specific legacy primary user who is currently operating at the notched frequency band.

3.10 Summary

This chapter has investigated the reconfigurability of a microstrip circular disk monopole ultra-wideband antenna. The reconfiguration was done simply by switching microstrip stubs with different lengths which are connected to the main microstrip feedline of the circular radiating disk of the antenna. The proposed topology is versatile in terms of the availability of different reconfiguration bands.

A physical interpretation of the reconfiguration mechanism was discussed. First when using ideal switches, the simulated and measured return loss, radiation pattern and gain were presented, the overall efficiency was characterised experimentally. Then p-i-n diodes were integrated in a prototype antenna as switching elements and they required proper dc biasing in order not to affect the antenna performance. Initial results (e.g., return loss) were not satisfactory due to the bandwidth limitation of the used p-i-n diodes.

The plastic packaged silicon p-i-n diodes chips (BAR64-03W) chosen in the prototype are cheap and easy to solder on the PCB board as they have surface mountable SOD-323 package. This package can have high parasitic package inductance and capacitance that can limit the operation of the p-i-n diode in both the ON and OFF cases, especially at high frequencies. To overcome this problem, ceramic or beam lead packaged p-i-n diodes can be used. These types of diodes are the best choice of military and space applications. HPND-4005 beam lead p-i-n diode from Avago [90] have extremely low capacitance (0.017 pF) and they have good performance up to 18 GHz. MA4AGBLP912 beam lead p-i-n diodes from MA-COM [91] can also work up to 40 GHz. In the following chapters, the author will incorporate the HPND–4005 beam lead p-i-n diode in some novel reconfigurable

ultra-wideband monopole designs.

The use of GaAs transistors, as an alternative to p-i-n diodes, in frequency reconfigurable ultra-wideband antennas has proved to be simple with less adverse biasing effects on the antenna return loss, radiation pattern, gain and efficiency. There was no need for RF chokes in the biasing lines of the FET switches (unlike p-i-n diodes) because the dc control pins of the switch are different from the RF pins. The power consumption of each ON switch is very low ($\approx 16.5\ \mu W$). This will reduce the total dc power consumption and will lead to simple integration of the antenna in portable communication systems or future Cognitive Radio front-ends.

Since wireless portable devices have very limited mounting space, more research on reconfiguration methods for compact antennas is essential. In this chapter, the author has also proposed a compact ultra-wideband tapered slot antenna (TSA) which can be frequency reconfigured to switch operation from ultra-wideband to different narrower bands. Moreover, it can also operate in ultra-wideband mode with specific band rejection. This multi-mode compact antenna can be a very good candidate for future Cognitive Radio or smart wireless applications.

4 Pattern-Reconfigurable Ultra-wideband Antenna

4.1 Introduction

Frequency reconfigurability provides CR systems with the necessary flexibility to perform its main functions. In addition, being able to control other parameters such as antenna polarisation and patterns will further enhance the offered flexibility by the radio front-end. In the open literature, several designs have targeted ultra-wideband frequency reconfigurable antennas and pattern reconfigurable antennas However, most of these pattern reconfigurable designs have limited performance as they are narrowband antennas, so they cannot be integrated into ultra-wideband sensing CR devices. Few published designs have discussed pattern reconfiguration of wideband and ultra-wideband antennas as discussed before in Chapter 2.

In this chapter a simple, yet novel and compact pattern-reconfigurable planar circular disk ultra-wideband monopole antenna, capable of switching its maximum radiation direction across a very wideband impedance bandwidth from 3–6 GHz (approx. 66%) via incorporation of four p-i-n diodes placed on two parasitic microstrip stubs. The dc bias network required to control the switching elements is less complex and cost-effective than conventional ones as it does not require vias or dc blocking capacitors. Mo-

rover, the dc lines are physically realised by very thin and short microstrip lines to limit their adverse effect on the radiation patterns. Compared with previously designed pattern-reconfigurable antennas in the open literature, the proposed antenna has many advantages. Firstly, compared to designs in [56–58,92–96], pattern reconfiguration is achieved over a wide bandwidth. Secondly, the antenna does not have a complex three dimensional geometry as in [97], [98] or multiple feeding ports as in [99], [100]. Thirdly, compared to antennas in [92] and [101], no additional matching network is required. Lastly, compared to the designs in [59–61], the dc biasing network is easily realised for various applications where reconfigurability is necessary.

4.2 Antenna Design and Operation

The proposed pattern reconfigurable ultra-wideband monopole antenna shown in Figure 4.1 is also based on the design in [68]. The dielectric substrate used in this study is an FR4 substrate with a thickness of 1.52 mm, ϵ_r=4.5, and a loss tangent of 0.019. The detailed dimensions of the antenna are presented in Table 4.1. On the back side of the substrate, a partial rectangular ground plane and two parasitic microstrip arc-shaped stubs are printed. Also, by properly insetting a small triangular slit in the middle of the upper edge of the ground plane and by circularly truncating the upper right and left corners of the ground plane, optimum impedance matching across the whole operating band in the three different radiation pattern operation modes can be obtained.

The RF switching mechanism used in this study is realised using four beam lead p-i-n diodes (HPND-4005) [90]. The size of this diode is very small (640 $\mu m \times 220\ \mu m$) and to mount it on the PCB, the manufacturer

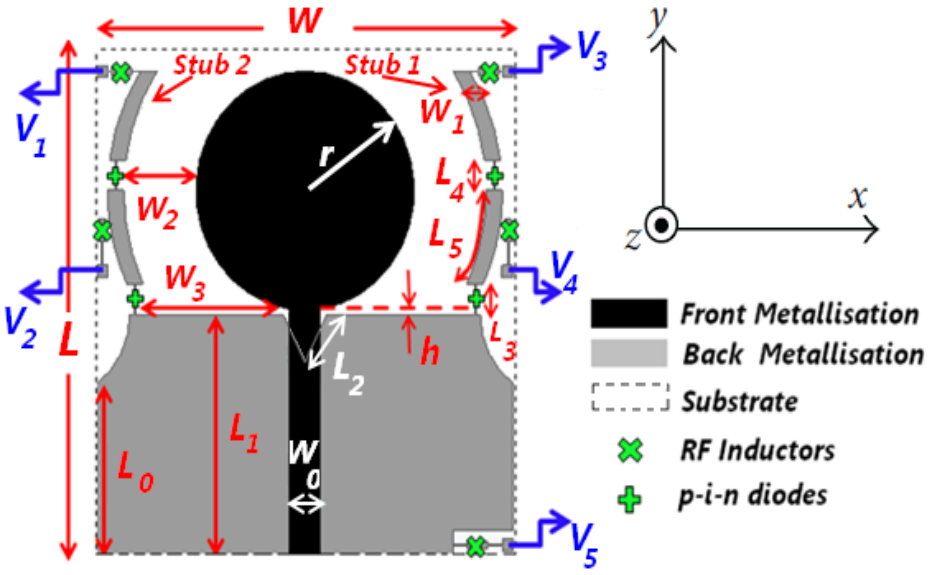

Figure 4.1: **Geometry of the proposed pattern-reconfigurable ultra-wideband antenna.**

Dimension	(mm)	Dimension	(mm)
W	38	W_0	2.9
W_1	1.5	W_2	7.0
W_3	14	L	42
L_0	14	L_1	20
L_2	4.5	L_3	2.5
L_4	2.5	L_5	8
r	10	h	0.4

Table 4.1: **Dimensions of the proposed antenna.**

recommends thermo-compression bonding. However, we have used conductive epoxy (e.g., silver paste so as not to dissolve the gold from the diode leads) and hot air. Not only have these switches got very low capacitances in the OFF state and low resistances in the ON state, but they also have low package parasitics which will have minimum adverse effects on the isolation and insertion loss of the switches. Figure 4.2 depicts the equivalent circuit for the HPND–4005 in the ON and OFF states.

Figure 4.3 shows a photo of the fabricated antenna. Each stub has two

p-i-n diodes switches, connected back to back. When both switches (a, a') are ON and (b, b') are OFF, the antenna is operating in Mode–1 and stub 1 will be connected to the ground plane and will act as a reflector that will direct the radiation towards the (-x) direction. This is due to the surface currents on the stub and the nearby disk edge being in opposite directions and their phase relationship results in concentrating radiation away from the reflector, similar to the principle of operation of a Yagi-Uda antenna. When both switches (b, b') are ON, and (a, a') are OFF, the antenna will be operating in Mode–2 and stub 2 will act as a reflector that will direct the radiation towards the $(+x)$ direction. When all switches are OFF, the stubs are short enough to be almost transparent to the incident or radiated waves and Mode–0 which is the conventional ultra-wideband operation is achieved as in [68]. The three operation modes are controlled according to the switches states as summarised in Table 4.2. Table 4.3 shows the dc bias configuration for the control voltages for different operation modes of the antenna. A dc voltage drop of $\approx +0.9\ V$ between the anode and the cathode will turn on the diode and with a bias current of $\approx 20\ mA$, the insertion loss of the diode will be around 0.4 dB. A voltage of 0 V is sufficient to turn the diode off, but it is preferable to firmly reverse bias the diode with a higher reverse voltage (e.g., -10 V) in order to increase the isolation in the OFF state by decreasing the diode internal capacitance. In addition, the reverse biasing of diodes mounted in an antenna structure with 0 V can cause fluctuations and unpredictable performance if strong E fields existing in the antenna structure (usually in the transmitting mode) happen to turn on the diodes, or some noise can be picked up by the dc biasing lines that would induce voltage spikes which would accidentally turn on the diodes.

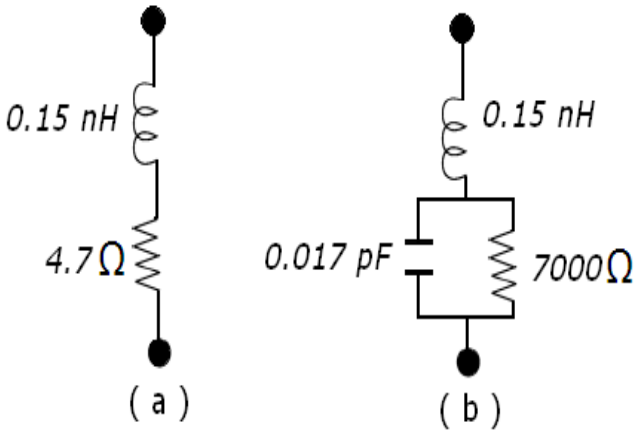

Figure 4.2: **Equivalent circuit of the HPND-4005 p-i-n diode in the: a) ON state, b) OFF state.**

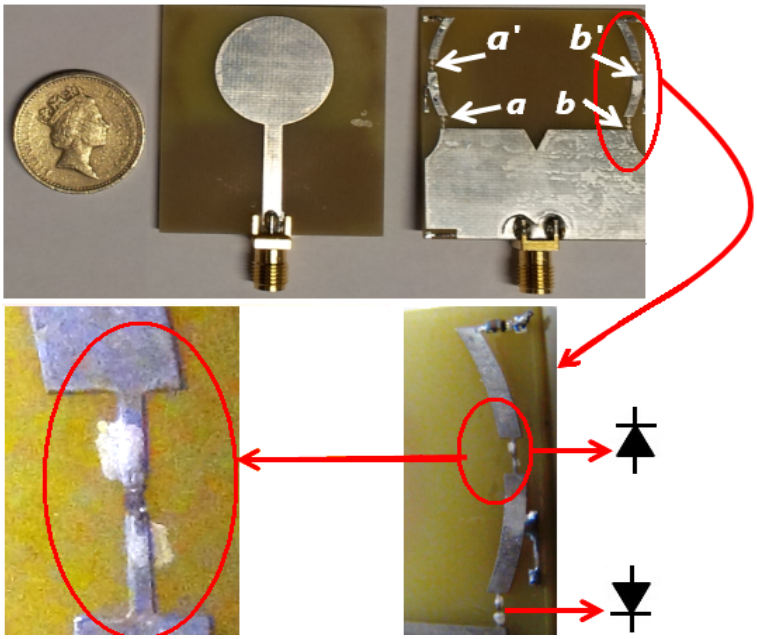

Figure 4.3: **Prototype of the proposed pattern-reconfigurable ultra-wideband antenna.**

The CST microwave studio package [69] which utilises the finite integration technique for electromagnetic computation was used in numerically analysing the structure proposed here and the diodes are represented in simulations by their equivalent circuits as in [102]. The dc biasing net-

Operation Mode	a	a'	b	b'
Mode–0	OFF	OFF	OFF	OFF
Mode–1	ON	ON	OFF	OFF
Mode–2	OFF	OFF	ON	ON

Table 4.2: **Operation modes of the antenna**

Operation Mode	V_1	V_2	V_3	V_4	V_5
Mode–0	+10 V	0 V	+10 V	0 V	+10 V
Mode–1	0 V	-10 V	0 V	+3 V	0 V
Mode–2	0 V	+3 V	0 V	-10 V	0 V

Table 4.3: **Bias configuration of the antenna**

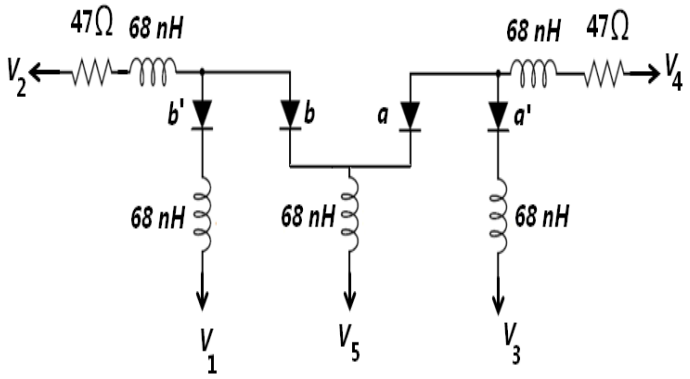

Figure 4.4: **Circuit diagram of the dc-bias circuit of the proposed reconfigurable antenna.**

work associated with our design is considered to be fairly simple as there is no need to cut slots in the antenna ground plane and short them with dc blocking capacitors for RF continuity. Moreover, the dc lines are physically realised by very thin (0.1 mm in width) and slightly short microstrip lines to limit their effect on the antenna operation by reducing losses and spurious radiation. 0402HPH–68N inductors ($L = 68\ nH$) from coilcraft served as RF chokes [103]. Also, the equivalent circuit of the RF choke, which takes into account the self-resonance frequency (SRF) of the inductors, has been used during all the simulations. The dc bias lines are then connected to

1 $mm \times 1$ mm square pads on which five wires (labelled: $V_1 - V_5$ in Figure 4.1) are soldered. These wires are connected to an external dc power supply. In Mode–1 or Mode–2, a 47 Ω current limiting axial-lead resistors should be connected in series between the power supply (+3 V) and the dc wire V_4 in Mode–1 or V_2 in Mode–2. Hence, the bias current will be $(3\ V - 0.9\ V)/(47\ \Omega + \frac{4.7\ \Omega}{2}) \approx 42\ mA$, where 0.9 V is approximately the voltage drop on the ON p-i-n diodes (a, a') in Mode–1 or (b, b') in Mode–2 and $\frac{4.7\ \Omega}{2}$ is their equivalent parallel resistance. It should be noted that from an RF point of view, the ON switches (a, a') or (b, b') are connected in their correspondent stub in series, albeit they are actually in parallel from a dc biasing circuitry view. The 42 mA current will be divided equally between the ON switches(a, a') in Mode–1 or (b, b') in Mode–2. In Mode–0, there is no need for current limiting resistors as the reverse bias current is very small. The complete dc biasing circuit is shown in Figure 4.3. In a real scenario, the dc bias lines will be connected directly or through current drivers to the I/O pins of a microcontroller, a CPLD or an FPGA which can electronically switch between the antenna operation modes.

4.3 Performance Analysis

4.3.1 Parametric Study

A parametric study was performed to understand how the dimensions of the arc-shaped stub affect the performance of the antenna. Throughout this parametric study of simulations, there are no p-i-n diodes or dc biasing lines connected to the arc-shaped stub. The first parameter studied was the total length of the stub (L'). When there is no stub connected to the antenna ground plane (e.g., $L' = 0$), the antenna resonates on the funda-

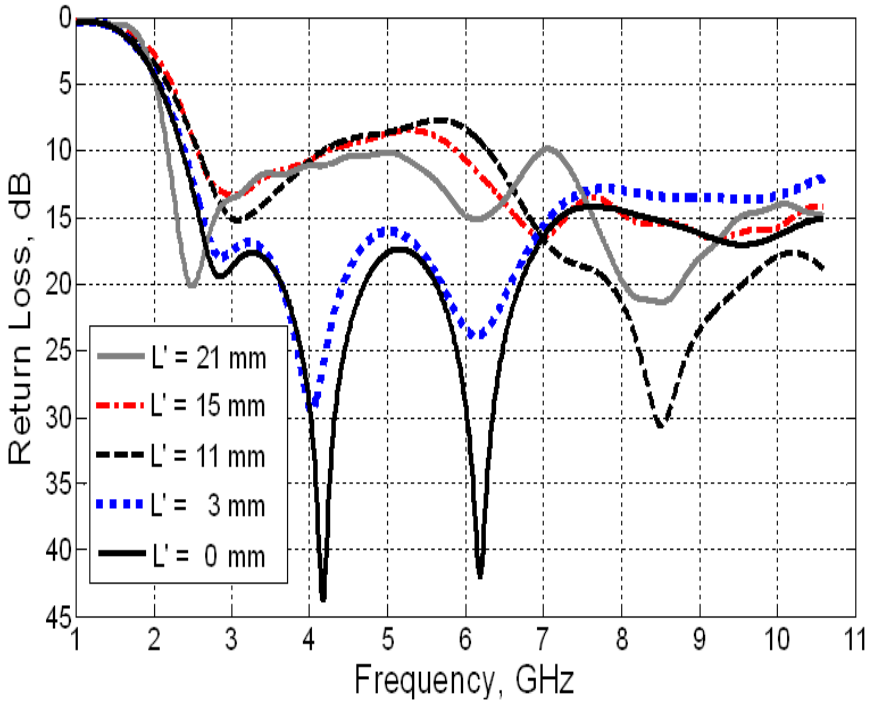

Figure 4.5: **Effects of L' (the total stub length) on the return loss of the proposed ultra-wideband antenna.**

mental mode of the circular disk and also on closely spaced higher order resonances, and by overlapping these resonances, the ultra-wideband bandwidth is achieved. Moreover, for a circular disk monopole, the ground plane (especially the upper edge along the $\pm x$ directions), serves as an impedance matching circuit that can tune the 10 dB return loss [68].

It can be observed from Figure 4.4 that the length of the stub affects the impedance bandwidth of the antenna. When changing the length, the stub adds an extra resonance f_n when its length is equal to $\lambda_g/4$, where λ_g is the guided wavelength. Moreover, the stub will also resonate at odd multiples of f_n and these resonances will also interact with the conventional ultra-wideband monopole antenna resonances. This will worsen the impedance bandwidth around the middle range of the ultra-wideband frequencies while

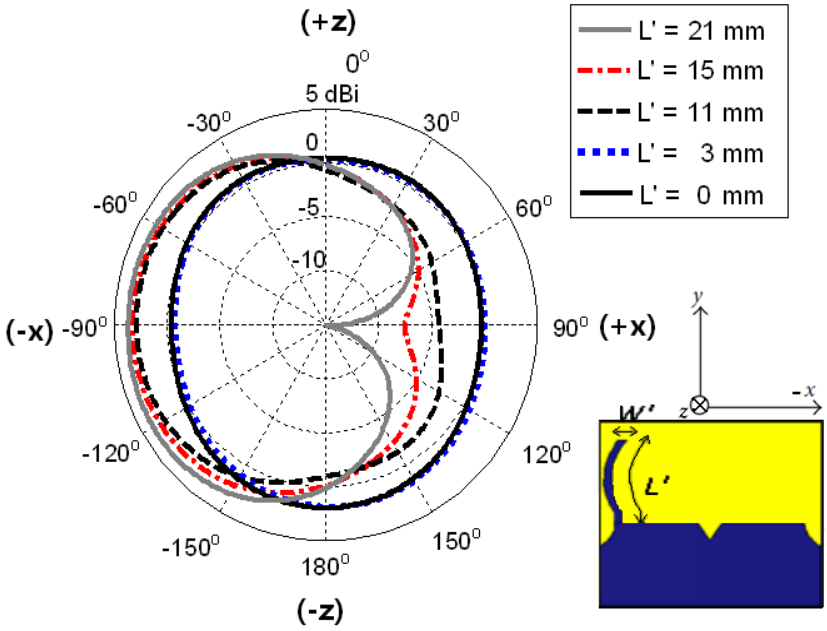

Figure 4.6: **Effects of L' (the total stub length) on the radiation gain pattern cut along the xz plane at 4.4 GHz.**

enhancing the return loss at the upper range of the ultra-wideband frequencies. Also, a larger L' will increase the bandwidth to cover lower frequencies because the stub will resonate at a lower frequency outside the FCC ultra-wideband range from 3.1–10.6 GHz. When $L' = 21$ mm, the lowest frequency of operation at which the return loss is equal to 10 dB is around 2.2 GHz and the length of the stub is approximately $\lambda_{eff}/4$, where λ_{eff} is the wavelength when the effective permittivity is taken into consideration as described in [104].

The effect of the stub length on the radiation pattern cut in the xz -plane (H–plane) at 4.4 GHz is also depicted in Figure 4.5. When L' is relatively small the antenna radiation patterns are almost omnidirectional as the stub will be almost transparent to the incident or transmitted electromagnetic waves at 4.4 GHz. When L' increases, more directional radiation patterns are produced in the $-x$-axis while radiation is reduced in the $+x$-axis. The

null is deepest when L'=21 mm, as the stub is acting as a good reflector when its length is about $\lambda_{eff}/2$ around 4.4 GHz. Therefore, based on the above analysis a stub length of 21 mm is chosen to provide an optimum performance from both impedance matching and radiation patterns prospective.

The second parameter studied was the width of the arc-shaped stub W'. When the length of the stub was fixed at $L' = 21$ mm and the value of W' changes from 0.5 to 4 mm, it was found that increasing W' will slightly worsen both the impedance bandwidth and the deepness of the null produced along the $+x$ axis as shown in Figure 4.6 and Figure 4.7. Although the effect of the width is not significant; however, care needs to be taken to ensure best optimum performance of the proposed structure and $W' = 1.5$ mm is chosen here.

The third parameter studied was the distance d' between the stub and the y-axis line of symmetry of the antenna. As shown in Figure 4.8 and Figure 4.9, when the length and width of the stub are fixed at 21 mm and 1.5 mm respectively, changing d' will affect the coupling between the currents on the stub and the circular disk. Increasing d' will enhance the 10 dB return loss bandwidth and will produce a more directive beam in the $-x$-axis. From these numerical simulations, the final design parameters of the arc-shaped stubs are set to L' =21 mm, W'=1.5 mm , and d'=16 mm. This choice achieves good return loss ($\geq$ 10 dB) over the whole ultra-wideband frequency range with good directional radiation patterns for the reconfigurable operation modes.

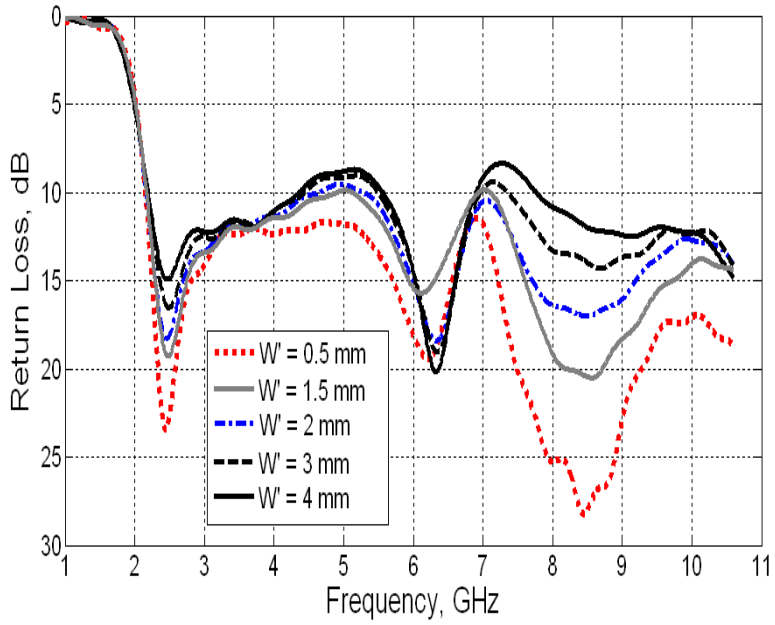

Figure 4.7: **Effects of W' (the stub width) on the return loss of the proposed ultra-wideband antenna.**

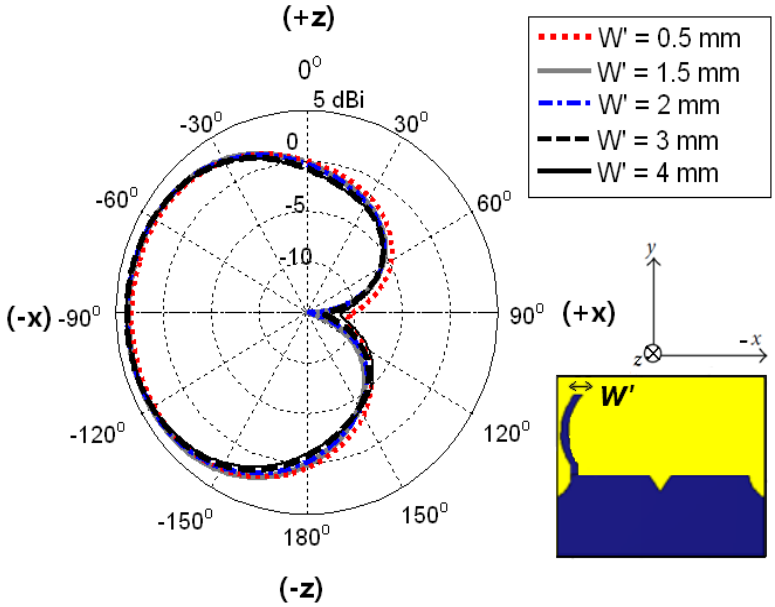

Figure 4.8: **Effects of W' (the stub width) on the radiation gain pattern cut along the xz plane at 4.4 GHz.**

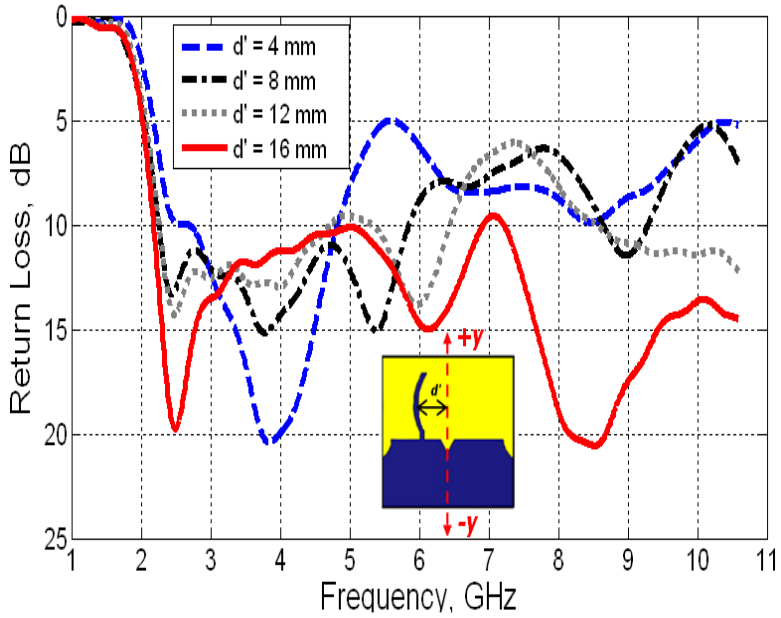

Figure 4.9: **Effects of d' (the distance between the stub and the antenna y-axis) on the return loss of the proposed ultra-wideband antenna.**

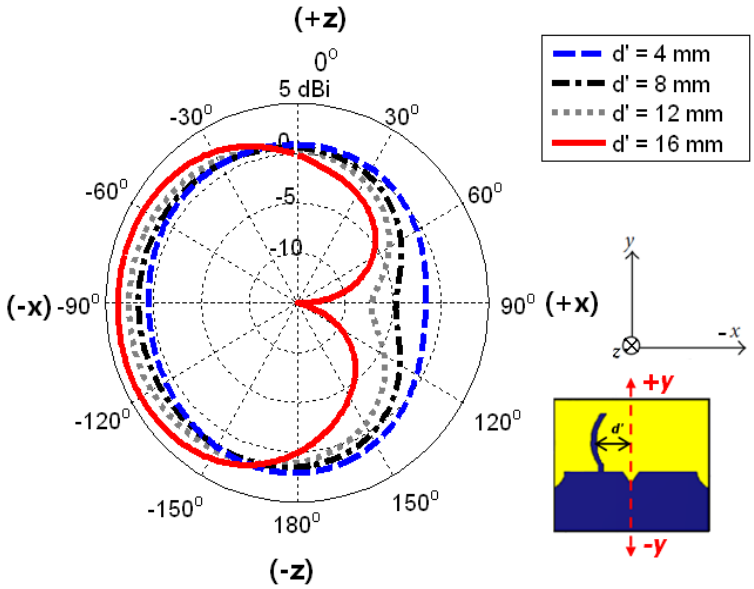

Figure 4.10: **Effects of d'(the distance between the stub and the antenna y-axis) on the radiation gain pattern cuts along the xz plane at 4.4 GHz.**

4.3.2 Surface Current

To illustrate how the antenna functions for different configurations, the surface current distribution was studied. The simulated average surface current distributions at 4 GHz when the antenna is working in Mode–0 and in Mode–1 are illustrated in Figure 4.10(a) and Figure 4.10(b), respectively. It can be noticed from Figure 4.10(a) that at the end of the feeding line, the current splits, on the disk and on the upper edge of the ground plane, into two equal streams and the surface current distribution is even and symmetrical about the y-axis. The current is primarily concentrated around the periphery of the disk and the upper edge of the ground plane, while there is little current within the interior of the disk and almost a null at the the top edge of the disk. Additionally, the antenna can be viewed as a planar slot bow-tie antenna since both the circular disk and the upper edge of the finite ground plane form two slots that equally contribute to the total radiation. Furthermore, it can be noticed that the two splitted arc-shaped stubs are non-resonating and thus transparent to the radiated or intercepted electromagnetic waves. The symmetry of the surface currents will lead to omnidirectional $xz-$plane (H-plane) patterns similar to those obtained in [68].

In Figure 4.10(b), when one of the stubs is activated by turning on the corresponding switches, the surface current distribution on the disk and on the ground plane are no longer symmetrical about the the y-axis. The activated stub is acting like a reflector and it will reduce radiation behind the stub. Moreover, if we look at the antenna as a two slots bow-tie antenna, we can see that the slot facing the activated stub has much less current than the other slot facing the non-activated stub. From the two slots, there is an unequal contribution to the total radiation and non-omnidirectional

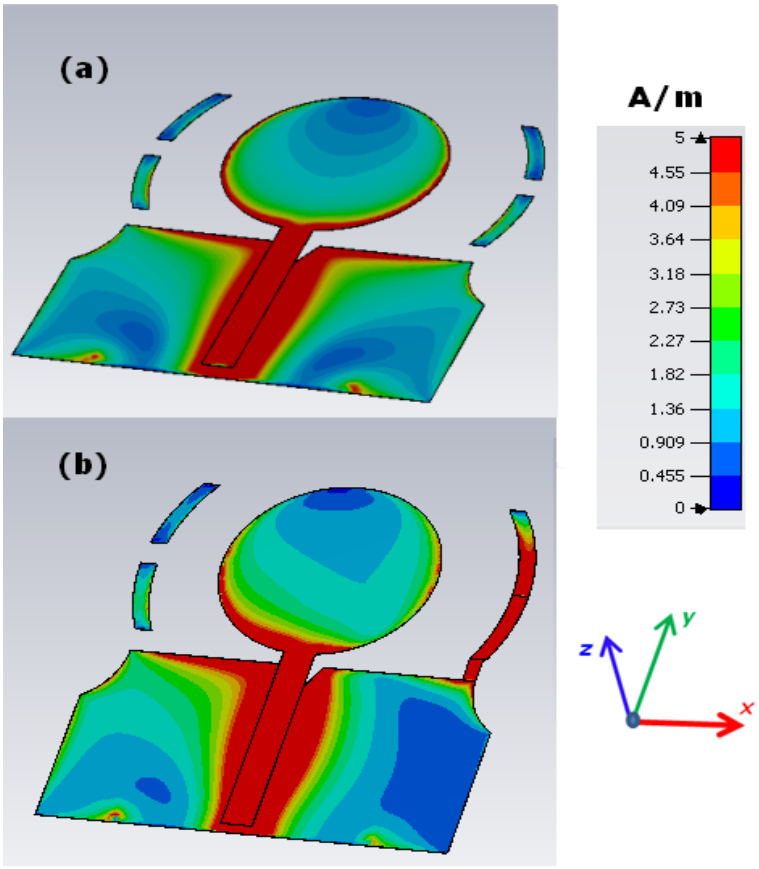

Figure 4.11: **Simulated average surface current distributions at 4 GHz on the top and bottom metallisation (while the substrate is hidden), when the antenna is operating in: a) Mode–0, b) Mode–1.**

patterns are produced in the H-plane.

4.3.3 Experimental Evaluation

The return loss measurements are performed using Agilent N5230C PNA-L microwave network analyser. A dc-block SMA connector [105] was connected to the coaxial measurement cable and the calibration was done with an Agilent-N4696B ECal module. Figure 4.11 and Figure 4.12 show the simulated and measured return losses when the proposed antenna is operating in different modes. The simulated return loss of Mode–1 and Mode–2

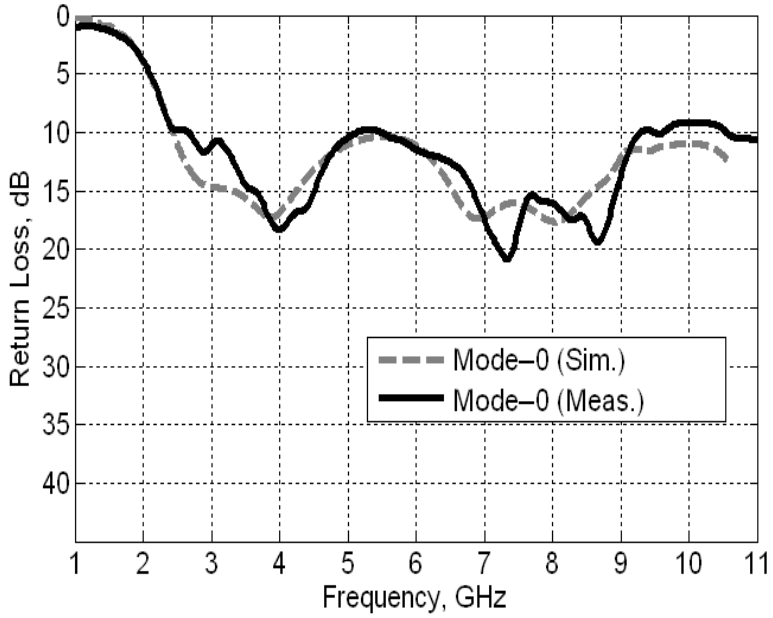

Figure 4.12: **Simulated and measured return loss curves when the proposed antenna is operating in Mode–0.**

are identical since the antenna is almost geometrically symmetrical with respect to the input microstrip feedline. However, the measured results are slightly different due to the tolerances in the real diodes and the lumped components. In addition, the soldering of the diodes and the lumped components can not be exactly identical, therefore this could have affected the symmetrical properties of the prototype. The measured bandwidths with return loss better than 9 dB are 2.4–11 GHz, 1.92–11 GHz and 1.96–11 GHz for Mode–0, Mode–1 and Mode–2, respectively. The bandwidth from 3 to 6 GHz is considered to be the frequency range over which the antenna radiation patterns are reconfigured; this is because at these frequencies in Mode–1 and Mode–2, the measured gain ratio between the $+x$ and the $-x$ directions is better than 8 dB compared to the omnidirectional Mode–0. This ratio can be better than 15 dB between 4–4.5 GHz as at these frequencies, the chosen length of the stub is around $\lambda_{eff}/2$, and the stub acts as a

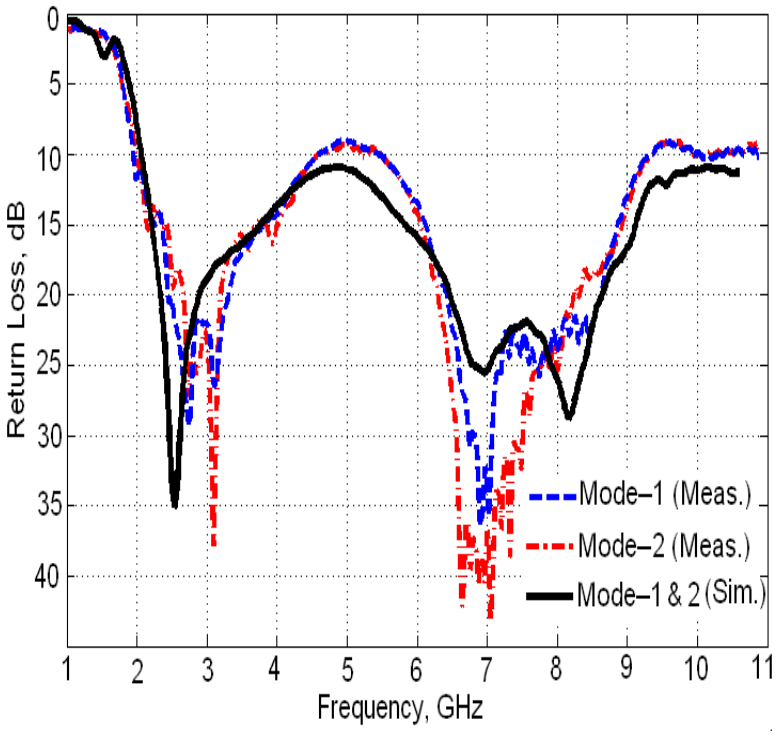

Figure 4.13: **Simulated and measured return loss curves when the proposed antenna is operating in Mode–1 and Mode–2.**

good reflector.

The differences between the simulated and measured return loss results are attributed to the fabrication tolerances and the approximate boundary conditions in the computational domain. Also, for small antennas the RF cable and bulky SMA connectors can affect the obtained return loss measurements [106, 107]. Furthermore, the non-exact modelling of the biasing network including the external dc wires coming from power supply, the parasitic effects of the p-i-n diodes and the difficulties in numerically modelling all relevant aspects of the real p-i-n diodes characteristics introduce slight uncertainties in the observed results.

The simulated 3-D radiation patterns of the proposed reconfigurable in different modes at 4.5 GHz are shown in Figure 4.13. The radiation patterns

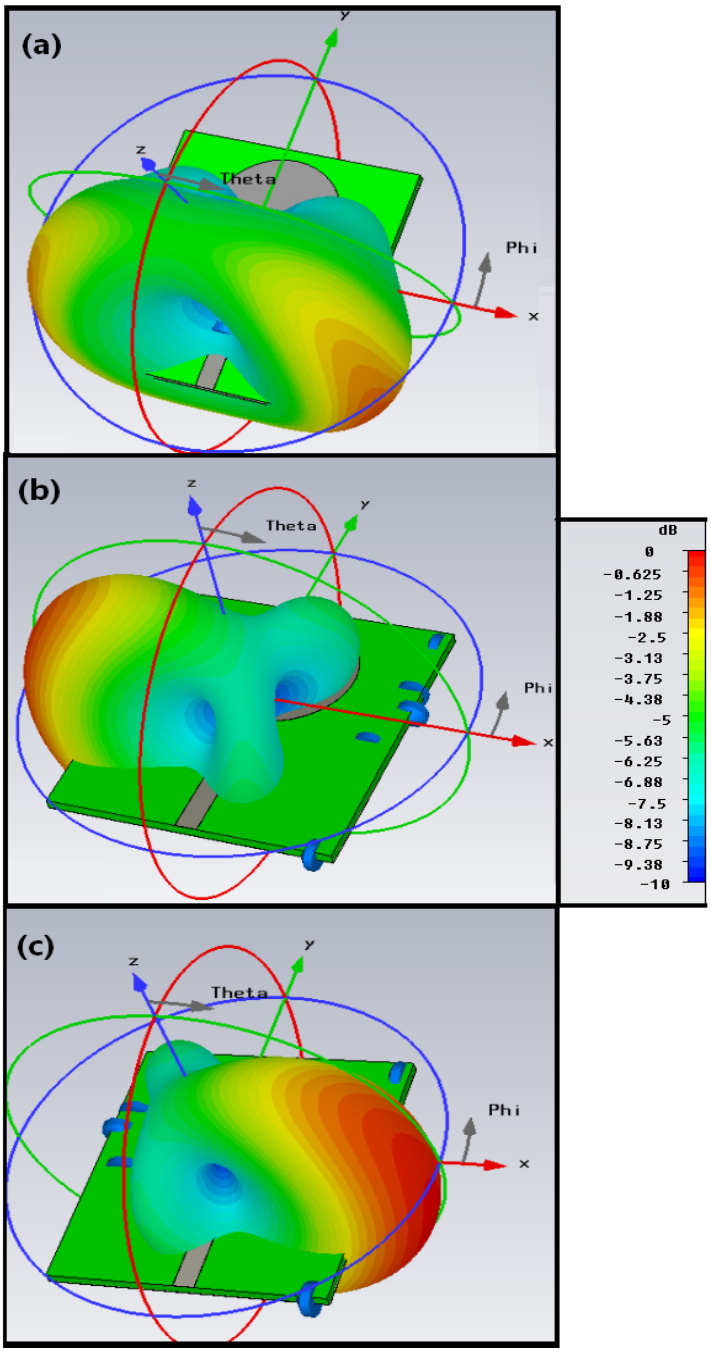

Figure 4.14: **Simulated 3-D normalised realised gain patterns when the antenna is operating at 4.5 GHz in: a) Mode–0, b) Mode–1, and c) Mode–2.**

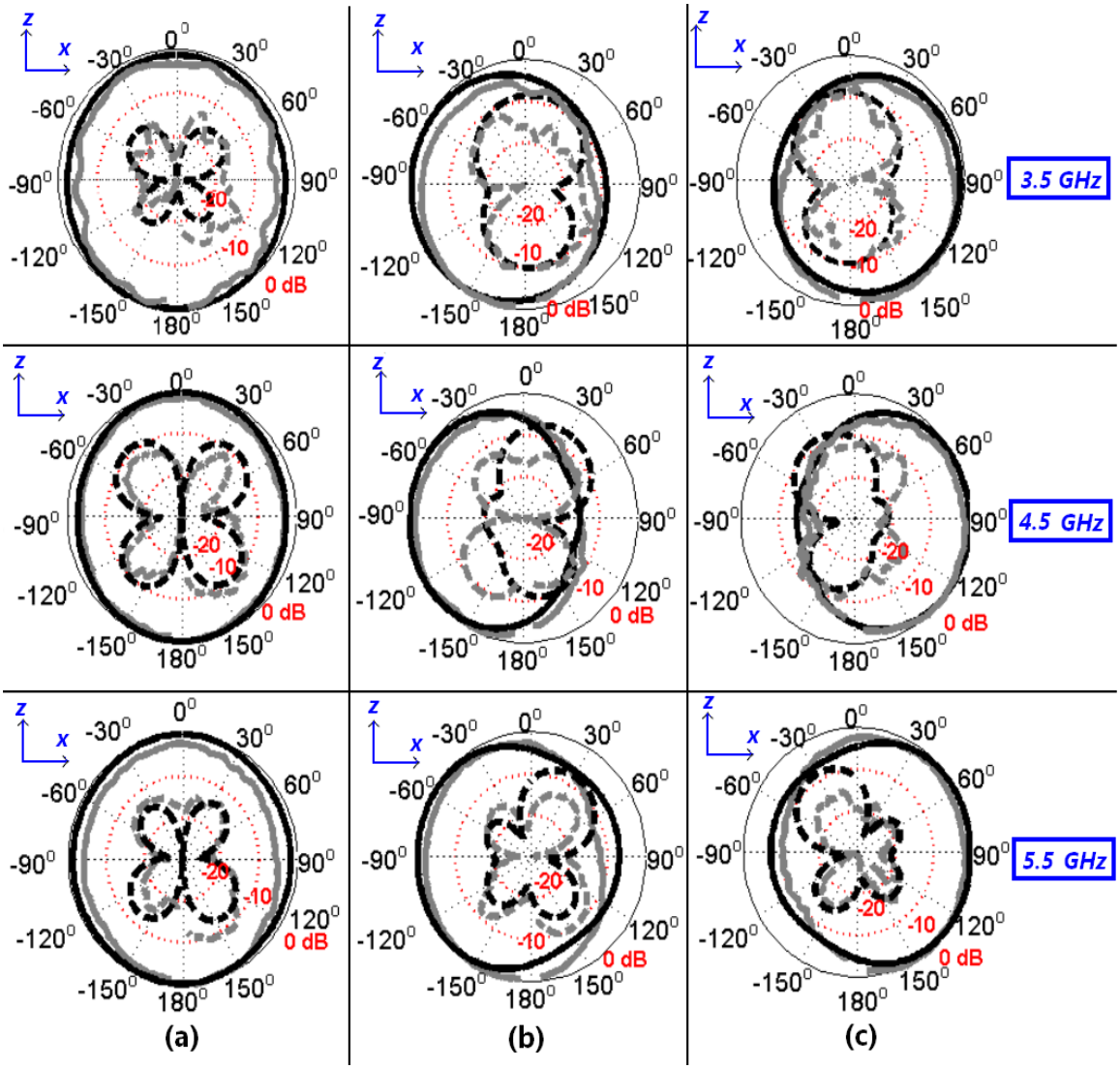

Figure 4.15: **Simulated (black curves) and measured (grey curves) normalised radiation patterns in the H-plane when the antenna is operating in: a) Mode–0, b) Mode–1, and c) Mode–2. Solid lines are for the (co-polar) component and dashed lines represent the (cross-polar) component.**

of the proposed antenna were also measured in an anechoic chamber. The simulated and measured normalised radiation patterns in the H-plane (xz-plane), when the antenna is operating in Mode–0, Mode–1 and Mode–2 are depicted in Figure 4.14 for different frequencies. The normalised co-polar

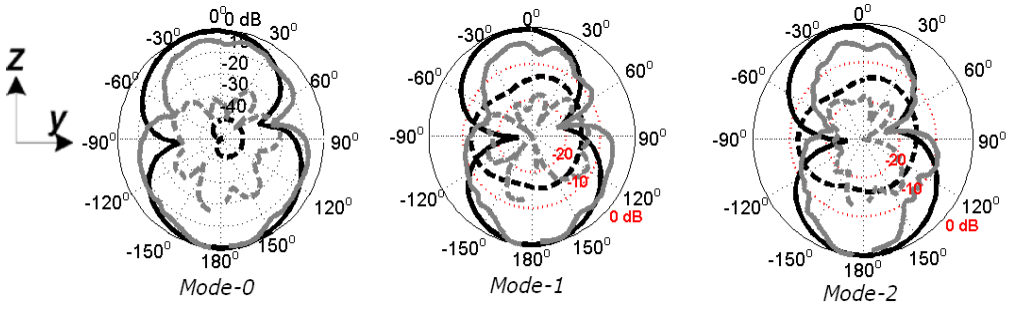

Figure 4.16: **Simulated (black curves) and measured (grey curves) normalised radiation patterns at 4.5 GHz in the E-plane, when the antenna is operating in different modes. Solid lines are for the (co-polar) component and dashed lines represent the (cross-polar) component.**

E-plane patterns (yz-plane) at 4.5 GHz are also shown in Figure 4.15 and they do not significantly change when the antenna is operating in the three proposed operation modes.

The dc power supply was mounted under the turn table and was covered by microwave absorber as shown in Figure 4.16. It was noted that covering the antenna's SMA connector with a piece of absorber would reduce the ripples in the radiation patterns. Although the bias lines are RF choked, they are also shielded with aluminium foil to prevent them from picking up noise and to reduce their spurious radiation. When the antenna is operating in Mode–0, omni-like radiation patterns are achieved in the xz-plane (H-plane). For Mode–1 and Mode–2 the beams are concentrated along the $-x$ and $+x$ direction, respectively. Slight differences between simulated and measured radiation patterns are attributed to the antenna fabrication tolerances and the slight misalignment uncertainties in the antenna under test (AUT) positioning.

Table 4.4 shows the measured gain ratio between the realised gain in the $+x$ and $-x$ directions and the maximum realised gain in the xz-plane,

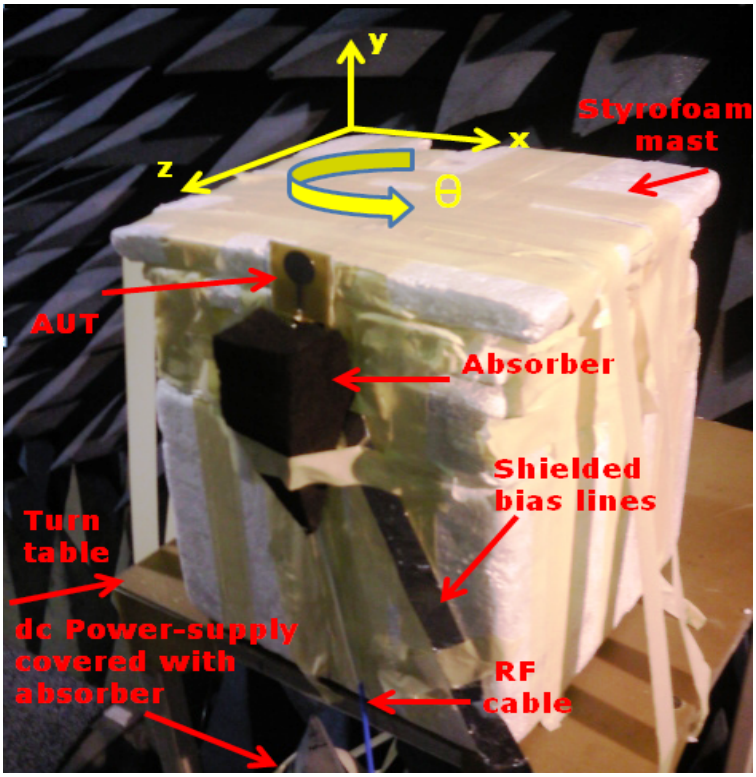

Figure 4.17: **Prototype mounted inside the anechoic chamber, the antenna's SMA connector is covered with absorber and the dc wires are shielded with aluminium foil.**

at different frequencies, when the antenna is working in different operation modes. The gain was measured in the anechoic chamber using the Gain-Transfer method in the far field [71]. Uncertainties in measuring the transmission coefficient (S_{21}) between the AUT or the standard gain horn (SGH) and the transmitting horn can add some slight differences in the gain measurement. Tolerances in the gain standard curves published by manufacturer, the coaxial adaptor connected to the SGH and misalignments of the antennas can also add some uncertainties in the gain measurements. The realised gain was also measured with another prototype on which the p-i-n diode switches were replaced with ideal switches (e.g., putting metal copper bridge to resemble an ON switch state and removing it for the OFF

case). In Mode–1 and Mode–2, the gain was at least 1 dB better than the values listed in Table 4.4. At 4.5 GHz, the measured realised gain was 3 dBi in Mode–1 and 3.1 dBi in Mode–2. This highlights the major role that the bias network, the parasitics of the p-i-n diodes, and also the current dissipated in the ON p-i-n diode series resistance, play in reducing the measured gain of reconfigurable antennas.

Finally, the total dc power consumption was measured in different operation modes. In Mode–0, the dc power is very low as each diode will have a reverse current (I_r) in the order of nanoamperes. In Mode–1 or Mode–2, two diodes are on at a time and the forward current (I_f) is in the milliamperes range, hence the total dc power consumption is $2 \times 20\,mA \times 3.0\,V = 120\,mW$. The power consumption can be further reduced using current drivers to decrease the bias current, albeit this will increase the insertion loss of the diodes and will slightly degrade the performance of the stub as a reflector element. The simulated total efficiency (η_t) of the proposed antenna at 4.5 GHz is 80 % in Mode–0 and 77 % in Mode–1 and Mode–2. The efficiency values of the antenna modes were calculated numerically through the CST Microwave Studio package applying conventional antenna parameters calculations using the simulated realised gain and directivity of the antenna.

Although the measurements did not show substantial increase in gain values, it clearly indicates that reconfiguration using the p-i-n diodes and our technique did not negatively affect the overall gain at the measured frequencies. The proposed antenna structure represents a simple, yet flexible solution for radio front-ends in smart wireless applications and potentially future Cognitive Radio systems. As these systems need frequency and polarisation reconfigurability, pattern reconfiguration could provide another degree of flexibility and help in minimising interferences and hence signif-

	Mode-0		Mode–1		Mode–2	
Frequency (GHz)	Gain (dBi)	$\frac{+x}{-x}$ (dB)	Gain (dBi)	$\frac{+x}{-x}$ (dB)	Gain (dBi)	$\frac{+x}{-x}$ (dB)
3.5	2.1	0.4	1.3	-9.2	1.5	9.5
4.5	1.4	0.7	1.9	-14	2.1	15.5
5.5	1.9	-1.3	2.1	-9.9	2.0	9.2

Table 4.4: **Measured gain ratio between the $+x$ direction and $-x$ direction and the maximum realised gain in the xz-plane for the proposed antenna**

icantly improving system performance when a combination of congested spectrum and imbalanced demand for the bandwidth and spectrum exist.

4.4 Summary

A simple and novel design for a compact planar pattern-reconfigurable ultra-wideband antenna is presented. When the antenna is pattern reconfigured, the radiation patterns change from a nearly omnidirectional to two opposite end-fire patterns. This can assist CR and other smart wireless communication systems through spatial rather than frequency means. A wide measured fractional bandwidth of 66% from 3 to 6 GHz is achieved for reconfigurable patterns with measured return loss better than 9 dB. The compact volume of the antenna ($42 \times 38 \times 1.52\ mm^3$) and the moderate average power consumption (e.g., the diodes are not on all the time and the bias current can be controlled by current drivers), will lead to simple integration in portable future smart radios and CR devices for various consumer and specialised applications.

5 Polarisation-Reconfigurable Ultra-wideband Antennas

5.1 Introduction

When considering EM waves, the plane containing the electric field that is orthogonal to the direction of propagation is called the plane of polarisation. In this plane, the tip of the electric field vector moves along an ellipse. The shape and orientation of the ellipse and the direction in which the electric field vector traverses the ellipse specifies the electromagnetic wave polarisation [108]. *Axial ratio* specifies the shape of the ellipse and it is the ratio of the major axis to the minor axis. The *tilt angle* is the angle between the major axis and a reference direction and it specifies the orientation of the polarisation ellipse. The direction in which the electric field vector move along the ellipse is the *sense of polarisation* and it can be right-handed or left-handed when viewed looking in the direction of propagation [108]. The axial ratio sometimes carries a sign that is taken as plus if the sense of polarisation is right-handed and minus if it is left-handed [109].

Circular Polarised (CP) antennas are good in combating fading and multi-path interferences and hence can decrease the BER performance of the wireless communication system and enhance the system performance [110, 111]. Moreover, CP antennas are popular for satellite positioning, radar and radio

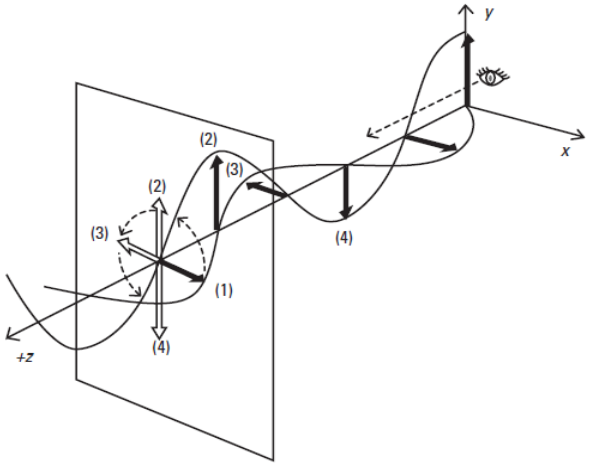

Figure 5.1: **A circularly polarised wave as in [113].**

frequency identification (RFID) applications as they decrease the severe polarisation mismatch between transmitters and receivers [112]. In a linearly polarised field vector and at a certain point in space, the tip of the field vector describes a straight line segment as a function of time and it may be viewed as a special case of elliptical polarisation where the axial ratio is equal to ∞ [109]. In a circularly polarised field vector, the field vector tip describes a circle as a function of time and may be viewed as a special case of elliptical polarisation where the axial ratio is equal to one [109]. A circularly polarised wave is generated by adding two linearly polarised waves that are orthogonal in polarisation planes and with 90° phase difference between them as shown in Figure 5.1 [113].

Most of ultra-wideband monopole antennas are linearly polarised and exciting CP in these ultra-wideband antennas is difficult. However, in [114, 115] two CP polarised ultra-wideband antenna are introduced, but their axial ratio fractional operating bandwidths are still narrow and the effective techniques used to produce and expand their CP bandwidths are not that simple.

In [116] a compact CP ultra-wideband monopole antenna with a fractional AR bandwidth of 33%(7.17-10.01 GHz) is presented, however to achieve this very wideband CP, the dimensions of the monopole patch edges and corners should be carefully optimised and it is very difficult to reconfigure this antenna to switch its polarisation operation. In the past literature, many reconfigurable antennas with polarisation diversity between linear and circular polarisation or between LHCP and RHCP have been discussed [117–120]. However, the author presents in this chapter a simple polarisation reconfigured single microstrip fed ultra-wideband monopole antenna, in which its polarisation can change from LP to either RHCP or LHCP with a wideband 3 dB axial-ratio. On top of that, the author will try to re-tune the 3-dB axial ratio bandwidth to cover multiple distinct frequency bands.

5.2 Polarisation Reconfigurable Ultra-wideband Antenna Element

5.2.1 Antenna Design

The proposed polarisation reconfigurable ultra-wideband monopole antenna is shown in Figure 5.2 and the photograph of the prototype antenna is shown in Figure 5.3. The dielectric substrate used in this study is a Taconic TLC-30 substrate with a thickness of 0.88 mm, $\epsilon_r = 3.0$ and loss tangent=0.003. The length and width of the dielectric substrate is 28.5 mm and 34 mm respectively. A 10 mm $\times$10 mm patch is printed on one side of the substrate and fed by 50 Ω microstrip line. The input microstrip line is connected to a 50 Ω SMA connector. The main input feed line is divided into 2 parts, the width of the microstrip at the start of the main input feedline is 2.2 mm to achieve 50 Ω impedance and the length of this part is 4.1 mm. The

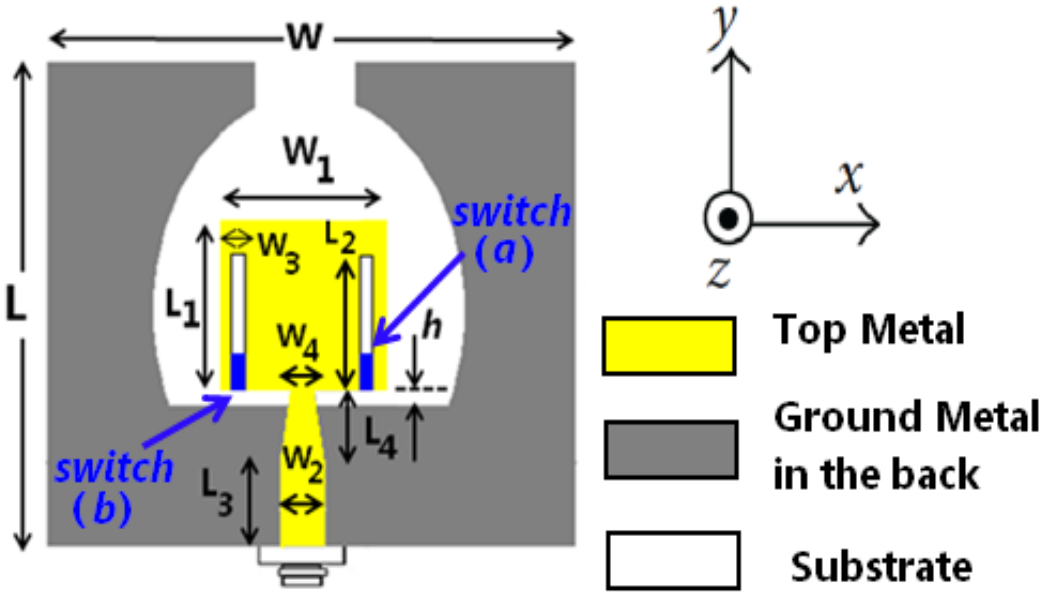

Figure 5.2: **Geometry of the proposed polarisation reconfigurable ultra-wideband antenna.**

Dimension	(mm)
Substrate width (W)	34
Substrate length (L)	28.5
Patch width (W1)	10
Patch length (L1)	10
Gap between patch and ground plane (h)	0.88
Slit length (L2)	8
Slit width (W3)	1
Feedline starting width (W2)	2.2
Feedline end width (W4)	1
Feedline straight length(L3)	4.1
Feedline tapered length(L4)	6.1

Table 5.1: **Dimensions of the polarisation reconfigured ultra-wideband antenna.**

second part of the feedline is linearly tapered for a length of 6.1 mm to achieve a width of 1 mm at the point where it connects to the square patch, this will enhance the input impedance bandwidth of the antenna. On the back side of the substrate, a section of metallisation in the shape of a wine

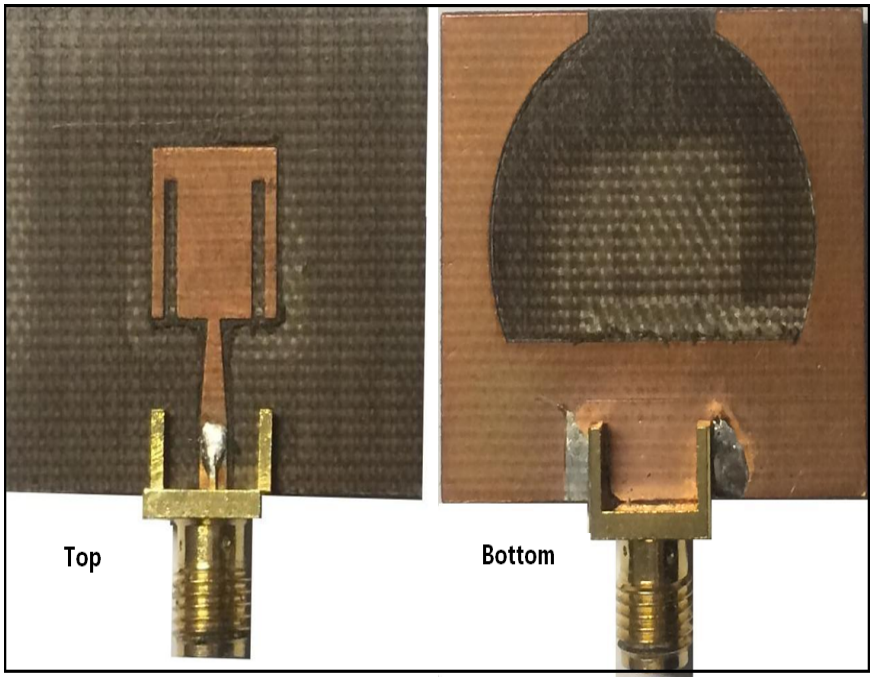

Figure 5.3: **Prototype of the proposed polarisation reconfigurable ultra-wideband antenna.**

glass is removed; this improves the impedance matching bandwidth and shape the radiation patterns. The height of the feed gap between the feed point and the ground plane is fixed at h=0.88 mm. The dimensions of the proposed antenna are summarised in Table 5.1. Two vertical rectangular slits, 8 $mm \times 1$ mm, are embedded 1 mm away from the right and left patch edges. The slit can generate two orthogonal electric field vectors (E_V, E_H) with equal amplitude and 90° phase difference. The two slits are terminated by two RF switching devices (e.g., p-i-n diodes or MEMS switches). The RF switches used in this prototype are realised as metal pads with dimensions of 1 $mm \times 1$ mm. When both switches are ON, the two etched slits are shorted and the antenna is linearly polarised and behaves like a conventional ultra-wideband monopole antenna. When switch (**a**) is OFF and switch (**b**) is ON, the slit near the right edge of the patch will

Polarisation State	Switch (a)	Switch (b)
LP	ON	ON
RHCP	OFF	ON
LHCP	ON	OFF

Table 5.2: **Operation modes of the proposed antenna.**

perturb the current, thereby leading to excite two orthogonal E vectors (E_V, E_H) with same amplitude and a $-90°$ phase shift and hence LHCP is radiated, When switch (**b**) is OFF and switch (**a**) is ON, the slit near the left edge of the patch will perturb the current and the orthogonal modes will have the same amplitude but with $+90°$ phase shift and hence RHCP radiation is achieved. The three polarisation states are controlled according to the switches states as summarised in Table 5.2.

5.2.2 Proposed Antenna Performance Analysis

(a) Return Loss

Figure 5.4 demonstrates the simulated and measured results of return loss curves for the three polarisation reconfigurable states. For the LP case, the simulated 10 dB return loss bandwidth covers the frequency range from 3.3 GHz up to 10.7 GHz. When the antenna is operating in the RHCP or LHCP modes, the simulated return loss is degraded from 4 GHz to 6.2 GHz but it is still acceptable above 6 dB. This degradation is necessarily due to the resonance of the slit embedded in the patch when its length is equal to $\lambda_g/4$, where λ_g is the guided wavelength at the notched frequency. The directions of current on the two edges of the slit are opposite and they almost try to cancel each other creating a frequency notched band operation around f_{notch}=5.7 GHz for an 8 *mm* slit. In this design, the author concerns about

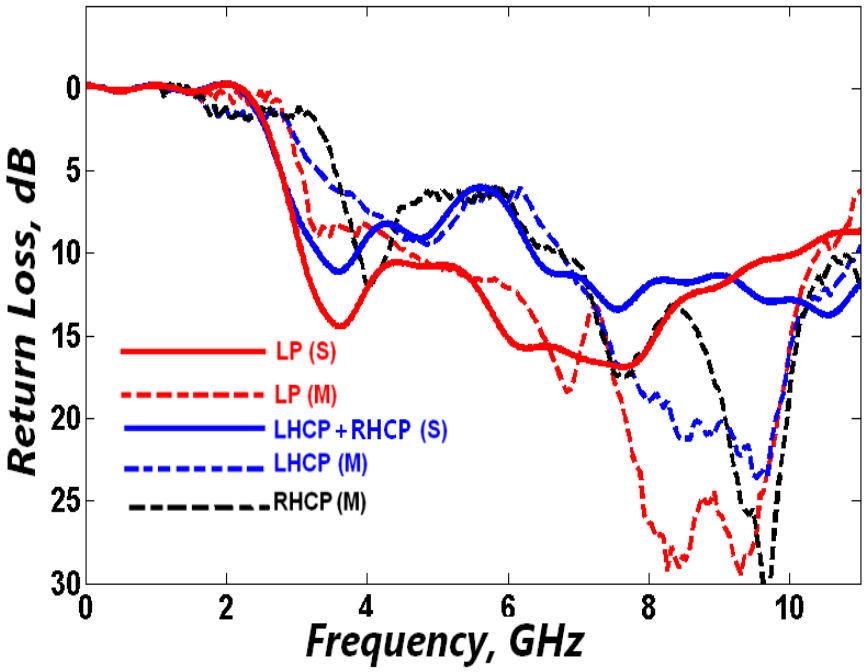

Figure 5.4: **Simulated (S) (solid lines) and measured (M) (dashed lines) return loss curves for the proposed antenna when it is working in the LP, LHCP and RHCP states.**

polarisation reconfiguration, not notched ultra-wideband operation. Moreover, the RHCP or LHCP operation occurs at frequencies beyond the notch frequency and the optimal axial ratio (AR) occurs inside the optimal return loss bandwidth ($RL \geq 10\ dB$). The return loss curves for the RHCP and LHCP states are almost similar due to the symmetry in the antenna geometry with respect to the input feed line. In general, a fair agreement between simulated and measured results has been achieved. Small frequency shifts and slight degradation of the antenna return loss occurred; this can be accounted for by the fabrication tolerances.

(b) Radiation Patterns

The simulated 3-D radiation patterns at 7 GHz for the three re-

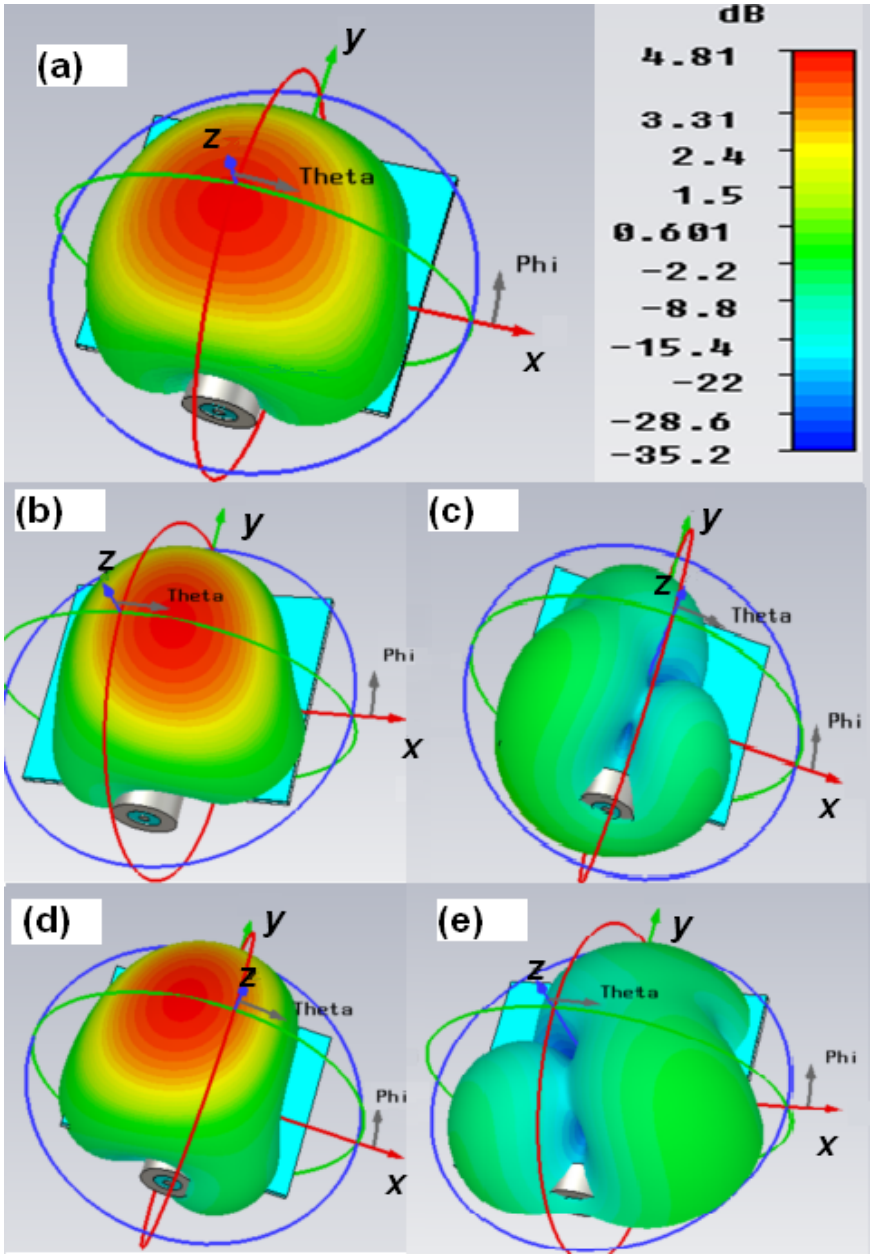

Figure 5.5: **Simulated 3-D realised gain patterns for the proposed antenna at 7 GHz when the antenna is reconfigured to work in different states: (a) LP state , b) LHCP state, co-polarisation, (c) LHCP state, cross-polarisation, d) RHCP state, co-polarisation component, e) RHCP state, cross-polarisation component .**

configurable states of the antenna are depicted in Figure 5.5. The measured normalised radiation patters in the xz- plane and yz-plane of the proposed antenna when reconfigured to work in different polarisation states are also displayed in Figure 5.6. It is noted that in the LP case and in the xz plane the radiation patters are nearly omnidirectional with reduced gain in the $\pm$ x-direction, while in the yz plane the gain largely drops in the $\pm$ y-direction and the radiation patterns are like dipole E-plane patterns. In Figures 5.5 and 5.6, it can be noticed that some good isolation ($\geq 15\ dB$) near the bore-sight direction between the co–polarisation and cross-polarisation patterns for both the RHCP and LHCP antenna states. In addition, when the antenna is configured to work in the LHCP state, the LHCP radiation occurs in the $z > 0$ half space. The same judgements apply in the RHCP case.

It can also be noticed that the antenna radiates RHCP or LHCP in the upper half-plane ($z > 0$) direction and the opposite sense in the lower half-plane ($z < 0$) direction, a known trait of CP planar monopoles [121]. This is due to the observation point in the lower half plane seeing the mirror image of the top substrate surface current seen from the opposite observation point (e.g., $E_{vertical}$ stays the same but $E_{horizontal}$ is mirrored and thus rotated 180° so RHCP becomes LHCP or vice versa). This type of performance (in which the antenna receives both orthogonal CP senses) may be suitable for applications in which the antenna can receive the reflected signal if there is an obstruction for the direct signal because when signal is reflected, the RHCP changes to LHCP or vice versa.

To minimise radiation in the antenna's lower half plane and obtain

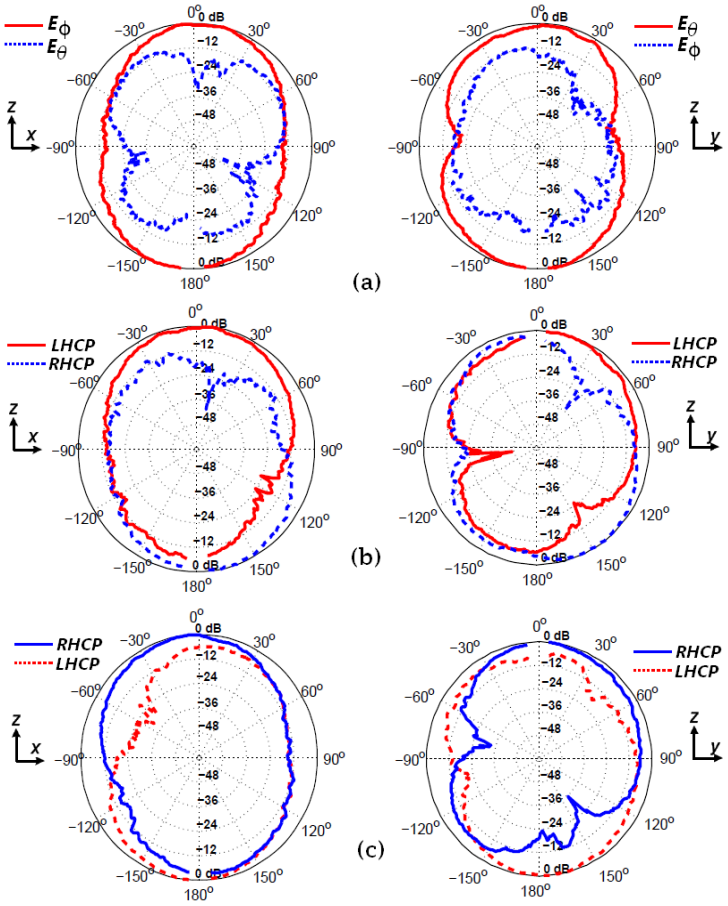

Figure 5.6: **Measured co-polarisation (solid lines) and cross-polarisation (dashed lines) normalised radiation patterns in the xz and yz planes at 7 GHz when the proposed antenna is reconfigured to work in different polarisation states, a) LP state, b) LHCP state, c) RHCP state.**

unidirectional radiation, an absorptive cavity can back the antenna or a reflector can be used. Unidirectional patterns can be preferable in some cognitive radio networks, especially in point-to-point communication between the network nodes.

(c) Surface Current

Figure 5.7 shows the simulated surface current distribution vector at 7 GHz, when the antenna is reconfigured in the LHCP mode, at four

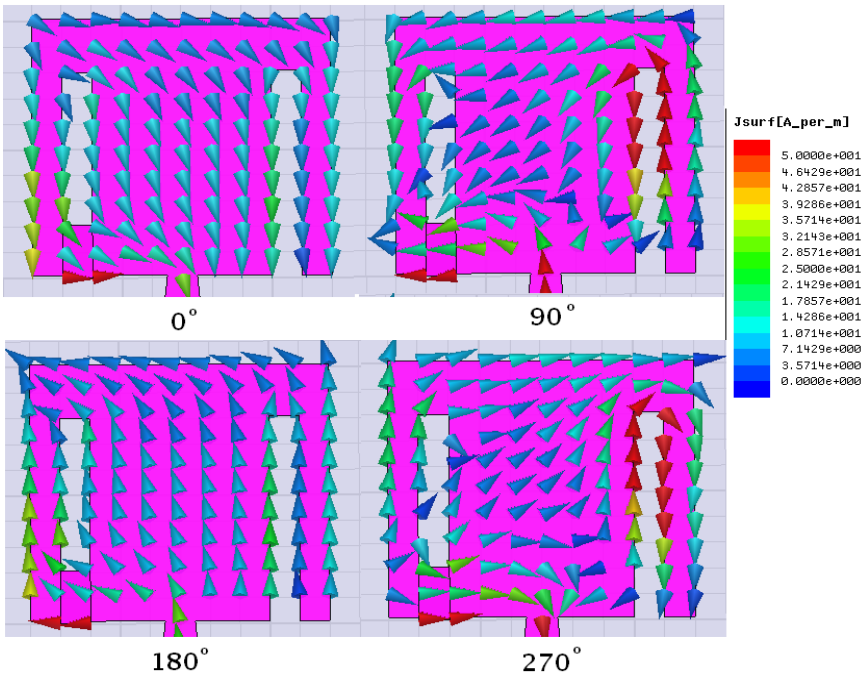

Figure 5.7: **Simulated surface current distributions when the antenna is in the LHCP state at 7 GHz when the phase is advancing from** $0°$ **to** $270°$**.**

different consecutive time instances ($\omega t = 0°, 90°, 180°, 270°$). As the phase of excitation advances and looking in the direction of propagation, the surface current vector is rotating clockwise which yields LHCP radiation in the $+z$ half sphere. The same principle applies for the RHCP case but for this scenario the current vector will rotate anti-clockwise.

(d) Axial Ratio and Gain

Figure 5.8 depicts the simulated and measured realised peak gain and the simulated and measured AR in the boresight direction, when the proposed antenna is reconfigured to work in the LHCP state. It is clear from Figure 5.8 that the reconfigured antenna exhibits a simu-

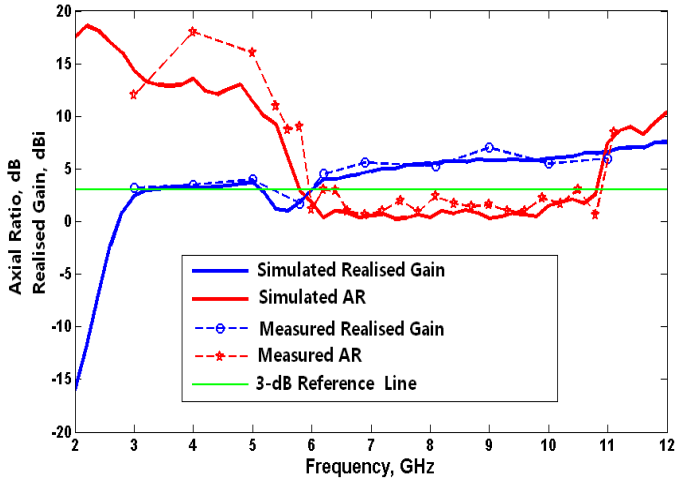

Figure 5.8: **Simulated and measured realised gain and axial ratio, when the antenna is reconfigured in the LHCP state.**

lated 3 dB AR fractional bandwidth of 60% (from 5.8 GHz to 10.8 GHz). To measure the axial ratio of the proposed antenna, the received phase and amplitude are measured across the xz and yz planes with a diagonal dual linear polarised transmitting horn antenna. After obtaining two measured sets of data across each plane, the data are post-processed to reconstruct the RHCP and LHCP components of the CP radiation pattern across the two plane cuts. The axial ratio is calculated from the RHCP and LHCP components as described in [122]. The measured 3 dB AR fractional bandwidth is approximately 59.5 % (from 5.9 GHz to 10.9 GHz). There is a very good agreement between the simulated and measured results and the small discrepancies between the simulated and measured results are mainly due to the antenna fabrication tolerances and the coaxial RF cables used in the measurements affecting the small antenna. The axial ratio and gain performance for the RHCP state should almost be similar to the LHCP case because in both cases the antenna is geometrically

symmetrical with respect to the feed line. Similar gain and AR values in both RHCP and LHCP operation of the proposed antenna are desirable in most polarisation diversity wireless applications.

5.3 Tuning Circular Polarisation Bandwidth of the Polarisation Reconfigurable Antenna

5.3.1 Antenna Re-design

Lets call the previously designed antenna (ANT I), Now to tune the polarisation CP bandwidth of ANT I, a larger version of the antenna (longer by 19%) is required. (Ant II) was designed and manufactured as shown in Figures 5.9 and 5.10. ANT II dielectric substrate is the same as ANT I substrate. ANT II detailed dimensions are presented in Table 5.3.

The new larger design allows us to increase the length of the etched slits in the rectangular patch. By adding extra switches, we can change the electrical length of the etched slits and hence the frequencies at which the antenna is radiating CP (RHCP or LHCP) are well controlled. Two vertical rectangular slits, 11.5 $mm \times 1\ mm$, are embedded 1 mm away from the right and left patch edges. The slit can generate two orthogonal E electric field vectors with equal amplitude and 90° phase difference. The 2 slits lengths are controlled by 4 RF switching devices (e.g. p-i-n diodes or MEMS switches). The RF Switches (a, b, a', b') used in this prototype are realised as metal pads (e.g., ideal switches for analysis purposes to proof the concept proposed) with dimensions 1 $mm \times 1\ mm$.

When both switches **(a, a')** are ON, the 2 slits are shorted and the antenna is linearly polarised and behaves like a conventional ultra-wideband monopole antenna. When switch **a** is OFF and switch **a'** is ON, the slit near

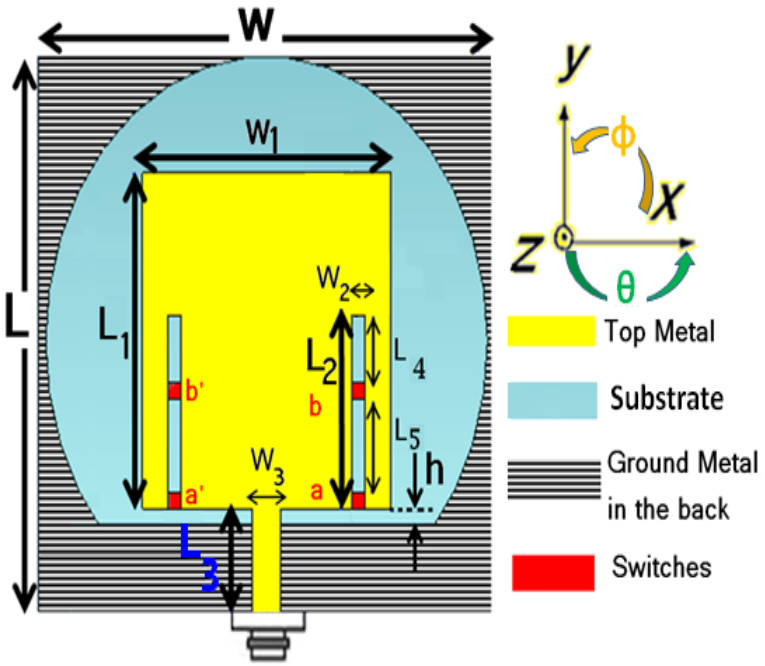

Figure 5.9: **Geometry of the polarisation reconfigurable ultra-wideband antenna (ANT II).**

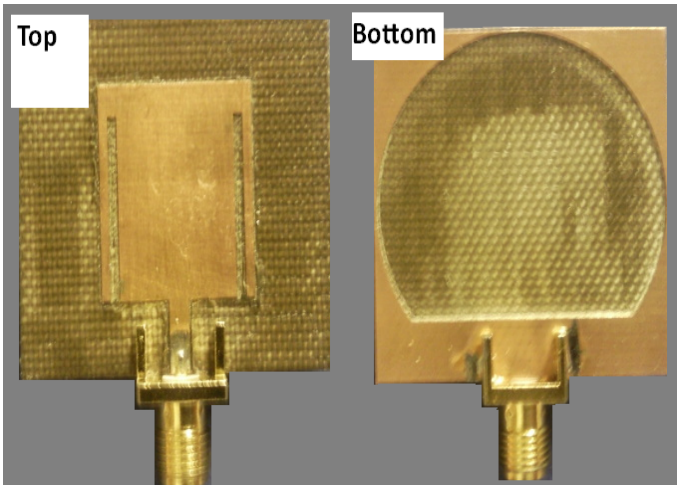

Figure 5.10: **Prototype of ANT II**

the right edge of the patch will perturb the current leading to excite two near degenerate orthogonal modes with same amplitude and a -90° phase shift and hence LHCP is achieved at specific frequency band , When switch

Dimension	(mm)
Substrate width (W)	35
Substrate length (L)	34
Patch width (W1)	17
Patch length (L1)	20
Gap between patch and ground plane (h)	0.88
Slit length (L2)	11.5
Slit width (W3)	1
Feedline starting width (W2)	2.2
Feedline end width (W4)	1
Feedline straight length(L3)	7
(L4)	3.5
(L5)	6

Table 5.3: **Dimensions of ANT. II.**

Polarisation	Frequency	Switch a	Switch b	Switch a'	Switch b'
LP	ultra-wideband	ON	X	ON	X
LHCP	Band I	OFF	ON	ON	X
	Band II	OFF	OFF	ON	X
RHCP	Band I	ON	X	OFF	ON
	Band II	ON	X	OFF	OFF

Table 5.4: **Operation modes of ANT. II**

a' is OFF and switch **a** is ON, the slit near the left edge of the patch will perturb the current and the near degenerate orthogonal modes will have the same amplitude but with $+90^{\circ}$ phase shift and hence RHCP is achieved. Switches **b** , **b'** are used to change the electrical length of the slits and hence control the frequency band on which the antenna is CP. The three polarisation states over different frequency bands are controlled according to the switches states as summarised in Table 5.4. The **X** state of a switch indicates a "Don't care"state.

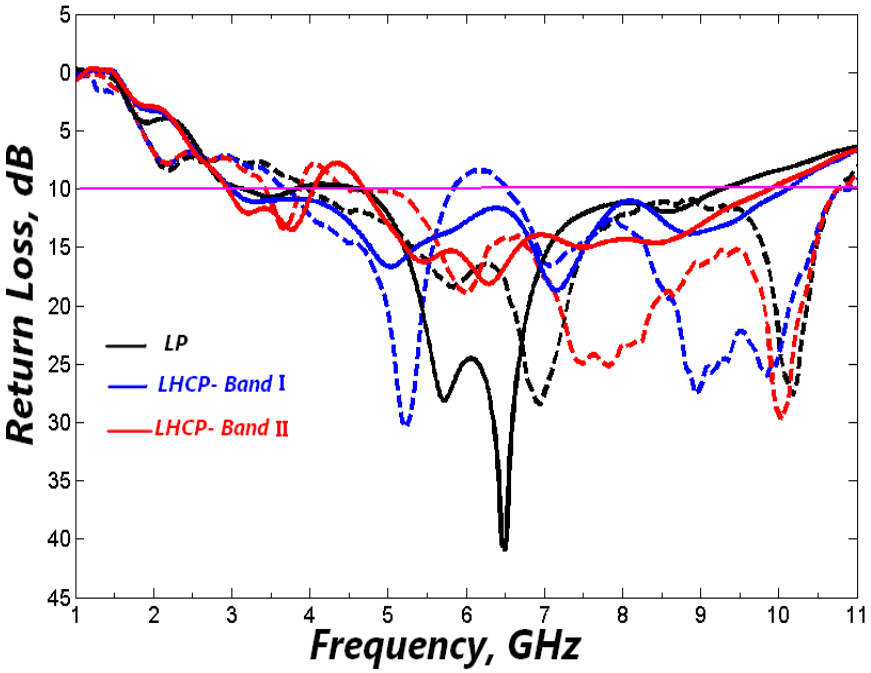

Figure 5.11: **Simulated (solid lines) and measured (dashed lines) return loss curves for ANT II when it is working in the LP, LHCP-Band I and LHCP–Band II.**

5.3.2 Numerical and Experimental Results

(a) Return Loss

The simulations are performed using the CST Microwave Studio package. Return loss measurements are performed using Agilent N5230C PNA-L microwave network analyser. Figure 5.11 demonstrates the simulated and measured results of return loss curves for 3 operation modes of the antenna. Band I and Band II are defined later in the axial ratio subsection of this chapter. When the antenna is operating in the LHCP modes, the simulated return loss is degraded over a small set of frequencies of the ultra-wideband bandwidth but it is still acceptable above 6 dB over the entire ultra-wideband bandwidth. The return loss curves for the RHCP and LHCP states are almost

similar due to the symmetry in the antenna geometry with respect to the input feed line.

In general, a fair agreement between simulated and measured results has been achieved as both the simulated and measured curves showed return loss better than 6 dB in the whole ultra-wideband spectrum. Small frequency shifts and slight degradation of the antenna return loss occurred; the discrepancies between simulated and measured curves can be accounted for by the fabrication tolerances. The substrate thickness tolerances can decrease the return loss, especially in the upper ultra-wideband operation. Moreover, uncertainties in the relative permittivity of the substrate can degrade the performance, especially around the center frequency band.

(b) Radiation Patterns

The simulated and measured radiation patterns of the antenna when operating in the LP mode are depicted in Figure 5.12 for different frequencies. The measured patterns agrees well with the simulated ones. It is noted that in the xz plane and at the low frequency band in the allocated ultra-wideband spectrum, the radiation patterns are nearly omni-directional and at high frequencies the gain drops in the $\pm x$-direction, while in the yz plane the gain largely drops in the $\pm y$-direction and the radiation patterns are as typical for a monopole. Figure. 5.13 and Figure. 5.14 display the simulated and measured radiation patterns of the antenna when it is in the LHCP and RHCP states. The measured patterns follow the simulated ones and we can notice some good isolation near the boresight (e.g., maximum radiation) direction between the co–polarisation and cross-polarisation patterns for both the RHCP and LHCP antenna states. Differences

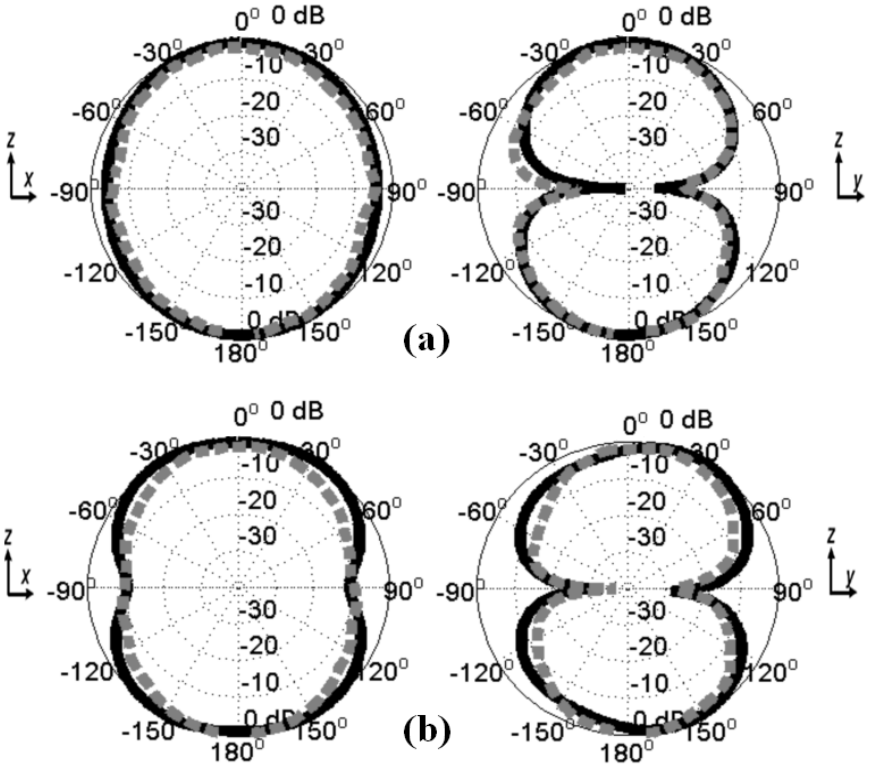

Figure 5.12: **Simulated (solid black lines) and measured (dashed grey lines) normalised radiation patterns for ANT II when it is working in the LP state, a) 4 GHz, b) 6 GHz.**

between simulated and measured radiation patterns are mainly due to the antenna fabrication tolerances and the slight misalignment uncertainties in the antenna under test (AUT) positioning. Moreover, connectors and cables connected to the AUT and the AUT support structure can add some reflections in the chamber and deteriorate the perfect line-of-sight (LOS) assumption and add some ripples on the radiation patterns. From Figures. 5.13 and 5.14, is is also noticed that the antenna radiates RHCP or LHCP in the upper half-plane ($z > 0$) direction and the opposite sense in the lower half-plane ($z < 0$) direction.

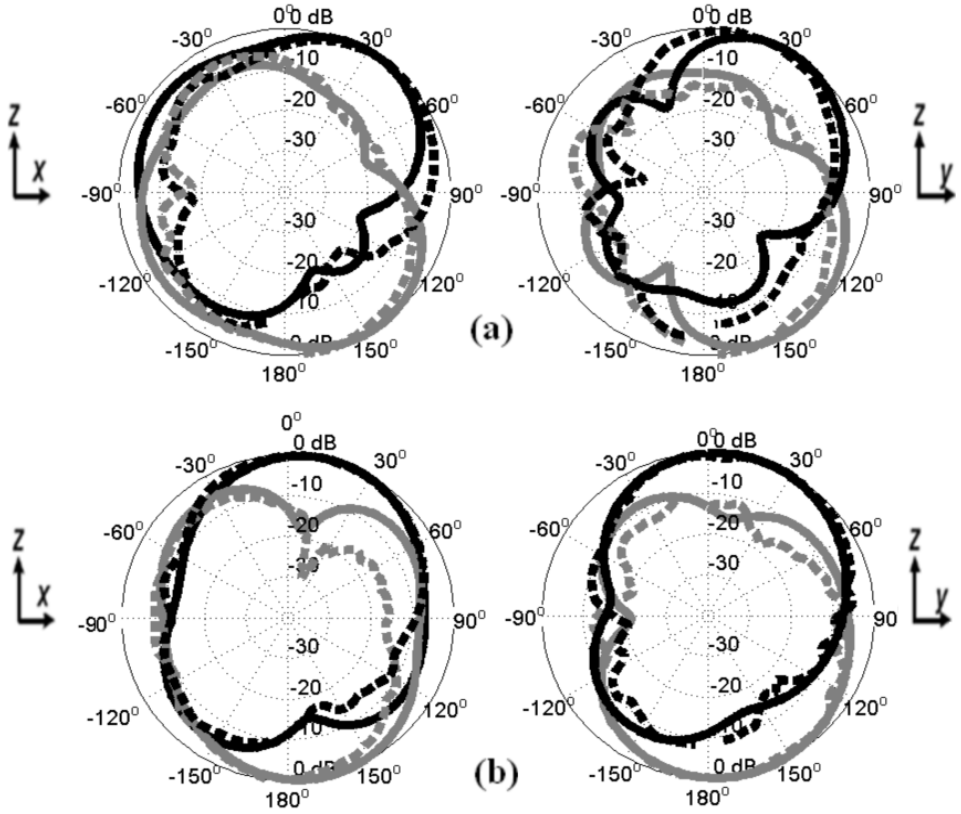

Figure 5.13: **Simulated (solid lines) and measured (dashed lines) normalised radiation patterns for ANT II when it is reconfigured in the LHCP state, a) 6 GHz in Band I, b) 5 GHz in Band II. The co-polarisation (LHCP component) is shown in black colour and cross-polarisation (RHCP component) is shown in grey.**

(c) Axial ratio and Gain

Figure. 5.15 depicts the simulated and measured minimum axial ratio (AR) in the boresight direction when the proposed antenna is reconfigured to work in the LHCP state. It is clear from Figure. 5.15 that when the antenna is reconfigured in LHCP-Band II state, the antenna exhibits a simulated and measured 3 dB AR fractional bandwidth of 20% (from 4.6 to 5.6 GHz) and 21% (from 4.7 to 5.8 GHz) respectively. When the antenna is reconfigured in the LHCP-Band

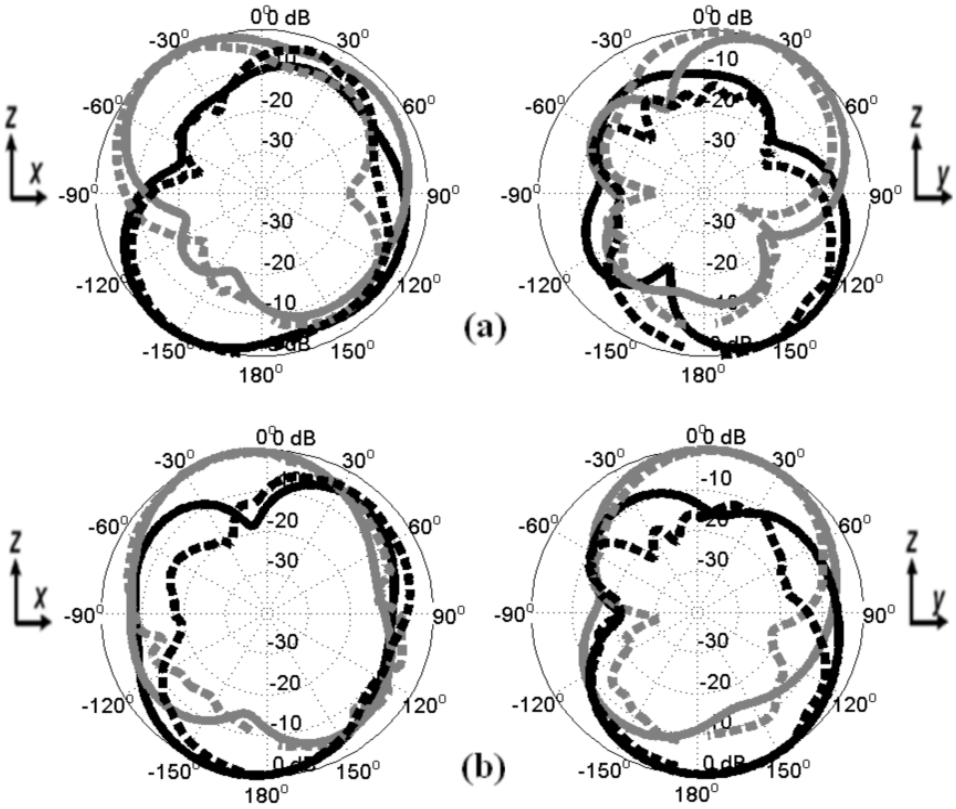

Figure 5.14: **Simulated (solid lines) and measured (dashed lines) normalised radiation patterns for ANT II when it is reconfigured in the RHCP state, a) 6 GHz in Band I, b) 5 GHz in Band II. The co-polarisation (RHCP component) is shown in grey colour and cross-polarisation (LHCP component) is shown in black.**

I state, the antenna exhibits simulated and measured 3-dB AR fractional bandwidth of 41% (from 5.2 to 7.9 GHz) and 37% (from 5.8 to 8.4 GHz) respectively. There is a good agreement between the simulated and measured results, differences are mainly due to the antenna fabrication tolerances, the coaxial RF cables and connectors and the associated uncertainties in the measurement of the phase and amplitude which can lead to axial ratio value uncertainties. Table 5.5 shows the simulated realised peak gain and the measured realised gain

at different frequencies when the antenna is working in different polarisation states. The axial ratio and gain performance for the RHCP cases should almost be similar to the LHCP case because in both cases the antenna is geometrically symmetrical with respect to the feedline.

(d) Surface Current

To illustrate how the CP is achieved for different configurations, the surface current distribution should be studied. The simulated surface current distributions at 7 GHz and at orthogonal phases when the source phase advances from 0° to 270° and when the antenna is working in the LHCP mode in Band I, are illustrated in Figure 5.16(a)-(d). As the excitation phase advances, the current vector on the patch is rotating clockwise and hence the antenna is radiating LHCP in the $z > 0$ direction.

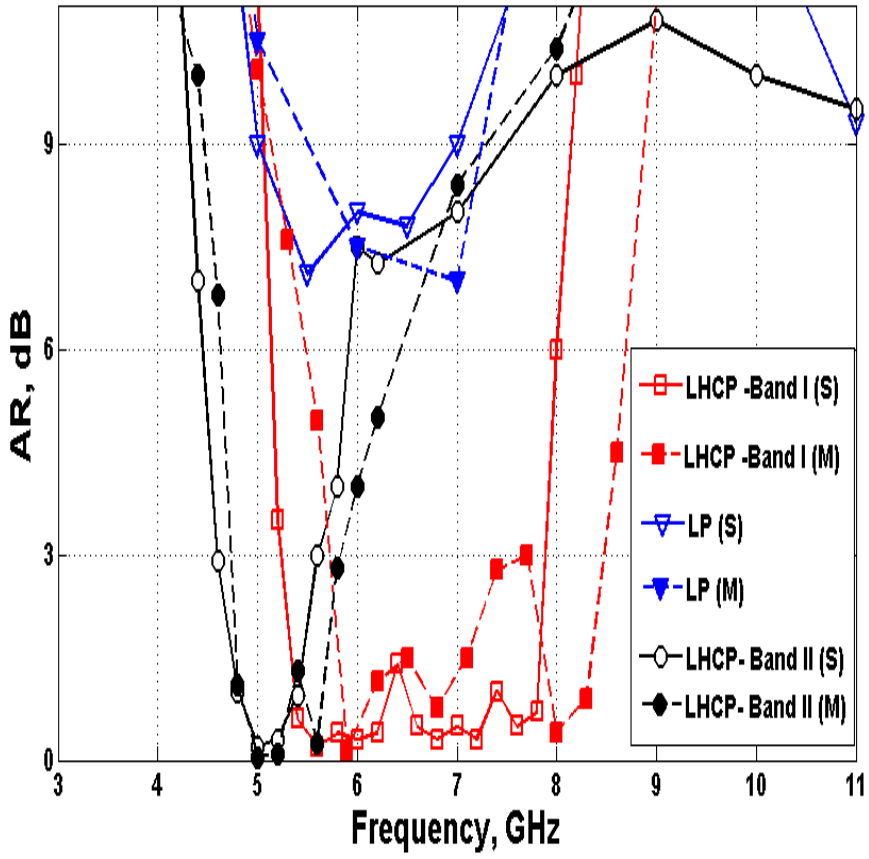

Figure 5.15: **Simulated (S) and Measured (M) Axial ratio, when the antenna is reconfigured in the LP and LHCP state (Band I and Band II).**

	Gain (dBi)	
Frequency(GHz)	Simulated	Measured
4 (LP)	3.2	3.9
5 (LP)	3.4	4
6 (LP)	4	4.5
6 (LHCP-Band I)	3.9	4
5.0 (LHCP-Band II)	3.5	3.6

Table 5.5: **Simulated and measured gain of ANT. II.**

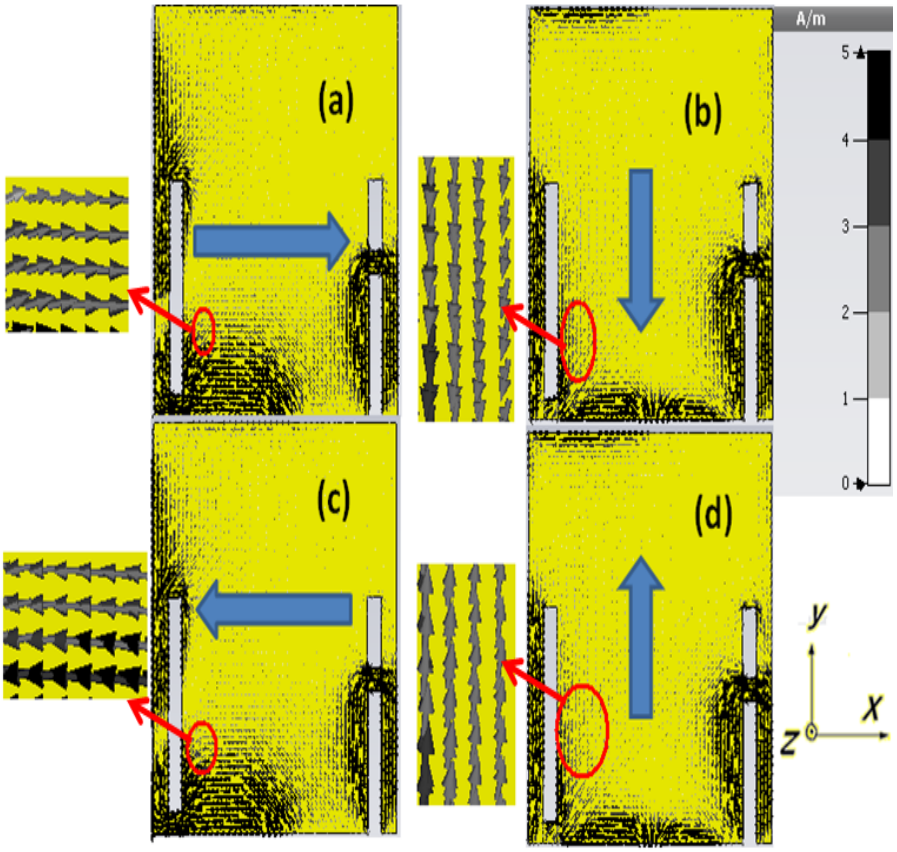

Figure 5.16: **Simulated surface current vector distribution when the antenna is working in the LHCP-Band I at, a) 7 GHz$\angle 0°$, b) 7 GHz $\angle 90°$, c) 7 GHz$\angle 180°$, and d) 7 GHz$\angle 270°$.**

From Figure 5.16, we can also see how the slit introduces asymmetry in the patch and the length of the slit will directly change the electrical length of the x-directed current, so that the x and y directed current are equal in magnitude and quadrature in phase. In the LP operation mode, the slits are shorted and no asymmetry is introduced. The current vector tip will almost keep swinging in the $\pm y$ direction as the phase advances from 0° to 360°. The surface current will flow smoothly on both the right and left edges of the patch and there will be no strong x directed current.

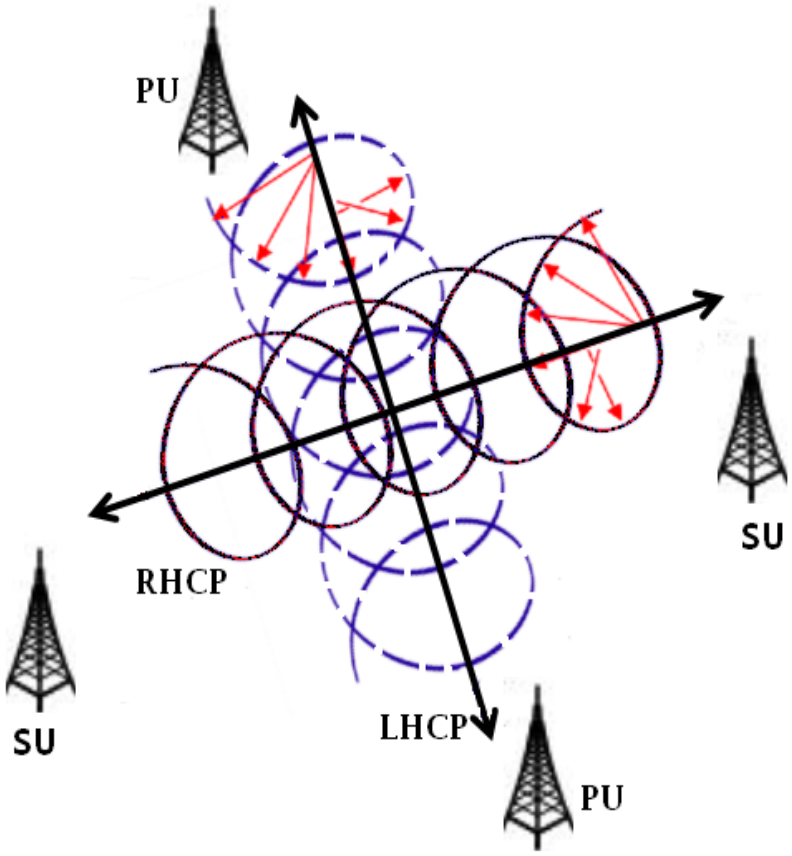

Figure 5.17: **Spectrum sharing in the polarisation domain in a simple CR network. Secondary devices (SU) are communicating with their antennas configured as RHCP while primary (legacy) users (PU) antennas are configured as LHCP, assuming line-of-sight (LOS) operation.**

5.4 Applications in Cognitive Radio

Conventional Cognitive Radio (CR) antenna may sense the spectrum to locate unused frequency spectrum holes, and then secondary devices can communicate using these frequencies without interfering with primary legacy users. In Chapter 3, Some application of frequency reconfigurable antennas were discussed and in this section the author presents some analogy between the spectrum domain and the polarisation domain and discuss how these terms are achieved by the proposed polarisation ultra-wideband antenna.

It is also worth mentioning here that line-of-sight (LOS) operation with no multipath is assumed in the following applications.

(a) Frequency Sensing ↔ Polarisation Sensing.

The spectrum resources utilisation can be increased if we can also do sensing in the polarisation domain. In [123] a feasible scheme for polar-metric sensing based on the principle of Virtual Polarisation Adaptation is introduced. The proposed reconfigured antenna can simplify this sensing process and ease the burden on the CR front end digital signal processing unit, allowing switching between different states of polarisation and by analysing the received signal strength, the polarisation sense of primary users can be determined. In contrast to conventional CR reconfigurable antennas, in which the antenna after sensing the spectrum has to be frequency reconfigured to work in narrowband at available spectrum holes, the proposed CR devices will use decisions based on polarisation sensing to reconfigure their antenna polarisation states to allow communication on a specific polarisation sense (e.g., RHCP) without affecting or being affected by primary (legacy) users (PUs) operating on an opposite polarisation sense (e.g., LHCP) as shown in Figure 5.17.

(b) Frequency Notching ↔ Polarisation Notching.

In Conventional CR, one can use reconfigurable frequency notched antennas to notch out the frequency spectrum around legacy users or possible interferers. Using a similar idea and since we can control the frequency band at which the antenna is radiating a specific sense of CP, we can integrate the proposed antenna in a CR device, by

applying *Polarisation Notching* in which at the interfering frequency band, we change the polarisation sense of our antenna reception to be opposite to the polarisation sense of the interferer. From a system point of view this is beneficial in mitigating serious interferers before they saturate the CR RF front-ends.

5.5 Summary

Two novel compact ultra-wideband microstrip antennas with reconfigurable polarisation capability have been presented. The first antenna can be switched from linear polarisation (LP) to right hand circularly polarisation (RHCP) or left hand circular polarisation (LHCP). The measured 3 dB axial-ratio (AR) fractional bandwidths for the RHCP or the LHCP after reconfiguration is 59.5 % from 5.9 to 10.9 GHz. In the second antenna, the CP bandwidth (RHCP or LHCP) can be changed at different frequency bands. The experimental fractional bandwidths of the 3-dB axial ratio are 37 % from (5.8 to 8.4 GHz) for Band I and 21 % from (4.7 to 5.8 GHz) for Band II.

The proposed antennas are suitable candidates for Cognitive Radio applications or smart wireless applications where polarisation reconfiguration (in addition to frequency and pattern reconfiguration) is needed to minimise interference and allow for efficient communication links and more intelligent CR and wireless devices.

6 Planar Ultra-wideband Antenna with Multiple Degrees of Reconfiguration

6.1 Introduction

Frequency reconfigurability provides CR systems with the necessary flexibility to perform their main functions. In addition, being able to control other parameters such as antenna polarisation and patterns will further enhance the offered flexibility by the radio front-end. In the open literature, several designs have targeted frequency, pattern or polarisation reconfiguration and in certain cases a combination of two of these parameters. To the best of the author's knowledge and based on extensive literature review (as discussed in Chapter 2), no attempt has yet been reported to combine the main three categories of reconfigurable antennas, namely frequency, pattern and polarisation, in one single design. Thereby, in this chapter, the author goes one step further in the design of reconfigurable antennas and we presents a novel planar reconfigurable antenna with multiple degrees of reconfiguration that meets the growing demand of CR and similar smart wireless devices for more intelligent and multi-functional antennas.

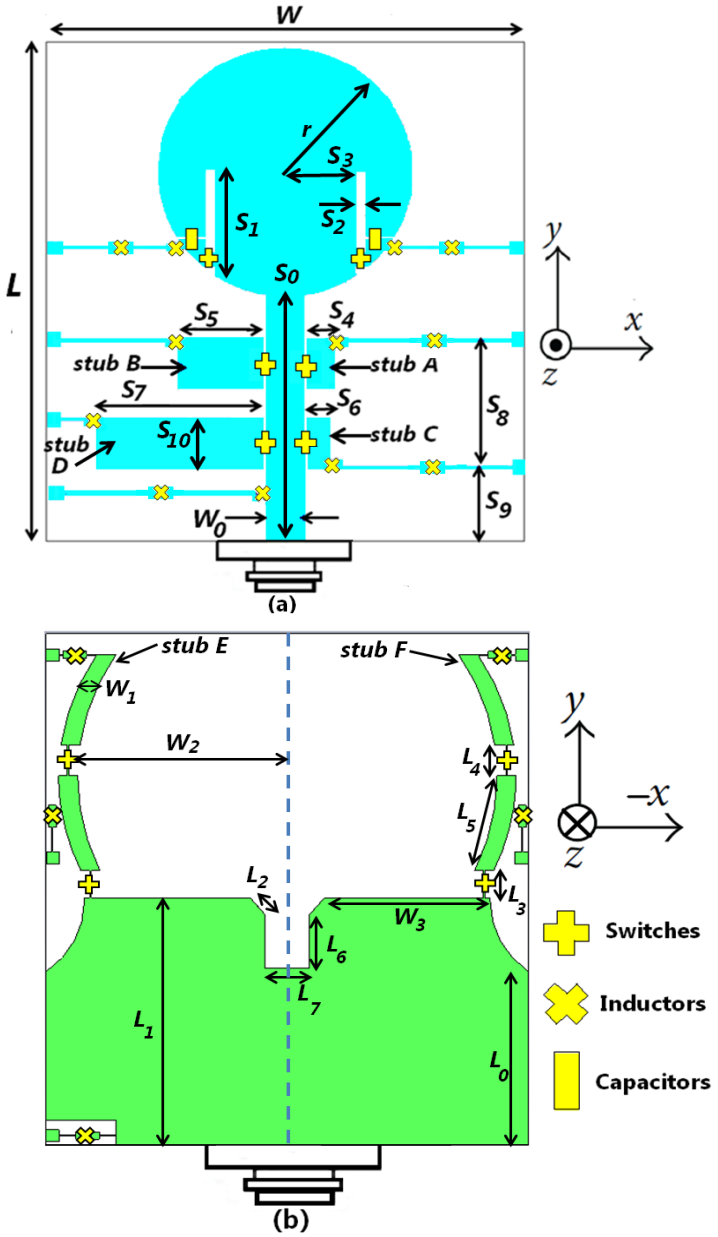

Figure 6.1: **Geometry of the proposed reconfigurable ultra-wideband antenna. a) Front view, b) Back view.**

6.2 The Proposed Antenna Design

The front and back views of the proposed reconfigurable ultra-wideband monopole antenna are shown in Figure 6.1 and the fabricated prototype of

Dimension	(mm)	Dimension	(mm)
W	38	W_0	2.9
W_1	1.5	W_2	17.2
W_3	13	L	42
L_0	14	L_1	20
L_2	1.8	L_3	2.5
L_4	2.5	L_5	8
L_6	4.4	L_7	3.5
S_0	20.4	S_1	9.5
S_2	1.0	S_3	5.5
S_4	2.0	S_5	6.6
S_6	1.6	S_7	13.1
S_8	10.3	S_9	6.2
S_{10}	4	r	10

Table 6.1: **Dimensions of the proposed antenna**

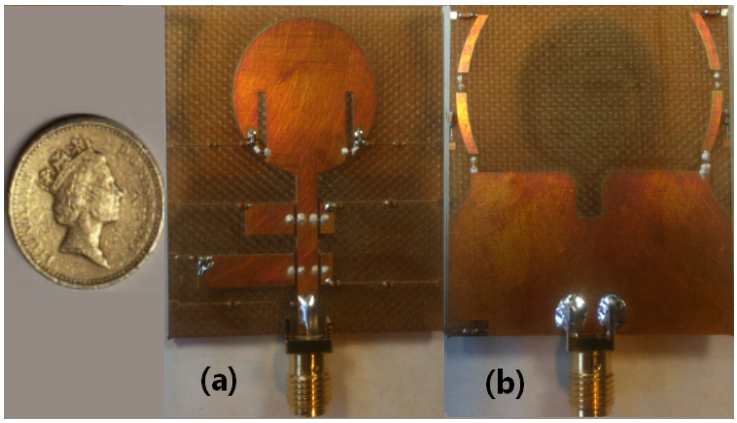

Figure 6.2: **Prototype of the proposed reconfigurable ultra-wideband antenna. a) Front view, b) Back view.**

the antenna is shown in Figure 6.2. The dielectric substrate used in this prototype is an FR4 substrate with a thickness of 1.52 mm, ϵ_r=4.3, and a loss tangent of 0.02. Four switches (a, b, c, d) are used to connect or disconnect a combination of four printed stubs (A, B, C, D) to the main microstrip feedline. The labelling of the switches is illustrated in Figure 6.3.

To achieve circular polarisation at specific frequencies, the disk patch has two parallel vertical rectangular slits; each slit is 9.5 $mm \times 1$ mm. Switches

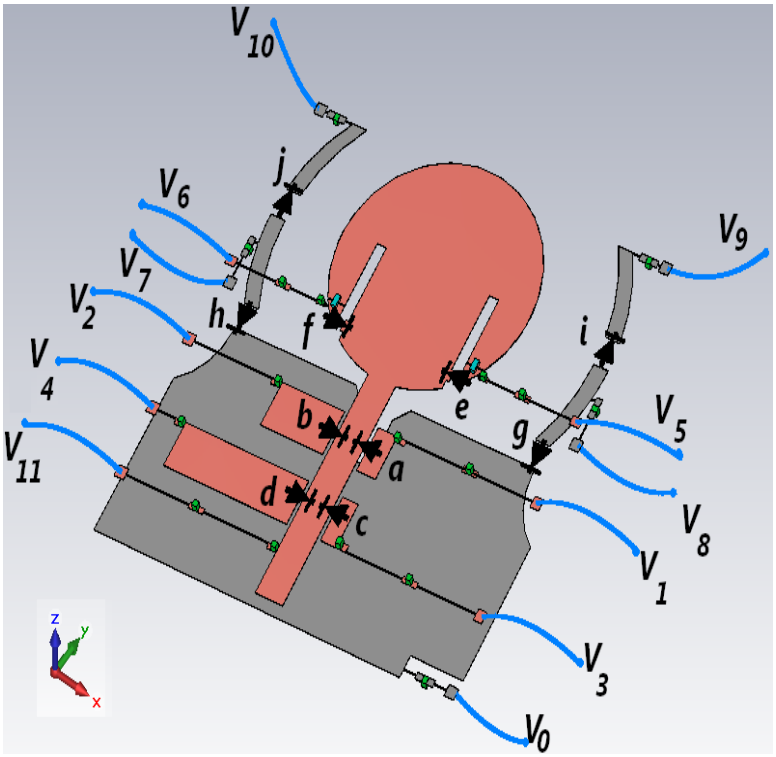

Figure 6.3: **3-D Geometry of the proposed antenna showing the p-i-n diodes labellings and orientations when mounted on the antenna and the labelling of the bias wires coming from the power supply and soldered on the antenna PCB.**

(e, f) control the shorting of the embedded slits. When switches (e, f) are shorted, the antenna is linearly polarised. If one switch is ON and the other is OFF, circular polarisation is achieved. The sense of the circular polarisation (RHCP or LHCP) depends on the locations of the shorted slit (i.e., being in the left or right corner of the circular radiator). On the back side of the substrate, a partial rectangular ground plane and two parasitic microstrip arc-shaped stubs are printed. Also, by properly insetting a small slit in the middle of the upper edge of the ground plane and by circularly truncating the upper right and left corners of the ground plane, optimum impedance matching across the whole operating band in different operation modes can be obtained. Four switches (g, h, i, j) are placed on the arc-

shaped stubs (E, F). Switches (g, h) can connect/disconnect the stubs to the partial ground plane, while switches (i, j) will control the length of the stubs. The detailed dimensions of the antenna are summarised in Table 6.1.

The RF switching mechanism used in this study is realised using beam lead p-i-n diodes (HPND-4005) [90]. The size of this diode is very small ($640\ \mu m \times 220\ \mu m$) and to mount it on the PCB, we have used conductive epoxy (e.g., silver paste so as not to dissolve the gold from the diode leads) and hot air. Not only have these switches posses very low capacitances ($C = 0.017\ pF$) in the OFF state and low resistances ($R = 4.7\ \Omega$) in the ON state, but they also have low package parasitics which will have minimum adverse effects on the isolation and insertion loss of the switches.

The CST microwave studio package [69] was used for numerically analysing the structure proposed here, and the diodes are represented in simulations by their equivalent circuits as shown before in Chapter 4. The dc lines are physically realised by very thin microstrip lines ($0.1\ mm$ in width). Inductors (0402HPH–68N) ($L = 68\ nH$) from coilcraft served as RF chokes [103]. For more effective RF attenuation, two chokes are used for the long dc bias lines. For the dc biasing of switches (e, f), two surface mounted RF capacitors (RFCS-04022700BJTT1)($C = 27\ pF$) from Vishay [124] are used as dc blocking capacitors. Table 6.2 summarises all the operation modes of the antenna. It should be noted that in Table 6.2, the UWB mode in the frequency reconfiguration is the same as Mode–I in the pattern reconfiguration, which is also the LP mode in the polarisation reconfiguration.

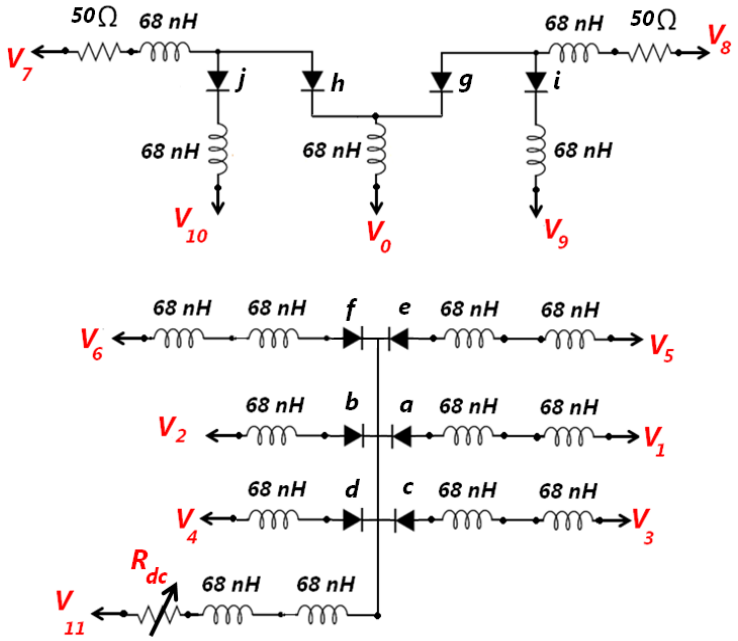

Figure 6.4: **Circuit diagram of the dc-bias circuit of the proposed reconfigurable antenna. Current limiting resistances are external to the antenna and they are in series with the wires (V_7, V_8, V_{11}) coming from the dc power supply.**

6.3 DC Biasing and Power Consumption

Figure 6.3 shows the polarity of the p-i-n diodes incorporated in the antenna structure and Figure 6.4 depicts the full dc biaisng circuit. A dc voltage drop around $+0.9\ V$ between the anode and the cathode will turn on the diode and with a bias current of 20 mA, the insertion loss of the diode will be around 0.4 dB. A voltage drop of 0 V is sufficient to turn the diode off. The dc bias lines are connected to 1 $mm \times 1\ mm$ square pads on which 12 wires (labelled: $V_0 - V_{11}$) are soldered. These wires are connected to an external dc power supply. Table 6.3 shows the dc bias configuration for the control voltages of the operation modes of the antenna and also the total dc power consumption of the antenna at each operating mode.

	Frequency Reconfiguration		Pattern Reconfiguration			Polarisation Reconfiguration		
Switch	**UWB**	**Band I**	**Mode I**	**Mode II**	**Mode III**	**LP**	**LHCP**	**RHCP**
a	OFF	ON	OFF	OFF	OFF	OFF	OFF	OFF
b	OFF	ON	OFF	OFF	OFF	OFF	OFF	OFF
c	OFF	ON	OFF	OFF	OFF	OFF	OFF	OFF
d	OFF	ON	OFF	OFF	OFF	OFF	OFF	OFF
e	ON	ON	ON	ON	ON	ON	OFF	ON
f	ON	ON	ON	ON	ON	ON	ON	OFF
g	OFF	OFF	OFF	ON	OFF	OFF	OFF	OFF
h	OFF	OFF	OFF	OFF	ON	OFF	OFF	OFF
i	OFF	OFF	OFF	ON	OFF	OFF	OFF	OFF
j	OFF	OFF	OFF	OFF	ON	OFF	OFF	OFF

Table 6.2: **Switches states for different operation modes of the proposed reconfigurable antenna. In each operating mode, all of the 10 switches ($a - j$) have to be set to their corresponding state as in the table columns.**

	Frequency Reconfiguration		Pattern Reconfiguration			Polarisation Reconfiguration		
Voltage	**UWB**	**Band I**	**Mode I**	**Mode II**	**Mode III**	**LP**	**LHCP**	**RHCP**
V_0	$0V$	$0V$	$0V$	$0V$	$0V$	$0V$	$0V$	$0V$
V_1	$0V$	$+3V$	$0V$	$0V$	$0V$	$0V$	$0V$	$0V$
V_2	$0V$	$+3V$	$0V$	$0V$	$0V$	$0V$	$0V$	$0V$
V_3	$0V$	$+3V$	$0V$	$0V$	$0V$	$0V$	$0V$	$0V$
V_4	$0V$	$+3V$	$0V$	$0V$	$0V$	$0V$	$0V$	$0V$
V_5	$+3V$	$+3V$	$+3V$	$+3V$	$+3V$	$+3V$	$0V$	$+3V$
V_6	$+3V$	$+3V$	$+3V$	$+3V$	$+3V$	$+3V$	$+3V$	$0V$
V_7	$0V$	$0V$	$0V$	$0V$	$+3V$	$0V$	$0V$	$0V$
V_8	$0V$	$0V$	$0V$	$+3V$	$0V$	$0V$	$0V$	$0V$
V_9	$0V$	$0V$	$0V$	$0V$	$0V$	$0V$	$0V$	$0V$
V_{10}	$0V$	$0V$	$0V$	$0V$	$0V$	$0V$	$0V$	$0V$
V_{11}	$0V$	$0V$	$0V$	$0V$	$0V$	$0V$	$0V$	$0V$
R_{dc}	50Ω	20Ω	50Ω	50Ω	50Ω	50Ω	100Ω	100Ω
P	$0.12W$	$0.36W$	$0.12W$	$0.24W$	$0.24W$	$0.12W$	$0.06W$	$0.06W$

Table 6.3: **DC biasing and power consumption for different operation modes of the proposed reconfigurable antenna. In each operating mode, all of the 12 voltages ($V_0 - V_{11}$) have to be set to their corresponding values as in the table columns.**

An example of how to estimate the power consumption for one case (e.g., pattern-reconfigurable-Mode III) is shown here. In Mode III , a 50 Ω current limiting axial-lead resistors should be connected in series between the power supply (+3 V) and the dc wire V_7. Hence, the bias current will be (3 V − 0.9 V)/(50 $\Omega + \frac{4.7\ \Omega}{2}$) $\approx$ 40 mA, where 0.9 V is approximately the voltage drop on the ON p-i-n diodes (h, j) and $\frac{4.7\ \Omega}{2}$ is their equivalent parallel resistance. It should be noted that from an RF point of view, the ON switches (h, j) are connected in their correspondent stub in series, albeit they are actually in parallel from a dc biasing circuitry view. The 40 mA current will be divided equally between the ON switches(h, j). Moreover, in Mode–III, switches (e, f) should be ON by applying +3 V at V_5, V_6 and the value of the variable resistance R_{dc} should be 50 Ω to limit the bias current driving e or f at $\approx$ 20 mA. In this prototype, we have used axial-lead external resistors connected in series between the power supply and the antenna. It should be noted that the values of R_{dc} where chosen as in Table 6.3 to fix the forward bias current of each ON diode at $\approx$ 20 mA. In industrial realisation designs, these resistances should be replaced with a bank of resistors or a low-cost digital potentiometer chip, interfaced to a μ-controller, acting as the "brain"of the reconfigurable antenna. In Mode–III, as there are four ON diodes, the total power consumption P is 4 $\times$ 20 $mA \times 3\ V \approx 0.24\ W$. From Table 6.3, we can notice that the antenna consumes the largest dc power when it is operating in Band-I as there are six ON diodes, while the minimum power consumption occurs in the RHCP or LHCP modes as there is only a single ON diode.

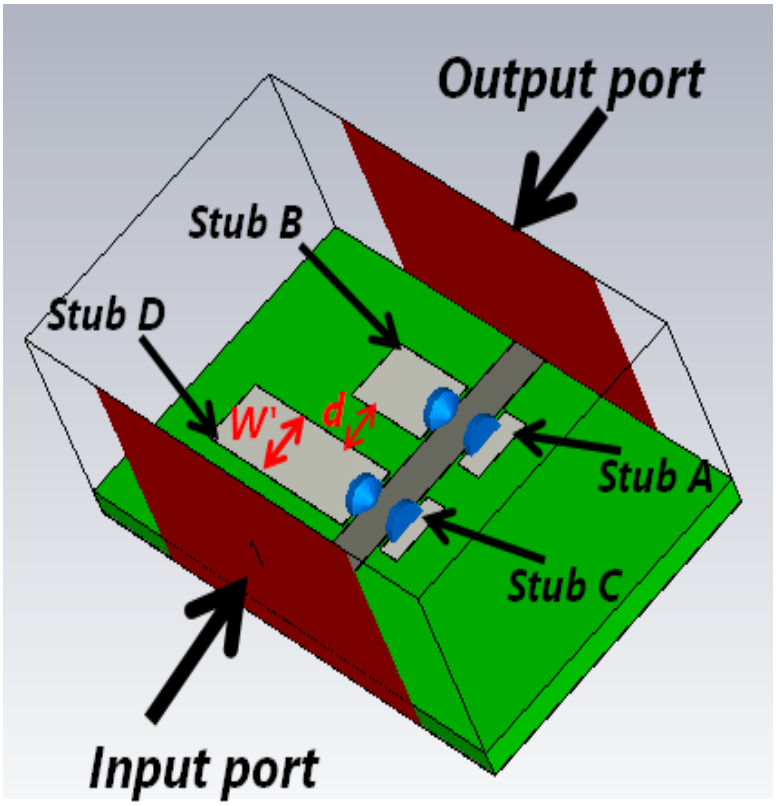

Figure 6.5: **A BPF filter using four quarter wavelength stub resonators connected to a microstrip line. The stub lengths are as illustrated in Figure 6.1 and Table 6.1. The width of each stub is W'= 4 mm and the vertical distances between stubs d=2.5 mm.**

6.4 Principles of Operation and Design Guidelines

6.4.1 Frequency Reconfiguration

To better understand the proposed frequency reconfiguration mechanism, only the antenna microstrip feed line and the stub resonators were simulated as a planar filter as shown in Figure 6.5. Frequency reconfiguration is achieved by using multiple stubs connected to the main feedline, each stub acts as a $\frac{\lambda_g}{4}$ resonator, where λ_g is the guided wavelength. Each stub will act as a Band Stop Filter (BSF) around its resonance frequency. A Band-

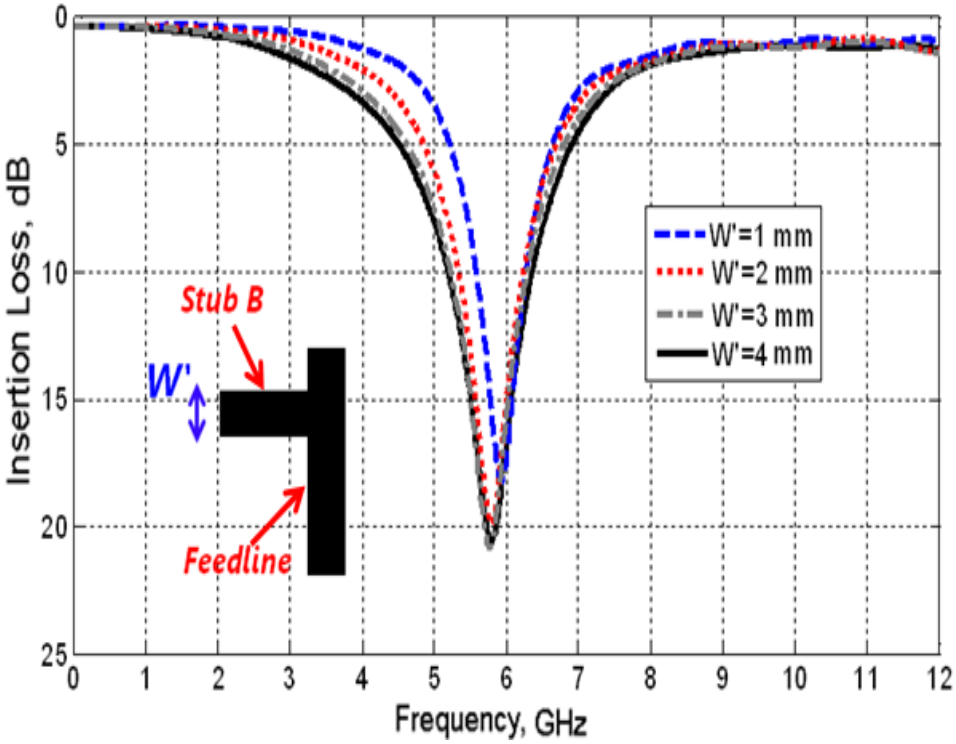

Figure 6.6: **Effects of the stub width (W') on the quality factor (Q) of stub B.**

Pass Filter (BPF) filter can be achieved by combining BSF filters operating in the FCC ultra-wideband spectrum by forcing transmission zeros on both sides of the pass-band of the BPF. Low Q stubs and hence more rejection bandwidth are preferable here to reduce the number of resonators used in the BPF. Figure 6.6 illustrates the insertion loss of the BSF when the width of stub B varies from 1 mm to 4 mm. To decrease the quality factor (Q) of each stub and hence increase the bandwidth of rejection, the stub resonator width was chosen to be 4 mm.

Figure 6.7 depicts the Insertion Loss (IL) when stub B is connected to the main feedline in three different scenarios: 1) the stub is directly connected to the feedline, 2) the stub is connected to the feedline using an ideal switch

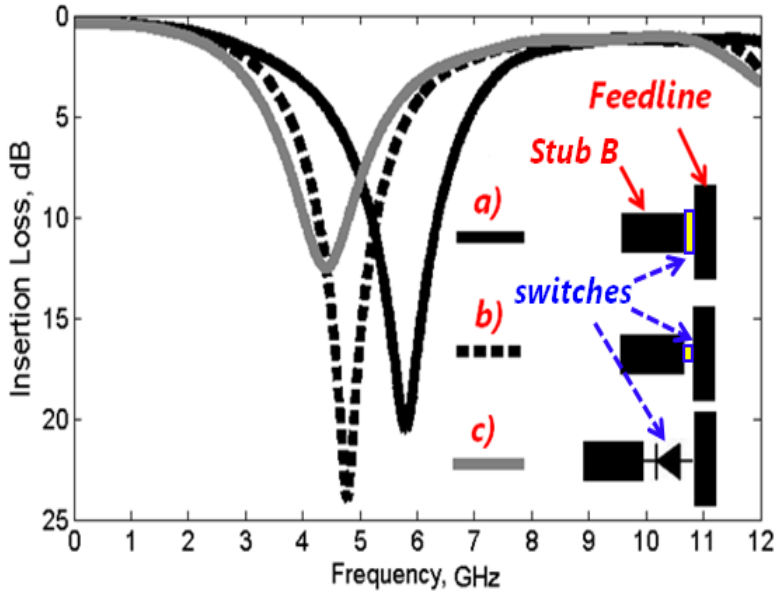

Figure 6.7: **Simulated insertion loss of the filter when only stub resonator, B, is connected to the main microstrip feedline using a switch, while the switch is mimicked in simulations as: a) a strip of copper metallisation with a width equals to the stub width, b) strip of copper metallisation when the width is equal to the real switch width (0.2 mm), and c) 4.7 Ω resistance in series with a 0.15 nH inductor (i.e., the equivalent circuit of the ON p-i-n diode switch).**

with size of (0.35 $mm \times$ 0.2mm), and 3) using the electrical equivalent circuit of the ON state p-i-n diode. It was observed that the resonance of the second scenario is shifted down in frequency compared to the first scenario, the reason for that is due to the width of the switch being less than the stub width and hence the the stub will act as a (Stepped Impedance Resonator) SIR [125], and a frequency shift will occur due to the capacitance introduced by the microstrip discontinuity (e.g., step in width) between the feedline and the resonator. It was also noticed in the third scenario that the package inductance found in the equivalent circuit of the switch will again shift down the resonance of the stub.

Table 6.4 shows the simulated resonances of stubs A, B, C, D when using

Stub	Length	f_0	$3f_0$
A	2 mm	7.7 GHz	–
B	6.6 mm	4.4 GHz	–
C	1.6 mm	8.2 GHz	–
D	13.1 mm	2.5 GHz	7.3 GHz

Table 6.4: **Simulated BSF operation for the four stubs in the proposed design**

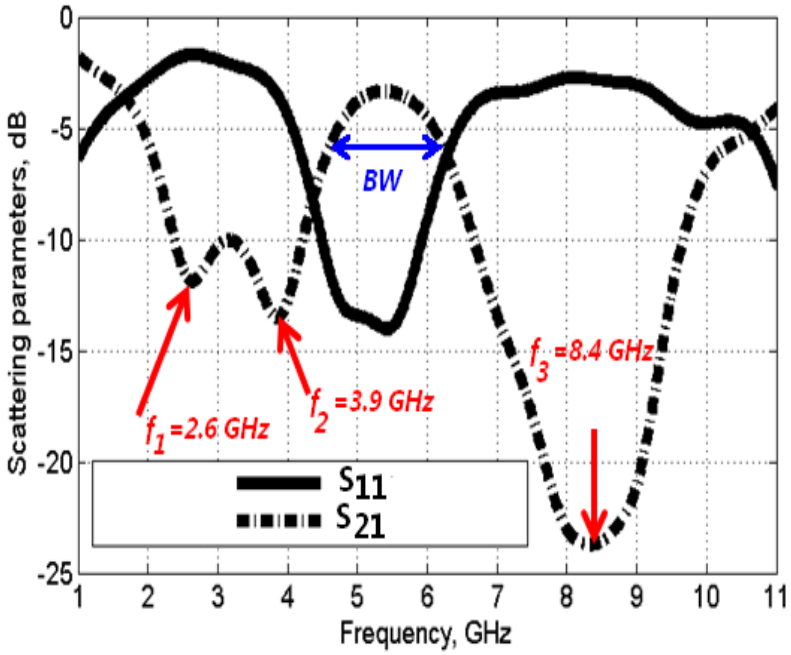

Figure 6.8: **Simulated return and insertion losses of the proposed BPF in Figure 6.5. All p-i-n diodes are switched ON.**

the equivalent circuit of the diode in the ON state. It should be noted here that the resonance value are obtained for each stub while the other three stubs are not connected to the feedline. From Table 6.4, we can also notice that these quarter wavelength stubs are resonating on their fundamental frequency f_0 and also on odd multiples of f_0. The higher order resonances of stubs A, B and C are outside the FCC ultra-wideband and therefore they are not shown in Table 6.4. Having four stubs allows to have 15 different filter combinations (i.e., $2^4 - 1$, as there is one case in which all stubs are

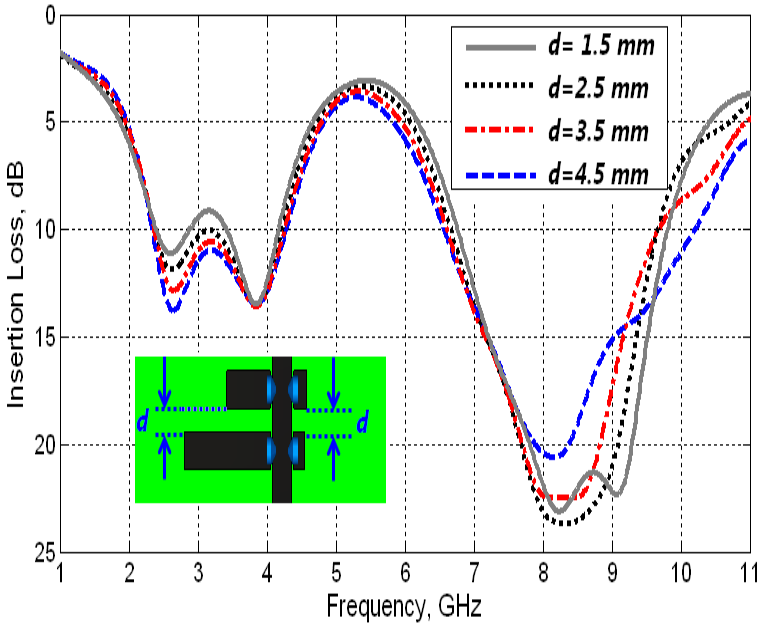

Figure 6.9: **Effects of the vertical distance between the stubs (d) on insertion loss of the proposed BPF.**

OFF and thus no filter will be connected to the ultra-wideband antenna). However, in this section, the filter case formed by combining all of the four stubs is investigated.

Figure 6.8 shows the simulated return loss and insertion loss of the BPF proposed in Figure 6.5, in which the stub resonators A, B, C, D are all connected to the main feedline through p-i-n diodes. Frequency (f_1) is attributed to the first order resonance of stub D. Frequency (f_2) is attributed to the resonance of stub B. The slight differences between these values and the resonance values found in Table 6.4 are due to the mutual coupling effects among the stubs when they are all connected to the main feedline. The resonance f_3 occurs because of the combined effect of the closely spaced resonances of stubs A, C and the second order resonance of stub D. The simulated half power bandwidth (BW) of the filter is 1.75 GHz from $f_L \approx$ 4.55 GHz to $f_H \approx 6.3$ GHz. The minimum simulated insertion loss in the

3-dB BW is $IL \approx 3.3$ dB. This value is mainly attributed to the losses in the ohmic resistances of the four p-i-n diodes switches ≈(2 dB) and the FR–4 substrate losses ≈(1 dB).

Since the insertion loss (IL) of the filter, which would be later integrated in the ultra-wideband antenna, will adversely affect the Noise Figure (NF) [126], it would be essential to reduce the insertion loss of the filter to reduce the overall cascaded NF of the system. This can be achieved (in future designs) by using low loss substrate material. Also, by dc-biasing the diodes with higher currents, the ON resistances of the p-i-n diodes can be reduced and the switches losses are minimised. Finally the effect of the vertical distance variations between the stubs of the BPF is studied, the insertion loss of the BPF is slightly affected when d is varied from 1.5 mm to 4.5 mm as shown in Figure 6.9 and in the proposed BPF design, an optimal $d = 2.5$ mm was chosen.

The following simple guidelines are presented to design frequency reconfigurable antennas using resonators connected to the feedlines of microstrip-fed ultra-wideband monopole antennas:

1) Pick the frequency at which the antenna should have notched operation, the electrical length of the stub should be $\approx \frac{\lambda_g}{4}$.

2) Tune the length of the stub to account for the package inductance of the switch.

3) Retune the stub length to account for the effect of the bias lines.

4) Stubs of different lengths can be connected to the main feedline in parallel to notch multiple frequency bands, retuning the length of the stubs is needed to account for the mutual coupling between the stubs.

5) The superposition effect of the stubs resonators (e.g., multiple BSFs at different bands) can also be combined to produce a Band Pass Filter (BPF) at a specific frequency band.

6.4.2 Pattern Reconfiguration

Stubs E and F each have two p-i-n diodes switches, connected back to back. When the stub length is equal to $\frac{\lambda_{eff}}{2}$, where λ_{eff} is the effective wavelength calculated as described in [104], the stub will resonate at frequency $\approx fo$. In our proposed prototype, the stub length was chosen to be 21 mm which is approximately $\frac{\lambda_{eff}}{2}$ at $fo = 4.2$ GHz. When switches (j, h) are ON and (i, g) are OFF, the antenna is operating in Mode–III and the whole length of stub (F) will be connected to the ground plane and will act as a reflector that will direct the radiation towards the $(+x)$ direction. This is due to the surface currents on the stub and the nearby disk edge being in opposite directions and their phase relationship results in concentrating radiation away from the reflector, similar to the principle of operation of a Yagi-Uda antenna. When both switches (i, g) are ON, and (j, h) are OFF, the antenna will be operating in Mode–II and stub (E) will act as a reflector that will direct the radiation towards the (-x) direction. When (i, g, j, h) are OFF, the stubs are short enough to be almost transparent to the incident or radiated waves at fo and the conventional ultra-wideband operation is achieved.

To better illustrate the concept of pattern reconfiguration, the surface current distribution was studied. The simulated average surface current distributions at f_o when the antenna is working in the omni-directional and in the directional mode are illustrated in Figure 6.10(a) and 6.10(b), respectively. It can be noticed from Figure 6.10(a) that at the end of the feeding

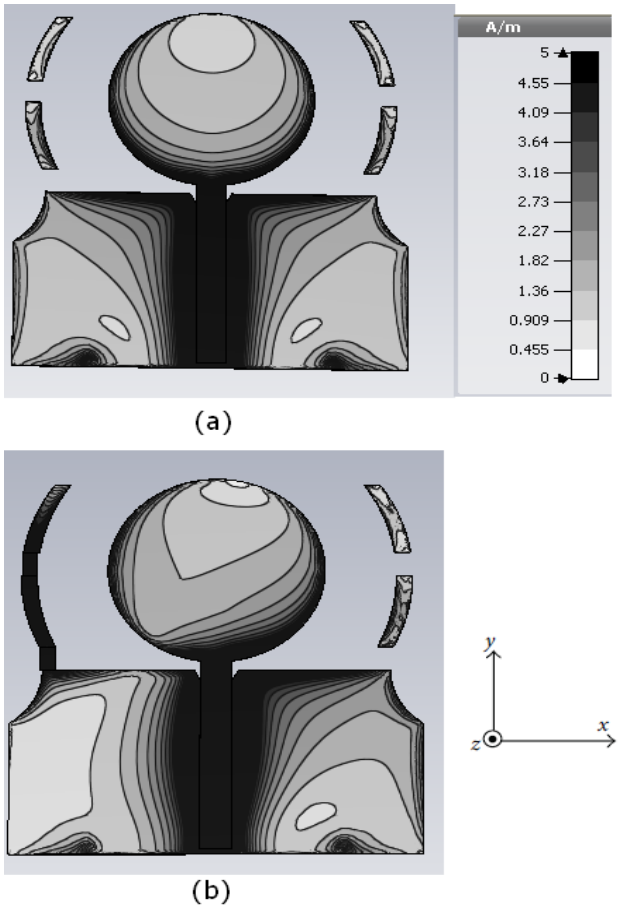

Figure 6.10: **Contour plots of simulated average surface current distributions at f_o , when the antenna is operating in: a) Omni-directional-mode, b) Directional-mode.**

line, the current splits, on the disk and on the upper edge of the ground plane, into two equal streams and the surface current distribution is even and symmetrical about the y-axis. The current is primarily concentrated around the periphery of the disk and the upper edge of the ground plane, while there is little current within the interior of the disk and almost a null at the the top edge of the disk. Additionally, the antenna can be viewed as a planar slot bow-tie antenna, as both the circular disk and the upper edge of the finite ground plane form two slots that equally contribute to

the total radiation. Furthermore, it can be noticed that the two splitted arc-shaped stubs are non-resonating and thus transparent to the radiated or intercepted electromagnetic waves. The symmetry of the surface currents will lead to omni-directional $xz-$plane (H-plane) patterns similar to those obtained in [68].

In Figure 6.10(b), when one of the stubs is activated by turning on the corresponding switches, the surface current distribution on the disk and on the ground plane are no longer symmetrical about the the y-axis. The currents on the activated stub and on the nearby disk edge are in opposite directions and their phase relationship results in reducing radiation behind the stub which is acting like a reflector. Moreover, if we look at the antenna as a two slots bow-tie antenna, we can see that the slot facing the activated stub has much less current than the other slot facing the non-activated stub. From the two slots, there is an unequal contribution to the total radiation and directional patterns are produced in the H-plane.

We are proposing the following simple guidelines to design a pattern reconfigurable antenna by using stubs connected to the partial ground plane of a microstrip or coplanar-waveguide (CPW) planar ultra wideband monopoles:

1) Pick the frequency f_o at which the antenna is functioning as a pattern reconfigurable antenna. The electrical length of the reflector stub should be $\frac{\lambda_{eff}}{2}$ at f_o.

2) The stub location should be located at least $\frac{\lambda_{eff}}{4}$ from the ultra-wideband main radiator (the circular patch in this study).

3) A switch should be used to connect the reflector stub to the ground to operate into the directional mode.

4) In the omni-directional mode, the stub should not be connected to

ground. Moreover, it would be essential to kill the resonance of the stub by turning off an extra switch located in the middle of stub, so the stub will be short enough to be almost transparent to incident or transmitted electromagnetic waves at f_o.

5) An additional reflector stub can be incorporated on the other side of the main radiator, to obtain the mirror image of the directional patterns in the H-plane.

6.4.3 Polarisation Reconfiguration

To excite circular polarisation radiation, two conditions have to be met: Firstly, the amplitudes of two near-degenerated electric field vectors (E_V, E_H) must be equal; secondly, the phase difference (PD) between the two electric field vectors should be $\pm 90^\circ$.

It is very difficult for a conventional monopole antenna to excite CP. This can be illustrated in Figures 6.11(a) and 6.11(c) which show the average x–directed and y–directed surface current distributions on the circular patch of the ultra-wideband monopole, respectively. As there is no slit, the monopole is symmetrical about the y–axis and the x-directed current distributions are 180° out of phase. Therefore, the radiation in the far field in the horizontal direction is weak because the horizontal current components tend to cancel each other and there will be a dominant strong vertical current component leading to a vertical linear polarisation (LP) radiation. Practically, due to some weak horizontal component, elliptical polarisation (EP) is usually generated by planar ultra-wideband monopole antennas.

To achieve CP radiation, introducing asymmetry in the circular patch tends to increase the horizontal current component. This is the same concept used in the previous chapter when asymmetry was introduced in the

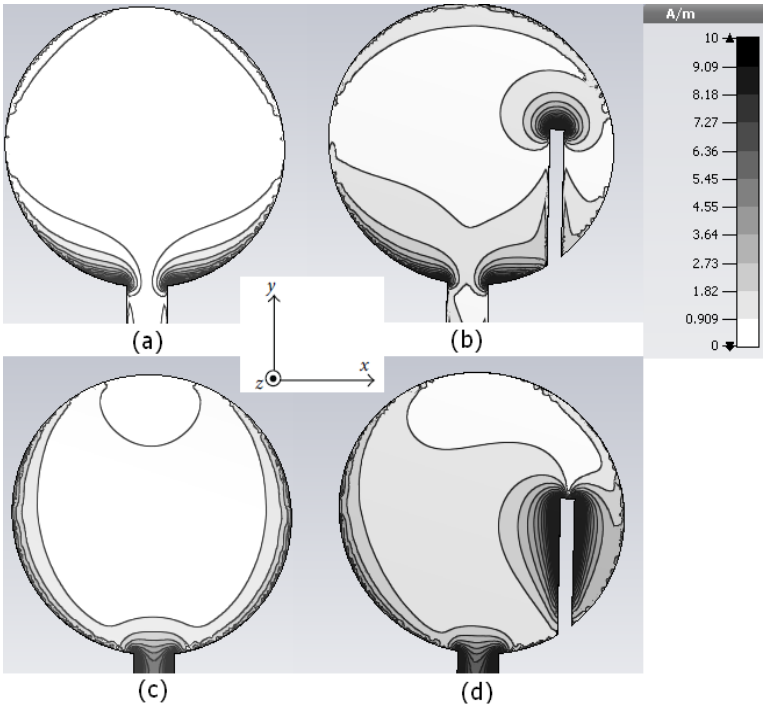

Figure 6.11: **Contour plots of simulated average surface current excited at f_o: a) x–directed current with no slit in the radiator, b) x–directed current with a slit in the radiator, c) y–directed current with no slit in the radiator, d)y–directed current with a slit in the radiator**

square patch of the polarisation reconfigurable ultra-wideband antenna. Figure 6.11(b) show the average x–directed surface current distributions on the circular patch of the ultra-wideband monopole with a slit in its right corner, while Figure 6.11(d) shows the y–directed surface current on the radiator. The length of the slit is tuned to perturb the surface current by lengthening the current path in the x–direction, thereby exciting two near degenerate orthogonal modes with the same amplitude. It was found that when the slit length is equal to $\approx \frac{\lambda_{eff}}{4}$ at f_o, the slit will resonate at frequency $\approx fo$ and approximately -90° phase shift occurs between the current components (e.g., vertical component lags the horizontal one), if the slit is at the right bottom corner of the circular patch and LHCP is

achieved. On the other hand, if the slit is located at the left bottom corner of the circular patch, 90° phase shift occurs (e.g., vertical component leads the horizontal one) and RHCP is achieved. Since the two main conditions for CP radiation are met, the antenna can be successfully reconfigured to work as a CP antenna at fo. The location of the slit was also studied in parametric simulations to observe the effect on the axial ratio value in the broadside direction. It was found that when the slit is moved towards the centre of the disk while keeping the slit length constant, fo, at which the axial ratio is less than 3 dB, will shift up. fo will also shift down if the slit is moved away from the centre of the disk. In the proposed design, the slit length is chosen to be 9.5 mm, which is $\approx \frac{\lambda_{eff}}{4}$ at $f_o = 4.8$ GHz and the slit is located 5.5 mm from the centre of the disk.

The author proposes the following simple guidelines to design an LP–RHCP–LHCP polarisation reconfigurable antenna by etching slits in the main radiator of ultra-wideband monopole antennas:

1) Pick the frequency (f_o) at which the antenna should have CP operation. The electrical length of the etched slit should be $\approx \frac{\lambda_{eff}}{4}$.

2) For RHCP radiation in the broadside, the slit should be located on the left bottom corner of the radiator and for LHCP the slit should be on the opposite corner.

3) A switch should be used to short the slit so that the antenna can operate into the original LP mode.

4) Retune the slit length and location to account for the effects of the switch equivalent circuit and the bias lines, until the axial-ratio (AR) at fo is less than 3 dB.

5) Two switches can also be incorporated in one slit to control the length of the slit and hence obtain CP radiation at two different frequency bands (e.g., dual band CP operation).

6.5 Proposed Antenna Performance Analysis

6.5.1 Frequency Reconfiguration

The return loss measurements are performed using Agilent N5230C PNA-L microwave network analyser. A dc-block SMA connector [105] was connected to the coaxial measurement cable and the calibration was done with an Agilent-N4696B ECal module. Figure 6.12 shows the simulated and measured return losses when the proposed antenna is operating in different modes. The measured bandwidths with return loss better than 9.5 dB, are 2.6–11 GHz, 4.39–5.85 GHz for the ultra-wideband mode and Band–1 operation, respectively.

The differences between the simulated and measured return loss results are attributed to the fabrication tolerances and the approximate boundary conditions in the computational domain. Furthermore, the non-exact modelling of the biasing network including the external dc wires coming from power supply, the parasitic effects of the p-i-n diodes and the difficulties in numerically modelling all relevant aspects of the real p-i-n diodes characteristics introduce slight uncertainties in the observed results.

The radiation patterns were measured in an anechoic chamber at Queen Mary University of London. The dc power supply was mounted under the turn table and was covered by microwave absorbers. It was noted that covering the antenna's SMA connector with a piece of absorber would reduce the ripples in the radiation patterns. Although the bias lines are RF choked,

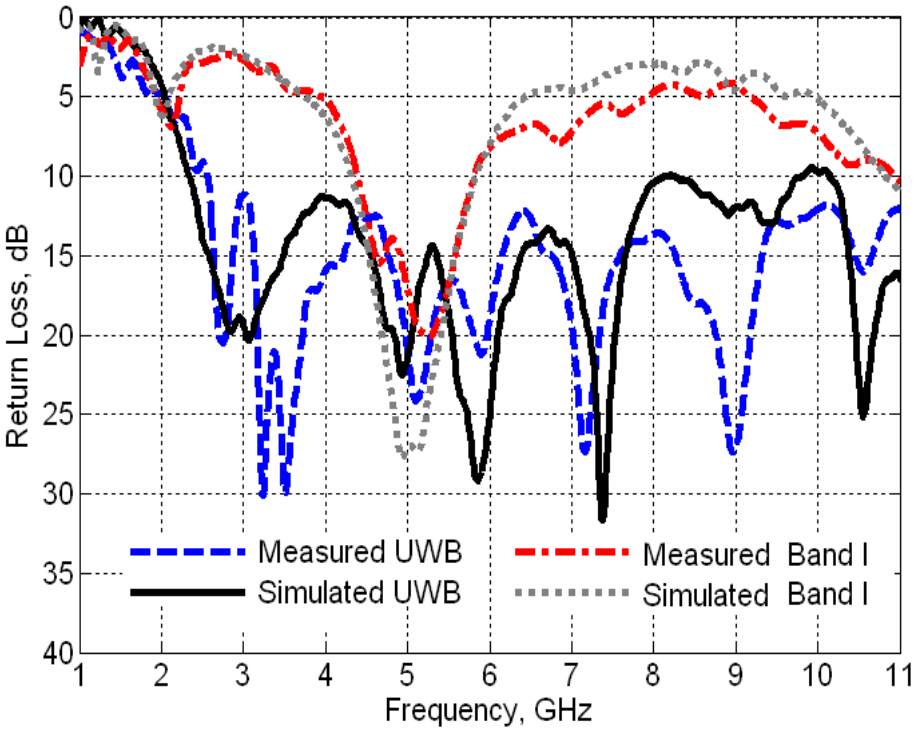

Figure 6.12: **Simulated and measured return loss curves when the proposed antenna is operating in the ultra-wideband mode and in Band–I.**

they are also shielded with aluminium foil to prevent them from picking up noise and to reduce their spurious radiation. The simulated and measured radiation patterns in the xz (H–plane) and yz (E–Plane) planes at 3, 5 and 7 GHz are illustrated in Figure 6.13 and they are typical for ultra-wideband monopoles as in [68, 104]. The realised gain was measured in the anechoic chamber using the Gain-Transfer method in the far field [71]. The measured realised peak gains in the xz plane at 3, 5 and 7 GHz are 1.0, 1.4 and 1.5 dBi respectively.

The numerically calculated total efficiency when the antenna is operating in the ultra-wideband mode is $\eta_t > 65\%$ for the whole operating frequency range. The simulated and measured radiation patterns when the antenna

is reconfigured at Band–I at 5 GHz are also shown in Figure 6.14. The measured peak realised gain in the xz plane at 5 GHz in Band-I operation is -0.6 dBi and the total numerically calculated efficiency is $\eta_t = 55\%$. The decrease in the efficiency and gain is mainly attributed to the losses of six ON p-i-n diodes and their associated bias network.

6.5.2 Pattern Reconfiguration

Figure 6.15 shows the simulated and measured return losses when the proposed antenna is operating in Mode–II and Mode–III. It should be noted that Mode–I (in Table 6.2 and 6.3) is an alias for the ultra-wideband mode and thus not shown in Figure 6.15. The simulated return loss of Mode–II and Mode–III are identical since the antenna is almost geometrically symmetrical with respect to the input microstrip feedline. However, the measured results are slightly different due to the tolerances in the real diodes and the lumped components. In addition, the soldering of the diodes and the lumped components can not be exactly identical, therefore this could have affected the symmetrical properties of the prototype.

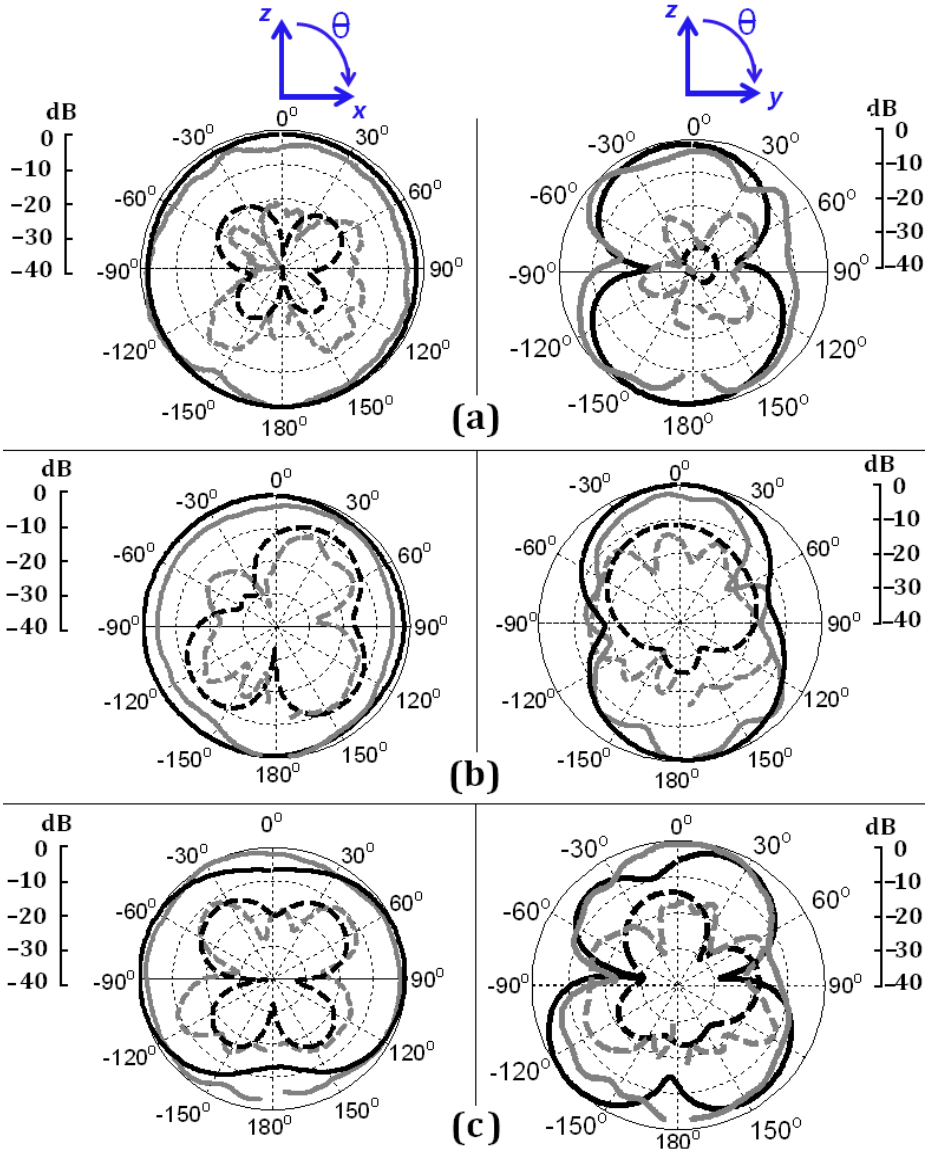

Figure 6.13: **Simulated (black curves) and measured (grey curves) normalised radiation patterns in the H-plane (xz) and E-plane (yz) when the antenna is operating in the ultra-wideband mode at: a) 3 GHz, b) 5 GHz, and c) 7 GHz. Solid lines are for the (co-polar) component and dashed lines represent the (cross-polar) component.**

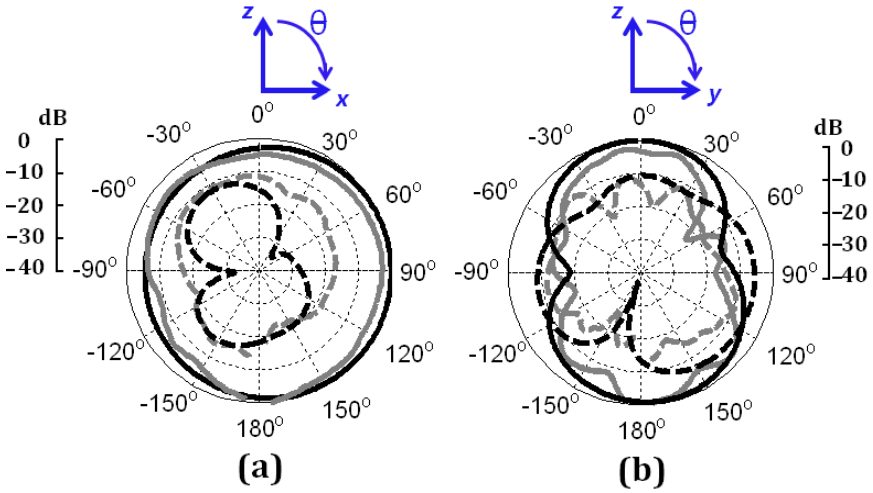

Figure 6.14: **Simulated (black curves) and measured (grey curves) normalised radiation patterns when the antenna is operating in Band-I at 5 GHz: a) H-plane (xz), b) E-plane (yz). Solid lines are for the (co-polar) component and dashed lines represent the (cross-polar) component.**

The measured bandwidths with return loss better than 9.5 dB, are 2.03–11 GHz, 1.96–11 GHz for Mode–II and Mode–III, respectively. The bandwidth from 3 to 5.5 GHz is considered to be the frequency range over which the antenna radiation patterns are reconfigured; this is because at these frequencies in Mode–II and Mode–III, the measured gain ratio between the $+x$ and the $-x$ directions is better than 8 dB compared to the omni-directional Mode–I.

The simulated and measured normalised radiation patterns in the H-plane (xz-plane), when the antenna is operating in Mode–II and Mode–III are depicted in Figure 6.16 for different frequencies. Mode–I radiation patterns are the same as in Figure 6.13 and in Mode–II and Mode–III, the H–plane beams are concentrated along the $-x$ and $+x$ direction, respectively. For the sake of brevity, the normalised co-polar E-plane patterns (yz-plane) are not shown here as they do not significantly change when the

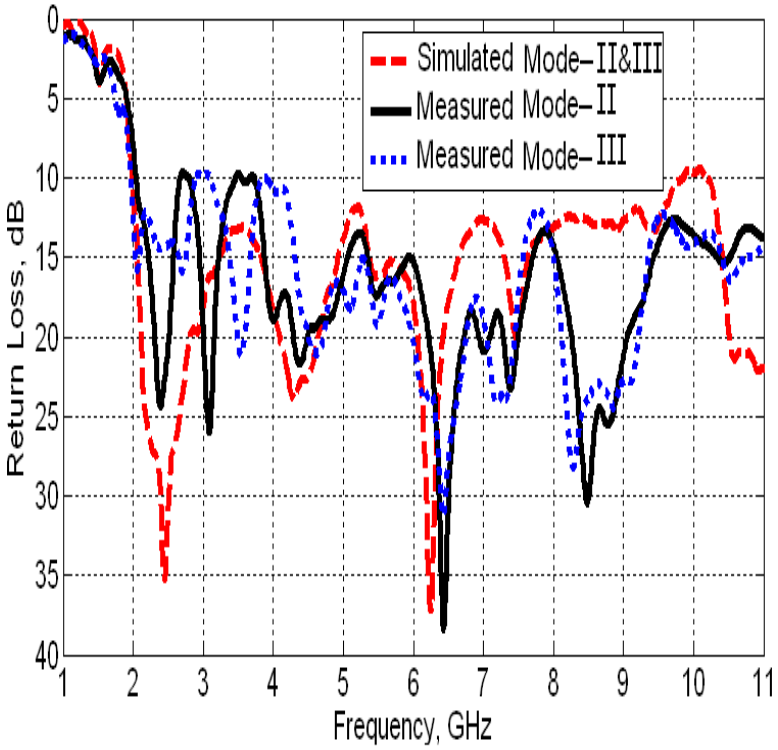

Figure 6.15: **Simulated and measured return loss curves when the proposed antenna is operating in Mode–II and Mode–III.**

antenna switches operation between Mode–I, Mode–II and Mode–III.

When the antenna is working in Mode–II, the peak realised gains in the xz-plane at 3 GHz and 5 GHz are 0.5 dBi, 2 dBi, respectively. In Mode–III, the peak realised gains in the xz-plane at 3 GHz and 5 GHz are 0.4 dBi, 1.8 dBi, respectively. The F/B ratios (e.g., gain ratios between the $+x$ and the $-x$ directions) in Mode–II and Mode–III are 10 dB at 3 GHz and 12 dB at 5 GHz.

6.5.3 Polarisation Reconfiguration

The simulated and measured return losses when the proposed antenna is operating in the LHCP and RHCP modes are shown in Figure 6.17. It

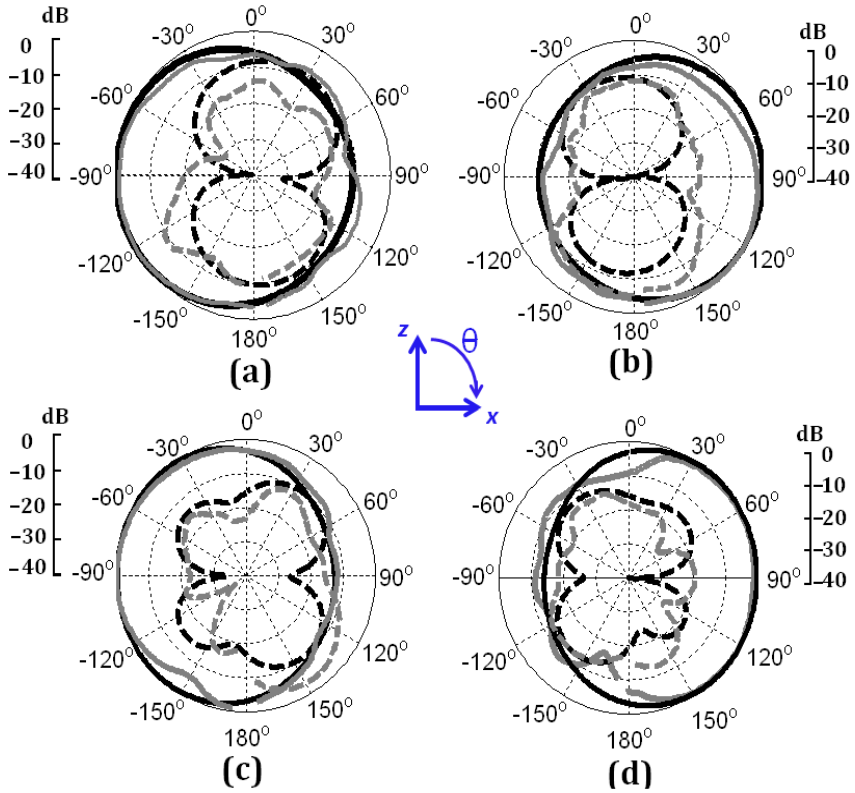

Figure 6.16: **Simulated (black curves) and measured (grey curves) normalised radiation patterns in the H-plane when the antenna is operating in: a) Mode–II at 3 GHz, b) Mode–III at 3 Ghz, c) Mode–II at 5 GHz and d) Mode–III at 5 GHz. Solid lines are for the (co-polar) component and dashed lines represent the (cross-polar) component.**

should be noted that LP mode (in Table 6.2 and 6.3) is an alias for the ultra-wideband mode and thus not shown in Figure 6.17. The simulated return loss of LHCP and RHCP are identical since the antenna is almost geometrically symmetrical with respect to the input microstrip feedline. The measured bandwidth with return loss better than 9.5 dB is 2.2–11 GHz for both the LHCP mode and RHCP modes.

The simulated and measured radiation patterns of the antenna when it is operating in the LHCP and RHCP modes at 4.8 GHz are depicted in Figure 6.18. The measured patterns follow the simulated ones and it can be

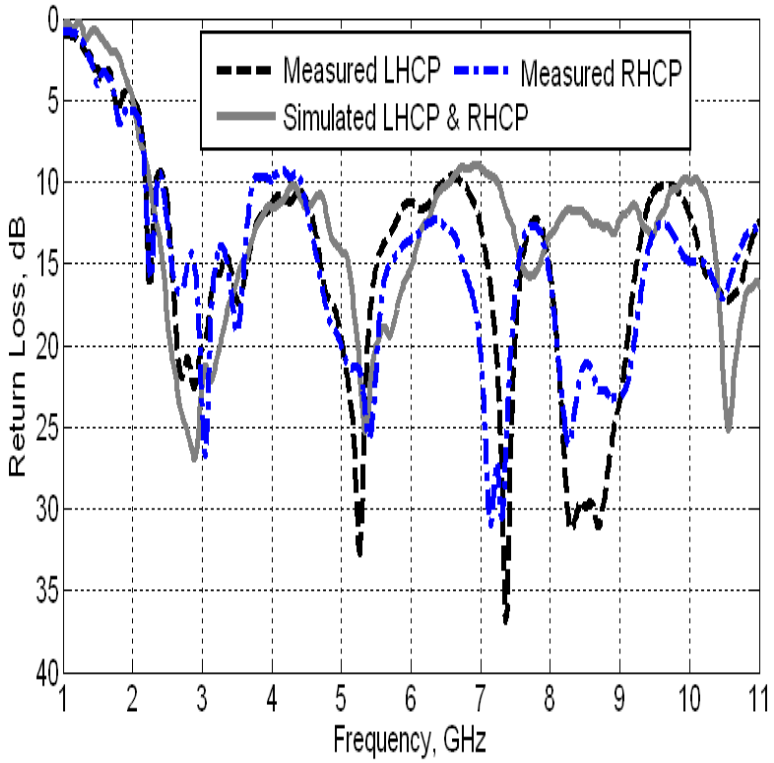

Figure 6.17: **Simulated and measured return loss curves when the proposed antenna is operating in the LHCP and RHCP modes.**

noticed that the antenna radiates RHCP or LHCP in the upper half-plane ($z > 0$) direction and the opposite sense in the lower half-plane ($z < 0$) direction, a known trait of CP planar monopoles as explained before in the previous chapter. The measured realised broadside gains at 4.8 GHz are 1.8 dBic and 1.7 dBic in the LHCP and RHCP sates, respectively.

Figure 6.19 depicts the measured axial ratio (AR) at broadside direction (e.g., $(\theta, \phi) = (0°, 0°)$), when the proposed antenna is operating in the LHCP, RHCP and LP states. To measure the axial ratio of the proposed antenna, the received phase and amplitude are measured across the two principle planes with a diagonal dual linear polarised transmitting horn antenna connected to an Agilent 8720ES VNA. After obtaining two measured

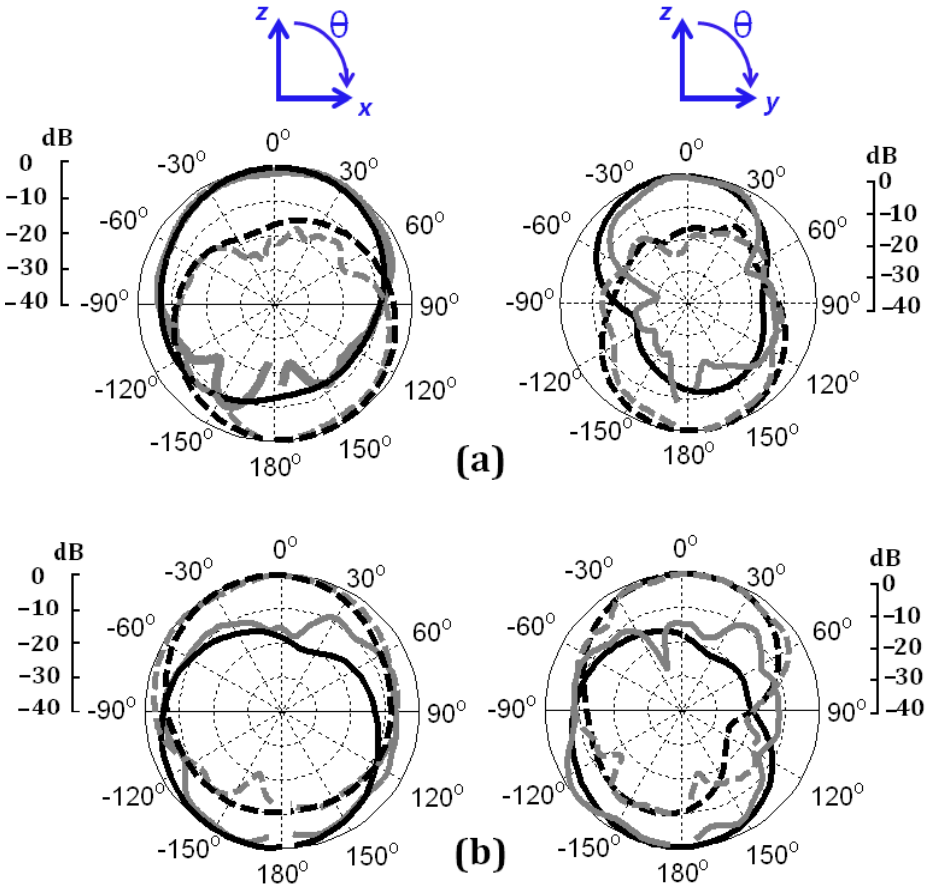

Figure 6.18: **Simulated (black curves) and measured (grey curves) normalised radiation patterns for the H-plane (xz) and E-plane (yz) at 4.8 GHz when the antenna is operating in: a) LHCP mode, b)RHCP mode. Solid lines are for the LHCP components and dashed lines represent the RHCP components.**

sets of data across each plane, the data are post-processed to reconstruct the RHCP and LHCP components of the CP radiation pattern across the two plane cuts as shown in Figure 6.18. It is clear from Figure 6.19 that when the antenna is reconfigured in LHCP, the antenna exhibits a measured 3 dB AR fractional bandwidth of 4.2% (from 4.7 to 4.9 GHz).

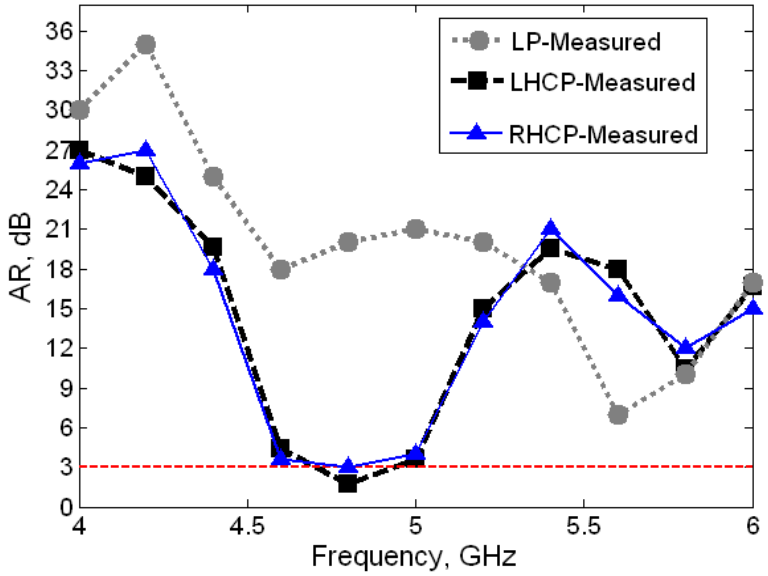

Figure 6.19: **Measured axial ratio at broadside when the antenna is reconfigured in the LP and LHCP/RHCP modes.**

6.6 Summary

A novel planar design for a compact frequency, pattern and polarisation reconfigurable ultra-wideband antenna is presented. The antenna is frequency reconfigurable to limit the impact of out-of-band interferers. Moreover, it provides basic pattern reconfiguration to enhance the scanning or the communication performance in cognitive radio operation by sensing interferers in the space domain and achieving pattern diversity to mitigate fading and increase signal-to-noise ratio (SNR). Another feature of the proposed antenna is that its polarisation is reconfigurable at specific frequencies to generate circular polarised (CP) radiation; this can improve the signal reception in multipath fading environments regardless of the orientation of the portable cognitive radio devices.

Clear design guidelines for the three reconfiguration cases have been introduced, allowing antenna engineers and researchers to apply the proposed

design to other frequency bands or applications. When the antenna is frequency reconfigured, the antenna can switch operation from ultra-wideband mode (2.6–11 GHz) which can be used in CR spectrum sensing, to Band–I (4.39–5.85 GHz) which can be used in CR communication. When the antenna is pattern reconfigured, the radiation patterns change from a nearly omni-directional (Mode–I) to two opposite directional patterns (Mode–II and III). This can assist CR systems through spatial rather than frequency means. A wide measured fractional bandwidth of 58.8% from 3 to 5.5 GHz is achieved for reconfigurable patterns with a measured return loss better than 9.5 dB. Finally, when the antenna is polarisation reconfigured at 4.8 GHz, the antenna can switch radiation from from LP to LHCP/RHCP.

7 Conclusions and Future Work

7.1 Conclusions

Cognitive Radio architectures and future smart wireless applications are exploring the application of different types of reconfigurable antenna to enhance performance and also to enable the transition to more efficient and intelligent radio front-ends. The work in this thesis has introduced some novel frequency, pattern and polarisation reconfigurable antennas for integration in Cognitive radio and future wireless front-ends.

A novel single element reconfigurable ultra-wideband circular disk monopole antenna design was presented. The antenna was simply reconfigured by employing stub tuners to support multiple narrowband frequency ranges. The antenna return loss, radiation patterns and gain were simulated and measured. Using stubs to reconfigure the antenna did not affect the original radiation patterns of the ultra-wideband antenna. The modified wheeler cap method was used to measure the radiation and total efficiency of the antenna. The total efficiency was good in the reconfigured bands, and it was poor in the out of band frequencies which emphasises the filtering role of the reconfiguration process.

A prototype was manufactured for one case of reconfiguration (2.4 GHz) and two p-i-n diodes were soldered onto the board with dc biasing. The

p-i-n diodes used in the prototype have plastic packages with high parasitic package inductance and capacitance that limit the operation of the p-i-n diodes in both the ON and OFF cases, especially at high frequencies.

To overcome most of the difficulties encountered in using p-i-n diodes to frequency reconfigure ultra-wideband antennas, GaAs ultra-wideband transistors were used instead of p-i-n diodes. These switches proved not to complicate the design by simplifying the biasing circuits and they did not affect the antenna's radiation patterns or severely degrade the efficiency and gain. On top of that, they exhibit very low power consumption (in the μW range) which makes them attractive in reconfiguring antennas used in portable wireless communication devices. A further design for a reconfigurable compact ultra wideband (TSA) antenna has been presented. The TSA with dimensions of ($16\ mm \times 27\ mm$) was frequency-reconfigured using microstrip variable length stub placed on the back side to achieve multi-band operation. In addition, this stub can be used as a resonator to notch the operation of the ultra-wideband mode at a specific frequency, this will add high degree of flexibility in the antenna operation as the reconfigurable TSA can work in three modes; namely, ultra-wideband mode, multi band mode and ultra-wideband notched mode.

A novel compact ultra-wideband microstrip monopole antenna with reconfigurable pattern capability has been designed. The antenna's radiation patterns can be shaped to concentrate energy in specific directions while minimising the gain in other unwanted directions, without significantly affecting the impedance bandwidth of the antenna. The designed antenna is highly recommended for providing future smart radio front-end with spatial flexibility by adding the benefits of pattern diversity and interference mitigation. Since most microstrip ultra-wideband monopole antennas are

linearly polarised, an attempt has been made to design microstrip ultra-wideband antenna that can radiate CP with a wide 3-dB axial-ratio fractional bandwidth. A measured 3-dB axial ratio fractional bandwidth of 59 % was achieved. Moreover, the ability to reconfigure the polarisation of the antenna to switch between RHCP and LHCP radiation was demonstrated. Another enhanced design was presented that allowed tuning the CP bandwidth to occur at different frequency bands, this will add more flexibility by allowing the reconfigured antenna to switch between LP and RHCP or LHCP at different frequency bands.

Finally, an attempt has been successfully made to combine the three categories of reconfigurable antennas; namely frequency, pattern and polarisation in one single and compact antenna design, that meets the growing demand of future wireless devices for more intelligent and multi-functional antennas.

In the previous chapters, some discussion and suggestions have been made on how to deploy the previously designed reconfigurable ultra-wideband antennas in a CR system and the author has also mentioned some of the benefits from these possible deployments, these suggestions can be summarised as bellow:

- Ultra-wideband operation is used for spectrum sensing in the frequency domain.
- Ultra-wideband operation can also be used in communication but at reduced range and power.
- Reconfigured frequency bands can be use in communication between CR devices.
- Ultra-wideband operation with a notched mode can limit the effect of

a specific strong interferer in the sensing or communication operation.

- Reconfigured radiation pattern capability allow sensing interferers in the space domain and then Cognitive Radio devices can communicate with nulls or reduced gain patterns steered to the interference directions.

- CP operation can increase CR device signal reception in harsh environments. Moreover, polarisation reconfiguration from RHCP/LHCP can add polarisation diversity benefits in CR systems.

7.2 Key Contributions

The major contributions of this work are summarised as follows:

- A frequency reconfigurable compact ultra-wideband antenna using GaAs switches. The antenna can switch operation from an ultra-wideband mode to three distinct frequency sub-bands.

- A compact ultra-wideband antenna with reconfigurable patterns. A fully functional prototype has been developed and tested. The radiation patterns can be reconfigured from a nearly omnidirectional to two opposite end-fire patterns with wide measured fractional bandwidth of 66% from 3 to 6 GHz.

- Two novel compact ultra-wideband microstrip monopole antennas with reconfigurable polarisation capabilities. The first antenna can be switched from linear polarisation to right hand circularly polarisation or left hand circular polarisation with a measured 3 dB axial-ratio (AR) fractional bandwidth of 59.5 % from 5.9 to 10.9 GHz. In the second antenna, the CP bandwidth can be changed at different frequency bands.

The experimental fractional bandwidths of the 3-dB axial ratio are 37 % from (5.8 to 8.4 GHz) for Band I and 21 % from (4.7 to 5.8 GHz) for Band II.

- A novel design in which the three categories of reconfigurable antennas; namely frequency, pattern and polarisation are combined in a single and compact reconfigurable antenna.

7.3 Future Work

Based on the conclusions drawn of the work presented in the previous chapters, the following issues could provide potential progress to the work introduced in this thesis:

Antenna Element Design

- The reconfigurable antenna element designs presented in this thesis can be enhanced by using MEMS switches instead of p-i-n diodes, this is due to the low losses they introduce in the antenna and to their inherent low dc power consumption and good linearity. Also, the use of optical switches can be investigated.

- The possibility of designing the proposed reconfigurable antennas using cheap organic substrates such as paper by using low-cost fabrication methods (e.g, ink-jet printing) can also be investigated.

- The bias lines form an integral part of the design of reconfigurable antennas. As metal bias lines can alter the performance of reconfigurable antennas, the use of resistive adhesive bias lines can be a practical and cost-effective solution [127].

- The antenna designed in Chapter 6, in which the three categories of reconfiguration are combined, can be further enhanced by having some reconfigurable band notching capabilities. This can be easily done by embedding slots (controlled by switches) in the middle of the circular radiator.

Reconfiguration Control and Integration with Software Defined-Radio

- The process of controlling the voltage/ current states of the switches in the designed reconfigurable antennas in the previous chapters, has been done manually and for future designs, a control board with a μ-controller or an FPGA would make the switching easier and more practical.

- System integration of reconfigurable antennas and Cognitive Radio can be investigated. Universal Software Radio Peripheral (USRP2) devices [128] can help deploying the designed reconfigurable antennas in a real time Cognitive Radio test-bed.

The Move Towards Reconfigurable Antenna Arrays

- A Conventional array has a fixed element factor and by controlling the array factor, the properties of the array can change. Nevertheless, significant additional degree of freedom is achieved if the previously designed reconfigurable single-element antennas are arranged in an array. Reconfigurable arrays can enhance the performance of future wireless networks at fraction of the cost of using complex phased arrays.

References

[1] C. A. Balanis, *Modern Antenna Handbook*. New York: John Wiley, 2008.

[2] J. Mitola and J. Maguire, "Cognitive radio: making software radios more personal," *Personal Communications, IEEE*, vol. 6, no. 4, pp. 13–18, 1999.

[3] FCC, "Report of the spectrum efficiency working," FCC spectrum policy task force, Tech. Rep., Nov. 2002.

[4] P. Hall, P. Gardner, J. Kelly, E. Ebrahimi, M. Hamid, F. Ghanem, F. Herraiz-Martinez, and D. Segovia-Vargas, "Reconfigurable antenna challenges for future radio systems," in *Proc. 3rd Eur. Conf. Antennas and Propag. (EUCAP)*, 2009, pp. 949–955.

[5] Software Defined Radio Forum. Accessed: 16-12-2013. [Online]. Available: http://www.sdrforum.org

[6] QinetiQ, "Cognitive radio technology, a study for Ofcom," QinetiQ, Tech. Rep., Feb. 2007.

[7] A. Wyglinski, *Cognitive Radio Communications and Networks: Principles and Practice*. Elsevier, 2010.

[8] FCC, "First report and order and further notice of proposed rule making in the matter of unlicensed operation in TV broadcast bands," FCC, Tech. Rep. 04/186, Oct. 2006.

[9] FCC, "FCC's office of engineering and technology release report on tests of prototype white space devices," FCC, Tech. Rep. 04/186, Oct. 2008.

[10] FCC. Accessed: 16-12-2013. [Online]. Available: http://hraunfoss.fcc.gov/edocs_public/attachmatch/DOC-286566A1.pdf

[11] Ofcom, "Dividend review, a statement on our approach to awarding the digital dividend," Ofcom, Tech. Rep., Dec. 2007.

[12] FCC, "Final rules for the cognitive use of TV white spaces in the US," FCC, Tech. Rep. 10/174.

[13] A blog on Cognitive Radio. Accessed: 16-12-2013. [Online]. Available: http://spectralholes.blogspot.co.uk/2010/09/final-fcc-rules-cognitive-radio-or-just.html

[14] FCC. Accessed: 16-12-2013. [Online]. Available: http://hraunfoss.fcc.gov/edocs_public/attachmatch/DA-11-131A1.pdf

[15] J. Perruisseau-Carrier, P. Pardo-Carrera, and P. Miskovsky, "Modeling, design and characterization of a very wideband slot antenna with reconfigurable band rejection," *IEEE Trans. Antennas Propag.*, vol. 58, no. 7, pp. 2218–2226, 2010.

[16] C. A. Balanis, *Antenna Theory: Analysis and Design.* New York: John Wiley, 2005.

[17] J. Desjardins, D. McNamara, S. Thirakoune, and A. Petosa, "Electronically frequency-reconfigurable rectangular dielectric resonator antennas," *IEEE Trans. Antennas Propag.*, vol. 60, no. 6, pp. 2997–3002, 2012.

[18] M. Zamudio, Y. Tawk, J. Costantine, J. Kim, and C. Christodoulou, "Integrated cognitive radio antenna using reconfigurable band pass filters," in *Proc. 5th Eur. Conf. Antennas and Propag. (EUCAP)*, Apr. 2011, pp. 2108 –2112.

[19] H. AbuTarboush, R. Nilavalan, S. W. Cheung, K. Nasr, T. Peter, D. Budimir, and H. Al-Raweshidy, "A reconfigurable wideband and multiband antenna using dual-patch elements for compact wireless devices," *IEEE Trans. Antennas Propag.*, vol. 60, no. 1, pp. 36–43, Jan. 2012.

[20] L. Pringle, P. Harms, S. Blalock, G. Kiesel, E. Kuster, P. Friederich, R. Prado, J. Morris, and G. Smith, "A reconfigurable aperture antenna based on switched links between electrically small metallic patches," *IEEE Trans. Antennas Propag.*, vol. 52, no. 6, pp. 1434–1445, 2004.

[21] E. Erdil, K. Topalli, M. Unlu, O. Civi, and T. Akin, "Frequency tunable microstrip patch antenna using rf MEMS technology," *IEEE Trans. Antennas Propag.*, vol. 55, no. 4, pp. 1193–1196, Apr. 2007.

[22] N. Behdad and K. Sarabandi, "A varactor-tuned dual-band slot an-

tenna," *IEEE Trans. Antennas Propag.*, vol. 54, no. 2, pp. 401–408, Feb. 2006.

[23] C. Panagamuwa, A. Chauraya, and J. Vardaxoglou, "Frequency and beam reconfigurable antenna using photoconducting switches," *IEEE Trans. Antennas Propag.*, vol. 54, no. 2, pp. 449–454, Feb. 2006.

[24] Y. Tawk, J. Costantine, and C. Christodoulou, "A frequency reconfigurable rotatable microstrip antenna design," in *Antennas and Propagation Society International Symposium (APSURSI), 2010 IEEE*, 2010, pp. 1–4.

[25] L. Liu and R. Langley, "Liquid crystal tunable microstrip patch antenna," *Electron. Lett.*, vol. 44, no. 20, pp. 1179–1180, 2008.

[26] D. Pozar and V. Sanchez, "Magnetic tuning of a microstrip antenna on a ferrite substrate," *Electron. Lett.*, vol. 24, no. 12, pp. 729–731, 1988.

[27] A. M. Yadav, C. Panagamuwa, and R. Seager, "Investigating the effects of control lines on a frequency reconfigurable patch antenna," in *Antennas and Propagation Conference (LAPC), 2010 Loughborough*, 2010, pp. 605–608.

[28] A. M. Yadav, C. Panagamuwa, and R. Seager, "Analysis of techniques to minimise the interference effects of metallic control lines on reconfigurable microstrip antennas," in *Antennas and Propagation Conference (LAPC), 2011 Loughborough*, 2011, pp. 1–6.

[29] A. J. KING, "A frequency reconfigurable slot antenna with a conductive microfluidic switching mechanism," Master's thesis, University

of Illinois at Urbana-Champaign, Department of Electrical and Computer Engineering, Urbana, Illinois, 2012.

[30] K. Buisman, L. de Vreede, L. Larson, M. Spirito, A. Akhnoukh, T. Scholtes, and L. Nanver, "Distortion-free varactor diode topologies for RF adaptivity," in *Microwave Symposium Digest, 2005 IEEE MTT-S International*, 2005, pp. 4 pp.–.

[31] R. Caverly and G. Hiller, "Distortion in p-i-n diode control circuits," *Microwave Theory and Techniques, IEEE Transactions on*, vol. 35, no. 5, pp. 492–501, 1987.

[32] V. Cojocaru and F. Sischka, "Non-linear modelling of microwave pin diode switches for harmonic and intermodulation distortion simulation," in *Microwave Symposium Digest, 2003 IEEE MTT-S International*, vol. 2, 2003, pp. 655–658 vol.2.

[33] C. Liessner, J. Barrett, J. Palma, D. Gleason, and S. Mil'shtein, "Improving FET switch linearity," *Electron Devices, IEEE Transactions on*, vol. 54, no. 3, pp. 391–397, 2007.

[34] H. Ishida, Y. Hirose, T. Murata, Y. Ikeda, T. Matsuno, K. Inoue, Y. Uemoto, T. Tanaka, T. Egawa, and D. Ueda, "A high-power RF switch IC using AlGaN/GaN HFETs with single-stage configuration," *Electron Devices, IEEE Transactions on*, vol. 52, no. 8, pp. 1893–1899, 2005.

[35] G. Rebeiz, C. Patel, S. Han, C.-H. Ko, and K. Ho, "The search for a reliable MEMS switch," *Microwave Magazine, IEEE*, vol. 14, no. 1, pp. 57–67, 2013.

[36] Radant MEMS. Accessed: 16-12-2013. [Online]. Available: http://www.radantmems.com/radantmems/products.html

[37] E. Kowalczuk, C. Panagamuwa, R. Seager, and J. Vardaxoglou, "Characterising the linearity of an optically controlled photoconductive microwave switch," in *Antennas and Propagation Conference (LAPC), 2010 Loughborough*, 2010, pp. 597–600.

[38] Y. Cai, Y. Guo, and T. Bird, "A frequency reconfigurable printed yagi-uda dipole antenna for cognitive radio applications," *IEEE Trans. Antennas Propag.*, vol. 60, no. 6, pp. 2905–2912, 2012.

[39] S. Yong, "Design and analysis of pattern null reconfigurable antennas," Ph.D. dissertation, University of Illinois at Urbana-Champaign, Department of Electrical and Computer Engineering, Urbana, Illinois, 2012.

[40] K. Kim, M. Zuo, and W. Kuo, "On the relationship of semiconductor yield and reliability," *Semiconductor Manufacturing, IEEE Transactions on*, vol. 18, no. 3, pp. 422–429, 2005.

[41] W. de Groot, J. Webster, D. Felnhofer, and E. Gusev, "Review of device and reliability physics of dielectrics in electrostatically driven mems devices," *Device and Materials Reliability, IEEE Transactions on*, vol. 9, no. 2, pp. 190–202, 2009.

[42] Y. Huang, A. Vasan, R. Doraiswami, M. Osterman, and M. Pecht, "Mems reliability review," *Device and Materials Reliability, IEEE Transactions on*, vol. 12, no. 2, pp. 482–493, 2012.

[43] C. Patel and G. Rebeiz, "A high-reliability high-linearity high-power RF MEMS metal-contact switch for dc –40-ghz applications," *Mi-*

crowave Theory and Techniques, IEEE Transactions on, vol. 60, no. 10, pp. 3096–3112, 2012.

[44] R. Haupt and M. Lanagan, "Reconfigurable antennas," *IEEE Antennas Propag. Mag.*, vol. 55, no. 1, pp. 49–61, 2013.

[45] H. AbuTarboush, R. Nilavalan, K. Nasr, S. W. Cheung, T. Peter, H. S. Al-Raweshidy, and D. Budimir, "Reconfigurable tri-band h-shaped antenna with frequency selectivity feature for compact wireless communication systems," *Microwaves, Antennas Propagation, IET*, vol. 5, no. 14, pp. 1675–1682, 2011.

[46] H. AbuTarboush, R. Nilavalan, S. Cheung, and K. Nasr, "Compact printed multiband antenna with independent setting suitable for fixed and reconfigurable wireless communication systems," *IEEE Trans. Antennas Propag.*, vol. 60, no. 8, pp. 3867–3874, 2012.

[47] E. Ebrahimi and P. Hall, "A dual port wide-narrowband antenna for cognitive radio," in *Proc. 3rd Eur. Conf. Antennas and Propag. (EUCAP)*, 2009, pp. 809–812.

[48] M. Al-Husseini, Y. Tawk, C. Christodoulou, K. Kabalan, and A. El-Hajj, "A reconfigurable cognitive radio antenna design," in *Antennas and Propagation Society International Symposium (APSURSI), 2010 IEEE*, 2010, pp. 1–4.

[49] E. Erfani, J. Nourinia, C. Ghobadi, M. Niroo-Jazi, and T. Denidni, "Design and implementation of an integrated UWB/reconfigurable-slot antenna for cognitive radio applications," *IEEE Antennas Wireless Propag. Lett.*, vol. 11, pp. 77–80, 2012.

[50] J. Kelly, P. Hall, and P. Gardner, "Integrated wide-narrow band antenna for switched operation," in *Proc. 3rd Eur. Conf. Antennas and Propag. (EUCAP)*, 2009, pp. 3757–3760.

[51] M. Hamid, P. Gardner, P. Hall, and F. Ghanem, "Switched-band vivaldi antenna," *IEEE Trans. Antennas Propag.*, vol. 59, no. 5, pp. 1472–1480, 2011.

[52] M. R. Hamid, P. Gardner, P. S. Hall, and F. Ghanem, , "Vivaldi antenna with integrated switchable band pass resonator," *IEEE Trans. Antennas Propag.*, vol. 59, no. 11, pp. 4008–4015, 2011.

[53] S. Nikolaou, N. Kingsley, G. Ponchak, J. Papapolymerou, and M. Tentzeris, "UWB elliptical monopoles with a reconfigurable band notch using MEMS switches actuated without bias lines," *IEEE Trans. Antennas Propag.*, vol. 57, no. 8, pp. 2242–2251, 2009.

[54] X. Artiga, J. Perruisseau-Carrier, P. Pardo-Carrera, I. Llamas-Garro, and Z. Brito-Brito, "Halved vivaldi antenna with reconfigurable band rejection," *IEEE Antennas Wireless Propag. Lett.*, vol. 10, pp. 56–58, 2011.

[55] M. R. Hamid, P. Gardner, P. S. Hall, and F. Ghanem, "Vivaldi with tunable narrow band rejection," *Microw. Opt. Technol. Lett.*, vol. 53, no. 5, pp. 1125–1128, 2011. [Online]. Available: http://dx.doi.org/10.1002/mop.25924

[56] W. Kang, S. Lee, and K. Kim, "Design of symmetric beam pattern reconfigurable antenna," *Electron. Lett.*, vol. 46, no. 23, pp. 1536–1537, 2010.

[57] W. Kang, J. Park, and Y. Yoon, "Simple reconfigurable antenna with radiation pattern," *Electron. Lett.*, vol. 44, no. 3, pp. 182–183, 2008.

[58] P.-Y. Qin, Y. Guo, A. Weily, and C.-H. Liang, "A pattern reconfigurable U-slot antenna and its applications in MIMO systems," *IEEE Trans. Antennas Propag.*, vol. 60, no. 2, pp. 516–528, 2012.

[59] S. J. Wu and T. G. Ma, "A wideband slotted bow-tie antenna with reconfigurable cpw-to-slotline transition for pattern diversity," *IEEE Trans. Antennas Propag.*, vol. 56, no. 2, pp. 327–334, Feb. 2008.

[60] Y. Li, Z. Zhang, J. Zheng, Z. Feng, and M. F. Iskander, "Experimental analysis of a wideband pattern diversity antenna with compact reconfigurable cpw-to-slotline transition feed," *IEEE Trans. Antennas Propag.*, vol. 59, no. 11, pp. 4222–4228, Nov. 2011.

[61] G. Zhang, J. Hong, B. Wang, G. Song, and P. Li, "Design and time-domain analysis for a novel pattern reconfigurable antenna," *IEEE Antennas Wireless Propag. Lett.*, vol. 10, pp. 365–368, 2011.

[62] A. Grau, J. Romeu, M.-J. Lee, S. Blanch, L. Jofre, and F. de Flaviis, "A dual-linearly-polarized MEMS-reconfigurable antenna for narrowband mimo communication systems," *IEEE Trans. Antennas Propag.*, vol. 58, no. 1, pp. 4–17, 2010.

[63] S.-H. Hsu and K. Chang, "A novel reconfigurable microstrip antenna with switchable circular polarization," *IEEE Antennas Wireless Propag. Lett.*, vol. 6, pp. 160–162, 2007.

[64] B. Kim, B. Pan, S. Nikolaou, Y.-S. Kim, J. Papapolymerou, and M. Tentzeris, "A novel single-feed circular microstrip antenna with re-

configurable polarization capability," *IEEE Trans. Antennas Propag.*, vol. 56, no. 3, pp. 630–638, 2008.

[65] W. Cao, B. Zhang, A. Liu, T. Yu, D. Guo, and K. Pan, "A reconfigurable microstrip antenna with radiation pattern selectivity and polarization diversity," *IEEE Antennas Wireless Propag. Lett.*, vol. 11, pp. 453–456, 2012.

[66] P.-Y. Qin, Y. Guo, Y. Cai, E. Dutkiewicz, and C.-H. Liang, "A reconfigurable antenna with frequency and polarization agility," *IEEE Antennas Wireless Propag. Lett.*, vol. 10, pp. 1373–1376, 2011.

[67] A. M. Yadav, C. Panagamuwa, and R. Seager, "Investigation of a plug hole shaped frequency and pattern reconfigurable antenna using photo-conductive microwave switches," in *Microwave Conference (EuMC), 2011 41st European*, 2011, pp. 878–881.

[68] J. Liang, C. C. Chiau, X. Chen, and C. G. Parini, "Study of a printed circular disc monopole antenna for UWB systems," *IEEE Trans. Antennas Propag.*, vol. 53, no. 11, pp. 3500–3504, Nov. 2005.

[69] CST vers. 12. Accessed: 16-12-2013. [Online]. Available: http://www.cst.com

[70] FCC. Accessed: 16-12-2013. [Online]. Available: http://hraunfoss.fcc.gov/edocs_public/attachmatch/FCC-02-48A1.pdf

[71] *IEEE Standard Test Procedures for Antennas*, ANSI/IEEE Std. 149-1979, 1979.

[72] W. L. Stutzman and G. Thiele, *Antenna Theory and Design.* New York: John Wiley, 2008.

[73] M.-C. Huynh, "Wideband compact antennas for wireless communication," Ph.D. dissertation, Virginia Polytechnic Institute, Department of Electrical and Computer Engineering, Virginia, 2004.

[74] G. Smith, "An analysis of the Wheeler method for measuring the radiating efficiency of antennas," *IEEE Trans. Antennas Propag.*, vol. 25, no. 4, pp. 552–556, 1977.

[75] H. Wheeler, "The radiansphere around a small antenna," *Proceedings of the IRE*, vol. 47, no. 8, pp. 1325–1331, 1959.

[76] E. Newman, P. Bohley, and C. H. Walter, "Two methods for the measurement of antenna efficiency," *IEEE Trans. Antennas Propag.*, vol. 23, no. 4, pp. 457–461, 1975.

[77] D. M. Pozar and B. Kaufman, "Comparison of three methods for the measurement of printed antenna efficiency," *IEEE Trans. Antennas Propag.*, vol. 36, no. 1, pp. 136–139, 1988.

[78] H. Schantz, "Radiation efficiency of UWB antennas," in *IEEE Conference on Ultra Wideband Systems and Technologies, 2002.*, 2002, pp. 351–355.

[79] BAR64-03W. Accessed: 16-12-2013. [Online]. Available: http://www.infineon.com/cms/en/product/index.html

[80] bcl-531J. Accessed: 16-12-2013. [Online]. Available: http://www.coilcraft.com/bcl.cfm

[81] Y.-S. Wang, J.-C. Lu, and S.-J. Chung, "A miniaturized ground edge current choke; design, measurement, and applications," *IEEE Trans. Antennas Propag.*, vol. 57, no. 5, pp. 1360–1366, 2009.

[82] C.-I. Yeh, D.-H. Yang, Y.-N. Chen, T.-H. Liu, J. Fu, H.-C. Chiu, and H.-L. Kao, "Dumbbell DGS based broadband RF choke for UWB LNA," in *International Conference on Applications of Electromagnetism and Student Innovation Competition Awards (AEM2C), 2010*, 2010, pp. 162–166.

[83] Y.-C. Jeong, S.-G. Jeong, J.-S. Lim, and S. Nam, "A new method to suppress harmonics using $\lambda/4$ bias line combined by defected ground structure in power amplifiers," *IEEE Microw. Wireless Compon. Lett.*, vol. 13, no. 12, pp. 538–540, 2003.

[84] D. Anagnostou, G. Zheng, M. Chryssomallis, J. Lyke, G. Ponchak, J. Papapolymerou, and C. Christodoulou, "Design, fabrication, and measurements of an RF-MEMS-based self-similar reconfigurable antenna," *IEEE Trans. Antennas Propag.*, vol. 54, no. 2, pp. 422–432, 2006.

[85] Skyworks, "Application Note, Design With PIN Diodes," skyworksin.com, Tech. Rep., Oct. 2012.

[86] Skyworks. Accessed: 16-12-2013. [Online]. Available: http://www.skyworksinc.com /uploads/documents/200797C.pdf

[87] A. Rahman and Y. Hao, "A novel tapered slot cpw-fed antenna for ultra-wideband applications and its on/off-body performance," in *Antenna Technology: Small and Smart Antennas Metamaterials and Ap-*

plications, 2007. IWAT '07. International Workshop on, 2007, pp. 503–506.

[88] Advanced Design System (ADS). Agilent Technologies, santa clara, CA, 2005. Accessed: 16-12-2013. [Online]. Available: http://www.agilent.com

[89] D. Cabric, S. Mishra, and R. Brodersen, "Implementation issues in spectrum sensing for cognitive radios," in *Conference Record of the Thirty-Eighth Asilomar Conference on Signals, Systems and Computers, 2004.*, vol. 1, 2004, pp. 772–776.

[90] Avago Technologies, San Jose, CA, 2012. Accessed: 16-12-2013. [Online]. Available: http://www.avagotech.com/docs/AV01-0593EN

[91] MA4AGBLP912. Accessed: 16-12-2013. [Online]. Available: https://www.macomtech.com/pin-switch-and-attenuator-diodes

[92] S. Nikolaou, R. Bairavasubramanian, C. Lugo, I. Carrasquillo, D. C. Thompson, G. E. Ponchak, J. Papapolymerou, and M. M. Tentzeris, "Pattern and frequency reconfigurable annular slot antenna using pin diodes," *IEEE Trans. Antennas Propag.*, vol. 54, no. 5, pp. 439–448, Feb. 2006.

[93] Q. Q. He and B. Z. Wang, "Pattern reconfigurable double folded slot antenna with background conductor," *Electron. Lett.*, vol. 43, no. 15, pp. 791–792, Jul. 2007.

[94] Y. Y. Bai, S. Xiao, M. C. Tang, C. Liu, and B. Z. Wang, "Pattern reconfigurable antenna with wide angle coverage," *Electron. Lett.*, vol. 47, no. 21, pp. 1163–1164, Oct. 2011.

[95] W. Cao, B. Zhang, A. Liu, T. Yu, D. Guo, and K. Pan, "A reconfigurable microstrip antenna with radiation pattern selectivity and polarization diversity," *IEEE Antennas Wireless Propag. Lett.*, vol. 11, pp. 453–456, 2012.

[96] S. Zhang, G. H. Huff, J. Feng, and J. T. Bernhard, "A pattern reconfigurable microstrip parasitic array," *IEEE Trans. Antennas Propag.*, vol. 52, no. 10, pp. 2773–2776, Oct. 2004.

[97] C. Ko, I. Tarn, and S. Chung, "A compact dual-band pattern diversity antenna by dual-band reconfigurable frequency selective reflectors with a minimum number of switches," *IEEE Trans. Antennas Propag.*, vol. 61, no. 2, pp. 646–654, Feb. 2013.

[98] S. Zhan, Z. Ruping, D. Jun, and G. Chenjiang, "A novel pattern-reconfigurable antenna using switched printed elements," *IEEE Antennas Wireless Propag. Lett.*, vol. 11, pp. 1100–1103, 2012.

[99] M. Gallo, E. Antonino-Daviu, M. Ferrando-Bataller, M. Bozzetti, J. M. Molina-Garcia-Pardo, and L. Juan-Llacer, "A broadband pattern diversity annular slot antenna," *IEEE Trans. Antennas Propag.*, vol. 60, no. 3, pp. 1596–1600, Mar. 2012.

[100] D. Yuandan and T. Itoh, "Planar ultra-wideband antennas in ku- and k-band for pattern or polarization diversity applications," *IEEE Trans. Antennas Propag.*, vol. 60, no. 6, pp. 2886–2895, Jun. 2012.

[101] G. H. Huff and J. T. Bernhard, "Integration of packaged RF MEMS switches with radiation pattern reconfigurable square spiral microstrip antennas," *IEEE Trans. Antennas Propag.*, vol. 54, no. 2, pp. 464–469, Feb. 2006.

[102] Agilent Technologies, Application Note 985. Accessed: 16-12-2013. [Online]. Available: http://cp.literature.agilent.com/litweb/pdf/5989-6257EN.pdf

[103] Coilcraft. Accessed: 16-12-2013. [Online]. Available: http://www.coilcraft.com/0402hp.cfm

[104] A. Abbosh and M. Bialkowski, "Design of ultrawideband planar monopole antennas of circular and elliptical shape," *IEEE Trans. Antennas Propag.*, vol. 56, pp. 17–23, 2008.

[105] Aeroflex/Inmet, Inc., Ann Arbor, MI. Accessed: 16-12-2013. [Online]. Available: http://www.aeroflex.com/AMS/inmet/pdfiles/8037.pdf

[106] L. S. Xiao, L. Li, and S. W. Cheung, "Dual-band antenna with compact radiator for 2.4/5.2/5.8 GHz WLAN applications," *IEEE Trans. Antennas Propag.*, vol. 60, pp. 5924–5931, 2012.

[107] G. Augustin and T. A. Denidni, "An integrated Ultra wideband/narrow band antenna in uniplanar configuration for cognitive radio systems," *IEEE Trans. Antennas Propag.*, vol. 60, pp. 5479–5484, 2012.

[108] J. L. Volakis, *Antenna Engineering Handbook*. McGraw -Hill, 2007.

[109] "IEEE standard definitions of terms for antennas," *IEEE Trans. Antennas Propag.*, vol. 17, no. 3, pp. 262–269, 1969.

[110] T. Rappaport and D. Hawbaker, "Wide-band microwave propagation parameters using circular and linear polarized antennas for indoor wireless channels," *Communications, IEEE Transactions on*, vol. 40, no. 2, pp. 240–245, 1992.

[111] X. Quan, R. Li, and M. Tentzeris, "A broadband omnidirectional circularly polarized antenna," *Antennas and Propagation, IEEE Transactions on*, vol. 61, no. 5, pp. 2363–2370, 2013.

[112] J. D. Kraus and R. J. Marhefka, *Antennas For All Applications*. McGraw Hill, 1997.

[113] H. Kogure, Y. Kogure, and J. C. Rautio, *Introduction to Antenna Analysis Using EM Simulators*. Artech House, 2011.

[114] M. Khalily, M. K. A. Rahim, M. R. Kamarudin, M. Shaneshin, and S. Danesh, "Ultra wideband printed monopole antenna with dual-band circular polarization," in *Proc. 5th Eur. Conf. Antennas and Propag. (EUCAP)*, 2011, pp. 365–368.

[115] J. Pourahmadazar and S. Mohammadi, "Compact circularly-polarised slot antenna for UWB applications," *Electron. Lett.*, vol. 47, no. 15, pp. 837–838, 2011.

[116] S. A. Rahim, S. Danesh, U. A. Okonkwo, M. Sabran, and M. Khalily, "UWB monopole antenna with circular polarization," *Microw. Opt. Technol. Lett.*, vol. 54, no. 4, pp. 949–953, 2012. [Online]. Available: http://dx.doi.org/10.1002/mop.26741

[117] M.-H. Ho, M.-T. Wu, C.-I. G. Hsu, and J.-Y. Sze, "An RHCP/LHCP switchable slotline-fed slot-ring antenna," *Microw. Opt. Technol. Lett.*, vol. 46, no. 1, pp. 30–33, 2005. [Online]. Available: http://dx.doi.org/10.1002/mop.20892

[118] H.-R. Chuang, L.-C. Kuo, C.-C. Lin, and W.-T. Chen, "A 2.4 GHz polarization-diversity planar printed antenna for WLAN and wireless

communication systems," in *Antennas and Propagation Society International Symposium, 2002. IEEE*, vol. 4, 2002, pp. 76–79 vol.4.

[119] F. Yang and Y. Rahmat-Samii, "Patch antennas with switchable slots (PASS) in wireless communications: concepts, designs, and applications," *IEEE Antennas Propag. Mag.*, vol. 47, no. 2, pp. 13–29, 2005.

[120] M. Fries, M. Grani, and R. Vahldieck, "A reconfigurable slot antenna with switchable polarization," *IEEE Microw. Wireless Compon. Lett.*, vol. 13, no. 11, pp. 490–492, 2003.

[121] W. Dorsey, A. Zaghloul, and M. Parent, "Perturbed square-ring slot antenna with reconfigurable polarization," *IEEE Antennas Wireless Propag. Lett.*, vol. 8, pp. 603–606, 2009.

[122] C. T. Rodenbeck, K. Chang, and J. Aubin, "Automated pattern measurement for circularly-polarized antennas using the phase-amplitude method," *Microwave Journal*, vol. 47, no. 7, pp. 68–78, 2004.

[123] F. Liu, C. Feng, C. Guo, Y. Wang, and D. Wei, "Polarization spectrum sensing scheme for cognitive radios," in *5th International Conference on Wireless Communications, Networking and Mobile Computing, WiCom 2009.*, 2009, pp. 1–4.

[124] Vishay. Accessed: 16-12-2013. [Online]. Available: http://www.vishay.com/docs/61090/rfcs.pdf

[125] M. Makimoto and S. Yamashita, "Bandpass filters using parallel coupled stripline stepped impedance resonators," *IEEE Trans. Microw. Theory Tech.*, vol. 28, no. 12, pp. 1413–1417, 1980.

[126] D. M. Pozar, *Microwave Engineering.* New York: John Wiley and Sons, 2005.

[127] J. Kovitz, H. Rajagopalan, and Y. Rahmat-Samii, "Practical and cost-effective bias line implementations for reconfigurable antennas," *IEEE Antennas Wireless Propag. Lett.*, vol. 11, pp. 1552–1555, 2012.

[128] Ettus Research. Accessed: 16-12-2013. [Online]. Available: https://www.ettus.com/product